Deciphering Dark Matter with Cosmological Observations

WILKINSON, RYAN

Deciphering Dark Matter with Cosmological Observations

Ryan Wilkinson

A thesis presented for the degree of
Doctor of Philosophy

Institute for Particle Physics Phenomenology
Department of Physics
Durham University
England, UK

June 2016

Deciphering Dark Matter with Cosmological Observations

Ryan Wilkinson

Submitted for the degree of Doctor of Philosophy

June 2016

Abstract

Determining the nature of dark matter (DM) remains one of the key challenges in both particle physics and cosmology. Although we know the approximate distribution of DM in the Universe, we lack an understanding of its fundamental properties such as its mass and potential couplings to Standard Model particles. In the weakly-interacting massive particle (WIMP) paradigm, DM was in thermal equilibrium in the early Universe and we should expect scattering to have occurred between DM and Standard Model particles. In this thesis, we first consider the impact of primordial scattering between DM and radiation (photons or neutrinos). Such interactions give rise to a modification in the amplitude and position of the cosmic microwave background (CMB) acoustic peaks and a series of damped oscillations in the matter power spectrum. We obtain constraints from the *Planck* satellite and other CMB experiments, and then derive limits from large-scale structure (LSS) surveys. By providing forecasts for future experiments, we illustrate the power of LSS surveys in probing deviations from the standard cold DM (CDM) model. Then, using high-resolution N-body simulations, we show that the suppressed matter power spectra in such interacting DM scenarios allows one to alleviate the small-scale challenges faced by CDM; in particular, the "missing satellite" and "too big to fail" problems. Finally, we show that the excess of 511 keV gamma-rays from the Galactic centre, which has been observed by numerous experiments for four decades, cannot be explained via annihilations of light WIMPs, suggesting an astrophysical or more exotic DM source of the signal.

Declaration

The work in this thesis is based on research carried out at the Institute of Particle Physics Phenomenology, Department of Physics, Durham University, England, UK. No part of this thesis has been submitted elsewhere for any other degree or qualification and it is all my own work unless referenced to the contrary in the text.

The following chapters have been published in the form of papers:

- Chapter 3 is based on Ref. [1]:

  R. J. Wilkinson, J. Lesgourgues, and C. Boehm, "Using the CMB angular power spectrum to study dark matter–photon interactions," JCAP **1404**, 026 (2014), arXiv:1309.7588.

- Chapter 4 is based on Refs. [2, 3]:

  R. J. Wilkinson, C. Boehm, and J. Lesgourgues, "Constraining dark matter–neutrino interactions using the CMB and large-scale structure," JCAP **1405**, 011 (2014), arXiv:1401.7597.

  M. Escudero, O. Mena, A. C. Vincent, R. J. Wilkinson, and C. Boehm, "Exploring dark matter microphysics with galaxy surveys," JCAP **1595**, 034 (2015), arXiv:1505.06735.

- Chapter 5 is based on Refs. [4–6]:

  C. Boehm, J. Schewtschenko, R. Wilkinson, C. Baugh, and S. Pascoli, "Using the Milky Way satellites to study interactions between cold dark matter and radiation," MNRAS **445**, L31-L35 (2014), arXiv:1404.7012.

  J. A. Schewtschenko, R. J. Wilkinson, C. M. Baugh, C. Boehm, and S. Pascoli, "Dark matter–radiation interactions: the impact on dark matter haloes," MNRAS **449**, 3587-3596 (2015), arXiv:1412.4905.

  J. A. Schewtschenko, C. M. Baugh, R. J. Wilkinson, C. Boehm, S. Pascoli, and T. Sawala, "Dark matter–radiation interactions: the structure of Milky Way satellite galaxies," MNRAS doi:10.1093/mnras/stw1078, arXiv:1512.06774.

- Chapter 6 is based on Ref. [7]:

  R. J. Wilkinson, A. C. Vincent, C. Boehm, and C. McCabe, "Ruling out the light WIMP explanation of the Galactic 511 keV line," arXiv:1602.01114.

Acknowledgements

This thesis would not have been possible without the invaluable guidance and advice from my supervisor, Céline Bœhm. I also acknowledge the expertise of my various collaborators: Carlton Baugh, Miguel Escudero, Julien Lesgourgues, Chris McCabe, Olga Mena, Silvia Pascoli, Till Sawala, Jascha Schewtschenko and Aaron Vincent.

My gratitude goes to all the staff and students at the IPPP; in particular, the past and present members of OC118 for providing an enthusiastic and friendly atmosphere in which to work. Most importantly, I thank my family for their unconditional support and encouragement.

I gratefully acknowledge financial support from the Science and Technology Facilities Council (STFC) for the duration of my studies.

Contents

List of Figures

List of Tables

List of Abbreviations

ACT	Atacama Cosmology Telescope
AMS	Alpha Magnetic Spectrometer
ANTARES	Astronomy with a Neutrino Telescope and Abyss Environmental Research project
BAO	Baryon Acoustic Oscillations
BB	Broad Bulge
BBN	Big Bang Nucleosynthesis
BICEP	Background Imaging of Cosmic Extragalactic Polarisation experiment
BOSS	Baryon Oscillation Spectroscopic Survey
CAMB	Code for Anisotropies in the Microwave Background
CDM	Cold Dark Matter
CDMS	Cryogenic Dark Matter Search
CFHT	Canada–France–Hawaii Telescope
CL	Confidence Level
CLASS	Cosmic Linear Anisotropy Solving System
CMB	Cosmic Microwave Background
COBE	Cosmic Background Explorer
COrE	Cosmic Origins Explorer
DASI	Degree Angular Scale Interferometer
DESI	Dark Energy Spectroscopic Instrument
DM	Dark Matter
DR	Data Release / Dark Radiation
EFT	Effective Field Theory

ELG	Emission Line Galaxy
ESA	European Space Agency
FLRW	Friedmann–Lemaître–Robertson–Walker
GUT	Grand Unified Theory
HAWC	High Altitude Water Cherenkov experiment
HDM	Hot Dark Matter
HESS	High Energy Stereoscopic System
HIRES	High-Resolution Echelle Spectrometer
HST	Hubble Space Telescope
IGM	Intergalactic Medium
INTEGRAL	International Gamma-Ray Astrophysics Laboratory
LAT	Large Area Telescope
LG	Local Group
LHC	Large Hadron Collider
LPT	Linear Perturbation Theory
LRG	Luminous Red Galaxy
LSS	Large-Scale Structure
LUX	Large Underground Xenon detector
MACHO	Massive Astrophysical Compact Halo Object
MAGIC	Major Atmospheric Gamma Imaging Cherenkov telescopes
MCMC	Monte Carlo Markov Chain
MIKE	Magellan–Inamori–Kyocera–Echelle spectrometer
MOND	Modified Newtonian Dynamics
MW	Milky Way
NB	Narrow Bulge
NFW	Navarro–Frenk–White
PAMELA	Payload for Antimatter Matter Exploration and Light-nuclei Astrophysics experiment
PArthENoPE	Public Algorithm Evaluating the Nucleosynthesis of Primordial Elements

PDG	Particle Data Group
PIXIE	Primordial Inflation Explorer
POLARBEAR	Polarisation of Background Radiation experiment
QCD	Quantum Chromodynamics
QSO	Quasi-Stellar Object
sDAO	Strong Dark Acoustic Oscillations
SDSS	Sloan Digital Sky Survey
SM	Standard Model
SPI	Spectrometer on INTEGRAL
SPT	South Pole Telescope
SZ	Sunyaev–Zel'dovich
VERITAS	Very Energetic Radiation Imaging Telescope Array System
WDM	Warm Dark Matter
WIMP	Weakly-Interacting Massive Particle
WMAP	Wilkinson Microwave Anisotropy Probe
XDM	Exciting Dark Matter
γCDM	ΛCDM with the addition of DM–photon scattering
ΛCDM	The "Standard Model" of cosmology
νCDM	ΛCDM with the addition of DM–neutrino scattering

Chapter 1

Introduction

The history of astronomy is a history of receding horizons.

— Edwin Hubble

One of the most important results in cosmology is the observation that around 85% of all matter in the universe is in the form of *dark matter* (DM) [8–11]. From numerical simulations, we know that DM plays a fundamental role in structure formation and the evolution of galaxies. However, despite its implications, direct evidence for the existence of DM and an understanding of its fundamental properties have remained elusive. Furthermore, there is no candidate in the *Standard Model* (SM) of particle physics that fulfils all the requirements for DM, demonstrating the need for new physics beyond the SM. The aim of this thesis is to shine light on one aspect of the DM puzzle: the potential interactions of DM beyond gravity. Namely, we wish to know if such interactions are allowed, and if so, what are their consequences and can we use cosmological observations to either constrain or detect them?

In this introductory chapter, we discuss the standard Big Bang cosmological model and the theoretical and experimental status of DM. In Sec. 1.1, we summarise the observational evidence for DM. In Sec. 1.2, we explain the underlying principles of the Big Bang and describe three important events in the chronology of the universe; namely, *Big Bang nucleosynthesis* (BBN) [Sec. 1.2.1], the production of the *cosmic microwave background* (CMB) [Sec. 1.2.2] and structure formation [Sec. 1.2.3]. In Sec. 1.3, we explain the important concept of *thermal* DM and the motivation for the *weakly-interacting massive particle*

(WIMP) paradigm. In Sec. 1.4, we discuss the current experimental status of DM from *direct* [Sec. 1.4.1], *indirect* [Sec. 1.4.2] and *collider* [Sec. 1.4.3] searches. Finally, we provide an outline for the thesis in Sec. 1.5.

1.1 Observational Evidence for Dark Matter

The evidence that DM is required to explain the observed structure of the universe has been building for over seventy years. In 1933, Fritz Zwicky discovered that the outer members of the Coma galaxy cluster are moving far too quickly to be merely following the gravitational potential of the visible matter [12]. He proposed the existence of non-luminous DM that would provide the necessary additional mass to explain the motion of the galaxies. Today, equivalent methods are used to weigh clusters in large-scale X-ray surveys and have consistently confirmed Zwicky's results (see e.g. Ref. [13]).

Almost forty years later, Vera Rubin and collaborators discovered that, like the galaxies of the Coma cluster, stars in the outer regions of spiral galaxies orbit the centre far more quickly than one would expect if galaxies consisted of only visible matter. In Fig. 1.1, we present a typical galaxy *rotation curve*, showing the orbital velocity V_c of stars as a function of their distance from the Galactic centre r. In Newtonian gravity, we have the simple relation[1]

$$V_c(r) = \sqrt{\frac{GM(r)}{r}} \,, \tag{1.1.1}$$

where G is Newton's gravitational constant, $M(r) = 4\pi \int \rho(r)\, r^2 \, \mathrm{d}r$ is the mass enclosed within radius r (assuming it is spherically symmetric) and $\rho(r)$ is the mass density.

It is thought that the flat rotation curves we observe away from the Galactic centre are a consequence of galaxies being embedded in a centrally-concentrated DM *halo* (see the dashed-dotted curve in Fig. 1.1). Using Eq. (1.1.1), a constant value of V_c implies that DM haloes have densities $\rho(r) \propto r^{-2}$ at large radii.

[1] This result follows from *Kepler's Third Law*: $P^2 = (4\pi^2/GM)\, r^3$, where $P = 2\pi r/V_c$ is the orbital period.

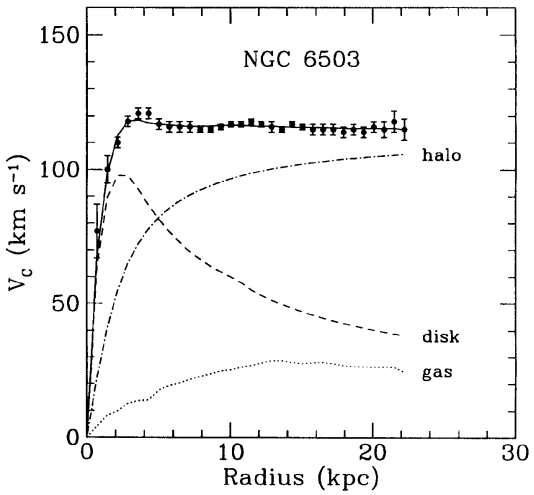

Figure 1.1: A typical rotation curve for a spiral galaxy (solid curve with data points), showing the orbital velocity of stars V_c as a function of their distance from the Galactic centre [14]. The dashed and dotted curves show the predicted contribution from the stellar disk and gas components of the galaxy, respectively. Including a DM halo (dashed-dotted) allows one to explain the discrepancy between theory and observation.

The existence of DM is also inferred on extragalactic scales. One of the most successful techniques for studying the large-scale distribution of DM in the universe has been *gravitational lensing* (see e.g. Refs. [15, 16]). An important consequence of *General Relativity* is that matter and energy curve space-time and deflect passing rays of light [17]. In particular, the presence of a galaxy cluster causes lensing effects; shifting, distorting and magnifying the images of background galaxies. By carefully modelling these effects in simulations, the matter distribution of the foreground object can be determined and compared to its observed structure. Again, such studies suggest that a large fraction of the matter is non-luminous [15, 16].

One dramatic example of gravitational lensing is seen in the *Bullet Cluster* (1E 0657-558), which is thought to have resulted from the collision of two separate galaxy clusters [18]. Fig. 1.2 shows the distribution of luminous matter in the cluster, in comparison to the total mass inferred from lensing measurements. One can see that after the collision, the majority of the mass lies away from the visible matter, implying an abundance of non-luminous DM with only weak-strength interactions. Similar results have been found in other merging clusters such as MACSJ0025.4-1222 [19]. However, the "dark core" observed in Abell 520 [20] (a concentration of

DM at the cluster's centre that is devoid of luminous galaxies) remains difficult to explain in conventional DM models [21].

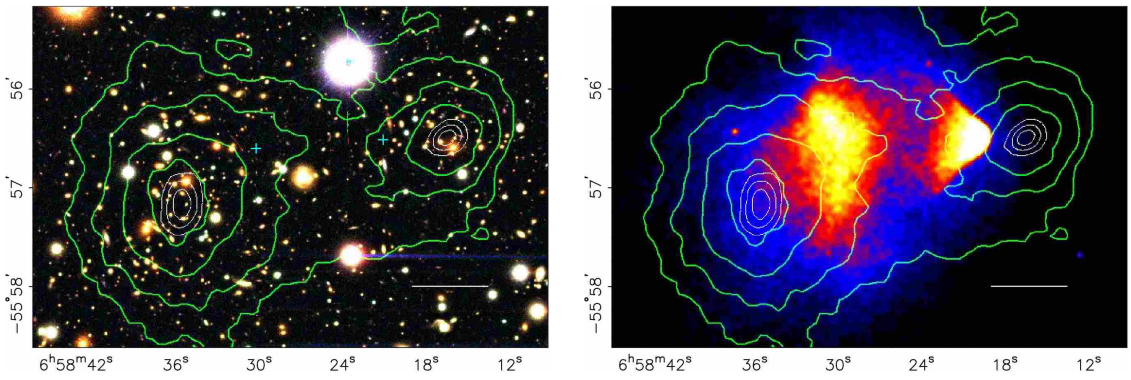

Figure 1.2: Colour images of the Bullet Cluster from the Magellan optical telescopes (left) and the Chandra X-ray observatory (right) [22]. The white bars indicate a distance of 200 kpc. The green contours show the distribution of mass that is inferred from weak lensing measurements. The luminous matter (illustrated by the coloured regions in the right-hand panel) does not coincide with the inferred mass distribution, implying a significant fraction of weakly-interacting DM.

Finally, we note that there have been attempts to explain the discrepancy in mass between prediction and observation using alternative models of gravity such as *modified Newtonian dynamics* (MOND) [23–25]. Although MOND can successfully predict a variety of Galactic phenomena, it cannot eliminate the need for DM in systems such as the Bullet Cluster [22]. Furthermore, there is extreme tension between the predictions of modified gravity theories and studies of the *cosmic microwave background* (CMB) and *large-scale structure* (LSS) of the universe [26]. In contrast, we present further evidence for DM from CMB and LSS observations in Sec. 1.2.

1.2 The Expanding Universe

In 1929, Edwin Hubble discovered that distant galaxies are receding away from us, with a velocity that is directly proportional to their distance [27] (see Fig. 1.3). This observation led to the remarkable conclusion that the universe is expanding and gave rise to the prevailing Big Bang model, where the universe has evolved from a hot, dense plasma for around 13.8 billion years [8–11].

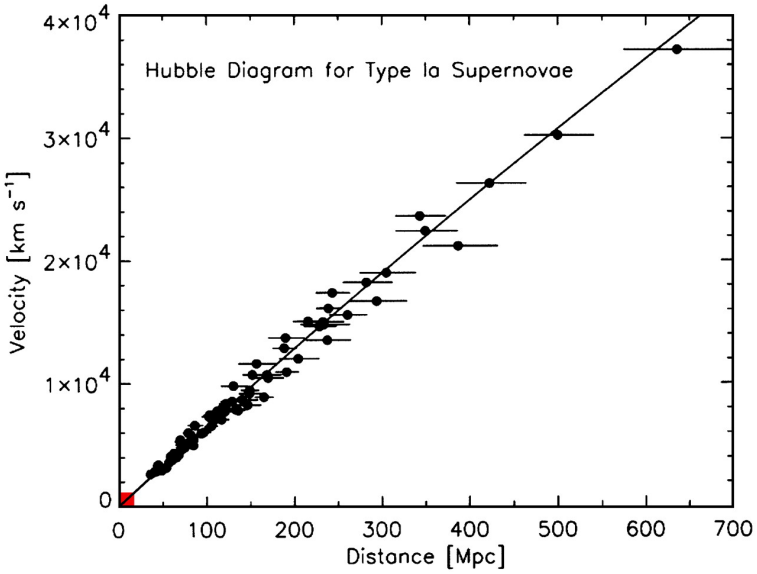

Figure 1.3: The recession velocity v as a function of the distance from Earth d for Type 1a supernovae (shown by the data points with error bars) [28]. The best-fit is given by the solid line, satisfying $v = H_0 d$, where H_0 is the present-day Hubble parameter. The small red region corresponds to the galaxies studied in the pioneering work of Hubble [27].

One can quantify the relative size of the universe by introducing the *cosmological scale factor* $a(t)$, which was smaller in the past and equal to unity today. The rate at which the universe is expanding is then given by the *Hubble parameter*

$$H(t) \equiv \frac{\dot{a}(t)}{a(t)} \ , \tag{1.2.2}$$

where the overdot denotes the time-derivative. The current value[2] of the Hubble rate, H_0, is equal to the gradient of the straight line in Fig. 1.3.

The Hubble parameter is usually expressed in terms of the dimensionless quantity

$$h(t) \equiv \frac{H(t)}{100 \text{ km s}^{-1} \text{ Mpc}^{-1}} \ . \tag{1.2.3}$$

As distant galaxies recede from us, the wavelength of light they emit λ_{emit} is stretched out or *redshifted*. The magnitude of the redshift z is related to the scale factor via

$$1 + z \equiv \frac{\lambda_{\text{obs}}}{\lambda_{\text{emit}}} = \frac{1}{a} \ , \tag{1.2.4}$$

[2]Note that throughout this thesis, we will denote present-day values of parameters by the subscript "0".

where λ_{obs} is the wavelength of light we observe. If the recession velocity of a galaxy v is much smaller than the speed of light c, the magnitude of its redshift can be used to infer v, using $z \simeq v/c$.

One can also define an effective temperature for the universe. As we will see in Sec. 1.2.2, the photons that comprise the *cosmic microwave background* (CMB) have a temperature today of $T_0 = 2.7255 \pm 0.0006$ K [29]. Since the energy of a photon is inversely proportional to its wavelength, Eq. (1.2.4) implies that the temperature of the CMB photons evolves with time as

$$T(t) = T_0/a(t) \ . \tag{1.2.5}$$

In terms of the total energy density of the universe $\rho(t)$ and the intrinsic *curvature* of the universe K, one can express the Hubble parameter using the *Friedmann equation* [30]

$$H^2(t) = \frac{8\pi G}{3}\rho(t) - \frac{Kc^2}{a^2} \ , \tag{1.2.6}$$

where G is Newton's gravitational constant.

Assuming that the universe is both *isotropic* and *homogeneous* on large scales[3], one can describe four-dimensional space-time by the *Friedmann–Lemaître–Robertson–Walker* (FLRW) metric

$$\mathrm{d}s^2 = \mathrm{d}t^2 - a^2(t)\left(\frac{\mathrm{d}r^2}{1-Kr^2} + r^2\,\mathrm{d}\theta^2 + r^2\sin^2\theta\,\mathrm{d}\phi^2\right) \ , \tag{1.2.7}$$

where $\mathrm{d}s^2$ is a *line element*, r is the comoving radial distance, and θ and ϕ are the angles in a comoving spherical coordinate system.

The geometry of the universe can be either *flat* ($K = 0$), *closed* ($K > 0$) or *open* ($K < 0$). Throughout this thesis, we will assume that $K = 0$, as indicated by the latest data [8–11]. Then, in the standard cosmological model (ΛCDM), there are only four components of energy in the universe: DM, *baryons* (ordinary matter[4]),

[3] Isotropic means "the same in all directions", while homogeneous means "the same in all locations". The assumption of isotropy and homogeneity is often called the *Cosmological Principle*.

[4] Note that this nomenclature contrasts with the definition of baryons in particle physics; in particular, it includes electrons.

radiation (photons and neutrinos), and *dark energy*[5] in the form of a *cosmological constant* Λ.

One can determine the dependence of $\rho(t)$ on a by considering 4-momentum conservation for each of the components (see Sec. 2.1):

$$\dot{\rho}(t) = -3H(\rho + P) \ , \tag{1.2.8}$$

where P is the pressure of the fluid ($\simeq 0$ for matter, $\rho/3$ for radiation and $-\rho$ for Λ). Using Eq. (1.2.8), the evolution of the total energy density is then given by[6]

$$\rho(t) = \rho_{\mathrm{DM},0}\, a^{-3} + \rho_{\mathrm{b},0}\, a^{-3} + \rho_{\mathrm{r},0}\, a^{-4} + \rho_{\Lambda,0} \ . \tag{1.2.9}$$

Next, one can define the dimensionless *density parameter*

$$\Omega(t) \equiv \frac{\rho(t)}{\rho_{\mathrm{crit}}(t)} \ , \tag{1.2.10}$$

where the *critical density*

$$\rho_{\mathrm{crit}}(t) \equiv \frac{3H^2}{8\pi G} \ . \tag{1.2.11}$$

From Eq. (1.2.6), it is clear that $\rho_{\mathrm{crit}}(t)$ corresponds to the total energy density required for a flat universe, which is equal to $\rho_{\mathrm{crit},0} \sim 10^{-26}$ kg m^{-3} today.

Finally, using Eqs. (1.2.9) and (1.2.10), we can rewrite Eq. (1.2.6) as

$$\left(\frac{h}{h_0}\right)^2 = \Omega_{\mathrm{DM},0}\, a^{-3} + \Omega_{\mathrm{b},0}\, a^{-3} + \Omega_{\mathrm{r},0}\, a^{-4} + \Omega_{\Lambda,0} \ , \tag{1.2.12}$$

which defines a first-order differential equation in the scale factor a.

Assuming the standard ΛCDM model, the latest determinations of these parameters are: $h_0 \sim 0.68$, $\Omega_{\mathrm{DM},0} \sim 0.26$, $\Omega_{\mathrm{b},0} \sim 0.05$, $\Omega_{\mathrm{r},0} \sim 10^{-4}$ and $\Omega_{\Lambda,0} \sim 0.69$ [11]. Thus, there is currently about five times as much DM as ordinary matter, while the energy density of the universe is dominated by the cosmological constant component (see Fig. 1.4).

[5] Dark energy is thought to be responsible for the accelerated expansion of the universe at late times, which was first observed by two groups studying supernovae in 1998 [31, 32].

[6] While the energy density of matter simply scales with the expansion, radiation receives an additional dilution factor as it is redshifted.

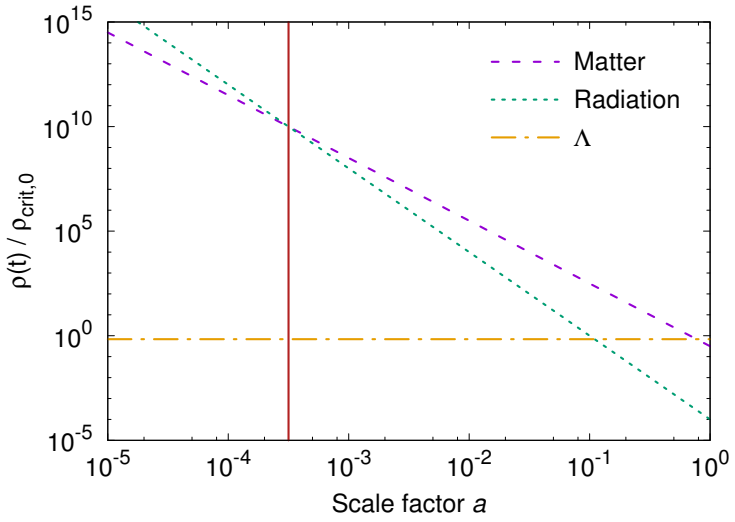

Figure 1.4: The time-evolution of the energy densities $\rho(t)$ in a flat ΛCDM universe for matter (purple, dashed), radiation (green, dotted), and dark energy in the form of a cosmological constant Λ (orange, dashed-dotted). The densities are normalised to the present-day critical density $\rho_{\mathrm{crit},0}$. The vertical red line corresponds to the epoch of matter-radiation equality, when $\rho_{\mathrm{m}}(t) = \rho_{\mathrm{r}}(t)$. Note that $a \equiv 1$ today.

The time at which the energy densities of matter (DM plus baryons) and radiation were equal is known as the epoch of *matter-radiation equality*, which occurred at a redshift $z_{\mathrm{eq}} \sim 3000$ [8–11]. Using Eq. (1.2.6), one can determine that in the radiation-dominated era ($z > z_{\mathrm{eq}}$), the scale factor evolves with time t as $a(t) \propto t^{1/2}$, while in the matter-dominated era ($z < z_{\mathrm{eq}}$), $a(t) \propto t^{2/3}$.

1.2.1 Big Bang Nucleosynthesis

Big Bang nucleosynthesis (BBN) refers to the process in which the first light nuclei (heavier than the lightest isotope of hydrogen H) were formed[7]; in particular, deuterium (D), helium (^{3}He, ^{4}He) and lithium (^{7}Li). BBN is thought to have occurred in the first few minutes after the Big Bang ($z \sim 10^8$) [33]. Before this epoch, the universe was extremely hot and dense, and any nuclei that formed were immediately destroyed by the high-energy photons. As the universe cooled, these light elements were able to survive.

[7]Heavier elements were created much later by stellar nucleosynthesis.

The first BBN calculations were carried out by Ralph Alpher in the 1940s, leading to a groundbreaking paper that outlined the theory of light-element production in the early universe [34]. The nuclear processes of BBN primarily lead to ^{4}He, with a *mass fraction* Y_p of $\sim 25\%$ with respect to hydrogen. For the other nuclei, the predicted number densities compared to hydrogen are D/H $\sim$ ^{3}He/H $\sim 10^{-5}$ and ^{7}Li/H $\sim 10^{-10}$ [35] (see Fig. 1.5).

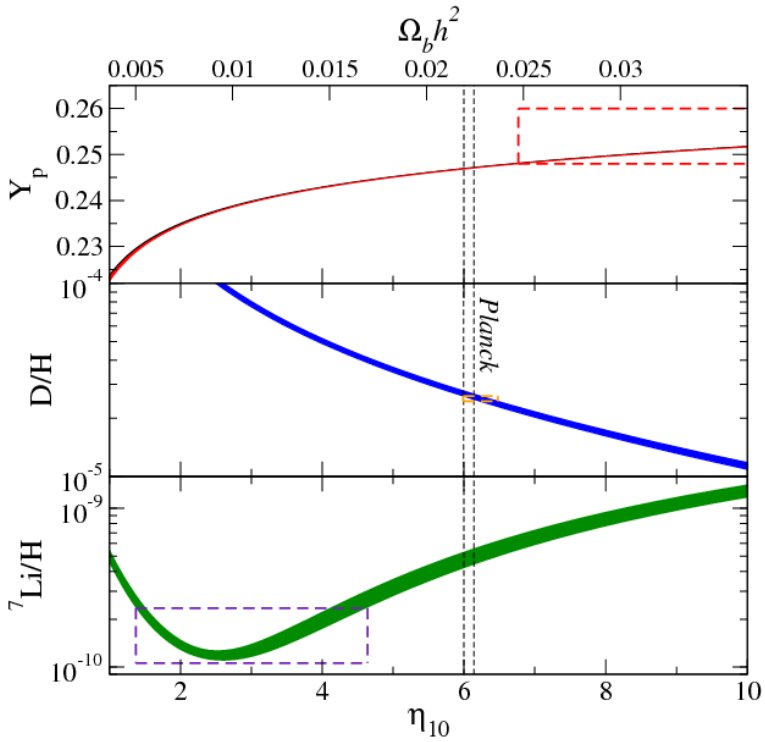

Figure 1.5: Primordial abundances of the light elements as a function of the baryon density $\Omega_\mathrm{b}h^2$ [36]. Y_p is the ^{4}He mass fraction, D/H and ^{7}Li/H are the number densities of deuterium and lithium relative to hydrogen, respectively, and $\eta_{10} \equiv 10^{10}\eta$, where η is the baryon-to-photon ratio. The coloured curves show the predictions from BBN (the thickness of the curves represents the 1σ uncertainty on the relevant nuclear reaction rates) [35]. The vertical band shows the allowed values of $\Omega_\mathrm{b}h^2$ from *Planck* 2013 CMB data [10] and the rectangular boxes show the observed light-element abundances [36].

The light-element abundances depend almost entirely on a single parameter: the *baryon-to-photon ratio* $\eta \equiv n_\mathrm{b}/n_\gamma \sim 10^{-10}$, which in turn can be expressed in terms of the baryon density $\Omega_\mathrm{b}h^2$. From Fig. 1.5, one can see that the observed abundances [36] are generally consistent with BBN predictions[8], providing strong

[8] However, the discrepancy in the ^{7}Li abundance, as shown in Fig. 1.5, has yet to be resolved [37].

evidence for the hot Big Bang model. This is particularly impressive given that the abundances span nine orders of magnitude. The extremely accurate measurement of D/H implies that $\Omega_{\rm b}h^2 \simeq 0.022$, which is significantly lower than the total matter density $\Omega_{\rm m}h^2 \simeq 0.14$ [8–11]. Therefore, BBN provides a compelling argument for a non-baryonic component of the universe; namely, DM.

1.2.2 The Cosmic Microwave Background

Around 380,000 years after the Big Bang ($z \sim 1100$), the temperature of the universe became low enough to allow electrons and protons to become bound in hydrogen atoms, in a process known as *recombination* [38]. Photons were no longer scattered from free electrons and fell out of *thermal equilibrium* with them (*thermal decoupling*). These photons then travelled from this *last-scattering surface* through the universe to constitute what we detect today as the *cosmic microwave background* (CMB) radiation.

The CMB was first detected by Penzias and Wilson in the mid-1960s [39]. An important prediction of the hot Big Bang model is that before recombination, these photons remained in thermal equilibrium due to frequent scattering with electrons. Therefore, they should have a *blackbody* spectrum, with a specific intensity

$$I(\nu, T) = \frac{2h\nu^3/c^2}{\exp(h\nu/k_{\rm B}T) - 1} \,, \tag{1.2.13}$$

where h is Planck's constant, $k_{\rm B}$ is Boltzmann's constant, ν is frequency and T is temperature. This prediction was confirmed with remarkable precision by the COBE satellite in the 1990s [40].

The temperature of the CMB is incredibly uniform (with a mean value today of $\bar{T} = 2.7255 \pm 0.0006$ K [29]), showing that the early universe was both isotropic and homogeneous on large scales. However, the CMB spectrum is not completely smooth due to small density perturbations or *anisotropies* at the level of 10^{-5} over a wide angular scale (see Fig. 1.6). Such density perturbations are thought to originate from the period of cosmic *inflation*, where quantum fluctuations were amplified as the size of the observable universe increased exponentially [41]. As we will see in Sec. 1.2.3, density perturbations in the early universe were the seeds for the eventual

formation of large-scale structures such as galaxies and galaxy clusters.

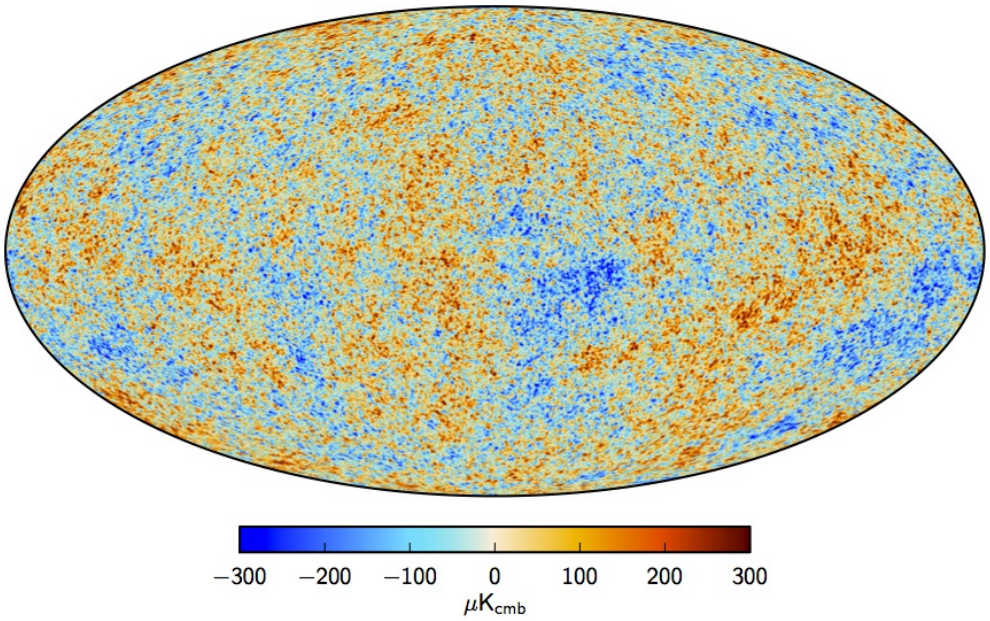

Figure 1.6: The map of CMB temperature fluctuations $\Delta T/\bar{T}$ over the whole sky, as measured by the *Planck* satellite [42]. The foreground emission from the Milky Way galaxy and the dipole component due to the motion of the galaxy relative to the CMB have been removed. The colours from blue to red indicate the magnitude of underdensity to overdensity.

Since the first detection of CMB anisotropies by COBE [43], there has been intense activity to map the sky with increasing sensitivity and angular resolution. The results from WMAP [8, 9] and *Planck* [10, 11], in addition to data from ACT [44] and SPT [45] at small angular scales, have led to a remarkable confirmation of the hot Big Bang model. In combination with other astrophysical data, CMB measurements have placed stringent constraints on the various cosmological parameters, launching us into an era of precision cosmology.

Observations of the CMB anisotropies, $\Delta T/\bar{T} \equiv (T-\bar{T})/\bar{T}$, are usually analysed using the *angular power spectrum* C_ℓ. Since the temperature of the CMB is a two-dimensional field (with angular coordinates θ and ϕ), projected on the surface of a sphere, it is convenient to expand the CMB temperature distribution over the sky using *spherical harmonics* $Y_{\ell m}(\theta, \phi)$:

$$\frac{\Delta T(\theta,\phi)}{\bar{T}} = \sum_{\ell=0}^{\infty} \sum_{m=-\ell}^{\ell} a_{\ell m}\, Y_{\ell m}(\theta,\phi) \ , \tag{1.2.14}$$

where ℓ is the total angular wavenumber (or *multipole order*), m is the azimuthal wavenumber and $a_{\ell m}$ are the associated amplitudes. A multipole of order ℓ is related to the angular size θ via

$$\theta \simeq \frac{\pi}{\ell} \text{ radians} = \frac{180^\circ}{\ell} \ . \tag{1.2.15}$$

The angular power spectrum is then defined as

$$C_\ell \equiv \frac{1}{(2\ell+1)} \sum_{m=-\ell}^{\ell} |a_{\ell m}|^2 \ , \tag{1.2.16}$$

where we have averaged over m for each ℓ. The C_ℓ is related to the *variance* in $\Delta T/\bar{T}$ by

$$\mathcal{D}_\ell \equiv \left\langle \left(\frac{\Delta T}{\bar{T}} \right)^2 \right\rangle_\ell = \frac{\ell(\ell+1)}{2\pi} C_\ell \ , \tag{1.2.17}$$

which is presented in Fig. 1.7 as a function of ℓ using the *Planck* 2015 data [11]. The cosmic variance is the main obstacle for better measurements of the C_ℓ on large scales (small ℓ), as shown by the light-blue shading in Fig. 1.7.

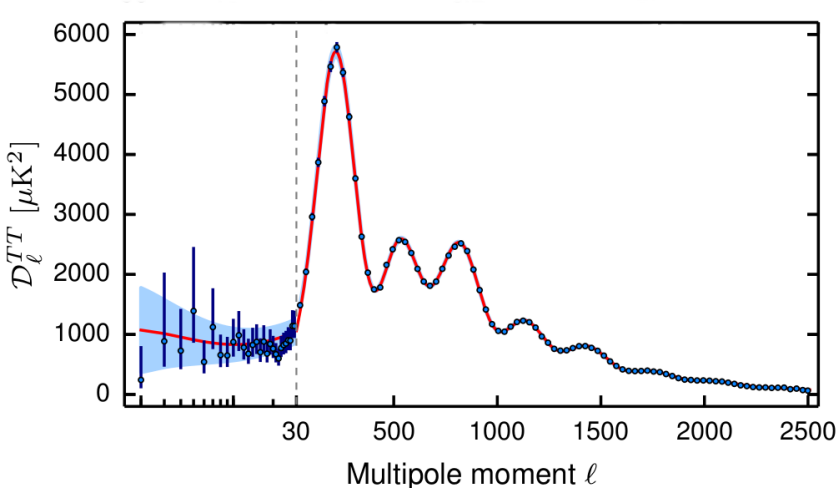

Figure 1.7: The angular power spectrum of CMB temperature fluctuations (TT) measured by *Planck* (blue data points with $\pm$ 1σ error bars) [11]. The best-fit ΛCDM model is given by the solid red curve, which can successfully fit the magnitude and position of the acoustic peaks. The light-blue shading represents the uncertainty from cosmic variance.

The cosmological parameters affect the CMB anisotropies via the well-understood physics of linear perturbation theory[9] within an FLRW cosmology

[9] Note that we can use linear perturbation theory at this epoch since the temperature fluctuations were still small ($\Delta T/\bar{T} \ll 1$).

(see Chapter 2). There are now fast, effective Boltzmann codes for computing the CMB anisotropy spectrum for a given cosmological model, which are considered to be accurate to at least the 1% level, e.g. CMBFAST [46], CAMB [47] and CLASS [48]. The precise shape of the spectrum can therefore provide us with important information about the constituents of the universe and how they interact.

We can consider the C_ℓ in three regimes:

1. Low ℓ ($\ell \lesssim 100$): At large angular scales, CMB photons are gravitationally redshifted via the *Sachs–Wolfe effect* [49], which produces small temperature fluctuations in the spectrum. There are two components to this effect. The *non-integrated* Sachs–Wolfe effect is caused by gravitational redshifting at the surface of last-scattering and is therefore a feature of the primordial CMB spectrum. The *integrated* Sachs–Wolfe effect occurs as the photons travel to the Earth, due to changes in the large-scale gravitational potential as the universe transitions from radiation- to matter- to Λ-domination.

2. Intermediate ℓ ($100 \lesssim \ell \lesssim 1000$): The CMB spectrum shows a series of *acoustic oscillations*, which can be understood as follows. Before the epoch of recombination, the baryons were strongly coupled to the photons, and the two components behaved as a single *baryon–photon fluid*. At this time, perturbations in the gravitational potential (dominated by the DM component) were steadily evolving. This potential drove oscillations in the baryon–photon fluid, with the photon pressure providing most of the restoring force.

3. High ℓ ($\ell \gtrsim 1000$): At small angular scales, the acoustic peaks are suppressed due to *Silk damping* [50]. This is the process in which, during recombination, photons diffused from overdense to underdense regions, dragging the baryons along with them, thus making the universe more isotropic. If there was no DM, Silk damping would be observed at intermediate ℓ (between the second and third peaks). Again, this emphasises the necessity of non-baryonic matter in the universe.

An important property of the CMB photons is that they are *linearly polarised*[10] via *Thomson scattering* with electrons[11], either at thermal decoupling or during *reionisation* (see Sec. 1.2.3). The magnitude of the polarisation is approximately $(1-10)\%$ of the temperature anisotropies, depending on the angular scale [11]. Observations of the CMB polarisation are important as they provide a complementary method to extract the cosmological parameters, and can independently test the predictions of a wide range of models beyond ΛCDM.

The pattern of linear polarisation can be decomposed in many ways, requiring two quantities to describe the polarisation state of each pixel on the CMB map. For instance, linear polarisation is often described by the two *Stokes parameters*: $Q \equiv \langle E_x^2 \rangle - \langle E_y^2 \rangle$ and $U \equiv \langle E_a^2 \rangle - \langle E_b^2 \rangle$, where E is the amplitude of the electric field, the angular brackets denote the expectation value, and the subscripts refer to the standard *Cartesian basis* $(\hat{x}, \hat{y})$ and a Cartesian basis rotated by 45° $(\hat{a}, \hat{b})$ [51].

However, it is more intuitive to separate the polarisation pattern geometrically into a part with a *divergence* (the *E-mode*) and a part with a *curl* (the *B-mode*)[12]. These modes are independent of the coordinate system and are related to the Q and U parameters by a non-local transformation [52]. The pattern of E- and B-modes is illustrated in Fig. 1.8 in the case of an underdensity and an overdensity.

In principle, there are six *cross power spectra* that can be obtained from data:

$$C_\ell^{i,j} \equiv \frac{1}{(2\ell+1)} \sum_{m=-\ell}^{\ell} a_{\ell m}^{i} \, a_{\ell m}^{j\star} \,, \tag{1.2.18}$$

where $\{i,j\} \in \{T,E,B\}$, which will contain the full temperature and polarisation information. However, from Fig. 1.8, one can see that the pattern of E-modes has mirror symmetry (a *scalar* field), while the B-modes are anti-symmetric (a *pseudoscalar* field). This implies that $C_\ell^{TB} = C_\ell^{EB} = 0$, leaving four observables: C_ℓ^{TT}, C_ℓ^{EE}, C_ℓ^{BB} and C_ℓ^{TE}.

[10] Electromagnetic radiation is linearly polarised if the electric field vector $\vec{E}$ is confined to a given plane along the direction of propagation.

[11] The Thomson elastic scattering cross section between free electrons and photons is temperature-independent and given by $\sigma_{\rm Th} = 8\pi\,\alpha^2/(3m^2)$, where α is the fine-structure constant.

[12] The E-mode is analogous to the electric field surrounding a charge, while the B-mode resembles the magnetic field around a current.

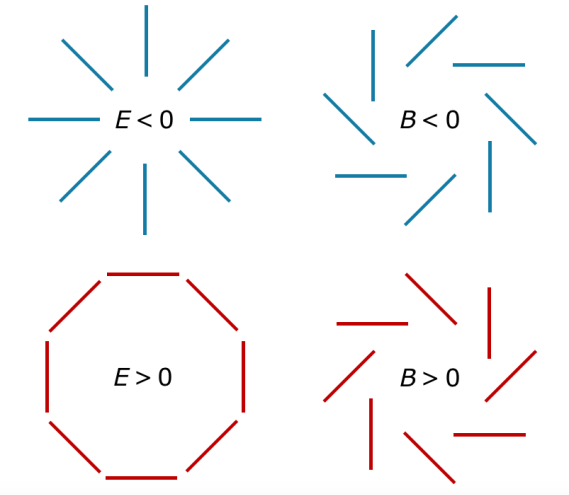

Figure 1.8: A representation of the E-modes (left) and B-modes (right) in the case of an underdensity (upper row, blue) and an overdensity (lower row, red). One can see that the B-modes are tilted by 45° with respect to the E-modes.

Crucially, density perturbations can only give rise to E-mode polarisation of the CMB photons, while *primordial gravitational waves* from inflation can produce both E- and B-modes [53]. Therefore, precise measurements of the B-mode signal can allow us to probe various inflationary scenarios (see e.g. Ref. [54]). However, the contribution from foregrounds and other systematic effects must be carefully eliminated; in particular, gravitational lensing of the CMB at late times converts a fraction of the E-mode polarisation into B-mode polarisation [55].

Since the amplitude of the CMB polarisation signal is so small with respect to the temperature anisotropies, E-mode polarisation was not discovered until 2002 by the DASI experiment [56], while B-modes due to gravitational lensing were first detected by SPT in 2013 [57]. Currently, there is no convincing evidence of B-modes from inflation[13].

1.2.3 Structure Formation

Between 150 million and one billion years after the Big Bang ($6 \lesssim z \lesssim 20$), the first stars and galaxies began to form due to gravitational collapse of the initially small

[13]The apparent discovery of such B-modes by the BICEP collaboration is now believed to be the result of interstellar dust [58].

density perturbations that were discussed in Sec. 1.2.2. Such objects were energetic enough to reionise neutral hydrogen via a process called *reionisation*.

The distribution of matter in the universe is usually described by the *matter power spectrum* $P(k)$ (see Fig. 1.9), defined via

$$\langle \delta(k)\delta(k') \rangle = (2\pi)^3 \, P(k) \, \delta^3(k - k') \ , \tag{1.2.19}$$

where $k = 2\pi/\lambda$ is the wavenumber, λ is the spatial scale, $\delta(k)$ is the Fourier transform of the density inhomogeneity $\delta(x) \equiv [n(x) - \bar{n}]/\bar{n}$, the angular brackets denote the average over the whole distribution, and $\delta^3(k - k')$ is the Dirac delta function. The $P(k)$ represents the variance in the matter distribution; it will be large if there are a significant number of very underdense and overdense regions, and small if the distribution is smooth.

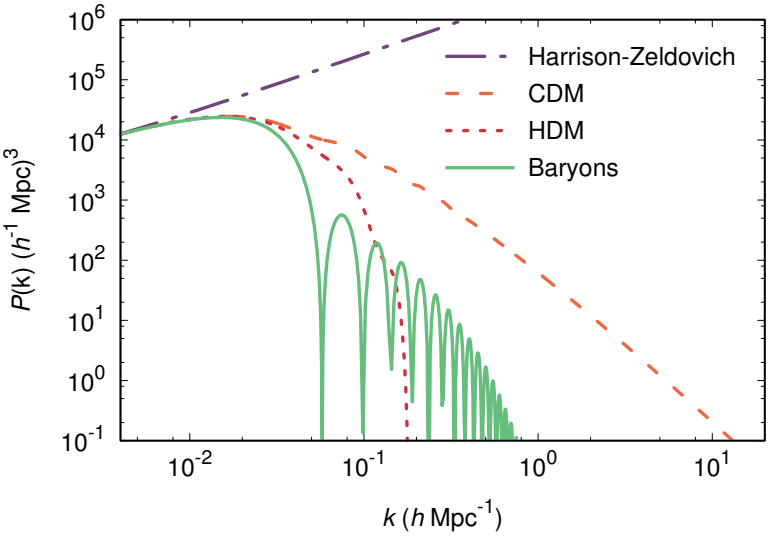

Figure 1.9: The linear matter power spectrum in four distinct models: the Harrison–Zel'dovich spectrum with $P(k) \propto k$ (purple, dashed-dotted), CDM (orange, dashed), HDM in the form of SM neutrinos (red, dotted) and DM in the form of baryons (green, solid).

The underlying principle of structure formation is that initially small density perturbations are amplified by gravity to form large-scale structure (LSS). On scales $k \lesssim 0.2 \ h \ \text{Mpc}^{-1}$, the fluctuations are still small enough (i.e. $\delta(k) \ll 1$) to be accurately described by linear perturbation theory[14]. Scales with higher

[14]More precisely, linear perturbation theory is valid when the *dimensionless power spectrum* $\Delta^2(k) \equiv k^3 P(k)/(2\pi^2) \lesssim 1$, which corresponds to $k \lesssim 0.2 \ h \ \text{Mpc}^{-1}$ for realistic models.

wavenumbers correspond to collapsed objects, which are *non-linear* (i.e. $\delta(k) \gtrsim 1$) and require N-body simulations to follow their evolution (see e.g. Refs. [59–63]).

As a result of inflation, there is no preferred length scale in the very early universe and the *primordial* matter power spectrum follows a simple power law: $P(k) = A\,k^n$, where A is the amplitude and n is the *spectral index*. The spectrum in which $n = 1$ is called the *scale-invariant*[15] or Harrison–Zel'dovich spectrum [64, 65] (see the purple, dashed-dotted line in Fig. 1.9). For *scalar* perturbations (see Chapter 2), the simplest inflationary models predict a nearly (but not exactly) scale-invariant spectrum, corresponding to a *slowly rolling inflaton field* and a slowly varying $H(t)$ during inflation[16]. Such a prediction is in agreement with the most recent constraints from *Planck* assuming ΛCDM: $n_s = 0.968 \pm 0.006$ and $A_s = (2.14 \pm 0.06) \times 10^{-9}$ [11]. Note that since $n_s < 1$, the primordial matter power spectrum has less power on small scales than the Harrison–Zel'dovich spectrum.

The epoch of matter–radiation equality corresponds to the scale at which the matter power spectrum turns over from the primordial shape and becomes proportional to k^{-3}. Before this epoch, the radiation density acts as a pressure that prevents the collapse of perturbations in the matter density (the *Mészáros effect* [67]). However, after this time, matter fluctuations not coupled to the radiation (such as *collisionless* DM) are able to grow gravitationally. Baryonic matter remains coupled to photons and resists collapse, resulting in *baryon acoustic oscillations* (BAO) in the $P(k)$ at $k \sim 0.1\ h\ \mathrm{Mpc}^{-1}$ (see Fig. 1.9). Such oscillations result from the competing forces of gravitational attraction and radiation pressure in the tightly-coupled baryon–photon fluid. The baryons behave like a *driven harmonic oscillator*, with gravity and the photon pressure acting as the driving and restoring forces, respectively.

[15] For scale invariance, we require the dimensionless power spectrum $\Delta^2_\Phi(k) \propto k^3 P_\Phi(k)$ (for fluctuations in the gravitational potential Φ) to be constant. From the *Poisson Equation* in Fourier space, $k^2\Phi(k) \propto \delta(k)$. Then from Eq. (1.2.19), $P_\Phi \propto \Phi(k)^2$ and $P(k) \propto \delta(k)^2$. Putting all this together, a scale-invariant spectrum requires $P(k) \propto k\Delta^2_\Phi \propto k$, i.e. $n = 1$.

[16] In this scenario, the scalar spectral index $n_s = 1 + 4\epsilon - 2\eta$, where ϵ and η are the slow-roll parameters, which depend on the shape of the inflaton potential [66]. Since $\epsilon \ll 1$ and $|\eta| \ll 1$, the scalar perturbations generated in slow-roll inflation are close to scale-invariant.

During the epoch of recombination, the electrons that were responsible for scattering the photons become locked up in neutral hydrogen. The *mean free path* of the photons increases and they diffuse out of overdense regions, smoothing out fluctuations in the baryon distribution (Silk damping) [50].

The shape of the matter power spectrum also depends very strongly on the properties of DM. If DM consisted of baryonic particles, the $P(k)$ would show oscillations on large scales due to the strong baryon–photon coupling prior to recombination (see the green, solid curve in Fig. 1.9). Therefore, the absence of such oscillations in observational data [68] provides further evidence that DM is non-baryonic.

In the standard cosmological framework, density fluctuations in collisionless DM are erased or *damped* by the *free-streaming* of its particles from overdense to underdense regions. Quantitatively, the cut-off in the $P(k)$ for a species i with velocity v_i is related to the *free-streaming length*

$$l_{\rm fs} \propto \int_{t_{{\rm dec}(i)}}^{t_0} \frac{v_i}{a}\, {\rm d}t \simeq \pi \, \max\left(\frac{v_i t}{a}\right) \,, \tag{1.2.20}$$

where "max" denotes the maximum value of the free-streaming scale within the integration interval $[t_{{\rm dec}(i)}, t_0]$ [69].

From Eq. (1.2.20), one can see that the scale at which fluctuations are damped depends on the velocity of the DM particles. For this reason, DM candidates are often described as being either *hot* (HDM), *warm* (WDM) or *cold* (CDM), depending on the cut-off scale that they induce in the $P(k)$. Fig. 1.9 shows examples for two extreme models: HDM (red, dotted) and collisionless CDM (orange, dashed). For comparison, the results of N-body simulations for HDM, WDM and CDM are shown in Fig. 1.10.

An example of HDM is the neutrino, which interacts only via the *weak force*[17] and gravity, and is abundant in the universe. Following the procedure of Sec. 1.3 for a *hot relic*, the energy density of neutrinos today is given by [70]

$$\Omega_\nu h^2 \simeq \frac{\sum_i m_{\nu_i}}{93.14 \text{ eV}} \,, \tag{1.2.21}$$

[17] The weak interaction is responsible for radioactive decay and plays an essential role in nuclear fission.

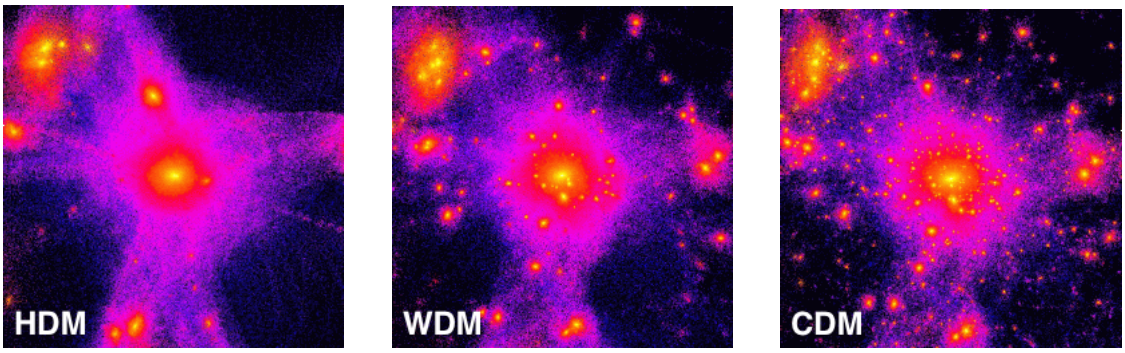

Figure 1.10: DM-only N-body simulations of structure formation in the case of HDM (left), WDM (centre) and CDM (right), where the side of each image corresponds to ~ 10 Mpc. The colours represent the local DM density on a logarithmic colour scale from black to purple to yellow. In HDM, small-scale fluctuations cannot be supported as they are washed out by the rapid motion of the particles. In WDM and CDM, smaller structures can survive to the current epoch, more closely resembling what we observe. Simulations by Ben Moore (University of Zurich).

where one sums over the three neutrino species $i \in \{\mathrm{e}, \mu, \tau\}$.

The most recent CMB measurements constrain the sum of the neutrino masses to be $\sum_i m_{\nu_i} \lesssim 0.23$ eV [11]. Using Eq. (1.2.21), it is clear that neutrinos cannot provide the required energy density to account for the entire DM relic abundance: $\Omega_{\mathrm{DM}} h^2 \sim 0.1$ [11]. Furthermore, for a neutrino with mass m_ν, Eq. (1.2.20) gives

$$l_{\mathrm{fs},\nu} \sim 1000 \text{ Mpc} \left(\frac{m_\nu}{\mathrm{eV}}\right)^{-1} , \tag{1.2.22}$$

which implies that free-streaming of neutrinos leads to damping on scales larger than the size of an average galaxy cluster. Therefore, such particles cannot give rise to the formation and distribution of galaxies that we observe in the universe today (see the left-hand panel of Fig. 1.10). Since neutrinos are the only electrically neutral, stable particle in the SM of particle physics, the existence of DM implies physics beyond the SM.

Candidates for CDM include heavy neutral particles such as the *supersymmetric neutralino*[18] [72–74] and light particles that are produced non-thermally such as

[18] *Supersymmetry* is a proposed space-time symmetry that relates bosons (with integer spin) and fermions (with half-integer spin), wherein every SM particle has a heavier *partner* that has yet to be discovered (see e.g. Ref. [71]).

the *axion* [75–77]. Since these particles are non-relativistic at the time of structure formation, perturbations on almost all scales are preserved (see the right-hand panel of Fig. 1.10). N-body simulations of LSS in the universe currently favour the CDM model [78]. However, as we will see in Chapter 5, there are a number of persistent discrepancies between CDM predictions and observations on small scales [79–81], which may point towards WDM or physics beyond collisionless CDM.

Finally, WDM has properties intermediate between those of HDM and CDM (see the centre panel of Fig. 1.10). Candidates for WDM include the *gravitino* (the supersymmetric partner of the *graviton*, a particle that is thought to mediate the gravitational force) [72–74] and the *sterile neutrino* (a massive neutrino that, unlike the SM neutrinos, does not interact via the weak force) [82–85]. The existence of sterile neutrinos is well-motivated and many experiments are currently searching for these particles (see e.g. Ref. [86]). Theoretically, their mass could take any value from ~ 1 eV to $\sim 10^{15}$ GeV [87]. Therefore, if sterile neutrinos are too massive, they may not be directly observable.

1.3 Thermal Production of Dark Matter

In this thesis, we will generally assume that DM is *thermal*, i.e. DM was produced in thermal equilibrium with the other particles in the early universe, sharing a common temperature with them. DM then *chemically decoupled* from the *thermal bath* of particles when its *annihilation rate* $\Gamma(t)$ became smaller than the expansion rate of the universe $H(t)$, i.e. $\Gamma(t) \lesssim H(t)$. After chemical decoupling, the total number of DM particles remained fixed, which set the relic density $\Omega_{\rm DM}h^2 \sim 0.1$ that we observe today.

To properly treat the chemical decoupling or *freeze-out*, it is necessary to consider the microscopic evolution of the DM particle's *phase space distribution function* $f(E,t)$. Here we will follow the methodology of Ref. [88], where $f(E,t)$ satisfies the *Boltzmann equation*

$$\hat{L}[f(E,t)] = C[f(E,t)] \ , \tag{1.3.23}$$

where E is energy, p is momentum and t is time. Here

$$\hat{L}[f] = E\,\frac{\partial f}{\partial t} - H\,p^2\,\frac{\partial f}{\partial E}\ , \tag{1.3.24}$$

is the *Liouville operator* and $C[f]$ is the *collision operator*, describing the evolution of the phase space volume and the processes of particle destruction/creation, respectively[19].

One can then define the number density $n(t)$ in terms of the phase space density via

$$n(t) = \frac{g}{(2\pi)^3}\int \mathrm{d}^3p\ f(E,t)\ , \tag{1.3.25}$$

where g is the internal number of *degrees of freedom* for the DM particle.

Integrating the Boltzmann equation in Eq. (1.3.23) over momentum, we have

$$\frac{g}{(2\pi)^3}\int \mathrm{d}^3p\left(\frac{\partial f}{\partial t} - H\,\frac{p^2}{E}\,\frac{\partial f}{\partial E}\right) = \frac{g}{(2\pi)^3}\int \frac{\mathrm{d}^3p}{E}\ C[f]\ . \tag{1.3.26}$$

Next, using Eq. (1.3.25), we can rewrite the left-hand side of Eq. (1.3.26) as

$$\begin{aligned}
&\frac{g}{(2\pi)^3}\int \mathrm{d}^3p\left[\frac{\partial f}{\partial t} - H\,\frac{(E^2-m^2)}{E}\,\frac{\partial f}{\partial E}\right]\\
=\ &\frac{\partial}{\partial t}\left[\frac{g}{(2\pi)^3}\int \mathrm{d}^3p\ f\right] - H\,\frac{g}{(2\pi)^3}\int \mathrm{d}^3p\,\frac{(E^2-m^2)}{E}\,\frac{\partial f}{\partial E}\\
=\ &\frac{\partial n}{\partial t} - H\,\frac{g}{2\pi^2}\int \mathrm{d}E\,(E^2-m^2)^{3/2}\,\frac{\partial f}{\partial E}\\
=\ &\frac{\partial n}{\partial t} + 3H\,\frac{g}{2\pi^2}\int \mathrm{d}E\,E\,\sqrt{E^2-m^2}\,f\\
=\ &\frac{\partial n}{\partial t} + 3H\left[\frac{g}{(2\pi)^3}\int \mathrm{d}^3p\ f\right]\\
=\ &\frac{\partial n}{\partial t} + 3Hn = \frac{g}{(2\pi)^3}\int \frac{\mathrm{d}^3p}{E}\ C[f]\ .
\end{aligned} \tag{1.3.27}$$

where we have integrated by parts over the energy derivative and used the change of variables $\mathrm{d}^3p = p^2\,\mathrm{d}p\,\mathrm{d}\Omega = 4\pi E\,\sqrt{E^2-m^2}\,\mathrm{d}E$.

If one sets the collisional term to zero, Eq. (1.3.27) reduces to $\dot{n} = -3Hn$, the solution of which is $n(t) \propto a^{-3}$. As expected, if a species is not interacting, its number density simply dilutes with the Hubble expansion.

[19] We assume spatial homogeneity and isotropy, in addition to an FLRW metric [see Eq. (1.2.7)].

We now turn to the interacting part of the Boltzmann equation; in particular, we will consider a simple $2 \to 2$ annihilation process for a stable DM particle[20], with the *thermally-averaged* annihilation cross section $\langle \sigma v \rangle$. In this case, we can rewrite Eq. (1.3.27) in a very simple form:

$$\frac{\mathrm{d}n}{\mathrm{d}t} = -3Hn - \langle \sigma v \rangle \left(n^2 - n_{\mathrm{eq}}^2 \right) \ , \tag{1.3.28}$$

where n is the average DM number density and n_{eq} is the number density assuming thermal equilibrium. The connection between the collision operator $C[f]$ and $\langle \sigma v \rangle$ is detailed in e.g. Ref. [88]. Eq. (1.3.28) is an example of a *Riccati* equation[21].

One can clearly see that there are two competing processes that determine the evolution of the DM number density: the expansion rate of the universe and the DM annihilation rate. DM particles are in chemical equilibrium with the thermal plasma if $\langle \sigma v \rangle \left(n^2 - n_{\mathrm{eq}}^2 \right) \gg 3Hn$ or equivalently, $\Gamma \equiv n \langle \sigma v \rangle \gg H$. As the annihilation rate falls below the Hubble rate, DM becomes chemically decoupled from the thermal bath and subsequently, its number density will scale as a^{-3}.

It is now convenient to consider the evolution of the number density within a comoving volume to scale out the expansion of the universe. We therefore define $Y \equiv n/s$, where $s \propto T^3$ is the entropy density, and rewrite Eq. (1.3.28) as

$$\begin{aligned} \frac{\mathrm{d}n}{\mathrm{d}t} &= -HT \frac{\mathrm{d}n}{\mathrm{d}T} = -HT \left(s \frac{\mathrm{d}Y}{\mathrm{d}T} + \frac{3Ys}{T} \right) \\ &= -3HYs - s^2 \langle \sigma v \rangle (Y^2 - Y_{\mathrm{eq}}^2) \ , \end{aligned} \tag{1.3.29}$$

where we have used the result that $\mathrm{d}T/\mathrm{d}t = (\mathrm{d}T/\mathrm{d}a)\,(\mathrm{d}a/\mathrm{d}t) = -T_0\, a^{-2}\, \dot{a} = -HT$. Eq. (1.3.29) then reduces to

$$\frac{\mathrm{d}Y}{\mathrm{d}T} = \frac{\langle \sigma v \rangle s}{HT} \left(Y^2 - Y_{\mathrm{eq}}^2 \right) \ . \tag{1.3.30}$$

Finally, we introduce the dimensionless quantity $x \equiv m_{\mathrm{DM}}/T$, such that Eq. (1.3.30) becomes

$$\begin{aligned} \frac{\mathrm{d}Y}{\mathrm{d}x} &= \frac{\mathrm{d}T}{\mathrm{d}x} \frac{\mathrm{d}Y}{\mathrm{d}T} = -\frac{m_{\mathrm{DM}}}{x^2} \frac{\langle \sigma v \rangle s}{HT} \left(Y^2 - Y_{\mathrm{eq}}^2 \right) \\ \implies \frac{\mathrm{d}Y}{\mathrm{d}x} &= -\frac{s}{x\, H(x)} \langle \sigma v \rangle \left(Y^2 - Y_{\mathrm{eq}}^2 \right) \ . \end{aligned} \tag{1.3.31}$$

[20] Bounds on the DM lifetime can be found in e.g. Ref. [89].

[21] A Riccati equation takes the form $y'(x) = a(x) + b(x)y(x) + c(x)y^2(x)$, where $a(x) \neq 0$ and $c(x) \neq 0$.

We now wish to solve Eq. (1.3.31) to find the time evolution of the comoving number density $Y(x)$, for a given value of the annihilation cross section $\langle\sigma v\rangle$. To do this, we require expressions for the entropy density $s(T)$, the Hubble rate $H(x)$ and the comoving number density of DM particles in thermal equilibrium $Y_{\rm eq}$. We consider the case in which freeze-out occurs when the DM particle is non-relativistic (a *cold relic*), whereby [88]

$$s(T) = \frac{2\pi^2}{45}\, g_{*s}\, T^3 \,, \tag{1.3.32}$$

$$H(x) = 1.67\, g_\star^{1/2}\, \frac{m_{\rm DM}^2}{m_{\rm Pl}}\, x^2 \,, \tag{1.3.33}$$

$$Y_{\rm eq} = \frac{45}{2\pi^4} \left(\frac{\pi}{8}\right)^{1/2} \frac{g}{g_{\star s}}\, x^{3/2}\, {\rm e}^{-x} \,, \tag{1.3.34}$$

where $m_{\rm Pl}$ is the Planck mass and we have defined

$$g_\star(T) \equiv \sum_{i={\rm bosons}} g_i \left(\frac{T_i}{T}\right)^4 + \frac{7}{8} \sum_{i={\rm fermions}} g_i \left(\frac{T_i}{T}\right)^4 \,, \tag{1.3.35}$$

$$g_{\star s}(T) \equiv \sum_{i={\rm bosons}} g_i \left(\frac{T_i}{T}\right)^3 + \frac{7}{8} \sum_{i={\rm fermions}} g_i \left(\frac{T_i}{T}\right)^3 \,, \tag{1.3.36}$$

where the factor of (7/8) accounts for the difference in the statistics between bosons and fermions. Eqs. (1.3.35) and (1.3.36) count the total number of effectively massless degrees of freedom, i.e. those species for which $m \ll T$. For example, if $T \ll$ MeV, only the three neutrino species and the photon contribute (assuming the ΛCDM model).

In general, the DM annihilation cross section has a velocity dependence $\langle\sigma v\rangle = \sigma_0\, v^n$, where $n = 0$ corresponds to *s-wave* annihilation, $n = 2$ corresponds to *p-wave* annihilation, etc. For simplicity, we will consider s-wave (temperature-independent) annihilation, i.e. $\langle\sigma v\rangle = \sigma_0$.

Putting all this together, Eq. (1.3.31) becomes

$$\frac{{\rm d}Y}{{\rm d}x} = -\lambda x^{-2}(Y^2 - Y_{\rm eq}^2) \,, \tag{1.3.37}$$

where

$$\lambda \simeq 0.264\, \left(g_{\star s}/g_\star^{1/2}\right)\, m_{\rm Pl}\, m_{\rm DM}\, \sigma_0 \,, \tag{1.3.38}$$

$$Y_{\rm eq} \simeq 0.145\, (g/g_{\star s})\, x^{3/2}\, {\rm e}^{-x} \,. \tag{1.3.39}$$

Eq (1.3.37) can then be solved numerically. However, since $m_{\rm DM}$ and σ_0 can vary by many orders of magnitude, one has a stiff differential equation that is difficult to integrate[22]. For illustrative purposes, solutions to Eq (1.3.37) are shown in Fig. 1.11 for different values of σ_0.

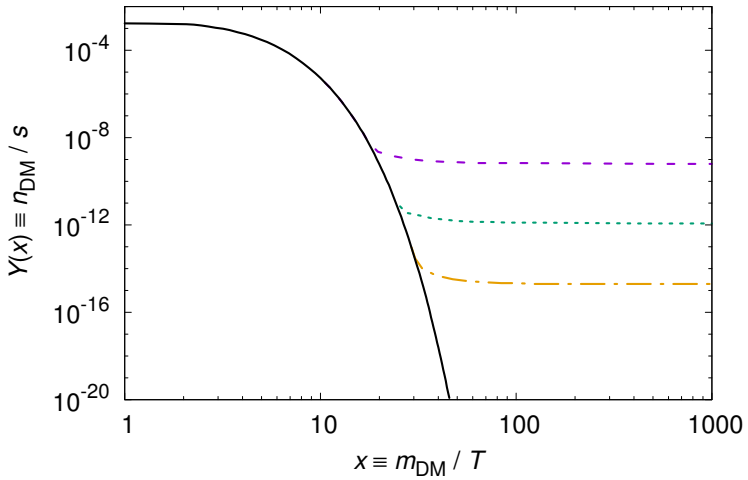

Figure 1.11: The evolution of the comoving number density $Y(x)$ for a thermal WIMP. The solid black curve is the DM abundance in thermal equilibrium $Y_{\rm eq}(x)$, while the coloured curves show the relic abundance for increasing values of σ_0 from top (purple, dashed) to bottom (orange, dashed-dotted). Figure adapted from Ref. [91].

However, it is possible to find an approximate analytical solution to Eq. (1.3.37). Since we are interested in the value of Y at late times, Y_∞, we can take $Y \gg Y_{\rm eq}$:

$$\frac{{\rm d}Y}{{\rm d}x} = -Y^2\,\lambda x^{-2}\,, \tag{1.3.40}$$

the solution of which is simply $Y_\infty = x_{\rm f}/\lambda$, where $x_{\rm f}$ is the value of x at freeze-out.

Using the expression for λ in Eq. (1.3.38), the relic density is then given by

$$\Omega_{\rm DM}h^2 = \frac{s_0\,Y_\infty\,m_{\rm DM}\,h^2}{\rho_{\rm crit,0}} = \frac{s_0\,x_{\rm f}\,h^2}{0.264\,\left(g_{\star s}/g_\star^{1/2}\right)\,m_{\rm Pl}\,\sigma_0\,\rho_{\rm crit,0}}\,, \tag{1.3.41}$$

which is importantly independent of the DM mass. One can also see that the larger the annihilation cross section σ_0, the smaller the DM relic density $\Omega_{\rm DM}h^2$ (as illustrated in Fig. 1.11).

[22] Nevertheless, efficient numerical techniques have been developed (see e.g. Ref. [90]).

For realistic values[23] of $x_\mathrm{f} \approx 20$ and $g_\star \simeq g_{\star s} \approx 100$ [88], one finds

$$\Omega_\mathrm{DM} h^2 \simeq \frac{3 \times 10^{-27}\ \mathrm{cm}^3\ \mathrm{s}^{-1}}{\sigma_0} \ . \tag{1.3.42}$$

By requiring that $\Omega_\mathrm{DM} h^2$ agrees with the observed value of ~ 0.1 [11], the necessary annihilation cross section in the non-relativistic regime is

$$\sigma_0 \simeq 3 \times 10^{-26}\ \mathrm{cm}^3\ \mathrm{s}^{-1} \ . \tag{1.3.43}$$

The magnitude of this cross section is typical for particles interacting via the weak force of the SM, leading many to conclude that DM likely consists of *weakly-interacting massive particles* (WIMPs). This result is often referred to as the "WIMP miracle".

We now apply our analysis to a simple model; namely, DM in the form of a heavy, stable neutrino species s annihilating through a Z^0 boson. In this scenario, the annihilation cross section is energy-independent (s-wave) and given by

$$\sigma_0 \simeq \frac{G_\mathrm{F}^2\, m_s^2}{2\pi} \ , \tag{1.3.44}$$

where G_F is the Fermi constant.

Substituting Eq. (1.3.44) into Eq. (1.3.41) and applying the requirement that $\Omega_s h^2 \lesssim \Omega_\mathrm{DM} h^2 \sim 0.1$, we obtain the so-called *Lee–Weinberg bound* [92, 93]:

$$m_s \gtrsim 6\ \mathrm{GeV} \ , \tag{1.3.45}$$

which sets a lower limit on the mass of the DM candidate. However, it is possible to evade this bound if the annihilation cross section is independent of the DM mass; for example, with certain configurations involving scalar DM (see e.g. Ref. [94]).

Finally, it is important to note that DM could also be produced via a non-thermal scenario, in contrast to the freeze-out mechanism described above. One of the most popular non-thermal DM candidates is the *axion*, a hypothetical particle with mass $\lesssim$ keV that was postulated to resolve the "strong CP problem" in quantum

[23] For cold relics, one can see from Fig. 1.11 that the relic density depends very weakly on the value of x at freeze-out, and that $x_\mathrm{f} \approx 20$.

chromodynamics (QCD) [75, 76]. Axions are expected to be extremely light ($\lesssim$ keV) but nevertheless, behave as CDM as they would be produced non-relativistically [77].

The correct DM relic density can also be achieved via a *freeze-in* mechanism [95]. In this scenario, in the early universe, there is a long-lived DM particle, which has feeble interactions with the thermal plasma and is therefore, decoupled from it. It is also assumed that the DM abundance at this time is negligibly small. As the universe evolves, DM particles are produced from collisions or decays of other particles in the thermal bath. The dominant production will occur at $T \sim m_{\mathrm{DM}}$, which will fix the DM abundance, before the interactions cease as T drops below m_{DM}. Increasing the interaction strength increases the DM relic density, which is the opposite behaviour to that of thermal freeze-out (cf. Fig. 1.11). The process is referred to as "freeze-in", since as T falls below m_{DM}, DM is heading towards (rather than away from) thermal equilibrium.

1.4 Dark Matter Detection Experiments

In this section, we discuss the three complementary techniques for detecting the non-gravitational interactions of DM: *direct* [Sec. 1.4.1], *indirect* [Sec. 1.4.2] and *collider* [Sec. 1.4.3]. Each detection method concerns a particular type of DM–SM interaction (see Fig. 1.12). We will see in Chapters 3, 4 and 5 that DM–SM scattering processes can also be constrained, or even discovered, using observations of the CMB or LSS of the universe.

1.4.1 Direct Detection

Direct detection experiments look for evidence of local DM particles from our Galactic halo scattering elastically off target nuclei [96]. A variety of detectors have now been built that are sensitive to the nuclear recoils induced by WIMP collisions (for a summary, see e.g. Ref. [97]).

The expected number of WIMP–*nucleon*[24] scattering events dN per recoil energy

[24] A nucleon is a particle that makes up the atomic nucleus, i.e. either a neutron or a proton.

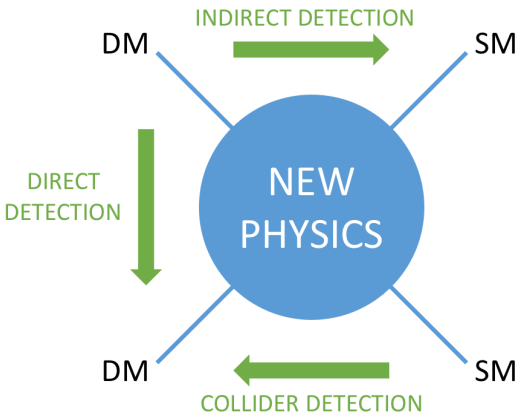

Figure 1.12: Diagram illustrating the three main DM detection techniques: direct (DM–SM scattering; top to bottom), indirect (DM annihilation; left to right) and collider (DM production; right to left).

window $\mathrm{d}E_\mathrm{r}$ is given by [98]

$$\frac{\mathrm{d}N}{\mathrm{d}E_\mathrm{r}} = \frac{\rho_\mathrm{DM}}{2\mu^2}\frac{\sigma}{m_\mathrm{DM}} F \int_{v_\mathrm{min}(E_\mathrm{r})}^{\infty} \mathrm{d}v \, \frac{f(v)}{v} \,, \tag{1.4.46}$$

where ρ_DM is the local WIMP density, $\mu \equiv (m_\mathrm{DM} \times m_\mathrm{nuc})/(m_\mathrm{DM} + m_\mathrm{nuc})$ is the *reduced mass*, σ is the WIMP–nucleon elastic scattering cross section, and F is the *nuclear form factor*, which takes into account the spatial extent and shape of the target nuclei. The velocity distribution of WIMPs in the halo is given by $f(v)$, which is integrated over all velocities larger than the minimum value necessary to produce a recoil with energy E_r.

Direct detection experiments aim to measure (or constrain) $\mathrm{d}N/\mathrm{d}E_\mathrm{r}$ directly. Then, assuming a particular halo model, it is possible to infer a relation between the cross section σ and the WIMP mass m_DM. The most common choice is the so-called *standard halo model* [99], which assumes a *Maxwell–Boltzmann* velocity distribution[25]. Alternative halo models are discussed in e.g. Refs. [100–102].

In the literature, the WIMP–nucleon scattering cross section is often expressed[26] in terms of: (i) a *spin-independent* interaction between WIMPs and all nucleons, and

[25] A Maxwell–Boltzmann distribution takes the form $f(v) \propto \exp(-3v^2/2v_\mathrm{rms}^2)$, where v is velocity and v_rms is the root-mean-square velocity.

[26] However, for a more comprehensive analysis, see Ref. [103].

(ii) a *spin-dependent* interaction between WIMPs and nucleons with a net *spin*[27] that depends on the total nuclear spin and the spins of the individual nucleons. Target nuclei can thus be chosen to optimise an experiment for either spin-independent or spin-dependent searches.

There are two detector technologies in common use: *cryogenic* detectors measure the thermal energy produced when a particle collides with an atom in the detector, while *noble liquid* detectors observe the flash of scintillation light released by a particle collision.

The lack of a DM signal above the background can be interpreted as a constraint on the WIMP–nucleon elastic scattering cross section. Fig. 1.13 shows the current limits on the (spin-independent) WIMP–nucleon scattering cross section. The strongest constraints are currently set by the LUX experiment (a noble liquid detector) for DM masses $m_{\mathrm{DM}} \gtrsim 10$ GeV [104], and CDMS (a cryogenic detector) for $m_{\mathrm{DM}} \sim 1$ GeV [105].

1.4.2 Indirect Detection

Indirect detection experiments search for the primary or secondary products of DM annihilations or decays, including photons, neutrinos and charged particles. Annihilations are expected to be non-negligible today if DM is thermal (see Sec. 1.3), or non-thermal if there is no *matter-antimatter asymmetry* in the dark sector. If the DM mass is relatively large, the annihilation or decay products may be energetic enough to be detected.

Since the DM density profile is peaked towards the centre (see Sec. 1.1), it makes sense to look for these particles from the Milky Way Galactic centre, where the DM concentration is large. However, the background is both complicated and poorly-understood [107], and the shape of the DM density profile at small radii remains uncertain (see below) [108]. One can also look for emissions from dwarf galaxies, which are believed to be DM-dominated with a low background from

[27] Here, spin refers to the intrinsic type of angular momentum that is carried by particles and atomic nuclei.

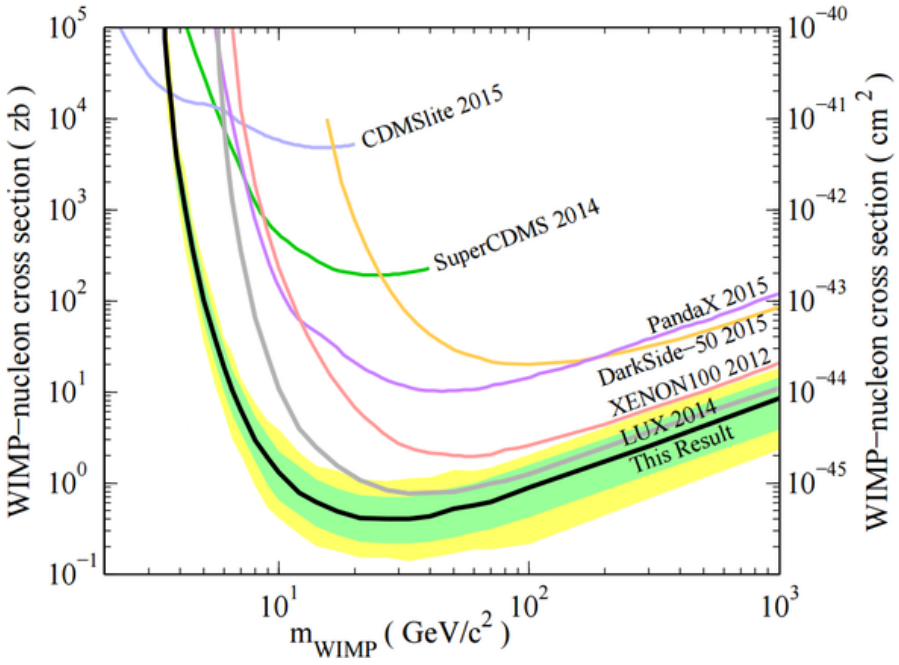

Figure 1.13: Upper limits on the spin-independent WIMP–nucleon elastic scattering cross section as a function of the WIMP mass m_{WIMP} at 90% CL from various direct DM experiments. The solid, black curve shows the most recent result from the LUX experiment, where the green and yellow bands represent the 1σ and 2σ uncertainties, respectively [106].

baryonic processes (see e.g. Ref. [109]).

It is generally assumed that the density of DM haloes $\rho(r)$ satisfies one of two profiles (see Fig. 1.14):

1. The *Navarro–Frenk–White* (NFW) profile has two free parameters (ρ_0 and R_s) [59]:
$$\rho_{\mathrm{NFW}}(r) = \frac{\rho_0}{(r/R_s)[1+(r/R_s)]^2} \ , \tag{1.4.47}$$
where $\rho_0 \equiv \rho(r=0)$ is the central DM density.

2. The *Einasto* profile has three free parameters (ρ_{-2}, r_{-2} and n) [110]:
$$\rho_{\mathrm{Einasto}}(r) = \rho_{-2} \exp\left\{-2n\left[\left(\frac{r}{r_{-2}}\right)^{1/n} - 1\right]\right\} \ , \tag{1.4.48}$$
where r_{-2} is the radius at which the logarithmic slope of the distribution has a value of -2, and $\rho_{-2} \equiv \rho(r=r_{-2})$.

The NFW and Einasto profiles were derived from numerical simulations of galaxy formation, assuming collisionless CDM. From Fig. 1.14, one can see that while the

NFW profile has a central r^{-1} cusp, the Einasto profile has a logarithmic slope that becomes shallower as $r \to 0$. Due to the limited resolution of N-body simulations as $r \to 0$, it is not yet known which of these profiles provides the best description for the central densities of simulated DM haloes (see e.g. Ref. [111]).

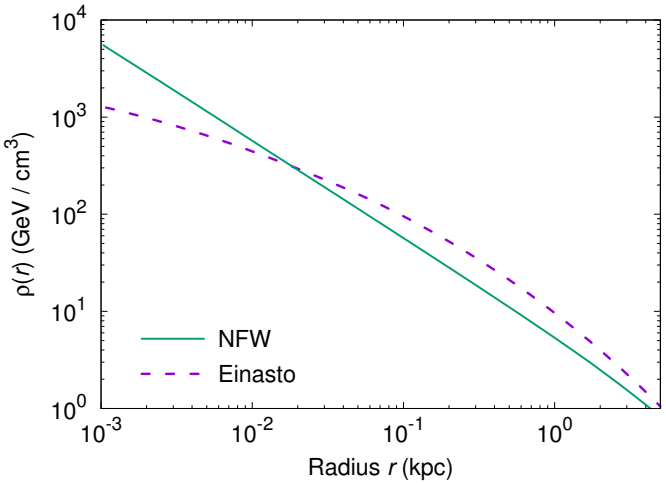

Figure 1.14: Comparison of the NFW (green, solid) and Einasto (purple, dashed) DM halo density profiles, using the values of the parameters as adopted in Ref. [112]. The profiles are normalised to the local DM density $\rho_{\rm DM} \simeq 0.3$ GeV cm^{-3} [113].

In the case of *gamma-rays* (high-energy photons), such particles would travel to us relatively unimpeded, allowing the source of their production to be identified. In general, the expected differential gamma-ray flux from WIMP annihilations can be written as [114]

$$\frac{\mathrm{d}^2\Phi}{\mathrm{d}E\,\mathrm{d}\Omega} = \left(\sum_{\rm f} \left\langle \frac{\mathrm{d}\sigma_{\rm f}}{\mathrm{d}E}\, v \right\rangle N_{\rm f}\right) \frac{1}{4\pi\, m_{\rm DM}^2} \int_{\Psi} \rho^2(l)\,\mathrm{d}l \ , \tag{1.4.49}$$

where E is energy, Ω is the solid angle, the sum runs over all possible final states f containing photons, v is the WIMP relative velocity, $\sigma_{\rm f}$ and $N_{\rm f}$ are the annihilation cross section and number of photons per event in a given annihilation channel, and $\rho(l)$ is the WIMP mass density at a distance l from the observer. The integral[28] runs over the line-of-sight to the source, parameterised by $\Psi = (\theta, \phi)$.

A smoking-gun signal for WIMP DM would be a monochromatic gamma-ray line, which is not produced by any standard astrophysical process. Such a line could

[28] In the literature, $\int_{\Psi} \rho^2(l)\,\mathrm{d}l$ is often referred to as the *J-factor*.

be produced through DM annihilations directly into photons via a loop process (although this would be naturally suppressed). In Chapter 6, we will consider a particular gamma-ray line centred on $E \simeq 511$ keV, which has been observed from the Galactic centre by many experiments for almost four decades [115–120].

In the energy range between $\sim$ 100 MeV and $\sim$ 100 GeV, the *Fermi Large Area Telescope* (LAT) [121] sets strong constraints on the DM annihilation rate into gamma-rays. Above 100 GeV, experiments such as HESS [122], MAGIC [123], VERITAS [124] and most recently, HAWC [125], become more sensitive.

Like gamma-rays, neutrinos preserve spectral information and point back towards the source, making them ideal for indirect DM searches. Detection of high-energy neutrinos generally involves observing the Cherenkov light produced as a neutrino passes through a large volume of water. Three key experiments in operation today are IceCube [126], ANTARES [127] and Super-Kamiokande [128], with energy thresholds of $\sim$ 10 GeV, $\sim$ 20 GeV and $\sim$ 5 MeV, respectively.

Finally, the main signature for DM in charged *cosmic rays*[29] are anti-protons and positrons. These searches can be highly-sensitive due to the low backgrounds of antimatter produced by known astrophysical processes. However, unlike photons and neutrinos, it is difficult to determine the source of cosmic rays due to their diffusion in the galaxy. Current experiments searching for antimatter from DM annihilation and decay include PAMELA [130] and more recently, AMS-02 [131], which are sensitive to particle energies of 100 MeV $-$ 100 GeV and 100 MeV $-$ 1 TeV, respectively. It is also worth noting that experiments such as GAPS [132] are being planned to detect anti-deuteron production.

1.4.3 Collider Searches

Particle accelerators such as the Large Hadron Collider (LHC) are currently attempting to produce DM in the high-energy collisions of proton beams (see e.g. Ref. [133]). Since WIMPs have only weak-strength interactions with matter, they

[29] Cosmic rays are immensely high-energy particles that strike the Earth from space; mainly originating from outside of the Solar System [129].

would simply escape the detector. Therefore, the most probable signature of WIMP production in such experiments is "missing" *transverse energy* (referring to the component of the total final-state momentum in the direction perpendicular to the proton beam), accompanied by a *mono-object*, such as a photon, Z^0 boson or QCD *jet*. In other words, if momentum conservation appears to be violated, it is possible that an invisible, massive particle was created, which did not interact with the surrounding material of the detector. However, if such a particle were to be produced, direct detection experiments would need to confirm whether they exist in sufficient numbers to account for the observed DM relic density.

The unknown interactions between DM and SM particles are usually described by a set of *effective operators* in an *effective field theory* (EFT). However, the EFT approach is no longer valid when the energy scale probed by the effective operators becomes smaller than the energy of the particles in the collision [134]. An alternative method is to characterise DM searches using *simplified models*, which comprise of only four parameters: the WIMP mass, the mediator mass, the WIMP–mediator coupling, and the WIMP–quark coupling [135]. These approaches allow one to compare constraints from direct detection and collider experiments.

So far, there is no convincing evidence for DM production from searches at the LHC [136, 137].

1.5 Outline of the Thesis

The main goal of this thesis is to probe the fundamental properties of DM; in particular, the potential non-gravitational interactions of DM with other particles and with itself.

In Chapter 2, we begin by deriving the linear perturbation equations for matter and radiation, which are required to predict the C_ℓ and linear $P(k)$ for a given cosmological model, and therefore form the basis for Boltzmann codes. We also discuss the tight-coupling equations, which are necessary for describing the baryon–photon fluid before recombination, and the line-of-sight integration approach, which significantly speeds up the computation time for the evolution of

the photon anisotropies. The equations provided in this chapter will be modified when we introduce DM couplings to SM particles in the later chapters.

In Chapter 3, we explore the impact of DM–photon scattering in the early universe (hereafter, γCDM) on the C_ℓ spectra. Using the latest data from the *Planck* satellite in combination with a modified version of the Boltzmann code CLASS, we derive upper limits on the elastic scattering cross section for both constant and temperature-dependent cases. Such constraints are importantly model-independent as one does not need to specify whether DM is annihilating, decaying or asymmetric. We also highlight the effect on the polarisation and matter power spectra, showing that forthcoming data from CMB polarisation experiments and LSS surveys will help to both constrain and characterise the dark sector.

In Chapter 4, we present analogous constraints for DM–neutrino interactions (νCDM), using the latest cosmological data from *Planck* and LSS experiments. We find that the strongest limits are set by the Lyman-α forest, demonstrating that one can use the distribution of matter in the universe to probe such "invisible" interactions. We also show that thermal MeV DM with a constant elastic scattering cross section naturally predicts a cut-off in the $P(k)$ at the Lyman-α scale, an enhancement of H_0 and the effective number of neutrino species $N_{\rm eff}$, and the possible generation of neutrino masses. By providing forecasts for future experiments, we illustrate the power of LSS surveys in probing deviations from the standard ΛCDM model.

In Chapter 5, we use high-resolution N-body simulations to show that the suppressed $P(k)$ predicted in the γCDM and νCDM scenarios can allow one to alleviate the small-scale challenges faced by CDM; in particular, the "missing satellite" and "too-big-to-fail" problems. Our results indicate that physics beyond gravity, which is expected if DM is a thermal WIMP, may be essential to make accurate predictions of structure formation on small scales. Furthermore, by comparing the abundance of satellite galaxies in the Milky Way with the predictions from our interacting DM simulations, we obtain constraints on the scattering cross section that are around three orders of magnitude tighter than

those derived from the CMB.

In Chapter 6, we address an excess of 511 keV gamma-rays that has been observed from the Galactic centre for four decades and is uncorrelated with known astrophysical sources. DM in the form of light ($\lesssim$ 10 MeV) WIMPs annihilating into electron–positron pairs has been one of the leading hypotheses of the observed emission. Given the small required cross section, $\langle \sigma v \rangle_{e^+e^-} \sim 10^{-30}$ cm^3 s^{-1}, a further coupling to lighter particles is required to produce the correct relic density. We first derive constraints from *Planck* on light WIMPs that were in equilibrium with either the neutrino or the electron sector in the early universe. Using these results, we show that the light WIMP explanation of the 511 keV excess is ruled out by the latest cosmological data for both NFW and Einasto DM density profiles, suggesting an astrophysical or more exotic DM source of the signal.

Finally, we provide our conclusions and an outlook for future work in Chapter 7.

Chapter 2

Cosmological Perturbation Theory

> *The answer to the ancient question "Why is there something rather than nothing?" would then be that 'nothing' is unstable.*
>
> — Frank Wilczek

To study the formation and evolution of large-scale structure (LSS) in the universe, one needs to consider density fluctuations around the homogeneous and isotropic background. If these fluctuations remain small, they can be treated in perturbation theory. In this chapter, we derive the *linear* (first-order) perturbation equations for both matter and radiation, assuming a flat universe with an FLRW metric. We use the *conformal Newtonian* (or *longitudinal*) gauge [138] and follow the methodology of Refs. [46, 139] and references therein. In Chapters 3 and 4, we will modify these evolution equations to introduce DM–photon and DM–neutrino scattering, respectively.

In Sec. 2.1, we derive the perturbed *continuity* and *Euler equations*, which describe the time-evolution of the density perturbations. In Sec. 2.2, we derive the *Boltzmann hierarchy* of equations that are necessary to properly account for the perturbations of relativistic species; in particular, neutrinos and photons. In Sec. 2.3, we present the baryon–photon *tight-coupling* equations, which are required prior to recombination. Finally, in Sec. 2.4, we discuss the *line-of-sight* integration method, which is implemented in numerical codes to reduce the time required to compute the photon anisotropy spectrum.

Symbol	Definition	Symbol	Definition
a	Cosmological scale factor	Ψ_ℓ	The ℓth Legendre component of Ψ
$\mathcal{H}$	Conformal Hubble parameter	F_ℓ	Momentum-averaged Ψ_ℓ
τ	Conformal time	δ	Density contrast ($= F_0$)
k	Comoving wavenumber	θ	Divergence of fluid velocity
ϕ, ψ	Metric perturbations	σ	Shear stress ($= F_2/2$)
P	Pressure	c_s	Baryon sound speed ($c_s^2 \equiv \delta P_\mathrm{b}/\delta\rho_\mathrm{b}$)
ρ	Energy density	$\dot{\kappa}$	Thomson rate ($\equiv a\,\sigma_\mathrm{Th}\,n_e$)
w	Equation of state ($= \bar{P}/\bar{\rho}$)	n_e	Free electron number density
f_0	Unperturbed phase space dist. func.	σ_Th	Thomson scattering cross section
Ψ	Perturbation to f_0	R	Density ratio [$\equiv (3/4)(\bar{\rho}_\mathrm{b}/\bar{\rho}_\gamma)$]
P_i	Conjugate momentum to position x^i	p_i	Proper momentum
q_i	Comoving momentum ($\equiv a\,p_i$)	ϵ	Proper energy ($= \sqrt{q^2 + a^2\,m^2}$)
$G_{\gamma\,\ell}$	Photon polarisation component	Π^μ_ν	Anisotropic stress tensor
$\dot{\Theta}_{\gamma\mathrm{b}}$	Baryon–photon slip ($\equiv \dot{\theta}_\gamma - \dot{\theta}_\mathrm{b}$)	τ_c	Thomson opacity ($\equiv \dot{\kappa}^{-1}$)
g	Visibility function [$\equiv \dot{\kappa}\exp(-\kappa)$]	Π	$F_{\gamma\,2} + G_{\gamma\,0} + G_{\gamma\,2}$

Table 2.1: List of parameters used in the perturbation equations of Chapter 2.

2.1 Perturbed Continuity and Euler Equations

The various parameters used in this chapter are defined in Table 2.1. Note that Greek indices α, β, γ etc. run from 0 to 3 (labelling the four space-time coordinates), while Roman indices i, j, k etc. run from 1 to 3 (labelling the spatial components). Repeated indices are summed over and the speed of light c is set to unity.

The geometry of space-time in an expanding homogeneous and isotropic universe can be described by the *line element*

$$\mathrm{d}s^2 = \bar{g}_{\mu\nu}x^\mu x^\nu = a^2(\tau)\left(\mathrm{d}\tau^2 - \mathrm{d}x_i\mathrm{d}x^i\right) \ , \tag{2.1.1}$$

where $a(\tau)$ is the conformal scale factor and τ is the conformal time. The *metric* tensor $\bar{g}_{\mu\nu}$ is both *symmetric* (i.e. $\bar{g}_{\mu\nu} = \bar{g}_{\nu\mu}$) and *diagonal* (i.e. $\bar{g}_{\mu\nu} = 0$ for $\mu \neq \nu$), with elements

$$\bar{g}_{00} = a^2(\tau) \ , \quad \bar{g}_{0i} = 0 \ , \quad \bar{g}_{ij} = -a^2(\tau)\,\delta_{ij} \ . \tag{2.1.2}$$

The evolution of $a(\tau)$ is described by the *Friedmann equation*

$$\mathcal{H}^2 = \left(\frac{\dot{a}}{a}\right)^2 = \frac{8\pi G}{3}\,a^2\rho \ , \tag{2.1.3}$$

and the *acceleration equation*

$$\frac{\mathrm{d}}{\mathrm{d}\tau}\left(\frac{\dot{a}}{a}\right) = -\frac{4\pi G}{3}\, a^2\,(\rho + 3P)\ , \tag{2.1.4}$$

where the overdot denotes a derivative with respect to conformal time, G is Newton's gravitational constant, ρ is energy density, P is pressure, and $\mathcal{H} \equiv \dot{a}/a$ is the conformal Hubble parameter[1].

To develop a general-relativistic treatment of cosmological perturbations, we consider small perturbations $\delta g_{\mu\nu}$ to the FLRW metric $\bar{g}_{\mu\nu}$, i.e.

$$g_{\mu\nu} = \bar{g}_{\mu\nu} + \delta g_{\mu\nu}\ . \tag{2.1.5}$$

Through the *Einstein equations*,

$$G_{\mu\nu} = 8\pi G\, T_{\mu\nu}\ , \tag{2.1.6}$$

perturbations in the metric will be coupled to perturbations in the matter distribution. Note that $G_{\mu\nu}$ is the *Einstein tensor*, which describes the curvature of space-time [17].

The perturbed metric is also symmetric[2] and therefore has 10 independent components (or *degrees of freedom*). One can decompose these components into three sectors according to how they transform under spatial rotations. It can be shown that there are four scalar, four vector and two tensor degrees of freedom [140], such that the perturbed line element can be written as

$$\mathrm{d}s^2 = a^2(\tau)\left\{(1+2\psi)\,\mathrm{d}\tau^2 + B_i\,\mathrm{d}x^i\,\mathrm{d}\tau - [(1-2\phi)\,\delta_{ij} + H_{ij}]\,\mathrm{d}x^i\,\mathrm{d}x^j\right\}\ , \tag{2.1.7}$$

where $B_i \equiv \partial_i b + \epsilon_{ijk}\partial^j b^k$ is a vector with three components, and $H_{ij} \equiv 2[\partial_i\partial_j - (\delta_{ij}\nabla^2)/3]\mu + (\partial_i A_j + \partial_j A_i) + H^T_{ij}$ is a symmetric and *traceless* matrix (i.e. $\mathrm{Tr}(H) \equiv H^i_i = 0$) with five components. The four scalar modes are ψ, ϕ, b and μ; the two

[1] The Friedmann and acceleration equations can be derived from the time–time and space–space components of the Einstein equations [Eq. (2.1.6)], respectively.

[2] One way to see this is that the inner product of two vectors should not depend on the order of the vectors: $g_{\mu\nu}a^\mu b^\nu = g_{\mu\nu}a^\nu b^\mu = g_{\nu\mu}a^\mu b^\nu$, where in the last step, we have renamed the indices. Therefore, $g_{\mu\nu} = g_{\nu\mu}$.

tensor modes comprise the *divergence-free* part of H_{ij} (i.e. the components for which $\partial^i H_{ij} = 0$); the four vector modes are the remaining components of B_i and H_{ij}. The important point is that the scalar, vector and tensor modes are not coupled in linear perturbation theory and one can follow their evolution independently.

The metric perturbations in Eq. (2.1.7) are not uniquely defined and depend on the choice of coordinates or the *gauge*; if we had chosen an alternative set of space-time coordinates, we would obtain different values for the perturbation variables. However, since any physical observation is independent of the coordinate system, we can simply fix the gauge and then keep track of the perturbations. It can be shown that two scalar and two vector components are gauge modes, so that each of the three sectors (scalar, vector and tensor) contain only two physical degrees of freedom [140].

As a further simplification, we can set the vector and tensor modes to zero. There are no sources of vector modes in ΛCDM (or the extensions to ΛCDM that we will be considering), and even if they were initially excited, vector modes would rapidly decay with the expansion of the universe[3]. The tensor modes can also be set to zero as there is no evidence that they are relevant today [58].

In the *Newtonian* (or *longitudinal*) gauge, as proposed by Ref. [138], the two remaining (scalar) degrees of freedom are simply ψ and ϕ and one sets $B_i = H_{ij} = 0$ in Eq. (2.1.7). The line element becomes

$$\mathrm{d}s^2 = a^2(\tau)\left[(1+2\psi)\,\mathrm{d}\tau^2 - (1-2\phi)\,\mathrm{d}x_i\,\mathrm{d}x^i\right] \ , \tag{2.1.8}$$

such that

$$g_{00} = a^2(\tau)\,(1+2\psi) \ , \quad g_{0i} = 0 \ , \quad g_{ij} = -a^2(\tau)\,(1-2\phi)\,\delta_{ij} \ . \tag{2.1.9}$$

One advantage of working in this gauge is that the perturbed metric is also diagonal. Additionally, the scalar mode ψ has a simple physical interpretation: it is the gravitational potential in the Newtonian limit.

[3]Note that at second-order in perturbation theory, vector modes are generated via gravitational collapse [141]. Additionally, in models beyond ΛCDM, there could be an active source of vector modes from cosmic defects such as *cosmic strings* [142].

Another popular choice of gauge in the literature is the *synchronous* gauge [139]. Here, one degree of freedom is usually removed by setting the divergence of the DM velocity in k-space, $\theta_{\rm DM}$, to zero. However, since we will be considering scattering between DM and relativistic particles in this thesis, $\theta_{\rm DM}$ will be non-zero and the synchronous gauge equations would need to be carefully reformulated. For simplicity, we therefore adopt the Newtonian gauge throughout this thesis.

In a homogeneous and isotropic universe, matter behaves as a *perfect fluid*[4] with the (unperturbed) *energy–momentum tensor*

$$\bar{T}^{\mu}_{\nu} = (\bar{\rho} + \bar{P})\bar{U}^{\mu}\bar{U}_{\nu} - \bar{P}\delta^{\mu}_{\nu} \ , \tag{2.1.10}$$

where U^{μ} is the four-velocity of the fluid.

As with the metric, we now consider small perturbations to Eq. (2.1.10), i.e.

$$T^{\mu}_{\nu} = \bar{T}^{\mu}_{\nu} + \delta T^{\mu}_{\nu} \ , \tag{2.1.11}$$

which leads to

$$\begin{aligned} & (\bar{\rho} + \delta\rho + \bar{P} + \delta P)(\bar{U}^{\mu} + \delta U^{\mu})(\bar{U}_{\nu} + \delta U_{\nu}) - (\bar{P} + \delta P)\delta^{\mu}_{\nu} \\ = \ & (\bar{\rho} + \bar{P})\bar{U}^{\mu}\bar{U}_{\nu} - \bar{P}\delta^{\mu}_{\nu} + \delta T^{\mu}_{\nu} \ . \end{aligned} \tag{2.1.12}$$

To first-order, Eq. (2.1.12) implies that

$$\delta T^{\mu}_{\nu} = (\delta\rho + \delta P)\bar{U}^{\mu}\bar{U}_{\nu} + (\bar{\rho} + \bar{P})(\delta U^{\mu}\bar{U}_{\nu} + \bar{U}^{\mu}\delta U_{\nu}) - \delta P\delta^{\mu}_{\nu} \ - \Pi^{\mu}_{\nu} \ . \tag{2.1.13}$$

The final term in Eq. (2.1.13) is the *anisotropic stress* tensor Π^{μ}_{ν}, which characterises the difference between the perturbed fluid and a perfect fluid. Since the energy–momentum tensor is symmetric, we have $\Pi^{\mu}_{\nu} = \Pi^{\nu}_{\mu}$. We can choose Π^{μ}_{ν} to be traceless (i.e. $\Pi^{\mu}_{\mu} = 0$), since its trace can be absorbed into a redefinition of the isotropic pressure δP. We can also choose Π^{μ}_{ν} to be orthogonal to U^{μ} (i.e. $U^{\mu}\Pi_{\mu\nu} = 0$). Thus, without loss of generality, we can set $\Pi^{0}_{0} = \Pi^{0}_{i} = 0$ so that we only need to

[4] A perfect fluid is one that can be completely characterised by its energy density ρ and isotropic pressure P. It has no heat conduction or viscosity, such that the energy–momentum tensor T^{μ}_{ν} is diagonal.

consider the spatial part $\Pi^i_j = T^i_j - \delta^i_j T^k_k/3$, which represents the traceless component of T^i_j.

The perturbed four-velocity is given by

$$U^\mu = a^{-1}(1-\psi, v^i) \ , \quad U_\mu = a(1+\psi, -v_i) \ , \tag{2.1.14}$$

where v_i is the three-velocity, which can be treated as a perturbation of the same order as $\delta\rho$, δP and the metric perturbations.

Combining Eqs. (2.1.13) and (2.1.14), the components of the perturbed energy–momentum tensor to linear order can be written as

$$\begin{aligned} T^0_0 &= \bar{\rho} + \delta\rho \ , \\ T^i_0 &= (\bar{\rho} + \bar{P}) v^i \ , \\ T^0_j &= -(\bar{\rho} + \bar{P}) v_j \ , \\ T^i_j &= -(\bar{P} + \delta P)\delta^i_j - \Pi^i_j \ . \end{aligned} \tag{2.1.15}$$

Next, we require the perturbed *connection coefficients*

$$\Gamma^\mu_{\nu\rho} = \frac{g^{\mu\lambda}}{2}\left(\partial_\nu g_{\lambda\rho} + \partial_\rho g_{\lambda\nu} - \partial_\lambda g_{\nu\rho}\right) . \tag{2.1.16}$$

Since the metric in Eq. (2.1.9) is diagonal, we have

$$g^{00} = a^{-2}(\tau)\,(1-2\psi) \ , \quad g^{0i} = 0 \ , \quad g^{ij} = -a^{-2}(\tau)\,(1+2\phi)\,\delta^{ij} \ . \tag{2.1.17}$$

Substituting Eqs. (2.1.9) and (2.1.17) into Eq. (2.1.16) gives

$$\begin{aligned} \Gamma^0_{00} &= \mathcal{H} + \dot{\psi} \ , \\ \Gamma^0_{0i} &= \partial_i \psi \ , \\ \Gamma^i_{00} &= \delta^{ij}\partial_j \psi \ , \\ \Gamma^0_{ij} &= \mathcal{H}\delta_{ij} - [\dot{\phi} + 2\mathcal{H}(\phi+\psi)]\delta_{ij} \ , \\ \Gamma^i_{j0} &= (\mathcal{H} - \dot{\phi})\delta^i_j \ , \\ \Gamma^i_{jk} &= -2\delta^i_{(j}\partial_{k)}\phi + \delta_{jk}\delta^{il}\partial_l\phi \ , \end{aligned} \tag{2.1.18}$$

where $\delta^i_{(j}\partial_{k)} \equiv (\delta^i_j\partial_k + \delta^i_k\partial_j)/2$.

Assuming energy and momentum conservation, the following condition must be satisfied:

$$\nabla_\mu T^\mu_\nu = \partial_\mu T^\mu_\nu + \Gamma^\mu_{\mu\alpha}T^\alpha_\nu - \Gamma^\alpha_{\mu\nu}T^\mu_\alpha = 0 \ . \tag{2.1.19}$$

First, considering the $\nu = 0$ component to linear order, we have

$$\partial_0 T^0_0 + \partial_i T^i_0 + \Gamma^\mu_{\mu 0} T^0_0 - \Gamma^0_{00} T^0_0 - \Gamma^i_{j0} T^j_i = 0 \ . \tag{2.1.20}$$

Substituting Eqs. (2.1.15) and (2.1.18) for the perturbed energy–momentum tensor and the connection coefficients, respectively, gives

$$\begin{aligned} &\partial_0(\bar\rho + \delta\rho) + \partial_i[(\bar\rho + \bar P)v^i] + (4\mathcal{H} + \dot\psi - 3\dot\phi)(\bar\rho + \delta\rho) \\ &-(\mathcal{H} + \dot\psi)(\bar\rho + \delta\rho) + (\mathcal{H} - \dot\phi)\delta^i_j[(\bar P + \delta P)\delta^j_i + \Pi^j_i] = 0 \ , \end{aligned} \tag{2.1.21}$$

which reduces to

$$\partial_0(\bar\rho + \delta\rho) + \partial_i[(\bar\rho + \bar P)v^i] + 3\mathcal{H}(\bar\rho + \delta\rho) - 3(\bar\rho + \bar P)\dot\phi + 3\mathcal{H}(\bar P + \delta P) = 0 \ , \tag{2.1.22}$$

using $\delta^i_i = 3$ and $\Pi^i_i = 0$.

Considering the zeroth-order and first-order terms separately gives

$$\partial_0 \bar\rho = -3\mathcal{H}(\bar\rho + \bar P) \ , \tag{2.1.23}$$

$$\delta\dot\rho = -3\mathcal{H}(\delta\rho + \delta P) + 3\dot\phi(\bar\rho + \bar P) - (\nabla\cdot v)(\bar\rho + \bar P) \ , \tag{2.1.24}$$

where Eq. (2.1.23) encapsulates energy conservation in the homogeneous background and Eq. (2.1.24) describes the time evolution of the density perturbation.

We now introduce the divergence of the fluid velocity in k-space $\theta \equiv \nabla\cdot v$, the density contrast $\delta \equiv \delta\rho/\bar\rho$ and its time-derivative $\dot\delta = (\bar\rho\,\delta\dot\rho - \delta\rho\,\partial_0\bar\rho)/\bar\rho^2$, and the equation of state $w = \bar P/\bar\rho$. Dividing Eq. (2.1.24) by $\bar\rho$ and using Eq. (2.1.23), we obtain the perturbed general-relativistic *continuity equation*

$$\boxed{\dot\delta = -(1+w)\left(\theta - 3\dot\phi\right) - 3\mathcal{H}\left(\frac{\delta P}{\delta\rho} - w\right)\delta} \tag{2.1.25}$$

The first term on the right-hand side of Eq. (2.1.25) reflects energy density conservation; the factor $(1 + w)$ appears since it is the energy flux rather than the matter flux that is important at the relativistic level. The second term is a damping contribution that appears if $w \neq \delta P/\delta\rho$. However, for all the fluids that we will consider here, w is a constant and therefore, $\delta P/\delta\rho = w + \rho\,\mathrm{d}w/\mathrm{d}\rho = w$, and this term vanishes.

Next, considering the $\nu = i$ component of Eq. (2.1.19) to linear order, we have

$$\partial_0 T^0_i + \partial_j T^j_i + \Gamma^\mu_{\mu 0} T^0_i + \Gamma^\mu_{\mu j} T^j_i - \Gamma^0_{0i} T^0_0 - \Gamma^0_{ji} T^j_0 - \Gamma^j_{0i} T^0_j - \Gamma^j_{ki} T^k_j = 0 \ . \tag{2.1.26}$$

Substituting Eqs. (2.1.15) and (2.1.18) for the perturbed energy–momentum tensor and the connection coefficients, respectively, gives

$$\begin{aligned} &-\partial_0[(\bar\rho + \bar P)v_i] - \partial_j \Pi^j_i - \partial_j(\bar P + \delta P)\delta^j_i - 4\mathcal{H}[(\bar\rho + \bar P)v_i] \\ &-(\partial_j\psi - 3\partial_j\phi)\delta^j_i \bar P - \partial_i\psi\bar\rho - \mathcal{H}\delta_{ji}[(\bar\rho + \bar P)v^j] + \mathcal{H}\delta^j_i[(\bar\rho + \bar P)v_j] \\ &-[2\delta^j_{(i}\partial_{k)}\phi - \delta_{ki}\delta^{jl}\partial_l\phi]\delta^k_j \bar P = 0 \ , \end{aligned} \tag{2.1.27}$$

which reduces to

$$-\partial_0[(\bar\rho + \bar P)v_i] - \partial_i \delta P - 4\mathcal{H}[(\bar\rho + \bar P)v_i] - (\bar\rho + \bar P)\partial_i\psi - \partial_j \Pi^j_i = 0 \ . \tag{2.1.28}$$

These terms are all first-order in the perturbation. Using Eq. (2.1.23) and dividing through by $(\bar\rho + \bar P)$, we obtain

$$\dot v_i = -\mathcal{H}v_i - \frac{\partial_0 \bar P v_i}{\bar\rho + \bar P} - \frac{\partial_i \delta P}{\bar\rho + \bar P} - \frac{\partial_j \Pi^j_i}{\bar\rho + \bar P} - \partial_i\psi \ . \tag{2.1.29}$$

Next, acting on each term with ∂^i,

$$\begin{aligned} \dot\theta &= -\mathcal{H}\theta - \frac{\partial_0 \bar P}{\bar\rho + \bar P}\theta + \frac{k^2\delta P}{\bar\rho + \bar P} - \frac{\partial^i\partial_j \Pi^j_i}{\bar\rho + \bar P} + k^2\psi \\ &= -\mathcal{H}\theta - \frac{\dot w}{1+w}\theta - \frac{\bar P \partial_0 \bar\rho}{\bar\rho^2(1+w)}\theta + \frac{k^2\delta P}{\bar\rho(1+w)} - \frac{\partial^i\partial_j(T^j_i - \delta^j_i T^k_k/3)}{\bar\rho + \bar P} + k^2\psi \\ &= -\mathcal{H}\theta - \frac{\dot w}{1+w}\theta + 3w\mathcal{H}\theta + \frac{\delta P/\delta\rho}{1+w}\,k^2\delta - \frac{2\bar P}{3(\bar\rho + \bar P)}k^2\Pi + k^2\psi \ , \end{aligned} \tag{2.1.30}$$

where we have used the relation $\Pi^i_j = T^i_j - \delta^i_j T^k_k/3$ and the result for $\partial_0\bar\rho$ in Eq. (2.1.23).

Finally, to simplify Eq. (2.1.30), we define $\sigma \equiv [2\bar P/3(\bar\rho + \bar P)]\Pi$, which we will refer to as the *shear stress* [139] as this term represents the stress arising from *shear viscosity*[5]. Unlike perfect fluids (for which $\sigma = 0$), free-streaming, relativistic species (such as massless neutrinos and photons after recombination) have long mean free

[5]Shear viscosity is the resistance to shearing flows and occurs when adjacent, parallel layers of a fluid move at different velocities or have different temperatures [143].

paths with respect to the other particles and travel much further in the perpendicular direction of the flow, thus providing a large shear viscosity and non-negligible σ.

We then obtain the perturbed general-relativistic *Euler equation*

$$\boxed{\dot{\theta} = -\mathcal{H}(1-3w)\theta - \frac{\dot{w}}{1+w}\theta + \frac{\delta P/\delta\rho}{1+w}\,k^2\delta - k^2\sigma + k^2\psi} \tag{2.1.31}$$

The third and fifth terms on the right-hand side of Eq. (2.1.31) drive $\dot{\theta}$, representing the effect of fluid pressure δP and the gravitational potential ψ on the growth of density perturbations, respectively. The first term is a damping factor due to the Hubble expansion, which has the effect of reducing the fluid velocity as a^{-1} for non-relativistic matter (for which $w = 0$). The second term will vanish since we assume w is constant. Finally, the fourth term illustrates the impact of shear stress in suppressing the growth of perturbations.

The perturbed continuity and Euler equations given in Eqs. (2.1.25) and (2.1.31) are sufficient for describing the evolution of matter perturbations, i.e. DM and baryons. However, the equations need to be modified for individual components if they interact with each other (for example, the coupling of the baryon and photon fluids before recombination).

Dark Matter

In the standard ΛCDM framework, DM is *cold* (non-relativistic) and *collisionless* (only interacting with other particles via gravity). Therefore, DM can be treated as a pressureless perfect fluid with $w_{\rm DM} = \delta P/\delta\rho = 0$ and $\sigma_{\rm DM} = 0$, leading to

$$\dot{\delta}_{\rm DM} = -\theta_{\rm DM} + 3\dot{\phi}\,, \tag{2.1.32}$$

$$\dot{\theta}_{\rm DM} = k^2\psi - \mathcal{H}\theta_{\rm DM}\,. \tag{2.1.33}$$

Baryons

Unlike collisionless DM, the Thomson scattering of baryons and photons prior to recombination implies a transfer of energy and momentum between the two fluids, which provides an additional "source term" in the Euler equations. In Sec. 2.2.2, we derive the corresponding source term for the photon component: "$-\dot{\kappa}(\theta_\gamma - \theta_{\rm b})$", where $\dot{\kappa}$ is the Thomson scattering rate.

Assuming that the total 4-momentum of the baryon–photon fluid is conserved in the elastic scattering process, we have

$$\begin{aligned} & (\bar{\rho}_\gamma + \bar{P}_\gamma)\,\delta\theta_\gamma = -(\bar{\rho}_\mathrm{b} + \bar{P}_\mathrm{b})\,\delta\theta_\mathrm{b} \\ \Longrightarrow \quad & \delta\theta_\mathrm{b} = -\frac{4}{3}\frac{\bar{\rho}_\gamma}{\bar{\rho}_\mathrm{b}}\,\delta\theta_\gamma \ , \end{aligned} \tag{2.1.34}$$

where we have used the expression for the momentum density T^i_0 in Eq. (2.1.15). Therefore, the source term for baryons is given by "$-R^{-1}\dot{\kappa}(\theta_\mathrm{b}-\theta_\gamma)$", where we have defined[6] $R \equiv (3/4)(\bar{\rho}_\mathrm{b}/\bar{\rho}_\gamma)$.

In addition, the acoustic term for baryons $c_s^2 k^2 \delta_\mathrm{b}$ is non-negligible at large k, where we have defined the baryon *sound speed* $c_s^2 \equiv \delta P_\mathrm{b}/\delta\rho_\mathrm{b}$. Therefore, taking $w_\mathrm{b} = \delta P/\delta\rho \simeq 0$ and $\sigma_\mathrm{b} \simeq 0$, one finds

$$\dot{\delta}_\mathrm{b} = -\theta_\mathrm{b} + 3\dot{\phi} \ , \tag{2.1.35}$$

$$\dot{\theta}_\mathrm{b} = k^2\psi - \mathcal{H}\theta_\mathrm{b} + c_s^2 k^2 \delta_\mathrm{b} - R^{-1}\dot{\kappa}(\theta_\mathrm{b} - \theta_\gamma) \ . \tag{2.1.36}$$

2.2 Boltzmann Hierarchy for Relativistic Species

For perturbations in relativistic species, one needs to follow the complete evolution of the *phase space distribution function* $f(x^i, P_j, \tau)$ to linear order. In the general case, the energy–momentum tensor $T_{\mu\nu}$ can be written in terms of $f(x^i, P_j, \tau)$ and the 4-momenta components as [139]

$$T_{\mu\nu} = \int \left(\prod_{k=1}^{3} \mathrm{d}P_k\right) [-\det(g)]^{-1/2}\, \frac{P_\mu P_\nu}{P^0}\, f(x^i, P_j, \tau) \ , \tag{2.2.37}$$

where $\det(g)$ is the determinant of the metric tensor $g_{\mu\nu}$. In the conformal Newtonian gauge, the conjugate momenta P_i are related to the proper momenta p_i by $P_i = a(1-\phi)p_i$. The time component of the conjugate 4-momentum is $P_0 = -(1+\psi)\epsilon$, where $\epsilon = a(p^2+m^2)^{1/2} = (P^2 + a^2 m^2)^{1/2}$ is the proper energy measured by a comoving observer.

It is then convenient to introduce the comoving 3-momentum $q_j \equiv a p_j$, which can be written in terms of its magnitude and direction as $q_j = q n_j$, where $n^i n_i = 1$.

[6] In the literature, an alternative definition is sometimes used: $R \equiv (4/3)(\bar{\rho}_\gamma/\bar{\rho}_\mathrm{b})$.

We can then express the phase space distribution function as a sum of the zeroth-order unperturbed distribution function $f_0(q)$ plus a perturbation in terms of q and n_j:

$$f(x^i, P_j, \tau) = f_0(q)\left[1 + \Psi(x^i, q, n_j, \tau)\right] \ . \tag{2.2.38}$$

The function $f_0(q)$ is given by the *Fermi–Dirac distribution* for fermions (+ sign) and the *Bose–Einstein distribution* for bosons (− sign):

$$f_0(q) = \frac{g_s}{h^3}\frac{1}{\exp[\epsilon/(k_{\rm B}T_0) \pm 1]} \ , \tag{2.2.39}$$

where g_s is the number of spin degrees of freedom, h is Planck's constant, $k_{\rm B}$ is Boltzmann's constant and T_0 is the temperature of the particles today.

Using the perturbed metric given in Eq. (2.1.9) and the result that the determinant of a diagonal matrix is the product of its diagonal elements, we have $[-\det(g)]^{-1/2} = a^{-4}(1 - \psi + 3\phi)$ to linear order. Additionally, we can write $\prod_{k=1}^{3} {\rm d}P_k = (1 - 3\phi)\, q^2\, {\rm d}q\, {\rm d}\Omega$, where ${\rm d}\Omega$ is the solid angle associated with the direction n_i. Therefore, Eq. (2.2.37) becomes

$$T_{\mu\nu} = a^{-4}\int q^2\, {\rm d}q\, {\rm d}\Omega\, (1 - \psi)\, \frac{P_\mu P_\nu}{P^0}\, f_0(q)\left[1 + \Psi(x^i, q, n_j, \tau)\right] \ . \tag{2.2.40}$$

It then follows that to first-order,

$$\begin{aligned} T^0_0 &= -a^{-4}\int q^2 dq\, d\Omega\, \sqrt{q^2 + m^2a^2}\, f_0(q)\,(1 + \Psi) \ , \\ T^0_i &= a^{-4}\int q^3 dq\, d\Omega\, n_i\, f_0(q)\, \Psi \ , \\ T^i_j &= a^{-4}\int q^2 dq d\Omega\, \frac{q^2 n_i n_j}{\sqrt{q^2 + m^2a^2}}\, f_0(q)\,(1 + \Psi) \ . \end{aligned} \tag{2.2.41}$$

The important point is that we have eliminated the dependence on the metric perturbations ϕ and ψ by the redefinition of P_i in terms of q and n_i.

The phase space distribution function evolves according to the Boltzmann equation [Eq. (1.3.23)], which in terms of the variables $\{x^i, q, n_i, \tau\}$ is given by

$$\frac{{\rm D}f}{{\rm d}\tau} = \frac{\partial f}{\partial \tau} + \frac{{\rm d}x^i}{{\rm d}\tau}\frac{\partial f}{\partial x^i} + \frac{{\rm d}q}{{\rm d}\tau}\frac{\partial f}{\partial q} + \frac{{\rm d}n_i}{{\rm d}\tau}\frac{\partial f}{\partial n_i} = \left(\frac{\partial f}{\partial \tau}\right)_{\rm C} \ , \tag{2.2.42}$$

where the right-hand side is the collisional term, which will be zero or non-zero depending on the species involved. We can ignore the term $({\rm d}n_i/{\rm d}\tau)(\partial f/\partial n_i)$ since both contributions are first-order.

Next, we can use the *geodesic equation*

$$P^0 \frac{\mathrm{d}P^\mu}{\mathrm{d}\tau} + \Gamma^\mu_{\alpha\beta} P^\alpha P^\beta = 0 \ , \tag{2.2.43}$$

and the connection coefficients given in Eq. (2.1.18) to write

$$\frac{\mathrm{d}q}{\mathrm{d}\tau} = q\dot{\phi} - \epsilon n_i \partial_i \psi \ . \tag{2.2.44}$$

Finally, Eq. (2.2.42) in momentum-space becomes

$$\frac{\partial \Psi}{\partial \tau} + i\frac{q}{\epsilon}(\vec{k}\cdot\hat{n})\,\Psi + \frac{\mathrm{d}\ln(f_0)}{\mathrm{d}\ln(q)}\left[\dot{\phi} - i\frac{\epsilon}{q}(\vec{k}\cdot\hat{n})\,\psi\right] = \frac{1}{f_0}\left(\frac{\partial f}{\partial \tau}\right)_{\mathrm{C}} \ , \tag{2.2.45}$$

where we have used the expansion in Eq. (2.2.38), $\partial_i = i(\vec{k}\cdot\hat{n})$ and $\mathrm{d}x/x \equiv \mathrm{d}\,\mathrm{In}(x)$.

2.2.1 Massless Neutrinos

In this thesis, for simplicity, we will impose the approximation of massless neutrinos[7]. The formalism for implementing massive neutrinos is provided in e.g. Ref. [139].

For relativistic particles, the equation of state $w = \bar{P}/\bar{\rho} = 1/3$. From Eq. (2.1.15), this implies that $\bar{\rho} = 3\bar{P} = -\bar{T}^0_0 = \bar{T}^i_i$. Using Eq. (2.2.41), the unperturbed energy density $\bar{\rho}_\nu$ and pressure $\bar{P}_\nu$ for neutrinos (with mass $m_\nu = 0$) are given by

$$\bar{\rho}_\nu = 3\bar{P}_\nu = a^{-4}\int q^3\,\mathrm{d}q\,\mathrm{d}\Omega\,f_0(q) \ , \tag{2.2.46}$$

while the unperturbed energy flux $\bar{T}^0_i$ and anisotropic stress $\bar{\Pi}^i_j = \bar{T}^i_j - \delta^i_j\bar{P}_\nu$ are zero.

Meanwhile, the first-order perturbations to these quantities are

$$\begin{aligned}
\delta\rho_\nu &= 3\,\delta P_\nu = a^{-4}\int q^3\,\mathrm{d}q\,\mathrm{d}\Omega\,f_0(q)\,\Psi \ , \\
\delta T^0_i &= a^{-4}\int q^3\,\mathrm{d}q\,\mathrm{d}\Omega\,n_i\,f_0(q)\,\Psi \ , \\
\Pi^i_j &= a^{-4}\int q^3\,\mathrm{d}q\,\mathrm{d}\Omega\,(n_i n_j - \frac{1}{3}\delta_{ij})\,f_0(q)\,\Psi \ .
\end{aligned} \tag{2.2.47}$$

[7]We note that neutrinos are expected to have masses $\sim \mathcal{O}(0.1)$ eV [11]. However, unless explicitly stated otherwise, the approximation of massless neutrinos will not affect the results of this thesis.

For massless particles, $\epsilon = (q^2 + a^2 m^2)^{1/2} = q$ and we can integrate out the q-dependence in the distribution function[8]. Furthermore, we expand the angular dependence of the perturbation in terms of *Legendre polynomials* $P_\ell(\hat{k}\cdot\hat{n})$:

$$F_\nu(\vec{k},\hat{n},\tau) \equiv \frac{\int q^3\,\mathrm{d}q\, f_0(q)\,\Psi}{\int q^3\,\mathrm{d}q\, f_0(q)} \equiv \sum_{\ell=0}^{\infty} (-i)^\ell\,(2\ell+1)\,F_{\nu\ell}(\vec{k},\tau)\,P_\ell(\hat{k}\cdot\hat{n})\;, \tag{2.2.48}$$

where the factor $(-i)^\ell(2\ell+1)$ is included to simplify the plane wave expansion of $F_\nu(\vec{k},\hat{n},\tau)$.

Combining the above equations with Eq. (2.1.15) gives the useful results

$$\begin{aligned}
\delta_\nu &= \frac{\delta\rho_\nu}{\bar{\rho}_\nu} = \frac{1}{4\pi}\int \mathrm{d}\Omega\, F_\nu(\vec{k},\hat{n},\tau) = F_{\nu\,0}\,,\\
\theta_\nu &= \frac{3i}{16\pi}\int \mathrm{d}\Omega\,\mu\, F_\nu(\vec{k},\hat{n},\tau) = \frac{3}{4}kF_{\nu\,1}\,,\\
\sigma_\nu &= -\frac{3}{16\pi}\int \mathrm{d}\Omega\left[\mu^2-\frac{1}{3}\right]F_\nu(\vec{k},\hat{n},\tau) = \frac{1}{2}F_{\nu\,2}\,,
\end{aligned} \tag{2.2.49}$$

where we have defined $\mu \equiv \hat{k}\cdot\hat{n}$ and used $\int \mathrm{d}\Omega = \int_0^{2\pi}\mathrm{d}\phi\int_{-1}^{1}\mathrm{d}\mu$, $P_0(\mu) = 1$, $P_1(\mu) = \mu$ and $P_2(\mu) = (1/2)(3\mu^2-1)$.

Next, integrating Eq. (2.2.45) over $q^3\,\mathrm{d}q\, f_0(q)$ and setting the collisional term to zero gives

$$\int q^3\,\mathrm{d}q\, f_0\frac{\partial\Psi}{\partial\tau} + ik\mu\int q^3\,\mathrm{d}q\, f_0\,\Psi = -(\dot{\phi}-ik\mu\psi)\int q^3\,\mathrm{d}q\, f_0\frac{\mathrm{d}\ln(f_0)}{\mathrm{d}\ln(q)}\;. \tag{2.2.50}$$

Dividing Eq. (2.2.50) by $\int q^3\,\mathrm{d}q\, f_0(q)$ and comparing to Eq. (2.2.48), we obtain the simple Boltzmann equation for massless neutrinos:

$$\frac{\partial F_\nu}{\partial\tau} + ik\mu F_\nu = 4(\dot{\phi}-ik\mu\psi)\;. \tag{2.2.51}$$

We can then use the orthogonality property of Legendre polynomials

$$\int_{-1}^{1}\mathrm{d}\mu\, P_\ell(\mu)\,P_{\ell'}(\mu) = \frac{2}{2\ell+1}\delta_{\ell\ell'}\;, \tag{2.2.52}$$

to invert Eq. (2.2.48):

$$F_{\nu\,\ell}(\vec{k},\tau) = i^\ell\int_{-1}^{1}\frac{\mathrm{d}\mu}{2}\,P_\ell(\mu)\,F_\nu(\vec{k},\hat{n},\tau)\;. \tag{2.2.53}$$

[8] In the case of massive neutrinos, the q-dependence cannot be removed and significantly more computation time is required to perform the integration of the resulting evolution equations [139].

Operating with $i^\ell \int_{-1}^{1} \mathrm{d}\mu\, P_\ell(\mu)$ on both sides of Eq. (2.2.51), we have

$$i^\ell \int_{-1}^{1} \mathrm{d}\mu\, P_\ell(\mu)\dot{F}_\nu + i^\ell\, ik \int_{-1}^{1} \mathrm{d}\mu\, \mu\, P_\ell(\mu)\, F_\nu = 4i^\ell \int_{-1}^{1} \mathrm{d}\mu\, P_\ell(\mu)\,(\dot{\phi} - ik\mu\psi)\ . \quad (2.2.54)$$

Using the recursion relation $(\ell+1)P_{\ell+1}(\mu) = (2\ell+1)\mu P_\ell(\mu) - \ell P_{\ell-1}(\mu)$,

$$\begin{aligned} & i^\ell \int_{-1}^{1} \mathrm{d}\mu\, P_\ell(\mu)\dot{F}_\nu + \frac{ik}{2\ell+1} i^\ell \int_{-1}^{1} \mathrm{d}\mu\, [\ell P_{\ell-1}(\mu) + (\ell+1)P_{\ell+1}(\mu)]\, F_\nu \\ = \ & 4i^\ell \int_{-1}^{1} \mathrm{d}\mu\, P_\ell(\mu)\,(\dot{\phi} - ik\mu\psi)\ , \end{aligned} \quad (2.2.55)$$

and comparing Eq. (2.2.55) to Eq. (2.2.53), we obtain

$$\dot{F}_{\nu\,\ell} - \frac{k}{2\ell+1}\left[\ell F_{\nu\,(\ell-1)} - (\ell+1)F_{\nu\,(\ell+1)}\right] = 2i^\ell \int_{-1}^{1} \mathrm{d}\mu\, P_\ell(\mu)\,(\dot{\phi} - ik\mu\psi)\ . \quad (2.2.56)$$

Finally, considering separately the $\ell = 0$, $\ell = 1$ and $\ell \geq 2$ modes, and the relations in Eq. (2.2.49), we obtain the *Boltzmann hierarchy* of equations for massless neutrinos:

$$\dot{\delta}_\nu = \dot{F}_{\nu\,0} = -\frac{4}{3}\theta_\nu + 4\dot{\phi}\ , \quad (2.2.57)$$

$$\dot{\theta}_\nu = \frac{3}{4}k\dot{F}_{\nu\,1} = k^2\psi + k^2\left(\frac{1}{4}\delta_\nu - \sigma_\nu\right)\ , \quad (2.2.58)$$

$$\dot{F}_{\nu\,\ell} = \frac{k}{2\ell+1}\left[\ell F_{\nu\,(\ell-1)} - (\ell+1)F_{\nu\,(\ell+1)}\right]\ , \quad \ell \geq 2 \quad (2.2.59)$$

where for Eq. (2.2.59), we have used the result that $\int_{-1}^{1} \mathrm{d}\mu\, P_\ell(\mu)(a + b\mu) = 0$ for $\ell \geq 2$, if a and b are constants with respect to μ.

Eqs. (2.2.57) and (2.2.58) are simply the perturbed continuity and Euler equations derived in Sec. 2.1 for a species with $w_\nu = \delta P/\delta\rho = 1/3$ and non-negligible shear stress σ_ν. Note that a given $F_{\nu\,\ell}$ is only coupled to its neighbouring $(\ell-1)$ and $(\ell+1)$ modes.

2.2.2 Photons

The evolution of the phase space distribution function for photons can be treated in a similar way to massless neutrinos. However, as a result of the tight-coupling of photons and baryons before recombination, the collisional term $(\partial f/\partial\tau)_{\mathrm{C}}$ on the right-hand side of the Boltzmann equation [Eq. (2.2.45)] is now present and is dependent on the photon polarisation.

We consider separately:

1. The momentum-averaged total phase space density perturbation, summed over the polarisation: $F_\gamma(\vec{k},\hat{n},\tau)$.

2. The difference between the two linear polarisation components: $G_\gamma(\vec{k},\hat{n},\tau)$.

To first-order, one finds [144]

$$\begin{aligned}\left(\frac{\partial F_\gamma}{\partial\tau}\right)_{\rm C} &= \dot\kappa\left\{-F_\gamma+F_{\gamma\,0}+4\hat{n}\cdot\vec{v}_e-\frac{1}{2}\left(F_{\gamma\,2}+G_{\gamma\,0}+G_{\gamma\,2}\right)P_2(\mu)\right\}\,,\\ \left(\frac{\partial G_\gamma}{\partial\tau}\right)_{\rm C} &= \dot\kappa\left\{-G_\gamma+\frac{1}{2}\left(F_{\gamma\,2}+G_{\gamma\,0}+G_{\gamma\,2}\right)\left[1-P_2(\mu)\right]\right\}\,,\end{aligned}\tag{2.2.60}$$

where $\dot\kappa\equiv an_e\sigma_{\rm Th}$ is the Thomson scattering rate, and n_e and $\vec{v}_e$ are the mean number density and velocity of the electrons, respectively.

We can now expand the above expressions in a Legendre series as in Eq. (2.2.48):

$$\begin{aligned}\left(\frac{\partial F_\gamma}{\partial\tau}\right)_{\rm C} &= \dot\kappa\left[\frac{4i}{k}(\theta_\gamma-\theta_b)\mu+\left(9\sigma_\gamma-\frac{1}{2}G_{\gamma\,0}-\frac{1}{2}G_{\gamma\,2}\right)P_2(\mu)\right.\\ &\qquad\left.-\sum_{\ell\geq3}^{\infty}(-i)^\ell(2\ell+1)F_{\gamma\,\ell}P_\ell(\mu)\right]\,,\end{aligned}\tag{2.2.61}$$

$$\begin{aligned}\left(\frac{\partial G_\gamma}{\partial\tau}\right)_{\rm C} &= \dot\kappa\left\{\frac{1}{2}\left(F_{\gamma\,2}+G_{\gamma\,0}+G_{\gamma\,2}\right)\left[1-P_2(\mu)\right]\right.\\ &\qquad\left.-\sum_{\ell\geq0}^{\infty}(-i)^\ell(2\ell+1)G_{\gamma\,\ell}P_\ell(\mu)\right\}\,,\end{aligned}\tag{2.2.62}$$

where we have used the substitution $\hat{n}\cdot\vec{v}_e=-(i\theta_b/k)\mu$, in addition to

$$\delta_\gamma=F_{\gamma\,0}\,,\quad \theta_\gamma=\frac{3}{4}kF_{\gamma\,1}\,,\quad \sigma_\gamma=\frac{1}{2}F_{\gamma\,2}\,,\tag{2.2.63}$$

as in Eq. (2.2.49).

The left-hand side of the Boltzmann equation is identical to that of massless neutrinos. Therefore, using Eq. (2.2.56), it follows that

$$\begin{aligned}\dot{F}_{\gamma\,\ell} &= \frac{k}{2\ell+1}\left[\ell F_{\gamma\,(\ell-1)}-(\ell+1)F_{\gamma\,(\ell+1)}\right]\\ &\quad+2i^\ell\int_{-1}^{1}{\rm d}\mu\,P_\ell(\mu)\left[\dot\phi-ik\mu\psi+\frac{1}{4}\left(\frac{\partial F_\gamma}{\partial\tau}\right)_{\rm C}\right]\,,\end{aligned}\tag{2.2.64}$$

$$\begin{aligned}\dot{G}_{\gamma\,\ell} &= \frac{k}{2\ell+1}\left[\ell G_{\gamma\,(\ell-1)}-(\ell+1)G_{\gamma\,(\ell+1)}\right]\\ &\quad+\frac{1}{2}i^\ell\int_{-1}^{1}{\rm d}\mu\,P_\ell(\mu)\left(\frac{\partial G_\gamma}{\partial\tau}\right)_{\rm C}\,.\end{aligned}\tag{2.2.65}$$

Finally, considering separately the $\ell = 0$, $\ell = 1$, $\ell = 2$ and $\ell \geq 3$ modes, and the relations in Eq. (2.2.63), we obtain the infinite Boltzmann hierarchy of equations for photons:

$$\dot{\delta}_\gamma = \dot{F}_{\gamma 0} = -\frac{4}{3}\theta_\gamma + 4\dot{\phi} \,, \tag{2.2.66}$$

$$\dot{\theta}_\gamma = \frac{3}{4}k\dot{F}_{\gamma 1} = k^2\psi + k^2\left(\frac{1}{4}\delta_\gamma - \sigma_\gamma\right) - \dot{\kappa}(\theta_\gamma - \theta_{\rm b}) \,, \tag{2.2.67}$$

$$\dot{F}_{\gamma 2} = 2\dot{\sigma}_\gamma = \frac{8}{15}\theta_\gamma - \frac{3}{5}kF_{\gamma 3} - \frac{9}{5}\dot{\kappa}\sigma_\gamma + \frac{1}{10}\dot{\kappa}\left(G_{\gamma 0} + G_{\gamma 2}\right) \,, \tag{2.2.68}$$

$$\dot{F}_{\gamma \ell} = \frac{k}{2\ell+1}\left[\ell F_{\gamma(\ell-1)} - (\ell+1)F_{\gamma(\ell+1)}\right] - \dot{\kappa}F_{\gamma\ell} \,, \quad \ell \geq 3 \tag{2.2.69}$$

$$\begin{aligned}\dot{G}_{\gamma l} = {} & \frac{k}{2\ell+1}\left[\ell G_{\gamma(\ell-1)} - (\ell+1)G_{\gamma(\ell+1)}\right] \\ & + \dot{\kappa}\left[-G_{\gamma\ell} + \frac{1}{2}\left(F_{\gamma 2} + G_{\gamma 0} + G_{\gamma 2}\right)\left(\delta_{\ell 0} + \frac{\delta_{\ell 2}}{5}\right)\right] \,,\end{aligned} \tag{2.2.70}$$

where we have used Eq. (2.2.52) to perform the integration over μ for general ℓ.

2.3 Baryon–Photon Tight-Coupling Equations

Before recombination, the baryons and photons are tightly coupled. More precisely, the reciprocal of the *Thomson opacity* ${\tau_c}^{-1} \equiv \dot{\kappa}$, which quantifies the interaction rate, is much greater than the Hubble rate $\mathcal{H} \equiv \dot{a}/a \sim \tau^{-1}$, which describes the expansion. As a result, the source terms in Eqs. (2.1.36) and (2.2.67) for $\dot{\theta}_{\rm b}$ and $\dot{\theta}_\gamma$ are large and the evolution equations become difficult to solve numerically. It is therefore beneficial to obtain alternative forms of the Euler equations that are valid in the limit that $\tau_c \ll \tau$ and $k\tau_c \ll 1$; an idea that was first proposed in Ref. [145].

We begin by combining Eqs. (2.1.36) and (2.2.67) for $\dot{\theta}_{\rm b}$ and $\dot{\theta}_\gamma$ to remove the dependence on $\dot{\kappa} \equiv {\tau_c}^{-1}$:

$$R\dot{\theta}_{\rm b} + \dot{\theta}_\gamma = R(-\mathcal{H}\theta_{\rm b} + c_s^2 k^2 \delta_{\rm b}) + k^2\left(\frac{\delta_\gamma}{4} - \sigma_\gamma\right) + (1+R)k^2\psi \,, \tag{2.3.71}$$

where we have used the definition[9] $R \equiv (3/4)(\bar{\rho}_{\rm b}/\bar{\rho}_\gamma)$.

We now introduce the quantity $\Theta_{\gamma{\rm b}} \equiv \theta_\gamma - \theta_{\rm b}$; the time-derivative of which, $\dot{\Theta}_{\gamma{\rm b}} \equiv \dot{\theta}_\gamma - \dot{\theta}_{\rm b}$, is often referred to as the *baryon–photon slip*. Then, Eq. (2.3.71) can

[9] Note that in the literature, the alternative definition $R \equiv (4/3)(\bar{\rho}_\gamma/\bar{\rho}_{\rm b})$ is sometimes used.

be written as

$$\dot{\theta}_{\rm b} = -\frac{1}{1+R}\left[R(\mathcal{H}\theta_{\rm b} - c_s^2 k^2 \delta_{\rm b}) - k^2\left(\frac{\delta_\gamma}{4} - \sigma_\gamma\right) + \dot{\Theta}_{\gamma{\rm b}}\right] + k^2\psi \ , \tag{2.3.72}$$

and Eq. (2.2.67) becomes

$$\dot{\theta}_\gamma = (1+R)k^2\psi + k^2\left(\frac{1}{4}\delta_\gamma - \sigma_\gamma\right) - R\left(\dot{\theta}_{\rm b} + \mathcal{H}\theta_{\rm b} - c_s^2 k^2 \delta_{\rm b}\right) \ . \tag{2.3.73}$$

The important point is that only the slip $\dot{\Theta}_{\gamma{\rm b}}$ and the photon shear σ_γ depend on τ_c in Eqs. (2.3.72) and (2.3.73). The next step is to find expressions for these quantities that are valid at the $n^{\rm th}$ order in τ_c.

Again, combining Eqs. (2.1.36) and (2.2.67) for $\dot{\theta}_{\rm b}$ and $\dot{\theta}_\gamma$, we can obtain a differential equation for $\Theta_{\gamma{\rm b}}$:

$$R\tau_c\left[\dot{\Theta}_{\gamma{\rm b}} - \mathcal{H}\theta_{\rm b} + k^2\left(c_s^2\delta_{\rm b} - \frac{\delta_\gamma}{4} + \sigma_\gamma\right)\right] + (1+R)\Theta_{\gamma{\rm b}} = 0 \ . \tag{2.3.74}$$

The time-evolution of the photon shear is given by Eq. (2.2.68):

$$\dot{\sigma}_\gamma = \frac{4}{15}\theta_\gamma - \frac{3}{10}kF_{\gamma\,3} - \frac{9}{10}\dot{\kappa}\sigma_\gamma + \frac{1}{20}\dot{\kappa}\left(G_{\gamma\,0} + G_{\gamma\,2}\right) \ , \tag{2.3.75}$$

which implies that

$$\sigma_\gamma = \frac{\tau_c}{9}\left(\frac{8}{3}\theta_\gamma - 3kF_{\gamma\,3} - 10\dot{\sigma}_\gamma\right) + \frac{1}{18}\left(G_{\gamma\,0} + G_{\gamma\,2}\right) \ . \tag{2.3.76}$$

For illustrative purposes, we will perturbatively expand $\dot{\Theta}_{\gamma{\rm b}}$ and σ_γ to linear order in τ_c. The second-order expressions can be found in Ref. [146]. Firstly, using Eq. (2.3.74),

$$\Theta_{\gamma{\rm b}} = -\frac{R\tau_c}{1+R}\left[-\mathcal{H}\theta_{\rm b} + k^2\left(c_s^2\delta_{\rm b} - \frac{\delta_\gamma}{4} + \sigma_\gamma\right)\right] + \mathcal{O}({\tau_c}^2) \ . \tag{2.3.77}$$

We now need to differentiate this expression with respect to conformal time to obtain a first-order approximation for the slip. In the literature, the derivative of the term

in square brackets is often written in a very particular way (see e.g. Ref. [139]):

$$\begin{aligned}\frac{\mathrm{d}}{\mathrm{d}\tau}[...] &= -\mathcal{H}\dot{\theta}_\mathrm{b} - \dot{\mathcal{H}}\theta_\mathrm{b} + k^2\left(\dot{c}_s^2\delta_\mathrm{b} + c_s^2\dot{\delta}_\mathrm{b} - \frac{\dot{\delta}_\gamma}{4} + \dot{\sigma}_\gamma\right) \\ &= -2\mathcal{H}\dot{\theta}_\mathrm{b} - (\dot{\mathcal{H}} + \mathcal{H}^2)\theta_\mathrm{b} + k^2\left[(\mathcal{H}c_s^2 + \dot{c}_s^2)\delta_\mathrm{b} + c_s^2\dot{\delta}_\mathrm{b} - \frac{\dot{\delta}_\gamma}{4} + \dot{\sigma}_\gamma + \mathcal{H}\psi\right] \\ &\quad + \frac{\mathcal{H}}{R\tau_c}\Theta_{\gamma\mathrm{b}} \\ &= 2\mathcal{H}\dot{\Theta}_{\gamma\mathrm{b}} - \frac{\ddot{a}}{a}\theta_\mathrm{b} + k^2\left(-\frac{\mathcal{H}}{2}\delta_\gamma + \bar{c}_s^2\delta_\mathrm{b} + c_s^2\dot{\delta}_\mathrm{b} - \frac{\dot{\delta}_\gamma}{4} + 2\mathcal{H}\sigma_\gamma + \dot{\sigma}_\gamma - \mathcal{H}\psi\right) \\ &\quad + \frac{(1+2R)\mathcal{H}}{R\tau_c}\Theta_{\gamma\mathrm{b}}\ , \end{aligned} \tag{2.3.78}$$

where we have defined $\bar{c}_s^2 \equiv (\mathcal{H}c_s^2 + \dot{c}_s^2)$. Then, using $\dot{R} = \mathcal{H}R$, the slip to first-order in τ_c is given by

$$\begin{aligned}\dot{\Theta}_{\gamma\mathrm{b}} &= -\frac{R\tau_c}{1+R}\left[-\frac{\ddot{a}}{a}\theta_\mathrm{b} + k^2\left(-\frac{\mathcal{H}}{2}\delta_\gamma + \bar{c}_s^2\delta_\mathrm{b} + c_s^2\dot{\delta}_\mathrm{b} - \frac{\dot{\delta}_\gamma}{4} - \mathcal{H}\psi\right)\right] \\ &\quad + \left(\frac{\dot{\tau}_c}{\tau_c} - \frac{2\mathcal{H}R}{1+R}\right)\Theta_{\gamma\mathrm{b}} + \mathcal{O}({\tau_c}^2)\ , \end{aligned} \tag{2.3.79}$$

where the terms involving $2\mathcal{H}\dot{\Theta}_{\gamma\mathrm{b}}$ and $(2\mathcal{H}\sigma_\gamma + \dot{\sigma}_\gamma)$ are not present to first-order.

For the shear stress, Eq. (2.3.76) can be written as

$$\sigma_\gamma = \frac{8\tau_c}{27}\theta_\gamma + \frac{1}{18}\left(G_{\gamma\,0} + G_{\gamma\,2}\right) + \mathcal{O}({\tau_c}^2)\ , \tag{2.3.80}$$

where we have used the fact that $F_{\gamma\,3} = \mathcal{O}({\tau_c}^2)$ and $G_{\gamma\,0} \sim G_{\gamma\,2} \sim \mathcal{O}(\tau_c)$.

From Eq. (2.2.70), the polarisation multipoles $\ell = 0$ and $\ell = 2$ satisfy

$$\begin{aligned}\dot{G}_{\gamma\,0} &= -kG_{\gamma\,1} + {\tau_c}^{-1}\left[\sigma_\gamma + \frac{1}{2}\left(-G_{\gamma\,0} + G_{\gamma\,2}\right)\right]\ , \\ \dot{G}_{\gamma\,2} &= \frac{k}{5}\left(2G_{\gamma\,1} - 3G_{\gamma\,3}\right) + {\tau_c}^{-1}\left[\frac{1}{10}\left(2\sigma_\gamma + G_{\gamma\,0} - 9G_{\gamma\,2}\right)\right]\ . \end{aligned} \tag{2.3.81}$$

Noting that $G_{\gamma\,1} \sim G_{\gamma\,3} \sim \mathcal{O}({\tau_c}^2)$, we can obtain a perturbative expansion of Eq. (2.3.81):

$$G_{\gamma\,0} = \frac{5\sigma_\gamma}{2} + \mathcal{O}({\tau_c}^2)\ , \quad G_{\gamma\,2} = \frac{\sigma_\gamma}{2} + \mathcal{O}({\tau_c}^2)\ , \tag{2.3.82}$$

which implies that the photon shear to first-order in τ_c is simply

$$\sigma_\gamma = \frac{16\tau_c}{45}\theta_\gamma + \mathcal{O}({\tau_c}^2)\ . \tag{2.3.83}$$

To summarise, in the baryon–photon tight-coupling regime, the perturbed Euler equations for the baryon and photon fluids are given by Eqs. (2.3.72) and (2.3.73), with $\dot{\Theta}_{\gamma \mathrm{b}}$ given by Eq. (2.3.79) and σ_γ given by Eq. (2.3.83), to first-order in τ_c. These equations will need to be modified when we introduce DM–photon scattering in Chapter 3.

2.4 Line-of-Sight Integration Approach

In Refs. [46, 147], the authors introduced a novel method for calculating the CMB anisotropy spectra using a *line-of-sight integration* approach. Their technique significantly reduced the computation time compared to solving the photon Boltzmann hierarchy in the traditional way (as described in Sec. 2.2.2).

Firstly, using Eqs. (2.2.51) and (2.2.60), the Boltzmann evolution equations can be written as

$$\dot{F}_\gamma + ik\mu F_\gamma = 4(\dot{\phi} - ik\mu\psi) + \dot{\kappa}\left\{-F_\gamma + F_{\gamma 0} + 4\hat{n}\cdot\vec{v}_e - \frac{1}{2}P_2(\mu)\Pi\right\} , \quad (2.4.84)$$

$$\dot{G}_\gamma + ik\mu G_\gamma = \dot{\kappa}\left[-G_\gamma + \frac{1}{2}\left[1 - P_2(\mu)\right]\Pi\right] , \quad (2.4.85)$$

where we have defined $\Pi \equiv F_{\gamma 2} + G_{\gamma 0} + G_{\gamma 2}$.

If we then define the photon temperature and polarisation *transfer functions* $\Delta^{\mathrm{T}} \equiv (1/4)F_\gamma$ and $\Delta^{\mathrm{P}} \equiv (1/4)G_\gamma$, we have:

$$\dot{\Delta}^{\mathrm{T}} + ik\mu\Delta^{\mathrm{T}} = \dot{\phi} - ik\mu\psi + \dot{\kappa}\left\{-\Delta^{\mathrm{T}} + \Delta^{\mathrm{T}}_0 + \mu v_{\mathrm{b}} - \frac{1}{8}P_2(\mu)\Pi\right\} , \quad (2.4.86)$$

$$\dot{\Delta}^{\mathrm{P}} + ik\mu\Delta^{\mathrm{P}} = \dot{\kappa}\left[-\Delta^{\mathrm{P}} + \frac{1}{8}\left[1 - P_2(\mu)\right]\Pi\right] , \quad (2.4.87)$$

where we have used the substitution $\hat{n}\cdot\vec{v}_e = -(i\theta_b/k)\mu = \mu v_{\mathrm{b}}$.

One can then expand these equations in multipole moments, which gives rise to the Boltzmann hierarchy of coupled differential equations as derived in Sec. 2.2.2. To predict the value of the CMB anisotropy spectrum at a given scale θ, these equations need to be solved up to a multipole $\ell \sim 1/\theta$. However, if one is interested in studying small angular scales with high accuracy, a very large system of equations needs to be evolved and the computation time becomes very long.

Instead, let us first consider the polarisation transfer function in Eq. (2.4.87) and multiply each side of the equation by $\exp(ik\mu\tau - \kappa)$:

$$\dot{\Delta}^{\rm P} e^{ik\mu\tau-\kappa} + (\dot{\kappa} + ik\mu)\Delta^{\rm P} e^{ik\mu\tau-\kappa} = \frac{1}{8}\dot{\kappa} e^{ik\mu\tau-\kappa}\left[1 - P_2(\mu)\right]\Pi \,, \tag{2.4.88}$$

where $\kappa(\tau) \equiv -\int_\tau^{\tau_0} \dot{\kappa}(\tau)\mathrm{d}\tau$, τ_0 is the time today, and we introduce the *visibility function* $g(\tau) \equiv \dot{\kappa}\exp(-\kappa)$. The maximum value of $g(\tau)$ defines the epoch of recombination, when the dominant contribution to the CMB anisotropies arises.

Next, using $\mathrm{d}(e^{-\kappa})/\mathrm{d}\tau = \dot{\kappa}e^{-\kappa}$, one can rewrite Eq. (2.4.88) as

$$\frac{\mathrm{d}}{\mathrm{d}\tau}\left(\Delta^{\rm P} e^{ik\mu\tau-\kappa}\right) = \frac{1}{8}\dot{\kappa} e^{-\kappa} e^{ik\mu\tau}\left[1 - P_2(\mu)\right]\Pi \,. \tag{2.4.89}$$

Integrating over conformal time (along the *past light-cone*), the left-hand side of Eq. (2.4.89) becomes

$$\begin{aligned}\int_0^{\tau_0} \mathrm{d}\tau \frac{\mathrm{d}}{\mathrm{d}\tau}\left(\Delta^{\rm P} e^{ik\mu\tau-\kappa}\right) &= \Delta^{\rm P}(\tau=\tau_0)\, e^{ik\mu\tau_0-\kappa(\tau=\tau_0)} - \Delta^{\rm P}(\tau=0)\, e^{-\kappa(\tau=0)} \\ &= \Delta^{\rm P}(\tau=\tau_0)\, e^{ik\mu\tau_0} \,,\end{aligned} \tag{2.4.90}$$

since by definition, $\kappa(\tau=\tau_0) = 0$ and $\kappa(\tau=0) \to \infty$.

Next, integrating the right-hand side of Eq. (2.4.89), we have

$$\begin{aligned}\Delta^{\rm P}(\tau=\tau_0) &= \frac{1}{8}\int_0^{\tau_0} \mathrm{d}\tau\, g(\tau)\, e^{ik\mu(\tau-\tau_0)}\left[1 - P_2(\mu)\right]\Pi \\ &= \frac{3}{16}\int_0^{\tau_0} \mathrm{d}\tau\, e^{ik\mu(\tau-\tau_0)}\left(1-\mu^2\right) g\Pi \,,\end{aligned} \tag{2.4.91}$$

where we have used $P_2(\mu) = (1/2)(3\mu^2 - 1)$.

Eq. (2.4.91) can be further simplified by eliminating the angle μ in the integrand via *integration by parts*. The boundary terms can be dropped since they vanish as $\tau \to 0$ and are unobservable for $\tau = \tau_0$ (i.e. we have $\int uv' = -\int u'v$). Thus,

$$\begin{aligned}\Delta^{\rm P}(\tau=\tau_0) &= \frac{3}{16}\int_0^{\tau_0} \mathrm{d}\tau\, e^{ik\mu(\tau-\tau_0)}\left[g\Pi - \frac{\mu^2}{(ik\mu)^2}\frac{\mathrm{d}^2}{\mathrm{d}\tau^2}(g\Pi)\right] \\ &= \frac{3}{16}\int_0^{\tau_0} \mathrm{d}\tau\, e^{ik\mu(\tau-\tau_0)}\left[g\Pi + \frac{1}{k^2}\frac{\mathrm{d}^2}{\mathrm{d}\tau^2}(g\Pi)\right] \,.\end{aligned} \tag{2.4.92}$$

Following the same procedure for the temperature transfer function in Eq. (2.4.86),

one obtains

$$\begin{aligned}\Delta^{\rm T}(\tau=\tau_0) &= \int_0^{\tau_0} {\rm d}\tau\, {\rm e}^{ik\mu(\tau-\tau_0)} \\ &\quad \left\{ {\rm e}^{-\kappa}\left(\dot\phi - ik\mu\psi\right) + g\left[\Delta_0^{\rm T} + \mu v_{\rm b} - \frac{1}{16}(3\mu^2-1)\Pi\right]\right\} \\ &= \int_0^{\tau_0} {\rm d}\tau\, {\rm e}^{ik\mu(\tau-\tau_0)} \\ &\quad \left\{ {\rm e}^{-\kappa}\dot\phi + g\left(\Delta_0^{\rm T} + \frac{\Pi}{16}\right) - \mu(ik\psi{\rm e}^{-\kappa} + g v_{\rm b}) - \frac{3}{16}\mu^2(g\Pi)\right\} \quad . \end{aligned} \tag{2.4.93}$$

After integration by parts, Eq. (2.4.93) becomes

$$\begin{aligned}\Delta^{\rm T}(\tau=\tau_0) &= \int_0^{\tau_0} {\rm d}\tau\, {\rm e}^{ik\mu(\tau-\tau_0)} \times \left\{ {\rm e}^{-\kappa}\dot\phi + g\left(\Delta_0^{\rm T} + \frac{\Pi}{16}\right)\right. \\ &\quad \left. -\frac{1}{ik}\frac{\rm d}{{\rm d}\tau}(ik\psi{\rm e}^{-\kappa} + g v_{\rm b}) + \frac{3}{16}\frac{1}{k^2}\frac{{\rm d}^2}{{\rm d}\tau^2}(g\Pi)\right\} \\ &= \int_0^{\tau_0} {\rm d}\tau\, {\rm e}^{ik\mu(\tau-\tau_0)} \times \left\{ {\rm e}^{-\kappa}\dot\phi + \frac{g}{4}\left(\delta_\gamma + \frac{\Pi}{4}\right) + \frac{\rm d}{{\rm d}\tau}\left({\rm e}^{-\kappa}\psi\right)\right. \\ &\quad \left. + \frac{1}{k^2}\frac{\rm d}{{\rm d}\tau}\left(g\theta_{\rm b}\right) + \frac{3}{16k^2}\frac{{\rm d}^2}{{\rm d}\tau^2}(g\Pi)\right\} \\ &= \int_0^{\tau_0} {\rm d}\tau\, {\rm e}^{ik\mu(\tau-\tau_0)} \times \left\{ {\rm e}^{-\kappa}\dot\phi + \frac{g}{4}\left(\delta_\gamma + \frac{\Pi}{4}\right)\right. \\ &\quad + \frac{e^{-\kappa}}{k^2}\left[\left(\ddot\kappa + \dot\kappa^2\right)\theta_{\rm b} + \dot\kappa\dot\theta_{\rm b}\right] \\ &\quad \left. + \frac{\rm d}{{\rm d}\tau}\left[e^{-\kappa}\psi + \frac{3}{16k^2}(\dot g\Pi + g\dot\Pi)\right]\right\} \quad . \end{aligned} \tag{2.4.94}$$

Next, defining the *source functions* $S^{\rm T,P}(k,\tau)$ via

$$\Delta^{\rm T,P}(\tau=\tau_0) = \int_0^{\tau_0} {\rm d}\tau\, {\rm e}^{ik\mu(\tau-\tau_0)} S^{\rm T,P}(k,\tau) \ , \tag{2.4.95}$$

one can see that the μ-dependence is confined to the factor ${\rm e}^{ik\mu(\tau-\tau_0)}$. Using Eqs. (2.4.92) and (2.4.94), the source functions are given by

$$\begin{aligned} S^{\rm T}(k,\tau) &= {\rm e}^{-\kappa}\dot\phi + \frac{g}{4}\left(\delta_\gamma + \frac{\Pi}{4}\right) + \frac{{\rm e}^{-\kappa}}{k^2} \times \left\{\left[\ddot\kappa + \dot\kappa^2\right]\theta_{\rm b} + \dot\kappa\dot\theta_{\rm b}\right\} \\ &\quad + \frac{\rm d}{{\rm d}\tau}\left[{\rm e}^{-\kappa}\psi + \frac{3}{16k^2}(\dot g\Pi + g\dot\Pi)\right] \ , \end{aligned} \tag{2.4.96}$$

$$S^{\rm P}(k,\tau) = \frac{3}{16}\left[g\Pi + \frac{1}{k^2}\frac{{\rm d}^2}{{\rm d}\tau^2}(g\Pi)\right] \ . \tag{2.4.97}$$

The final step is to expand the plane wave ${\rm e}^{ik\mu(\tau-\tau_0)}$ in Eq. (2.4.95) in terms of radial and angular eigenfunctions (spherical Bessel functions j_ℓ and Legendre polynomials

P_ℓ, respectively), i.e.

$$\mathrm{e}^{ik\mu(\tau-\tau_0)} = \sum_{\ell=0}^{\infty}(2\ell+1)\, i^\ell\, j_\ell[k(\tau_0-\tau)]\, P_\ell(\mu)\ . \tag{2.4.98}$$

After performing the ensemble average and integrating over the angular variable μ, Eq. (2.4.95) can be written as

$$\Delta_\ell^{\mathrm{T,P}}(k,\tau=\tau_0) = \int_0^{\tau_0} \mathrm{d}\tau\ S^{\mathrm{T,P}}(k,\tau)\ j_\ell[k(\tau_0-\tau)]\ . \tag{2.4.99}$$

One can see from Eq. (2.4.99) that the anisotropy has been decomposed into a source function $S^{\mathrm{T,P}}$, which is independent of the multipole moment ℓ, and a geometrical term j_ℓ, which is independent of the cosmological model. The advantage of this method is that the latter only needs to be computed once and can be stored for all subsequent calculations. Meanwhile, the source function is the same for all values of ℓ and only requires knowledge of the photon moments up to $\ell = 4$ (for which one uses the Boltzmann hierarchy of equations given in Sec. 2.2.2). By specifying the source function as a function of time, one can solve for higher moments using Eq. (2.4.99), and quickly compute the photon anisotropy spectrum C_ℓ.

In Chapter 3, we will modify the source functions in Eqs. (2.4.96) and (2.4.97) to account for DM–photon scattering.

Chapter 3

Constraints on Dark Matter–Photon Scattering

Happiness can be found, even in the darkest of times, if one only remembers to turn on the light.

— Albus Dumbledore

3.1 Introduction

Despite the large number of dedicated experiments, an understanding of the particle nature of dark matter (DM) and direct evidence for its existence have remained elusive, questioning our interpretation of this mysterious substance. One of the most popular theories is that DM consists of weakly-interacting massive particles (WIMPs; see Sec. 1.3) that are naturally difficult to detect using methods based on their interactions. As we saw in Sec. 1.4, indirect detection techniques assume that DM annihilates or decays at late times, while direct detection and collider searches generally assume a coupling to quarks.

However, such assumptions are not always appropriate; for instance, there are no significant late-time annihilations in asymmetric DM scenarios that could lead to a visible signal in Galactic or cosmic microwave background (CMB) data [148]. Additionally, the DM mass may be too small or too large to produce a visible signal

in direct detection experiments due to their limited sensitivity[1].

For example, if DM consists of sterile neutrinos (e.g. Refs. [82–85]) with a significant decay rate, X-ray observations [150–153] would be a more promising detection method than direct detection. Additionally, if DM is lighter than ~ 10 GeV [154] with a small annihilation cross section into electron–positron pairs [154, 155], it would be more appropriate to look for evidence in low-energy gamma-ray data [94], measurements of the electron or muon g–2 [156–159], or the neutrino mass generation mechanism [160]. However, such searches require one to assume a specific particle physics model and are therefore not universal. Finally, DM could be much heavier than a few TeV (e.g. Ref. [161]), posing problems for the usual detection techniques.

In this chapter, we propose an alternative method to determine how weak DM interactions with Standard Model particles need to be, independently of the standard DM assumptions. Our argument holds whether DM decays, annihilates, or is in the necessary mass range to interact significantly with nuclei. It is only based on the historical motivation for WIMPs, namely the mandatory absence of Silk damping (photon diffusion; see Sec. 1.2.2) at large scales [162–165].

To begin with, it is important to note that charge neutrality does not necessarily rule out DM–photon interactions since they could occur through more complicated processes involving Standard Model particles[2], or magnetic and electric dipole moments [167–169]. Therefore, in principle, DM could have an effective coupling to photons with a strength intermediate between those of the electromagnetic and weak interactions. From a phenomenological point of view, the prejudice is that the corresponding interaction rates should be relatively small[3]. However, since we lack evidence in favour of any particular DM model,

[1] However, new techniques are now being proposed to probe the lighter mass range, see e.g. Ref. [149].

[2] Recent arguments for limited electromagnetic interactions can be found in Ref. [166].

[3] For example, in Supersymmetry, the neutralino pair annihilation cross section into two photons $\langle \sigma v \rangle_{\gamma\gamma}$ is expected to be smaller than 10^{-38} cm^2 [170]. However, in certain conditions, $\langle \sigma v \rangle_{\gamma\gamma}$ can be much larger than 10^{-34} cm^2 [171]. Whether this translates into a large value of the DM–photon scattering cross section is beyond the scope of this thesis. Here, we will simply assume that there

deriving constraints from the accumulated cosmological data offers a more robust method to characterise the dark sector.

In Sec. 1.2.2, we saw that interactions between photons and baryons during recombination lead to a Silk damping effect [50] that suppresses the CMB angular power spectra C_ℓ at large ℓ (small scales). In Refs. [162–165], it was shown that scattering between DM and Standard Model particles prevents DM from clustering under gravity as effectively and leads to a reduction of small-scale power in analogy to Silk damping. Such "collisional damping" erases structure with a size smaller than the collisional damping length

$$l_{\rm cd}^2 \sim \sum_i \int_0^{t_{{\rm dec}({\rm DM}-i)}} \frac{\rho_i\, v_i^2}{\rho\, \Gamma_i\, a^2}\, {\rm d}t \ , \tag{3.1.1}$$

where i refers to all species that are coupled to DM, Γ_i is the total sum of the interaction rates of i, $\rho \equiv \sum_i \rho_i$, and $t_{{\rm dec}({\rm DM}-i)}$ refers to the time at which DM thermally decouples from species i (see Ref. [162] for the derivation). Note that we neglect the damping contribution from DM self-interactions.

Since the integral in Eq. (3.1.1) is dominated by the contribution at late times, the collisional damping scale can be approximated by

$$l_{\rm cd}^2 \sim \sum_i \left(\frac{\rho_i\, v_i^2}{\rho\, \Gamma_i\, a^2}\, t \right) |_{t_{{\rm dec}({\rm DM}-i)}} \sim \sum_i \left(\frac{\rho_i\, v_i^2}{\rho\, a^2}\, t^2 \right) |_{t_{{\rm dec}({\rm DM}-i)}} \ , \tag{3.1.2}$$

where we have used $\Gamma_i(t_{{\rm dec}({\rm DM}-i)}) = H \sim t^{-1}$. The collisional damping effect is exacerbated when DM couples to photons (since photons were both relativistic and highly abundant in the early universe). Therefore, one can set strong upper limits on the DM–photon interaction cross section by examining the resulting CMB spectra.

In fact, a non-zero DM–photon coupling has two specific signatures. Firstly, as was shown in Ref. [163], large interactions lead to the presence of significant damping in the C_ℓ, which can be constrained using the position and relative amplitude of the acoustic peaks. Secondly, after DM ceases to interact with photons, the collisional damping is supplemented by DM free-streaming[4]; this appears as a translation of the

are realistic DM scenarios in which the scattering cross section is significant.

[4]Assuming that the DM–photon decoupling happens before the gravitational collapse of such fluctuations and the DM velocity is not completely negligible at this time.

matter power spectrum $P(k)$ and can also be constrained (if the effect is substantial enough). Therefore, with the latest data from CMB experiments such as the *Planck* satellite [10], one can set a limit on DM–photon interactions with unprecedented precision.

Here we extend the preliminary analysis of Ref. [163] much further and show that a non-negligible DM–photon coupling also generates distinctive features in the polarisation power spectra (the E- and B-modes) and the temperature power spectrum C_ℓ^{TT} at high ℓ. One can use these effects to search for evidence of DM interactions in CMB data and determine (at least observationally) the strength of DM–photon interactions that is allowed.

The chapter is organised as follows. In Sec. 3.2, we discuss the implementation of DM–photon interactions and the qualitative effects on the TT and EE components of the C_ℓ. In Sec. 3.3.1, we constrain these interactions by comparing the spectra to the latest *Planck* data, and extract the best-fit cosmological parameters. In Sec. 3.3.2, we present our predictions for the temperature and polarisation spectra assuming the maximally allowed value of the elastic scattering cross section that we obtain. We also examine the impact of DM–photon scattering on the linear $P(k)$ as motivation for the N-body simulations that we will carry out in Chapter 5. Finally, we provide our conclusions in Sec. 3.4.

This chapter is based on the work carried out in Ref. [1].

3.2 Implementation

In Sec. 3.2.1, we describe how one can modify the linear perturbation equations to incorporate DM–photon interactions. In Sec. 3.2.2, we discuss their implementation in the Boltzmann code CLASS (version 1.7) [48, 146]. Finally, in Sec. 3.2.3, we discuss their impact on the TT and EE components of the CMB spectrum.

3.2.1 Modified Boltzmann Equations

In the standard ΛCDM model, the Euler equations for the baryon, photon and DM fluids in the conformal Newtonian gauge are given by (see Chapter 2):

$$\dot{\theta}_{\rm b} = k^2\psi - \mathcal{H}\theta_{\rm b} + c_s^2 k^2 \delta_{\rm b} - R^{-1}\dot{\kappa}(\theta_{\rm b} - \theta_\gamma) \ , \tag{3.2.3}$$

$$\dot{\theta}_\gamma = k^2\psi + k^2\left(\frac{1}{4}\delta_\gamma - \sigma_\gamma\right) - \dot{\kappa}(\theta_\gamma - \theta_{\rm b}) \ , \tag{3.2.4}$$

$$\dot{\theta}_{\rm DM} = k^2\psi - \mathcal{H}\theta_{\rm DM} \ , \tag{3.2.5}$$

where $\theta_{\rm b}$, θ_γ and $\theta_{\rm DM}$ are the baryon, photon and DM velocity divergences, respectively. δ_γ and σ_γ are the density fluctuation and anisotropic stress potential associated with the photon fluid, ψ is the gravitational potential, k is the comoving wavenumber, $\mathcal{H} \equiv \dot{a}/a$ is the conformal Hubble rate, $R \equiv (3/4)(\rho_{\rm b}/\rho_\gamma)$ is the ratio of the baryon to photon densities, c_s is the baryon sound speed, and $\dot{\kappa} \equiv a\,\sigma_{\rm Th}\,c\,n_{\rm e}$ is the Thomson scattering rate (the scale factor a appears since the derivative is taken with respect to conformal time).

DM–photon scattering can be incorporated in the DM and photon velocity equations with terms analogous to $-\dot{\kappa}(\theta_\gamma - \theta_{\rm b})$. The new interaction rate reads $\dot{\mu} \equiv a\,\sigma_{{\rm DM}-\gamma}\,c\,n_{\rm DM}$, where $\sigma_{{\rm DM}-\gamma}$ is the DM–photon elastic scattering cross section, $n_{\rm DM} = \rho_{\rm DM}/m_{\rm DM}$ is the DM number density, $\rho_{\rm DM}$ is the DM energy density and $m_{\rm DM}$ is the DM mass (assuming that DM is non-relativistic)[5]. Thus, the Euler equation for photons [Eq. (3.2.4)] receives the additional source term $-\dot{\mu}(\theta_\gamma - \theta_{\rm DM})$.

Assuming that the total 4-momentum of the DM–photon fluid is conserved in the elastic scattering process, from Eq. (2.1.15), we have

$$\begin{aligned} & (\rho_\gamma + P_\gamma)\,\delta\theta_\gamma = -(\rho_{\rm DM} + P_{\rm DM})\,\delta\theta_{\rm DM} \\ \Longrightarrow \quad & \delta\theta_{\rm DM} = -\frac{4}{3}\frac{\rho_\gamma}{\rho_{\rm DM}}\,\delta\theta_\gamma \ . \end{aligned} \tag{3.2.6}$$

Therefore, the source term in the Euler equation for DM has the opposite sign and is rescaled by a factor $S^{-1} \equiv (4/3)(\rho_\gamma/\rho_{\rm DM}) \propto a^{-1}$.

[5]Intuitively, one can understand why $\dot{\mu}$ must be proportional to the cross section and the DM number density; if either the number of DM particles or the cross section is completely negligible, the photon fluid will not be significantly modified by a DM–photon coupling.

Thus, the Euler equations become

$$\dot{\theta}_{\rm b} = k^2\psi - \mathcal{H}\theta_{\rm b} + c_s^2 k^2 \delta_{\rm b} - R^{-1}\dot{\kappa}(\theta_{\rm b} - \theta_\gamma) \ , \tag{3.2.7}$$

$$\dot{\theta}_\gamma = k^2\psi + k^2\left(\frac{1}{4}\delta_\gamma - \sigma_\gamma\right) - \dot{\kappa}(\theta_\gamma - \theta_{\rm b}) - \dot{\mu}(\theta_\gamma - \theta_{\rm DM}) \ , \tag{3.2.8}$$

$$\dot{\theta}_{\rm DM} = k^2\psi - \mathcal{H}\theta_{\rm DM} - S^{-1}\dot{\mu}(\theta_{\rm DM} - \theta_\gamma) \ . \tag{3.2.9}$$

The DM–photon elastic scattering cross section $\sigma_{{\rm DM}-\gamma}$ can be either constant (like the Thomson scattering between photons and charged particles) or proportional to the temperature, depending on the DM model that is being considered.

For a constant cross section, since both DM and baryons are non-relativistic when we begin the integration, the scattering rates $\dot{\mu}$ and $\dot{\kappa}$ behave as a^{-2} at high redshifts[6]. Therefore, the ratio of $\dot{\mu}$ and $\dot{\kappa}$ is proportional to the dimensionless quantity

$$u \equiv \left[\frac{\sigma_{{\rm DM}-\gamma}}{\sigma_{\rm Th}}\right]\left[\frac{m_{\rm DM}}{100\ {\rm GeV}}\right]^{-1} \ , \tag{3.2.10}$$

which depends on two essential parameters: the DM–photon scattering cross section $\sigma_{{\rm DM}-\gamma}$ and the DM mass $m_{\rm DM}$. We will use this parameter to quantify the effect of DM–photon interactions on the evolution of primordial fluctuations. If instead, the cross section is proportional to the temperature squared (e.g. dipole DM [167–169] or by analogy to neutrino–electron scattering), we can write $u = u_0\, a^{-2}$, where u_0 is the present-day value.

As the magnitude of the u parameter determines the collisional damping scale [163], one can see that the efficiency of the damping is simply governed by the ratio of the interaction cross section to the DM mass.

3.2.2 Incorporation in CLASS

The execution of CLASS begins by using three distinct modules for the background, thermodynamical and perturbation evolutions. In our study, all necessary modifications are confined to the thermodynamics and perturbation modules.

[6]Note that after recombination, $\dot{\kappa}$ is strongly suppressed (by a factor $\sim 10^{-4}$ [38]) due to the drastic subsequent drop in the free electron density $n_{\rm e}$, while $\dot{\mu}$ continues scaling like a^{-2}.

The standard thermodynamics module solves the recombination equations and stores an interpolation table for $\{\dot{\kappa},\, \ddot{\kappa},\, \dddot{\kappa},\, \exp(-\kappa)\}$ as a function of the redshift z. At the same time, we request that the module stores the corresponding values of $\dot{\mu}$ (inferred analytically from u, a, $\sigma_{\rm Th}$ and $\rho_{\rm DM}$), its higher derivatives, and $\exp(-\mu)$. It also stores values of the modified visibility function

$$g(\tau) = (\dot{\kappa} + \dot{\mu}) e^{-\kappa-\mu} \,, \tag{3.2.11}$$

along with its first and second time derivatives.

In the perturbation module, we begin by adding the new interaction terms to the photon and DM Euler equations [see Eqs. (3.2.8) and (3.2.9)] and in the full hierarchy of Boltzmann equations for photon temperature and polarisation. Apart from the source term in the photon velocity equation, this amounts to simply replacing all occurrences of $\dot{\kappa}$ with $(\dot{\kappa} + \dot{\mu})$. Therefore, the complete Boltzmann hierarchy for photons (derived in Sec. 2.2) becomes

$$\dot{\delta}_\gamma = -\frac{4}{3}\theta_\gamma + 4\dot{\phi} \,, \tag{3.2.12}$$

$$\dot{\theta}_\gamma = k^2\psi + k^2\left(\frac{1}{4}\delta_\gamma - \sigma_\gamma\right) - \dot{\kappa}(\theta_\gamma - \theta_{\rm b}) - \dot{\mu}(\theta_\gamma - \theta_{\rm DM}) \,, \tag{3.2.13}$$

$$\dot{F}_{\gamma 2} = \frac{8}{15}\theta_\gamma - \frac{3}{5}kF_{\gamma 3} - \frac{9}{5}(\dot{\kappa}+\dot{\mu})\sigma_\gamma + \frac{1}{10}(\dot{\kappa}+\dot{\mu})\left(G_{\gamma 0} + G_{\gamma 2}\right) \,, \tag{3.2.14}$$

$$\dot{F}_{\gamma \ell} = \frac{k}{2\ell+1}\left[\ell F_{\gamma(\ell-1)} - (\ell+1)F_{\gamma(\ell+1)}\right] - (\dot{\kappa}+\dot{\mu})F_{\gamma\ell} \,, \quad \ell \geq 3 \tag{3.2.15}$$

$$\begin{aligned}\dot{G}_{\gamma l} = {} & \frac{k}{2\ell+1}\left[\ell G_{\gamma(\ell-1)} - (\ell+1)G_{\gamma(\ell+1)}\right] \\ & +(\dot{\kappa}+\dot{\mu})\left[-G_{\gamma\ell} + \frac{1}{2}\left(F_{\gamma 2} + G_{\gamma 0} + G_{\gamma 2}\right)\left(\delta_{\ell 0} + \frac{\delta_{\ell 2}}{5}\right)\right] \,.\end{aligned} \tag{3.2.16}$$

At early times, the characteristic scale $\tau_c \equiv \dot{\kappa}^{-1}$ is extremely small, leading to a stiff system of equations. Integrating over time remains efficient in the baryon–photon tight-coupling regime (in which small quantities like $\dot{\Theta}_{\gamma{\rm b}} \equiv \dot{\theta}_\gamma - \dot{\theta}_{\rm b}$ and σ_γ are obtained analytically at order one or two in the expansion parameter), while the remaining evolution equations become independent of τ_c (see Sec. 2.3).

To obtain a CMB spectrum compatible with large-scale observations, we can limit our analysis to the case in which the new interaction rate is smaller than the Thomson scattering rate, i.e. $\dot{\mu} < \dot{\kappa}$. Therefore, there is no need to devise a specific

DM–photon tight-coupling regime; we need only to correct the baryon–photon tight-coupling approximation in order to account for the new interactions. This can be easily achieved by following the step-by-step calculation in Sec. 2.3, including the additional terms $-\dot{\mu}(\theta_\gamma - \theta_{\rm DM})$ and $-S^{-1}\dot{\mu}(\theta_{\rm DM} - \theta_\gamma)$ in the photon and DM Euler equations, respectively.

We implemented these modifications to linear order in τ_c (and even beyond that order, since we used the approximation scheme called `class_compromise` in Ref. [146]). The set of tight-coupling equations provided in Sec. 2.3 become:

$$\begin{aligned}\dot{\theta}_{\rm b} &= -\frac{1}{1+R}\left[R(\mathcal{H}\theta_{\rm b} - c_s^2 k^2 \delta_{\rm b}) - k^2\left(\frac{\delta_\gamma}{4} - \sigma_\gamma\right) + \dot{\Theta}_{\gamma{\rm b}} + \dot{\mu}(\theta_\gamma - \theta_{\rm DM})\right] \\ &\quad + k^2\psi \ , \qquad (3.2.17)\\ \dot{\theta}_\gamma &= (1+R)k^2\psi + k^2\left(\frac{1}{4}\delta_\gamma - \sigma_\gamma\right) - R\left(\dot{\theta}_{\rm b} + \mathcal{H}\theta_{\rm b} - c_s^2 k^2 \delta_{\rm b}\right) \\ &\quad - \dot{\mu}(\theta_\gamma - \theta_{\rm DM}) \ , \qquad (3.2.18)\end{aligned}$$

where to linear order, the baryon–photon slip and the photon shear stress are given by

$$\begin{aligned}\dot{\Theta}_{\gamma{\rm b}} &= -\frac{R\tau_c}{1+R}\left[-\frac{\ddot{a}}{a}\theta_{\rm b} + k^2\left(-\frac{\mathcal{H}}{2}\delta_\gamma + \bar{c}_s^2\delta_{\rm b} + c_s^2\dot{\delta}_{\rm b} - \frac{\dot{\delta}_\gamma}{4} - \mathcal{H}\psi\right) + \ddot{\mu}(\theta_\gamma - \theta_{\rm DM})\right] \\ &\quad + \left(\frac{\dot{\tau}_c}{\tau_c} - \frac{2\mathcal{H}R}{1+R}\right)\Theta_{\gamma{\rm b}} + \mathcal{O}({\tau_c}^2) \ , \qquad (3.2.19)\\ \sigma_\gamma &= \frac{16}{45}(\dot{\kappa} + \dot{\mu})^{-1}\theta_\gamma + \mathcal{O}({\tau_c}^2) \ . \qquad (3.2.20)\end{aligned}$$

We checked the consistency of our approach by varying the time at which the tight-coupling approximation is switched off in the presence of a non-zero interaction rate $\dot{\mu}$. As expected, the results are independent of the switching time, unless it gets too close to recombination (in which case, one would need to introduce a separate DM–photon tight-coupling regime).

Finally, in order to follow a reduced number of multipoles in the photon Boltzmann hierarchy, we express the final temperature and polarisation spectra using a line-of-sight integral (see Sec. 2.4) [46], i.e. we decompose the present-day temperature and polarisation transfer functions as

$$\Delta_\ell^{\rm T,P}(k, \tau = \tau_0) = \int_0^{\tau_0} {\rm d}\tau \ S^{\rm T,P}(k,\tau) \ j_\ell[k(\tau_0 - \tau)] \ , \qquad (3.2.21)$$

where τ is conformal time, τ_0 is the time today, $S^{\mathrm{T,P}}(k,\tau)$ is the temperature or polarisation source function, and the j_ℓ are spherical Bessel functions.

The source functions can be obtained by integrating the Boltzmann equation by parts along a given geodesic. For the scenario at hand, the temperature source function given in Eq. (2.4.96) becomes[7]

$$\begin{aligned} S^{\mathrm{T}}(k,\tau) \;=\; & e^{-\kappa-\mu}\dot{\phi} + \frac{g}{4}\left(\delta_\gamma + \frac{\Pi}{4}\right) + \frac{e^{-\kappa-\mu}}{k^2} \times \\ & \left\{\left[\ddot{\kappa} + \dot{\kappa}(\dot{\kappa}+\dot{\mu})\right]\theta_{\mathrm{b}} + \dot{\kappa}\dot{\theta}_{\mathrm{b}} + \left[\ddot{\mu} + \dot{\mu}(\dot{\kappa}+\dot{\mu})\right]\theta_{\mathrm{DM}} + \dot{\mu}\dot{\theta}_{\mathrm{DM}}\right\} \\ & + \frac{\mathrm{d}}{\mathrm{d}\tau}\left[e^{-\kappa-\mu}\psi + \frac{3}{16k^2}(\dot{g}\Pi + g\dot{\Pi})\right] \;, \end{aligned} \tag{3.2.22}$$

where for our numerical implementation in CLASS, derivatives of perturbations denoted with a dot are evaluated analytically using the evolution equations, while the derivative denoted by $\mathrm{d}/\mathrm{d}\tau$ is computed with a finite difference method, after storing the function between the square brackets.

The expression for the polarisation source function given in Eq. (2.4.97) remains unchanged:

$$S^{\mathrm{P}}(k,\tau) = \frac{3}{16}\left[g\Pi + \frac{1}{k^2}\frac{\mathrm{d}^2}{\mathrm{d}\tau^2}(g\Pi)\right] \;, \tag{3.2.23}$$

where the modified visibility function g is given by Eq. (3.2.11). Note that Π is a linear combination of temperature and polarisation multipoles, corresponding to $(F_{\gamma 2} + G_{\gamma 0} + G_{\gamma 2})$ in the notation of Ref. [139].

3.2.3 Impact on the CMB spectrum

In Fig. 3.1, we show the effect of introducing DM–photon interactions on the DM density constant δ_{DM} for a small-scale mode with wavenumber $k = 40$ Mpc^{-1}. Once the DM perturbation has entered the horizon, rather than growing under gravitational collapse as in the case of ΛCDM ($u = 0$), DM experiences collisional damping. Therefore, at the CMB epoch ($a \sim 10^{-3}$) and today ($a = 1$), δ_{DM} is suppressed and there is a greater level of isotropy on small scales.

[7] Note that in newer versions of CLASS (from version 2.0), one simply needs to replace $\dot{\kappa}$ with $(\dot{\kappa}+\dot{\mu})$ in the expressions for the source functions.

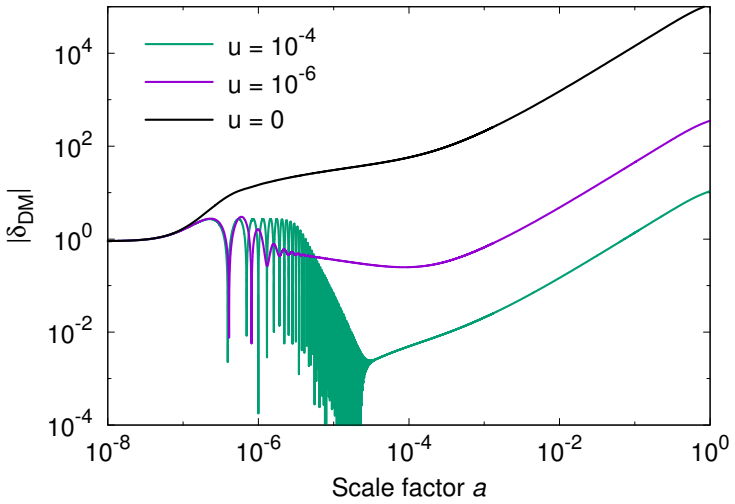

Figure 3.1: The evolution of the normalised DM density contrast $\delta_{\rm DM}$ with and without a coupling to photons, for a small-scale mode with wavenumber $k = 40$ Mpc^{-1}. The curves correspond to DM–photon couplings of $u = 0$ (black), $u = 10^{-6}$ (purple), and $u = 10^{-4}$ (green), where u is defined in Eq. (3.2.10).

Note that for large values of u ($u \gtrsim 10^{-5}$), there is a period of undamped oscillations before damping begins, referred to as the "strong coupling regime" in Ref. [163]. This occurs when the scattering rate $\dot{\mu}$ is larger than both the expansion rate of the universe $\mathcal{H}$ and the photon oscillation frequency. The photon fluctuations from the coupled baryon–photon fluid are fully transferred to DM.

The resulting impact on the TT and EE components of the CMB angular power spectrum is illustrated in Fig. 3.2 for large values of the parameter u. Here we take the DM–photon scattering cross section to be constant; however, we note that similar effects are observed for temperature-dependent cross sections. For illustrative purposes, we consider a flat ΛCDM cosmology, where the energy content of the universe today is divided between baryons ($\Omega_{\rm b} = 0.05$), DM ($\Omega_{\rm DM} = 0.25$), and dark energy in the form of a cosmological constant ($\Omega_\Lambda = 0.7$). We select a present-day value for the Hubble parameter of $h_0 = 0.7$ and the standard value of 3.046 for the effective number of neutrino species[8].

[8]In addition to the three neutrinos of the Standard Model, the 0.046 accounts for residual heating provided by electron–positron annihilations after neutrino decoupling [172].

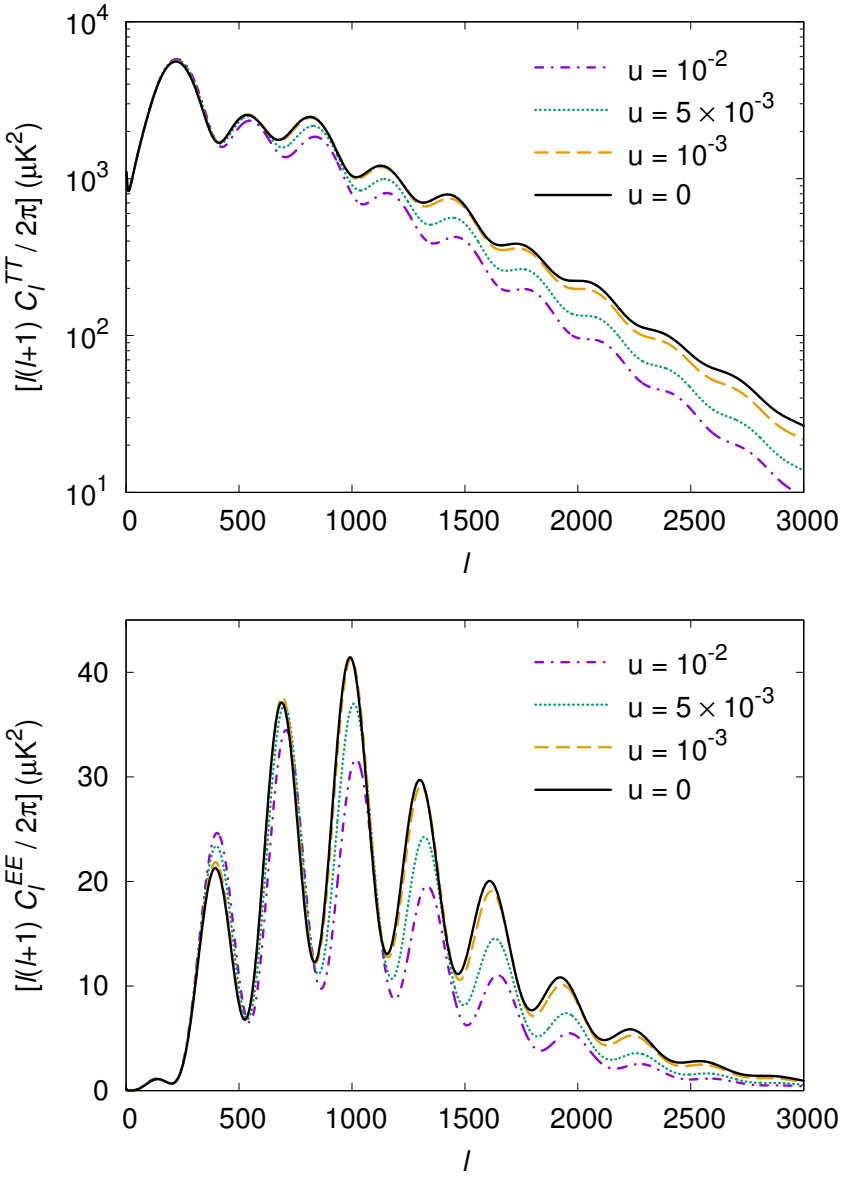

Figure 3.2: The effect of DM–photon interactions on the TT (top) and EE (bottom) components of the CMB angular power spectrum, where the interaction strength is characterised by the parameter $u \equiv [\sigma_{\mathrm{DM}-\gamma}/\sigma_{\mathrm{Th}}]\,[m_{\mathrm{DM}}/100\ \mathrm{GeV}]^{-1}$ ($u = 0$ corresponds to zero DM–photon coupling) and $\sigma_{\mathrm{DM}-\gamma}$ is constant.

There are two important effects on the relative amplitude and position of the acoustic peaks with respect to the standard ΛCDM model, both of which can be used to constrain the DM–photon elastic scattering cross section:

1. The scattering induces collisional damping, thus reducing the magnitude of the small-scale peaks and effectively cutting off the C_ℓ at lower values of ℓ. For very large cross sections, this effect is enhanced by a delay in the epoch of

recombination, as the coupling of photons to DM increases the width of the last-scattering surface.

2. The presence of significant DM–photon interactions decreases the sound speed of the thermal plasma:

$$c_s = \frac{1}{\sqrt{3}} \frac{1}{(1+R+S)^{1/2}} \,, \tag{3.2.24}$$

rather than $[3(1+R)]^{-1/2}$ as in the standard picture [163]. Acoustic oscillations have a lower frequency, leading to a shift in the position of the acoustic peaks to larger ℓ.

We note that there is also a slight enhancement of the first acoustic peak with respect to ΛCDM ($\sim 0.1\%$ in C_ℓ^{TT} and $\sim 0.3\%$ in C_ℓ^{EE} for $u = 10^{-4}$) due to a decrease in the diffusion length of the photons.

As expected, these effects are enhanced for either a larger cross section or a smaller DM mass (i.e. a greater number density of DM particles for the same relic density), corresponding to a larger value of u and a later epoch of DM–photon decoupling. Therefore, by fitting the CMB spectra to cosmological data, one can constrain the value of u and thus determine the maximal scattering cross section that is allowed for a given DM mass.

3.3 Results and Outlook

In Sec. 3.3.1, we present our constraints on the DM–photon elastic scattering cross section, which is considered to be either constant or proportional to the temperature squared. In Sec. 3.3.2, we then discuss important features of the CMB and matter power spectra in the presence of such interactions and outline prospects for future CMB experiments and large-scale structure (LSS) surveys.

3.3.1 CMB Constraints

To fit our CMB spectra to the data, we vary the parameters of the minimal flat ΛCDM cosmology, namely: the baryon density $\Omega_{\rm b}h^2$, the DM density $\Omega_{\rm DM}h^2$, the

scalar spectral index n_s, the primordial spectrum amplitude A_s, the reduced Hubble parameter h, and the redshift of reionisation $z_{\rm reio}$, supplemented by the additional parameter characterising the DM–photon interaction strength, u.

We assume three active neutrino species; two massless and the other with a small mass of 0.06 eV, reflecting the lower bound imposed by neutrino oscillation experiments[9] [35]. In addition, we choose the standard value of 3.046 for the effective number of neutrino species $N_{\rm eff}$ [172] (allowing $N_{\rm eff}$ to vary does not have a significant effect on our conclusions).

To efficiently sample the parameter space, we run the Markov Chain Monte Carlo (MCMC) code MONTE PYTHON [173] combined with the one-year data release from *Planck*, provided by the *Planck* Legacy Archive [174]. In particular, we use the high-ℓ and low-ℓ temperature data of *Planck* combined with the low-ℓ WMAP polarisation data (this corresponds to '*Planck* + WP' in Ref. [10]). We marginalise over the nuisance parameters listed in Ref. [10].

The bounds on the various cosmological parameters are displayed in Table 3.1, and illustrated in Figs. 3.3 and 3.4 for constant and T^2-dependent cross sections, respectively (we omit the nuisance parameters for clarity).

The posterior probability distribution for the u parameter peaks at $u \simeq 0$ showing that the data does not prefer a significant DM–photon coupling. For a constant elastic scattering cross section, we derive an upper limit of

$$\sigma_{\rm DM-\gamma} \leq \; 2 \times 10^{-30} \, (m_{\rm DM}/{\rm GeV}) \;\; {\rm cm}^2 \; , \tag{3.3.25}$$

corresponding to $u \leq 3.1 \times 10^{-4}$ (at 95% CL). This result constitutes an improvement by an order of magnitude on the pre-WMAP analysis of Ref. [163], which set a limit by comparing the CMB anisotropy spectra with ΛCDM predictions.

We note that including data from the 2500-square degree SPT survey [175] tightens the constraints on the standard cosmological parameters with respect to

[9] This is an approximation that is used throughout the literature, including in the *Planck* analysis [10]. Since the data is mainly sensitive to the sum of the neutrino masses [70] and it is faster to run a Boltzmann code with only one massive neutrino, we also use this excellent approximation.

	$\sigma_{\mathrm{DM}-\gamma}$ constant		$\sigma_{\mathrm{DM}-\gamma} \propto T^2$		
Parameter	Best-fit	Mean $\pm$ σ	Best-fit	Mean $\pm$ σ	'*Planck* + WP'
$100\,\Omega_{\mathrm{b}}h^2$	2.199	$2.210^{+0.029}_{-0.033}$	2.200	$2.194^{+0.029}_{-0.029}$	$2.205^{+0.028}_{-0.028}$
$\Omega_{\mathrm{DM}}h^2$	0.1195	$0.1201^{+0.0028}_{-0.0029}$	0.1199	$0.1199^{+0.0027}_{-0.0027}$	$0.1199^{+0.0027}_{-0.0027}$
$100\,h$	67.57	$67.6^{+1.2}_{-1.3}$	67.38	$67.3^{+1.2}_{-1.2}$	$67.3^{+1.2}_{-1.2}$
$10^{+9}\,A_s$	2.189	$2.201^{+0.054}_{-0.060}$	2.197	$2.184^{+0.053}_{-0.056}$	$2.196^{+0.051}_{-0.060}$
n_s	0.9627	$0.9625^{+0.0076}_{-0.0080}$	0.9632	$0.9577^{+0.0081}_{-0.0078}$	$0.9603^{+0.0073}_{-0.0073}$
z_{reio}	11.02	$11.2^{+1.2}_{-1.2}$	11.15	$11.0^{+1.1}_{-1.1}$	$11.1^{+1.1}_{-1.1}$
$10^{+4}\,u$	$\simeq 0$	< 1.173 (68% CL) < 3.132 (95% CL)	–	–	–
$10^{+14}\,u_0$	–	–	$\simeq 0$	< 9.043 (68% CL) < 24.15 (95% CL)	–

Table 3.1: Best-fit values and minimum credible intervals at 68% CL of the cosmological parameters set by *Planck*, with $u \equiv [\sigma_{\mathrm{DM}-\gamma}/\sigma_{\mathrm{Th}}]\,[m_{\mathrm{DM}}/100\ \mathrm{GeV}]^{-1}$ as a free parameter. For comparison, '*Planck* + WP' are the 68% limits taken from Ref. [10].

'*Planck* + WP' alone, giving best-fit values that are consistent at the 1σ level. We obtain a slightly weaker limit on u, in addition to a larger value of $h = 0.679^{+0.010}_{-0.011}$ and smaller value of $z_{\mathrm{reio}} = 10.7^{+1.0}_{-1.2}$ (at 68% CL)[10].

For a DM candidate that is lighter than a few MeV (see e.g. Refs. [154, 155]), Eq. (3.3.25) suggests that the particles must have a cross section in the range of weak interactions: $\sigma_{\mathrm{DM}-\gamma} \lesssim 10^{-33}\ \mathrm{cm}^2$. This result is relevant for scenarios in which DM cannot annihilate directly into the visible sector (i.e. where indirect detection techniques are inappropriate). Meanwhile, for a heavy DM particle ($m_{\mathrm{DM}} \sim$ TeV), we obtain a weaker bound on the scattering cross section: $\sigma_{\mathrm{DM}-\gamma} \lesssim 10^{-27}\ \mathrm{cm}^2$, such that large DM–photon interactions (with respect to weak interactions) cannot yet be ruled out by CMB data.

For scenarios in which DM cannot couple directly to photons, Eq. (3.3.25) translates into an upper bound on the DM coupling to charged particles, including those of the Standard Model. However, the requirement of a constant cross section

[10]Note that these results must be considered with care, given the small tension between the amplitudes of the CMB damping tail in the SPT and *Planck* data (as reported in Ref. [10], although the *Planck* collaboration now has a better understanding of the source of this tension).

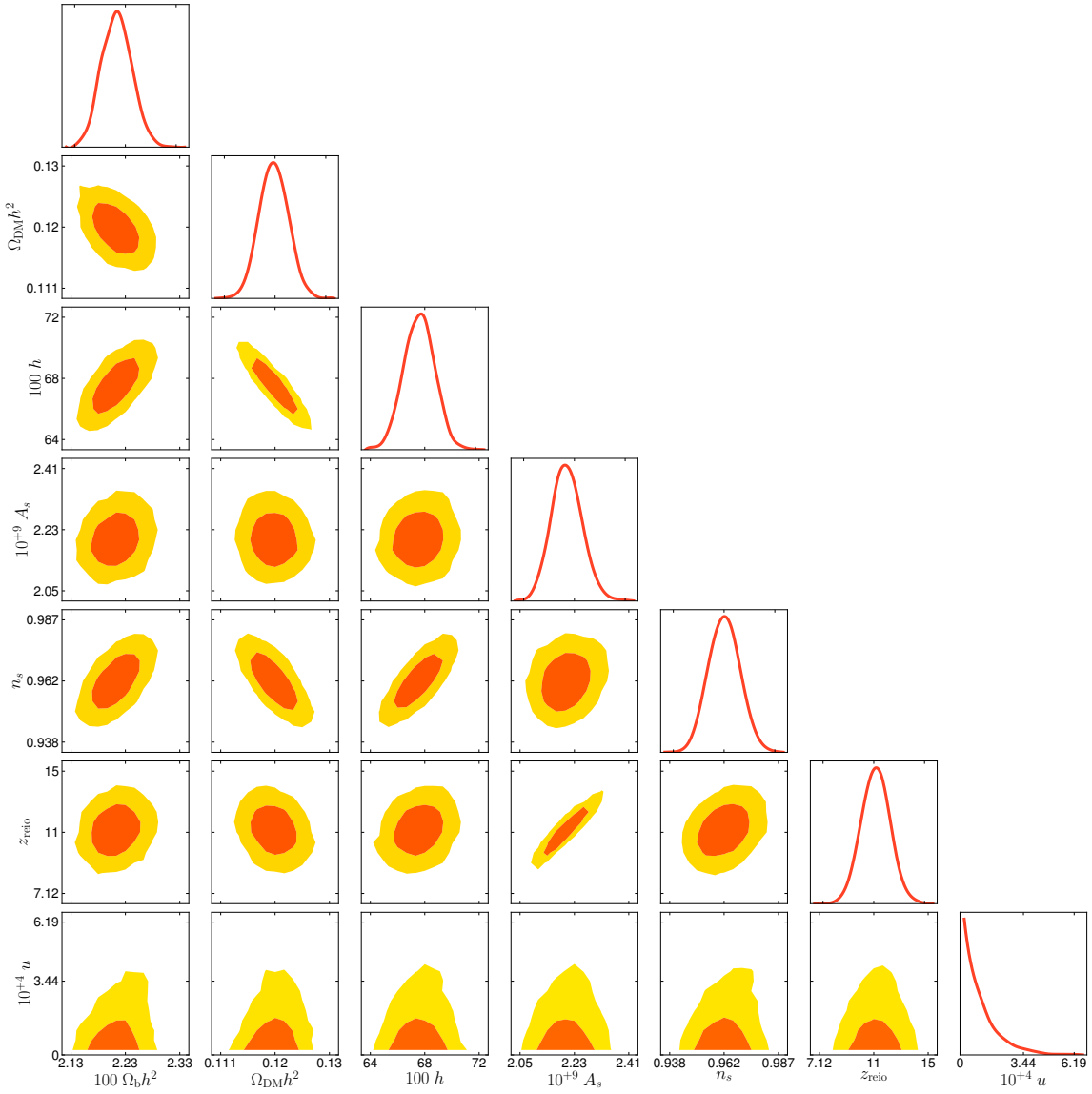

Figure 3.3: Triangle plot showing the one- and two-dimensional posterior distributions of the cosmological parameters set by *Planck*, with $u \equiv [\sigma_{\rm DM-\gamma}/\sigma_{\rm Th}]\,[m_{\rm DM}/100\ {\rm GeV}]^{-1}$ as a free parameter and constant $\sigma_{\rm DM-\gamma}$. The orange and yellow contours correspond to 68% and 95% CL, respectively.

implies that there is some cancellation that enables one to remove the dependence on the photon energy, as in the case of Thomson scattering. Scenarios in which the DM mass is degenerate with the mediator mass may therefore be more appropriate, provided that the mass degeneracy passes the cuts at the LHC (e.g. Ref. [176]) or the DM mass is large enough to satisfy the LHC constraints on new charged particles.

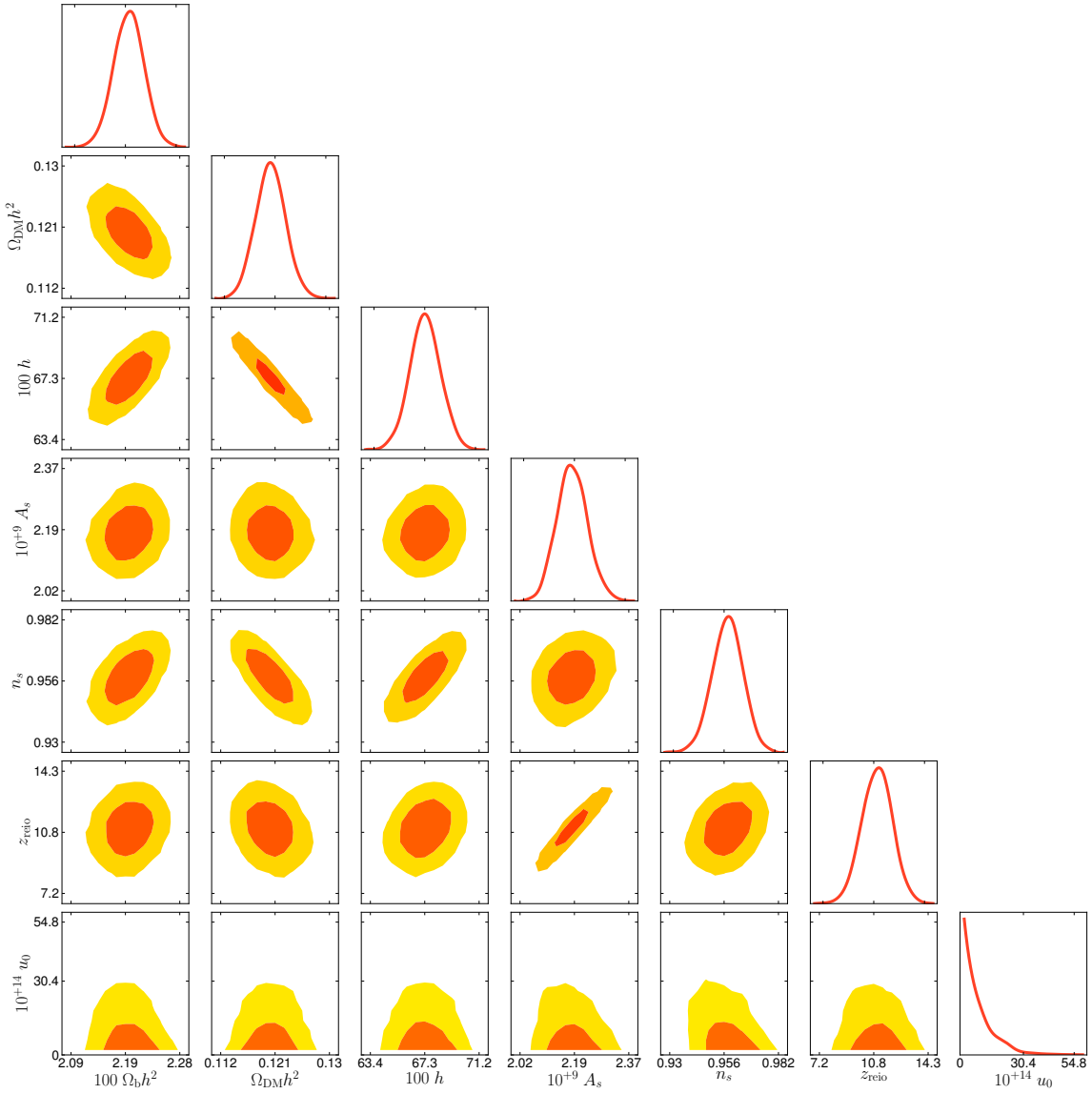

Figure 3.4: Triangle plot showing the one- and two-dimensional posterior distributions of the cosmological parameters set by *Planck*, with $u \equiv [\sigma_{\rm DM-\gamma}/\sigma_{\rm Th}]\,[m_{\rm DM}/100\ {\rm GeV}]^{-1}$ as a free parameter and $\sigma_{\rm DM-\gamma} \propto T^2$. The orange and yellow contours correspond to 68% and 95% CL, respectively.

A constant cross section is also expected in the presence of a Z'–γ or γ'–γ mixing (for a review on the limits of such a mixing, see for example, Ref. [177]). In this case, the cross section is essentially the Thomson cross section (where we replace the fine structure constant α by its equivalent for the DM-γ' coupling $\alpha_{\rm DM-\gamma'}$, and the electron mass by the DM mass) multiplied by the $Z'/\gamma' - \gamma$ coupling χ to the power four (i.e. $\sigma_{\rm DM-\gamma} = \chi^4\ \sigma_{\rm DM-\gamma'}$). For MeV DM, Eq. (3.3.25) translates into the

constraint $\chi \lesssim 10^{-2}$ in the limit of a massless Z'/γ' and $\alpha_{\mathrm{DM}-\gamma'} \simeq \alpha$. This is to be compared with the bounds on millicharged particles, which are about two to three orders of magnitude stronger in the MeV range [178].

If instead, the cross section is proportional to the temperature squared, we obtain the stringent upper bound of

$$\sigma_{\mathrm{DM}-\gamma,0} \leq \; 2 \times 10^{-39} \, (m_{\mathrm{DM}}/\mathrm{GeV}) \;\; \mathrm{cm}^2 \; , \tag{3.3.26}$$

for the present-day value of the scattering cross section (at 95% CL), corresponding to $u_0 \leq 2.4 \times 10^{-13}$, which is consistent with Eq. (3.3.25). For epochs much earlier than the CMB time, this result is clearly not as powerful as the constant cross section case (since $\sigma_{\mathrm{DM}-\gamma} = \sigma_{\mathrm{DM}-\gamma,0} \, a^{-2}$), but does apply to all scenarios where the dependence on the photon energy cannot be alleviated. In the case of dipole DM models [167–169], this enables one to constrain the DM dipole moment.

3.3.2 Prospects for Future Experiments

As shown in Table 3.1, our best fit to the *Planck* data for $u \lesssim 10^{-4}$ leads to values of the cosmological parameters that are consistent with those obtained by *Planck* at the 1σ level. However, there are a number of differences with respect to ΛCDM at high ℓ due to the impact of DM–photon interactions, which suppress power on very small scales.

The effect is particularly noticeable if one considers the TT angular power spectrum for $\ell \gtrsim 3000$, which has not yet been probed by *Planck* (see Fig. 3.5). Indeed, for $\ell \simeq 6000$, small-scale fluctuations are suppressed by a factor of ~ 4 with respect to ΛCDM for our maximally allowed cross section. This result could be promising for CMB experiments such as SPT [175] and ACT [44]; however, such a large value of ℓ corresponds to the region where the foregrounds (emission from extragalactic sources and the thermal Sunyaev–Zel'dovich effect[11]) are dominant [179]. Therefore, the detectability of DM–photon interactions in the

[11] The thermal Sunyaev–Zel'dovich effect is a small spectral distortion of the CMB spectrum caused by the scattering of CMB photons from the hot thermal distribution of electrons provided by the intracluster medium of galaxy clusters.

temperature anisotropy spectrum will depend on the accuracy of foreground modelling and removal.

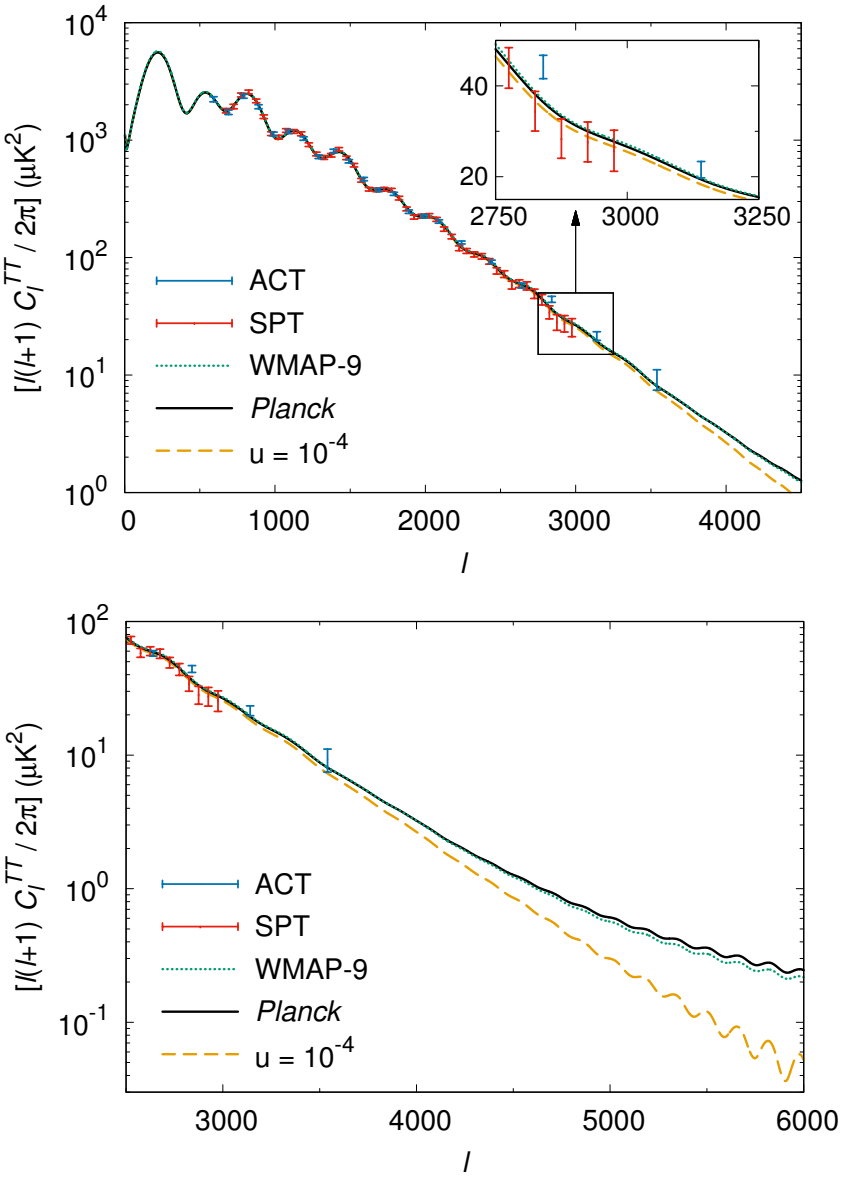

Figure 3.5: A comparison between the TT angular power spectra for the maximally allowed (constant) DM–photon cross section (orange, dashed), and the 9-year WMAP (green, dotted) [9] and one-year *Planck* (black, solid) [10] best-fit data. Also plotted are the full 3-year data from the SPT (red error bars) and ACT (blue error bars) experiments [180]. In the top panel, we see a suppression of power with respect to ΛCDM for $\ell \gtrsim 3000$, and in the bottom panel, we give a prediction for high ℓ.

The damping with respect to ΛCDM is also evident in the B-mode spectrum (a consequence of E-mode lensing by LSS; see Sec. 1.2.2), as shown in Fig. 3.6. The

reduction in power is due to the combined damping of the E-modes (see Fig. 3.2) and the matter power spectrum (see Fig. 3.7). While the overall effect is small for $u \lesssim 10^{-4}$, for $\ell \gtrsim 500$, one can use the B-modes alone combined with the first-season SPTpol data [57] to effectively rule out $u \gtrsim 5 \times 10^{-3}$. In fact, future polarisation data from e.g. SPT [175], POLARBEAR [181] and SPIDER [182] could be sensitive enough to distinguish $u \simeq 10^{-5}$ from ΛCDM.

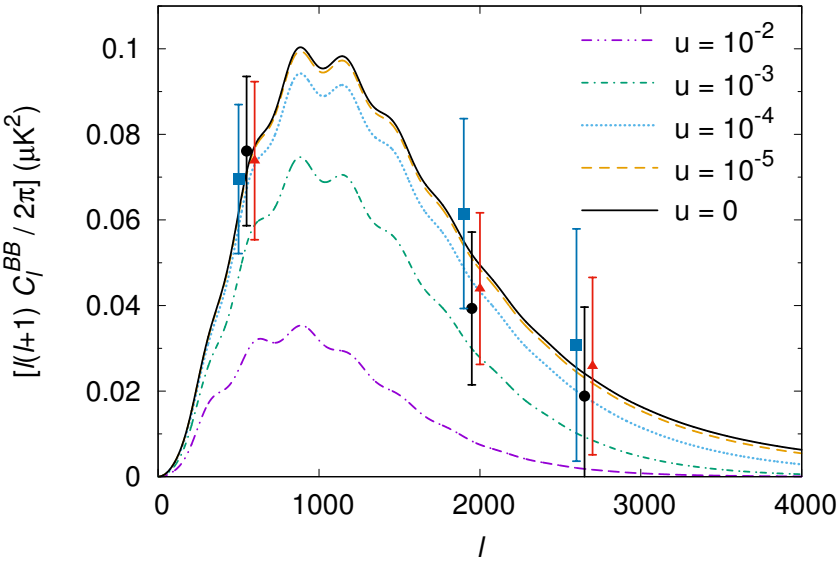

Figure 3.6: The effect of DM–photon interactions on the B-modes of the angular power spectrum, where the strength of the interaction is characterised by $u \equiv [\sigma_{\mathrm{DM}-\gamma}/\sigma_{\mathrm{Th}}]\,[m_{\mathrm{DM}}/100\ \mathrm{GeV}]^{-1}$ (with constant $\sigma_{\mathrm{DM}-\gamma}$) and we use the '*Planck* + WP' best-fit parameters from Ref. [10]. We have assumed that the tensor-to-scalar ratio $r = 0$. The data points are recent measurements from the SPTpol experiment [57]. For the maximally allowed DM–photon cross section ($u \simeq 10^{-4}$), we see a deviation from the ΛCDM model for $\ell \gtrsim 500$ and a significant suppression of power for larger ℓ.

Finally, a careful study of the matter power spectrum $P(k)$ (see Sec. 1.2.3) may provide us with an even stronger limit on DM–photon interactions (see Fig. 3.7). The pattern of oscillations together with the suppression of power at small scales, as noticed already in Ref. [163], could indeed constitute an interesting signature. The oscillations arise because the DM fluid acquires a non-zero pressure from its interactions with the thermal bath. Therefore, the oscillations are comparable to the usual baryon acoustic oscillations (BAO; see Sec. 1.2.3) but at larger k. The observability of such an effect depends on the non–linear evolution of the matter power spectrum (for which $k \gtrsim 0.2\ h\ \mathrm{Mpc}^{-1}$).

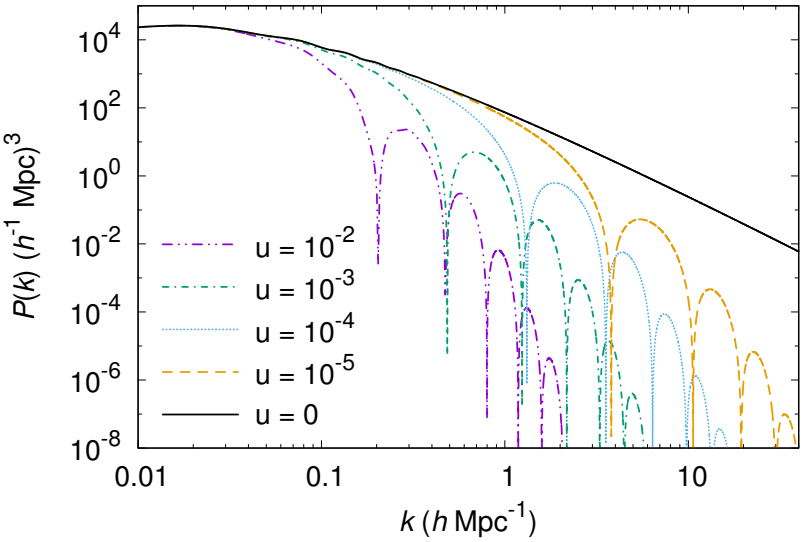

Figure 3.7: The influence of DM–photon interactions on the linear matter power spectrum, where the strength of the interaction is characterised by $u \equiv [\sigma_{\mathrm{DM}-\gamma}/\sigma_{\mathrm{Th}}]\,[m_{\mathrm{DM}}/100\ \mathrm{GeV}]^{-1}$ (with constant $\sigma_{\mathrm{DM}-\gamma}$) and we use the '*Planck* + WP' best-fit parameters from Ref. [10]. The new coupling produces (power-law) damped oscillations at large scales, reducing the number of small-scale structures, thus enabling the interaction strength to be constrained. For allowed DM–photon cross sections ($u \lesssim 10^{-4}$), significant damping effects are restricted to the non-linear regime ($k \gtrsim 0.2\ h\ \mathrm{Mpc}^{-1}$).

Typically, one would expect the non-linear matter power spectrum to be somewhat intermediate between cold DM (CDM) and warm DM (WDM) scenarios at large redshifts, and closer to WDM at small redshifts[12], so that the Lyman-α constraint on WDM models could apply. Using the latest bound on the mass of WDM candidates [184] together with the proposed transfer function in Ref. [163], we expect LSS data to set a more stringent limit than our CMB analysis (potentially by several orders of magnitude) but this would require a thorough investigation.

In Chapter 5, we run high-resolution N-body simulations assuming such oscillating $P(k)$, which enable us to study the impact of DM–photon interactions

[12]We note that acoustic oscillations are also expected in the $P(k)$ for certain WDM models at small scales (see e.g. Ref. [183]). However, at these scales, the $P(k)$ is already strongly suppressed by the free-streaming of the WDM particles. Therefore, the regeneration of power from these oscillations is expected to be much weaker than in our case.

in the non-linear regime and thereby determine the predicted number of substructures. These results will be particularly useful in light of forthcoming data from LSS surveys such as Euclid [185] and the *Dark Energy Spectroscopic Instrument* (DESI) [186].

Lastly, we note that we have assumed the interacting DM species accounts for the entire DM component of the universe; if more than one species were responsible for the observed relic density (e.g. Ref. [187]), larger DM–photon scattering cross sections would be allowed by both CMB and LSS data (see for example, Fig. 3.8).

3.4 Conclusion

In this chapter, we have studied the effects of introducing an effective coupling between DM and photons on the evolution of primordial matter fluctuations and in particular, the CMB temperature and polarisation power spectra. By comparing the TT and EE components of the C_ℓ in the presence of a DM–photon coupling with the latest data from *Planck*, we have set a stringent constraint on the elastic scattering cross section of $\sigma_{\mathrm{DM}-\gamma} \leq 2 \times 10^{-30} \, (m_{\mathrm{DM}}/\mathrm{GeV}) \ \mathrm{cm}^2$ (at 95% CL), assuming it is constant at late times. This bound is an order of magnitude stronger than the previous work of Ref. [163], where a limit was placed by comparing the temperature anisotropy spectrum with ΛCDM predictions (before the experimental results from WMAP were published).

For a heavy DM particle ($m_{\mathrm{DM}} \sim \mathrm{TeV}$), the maximal cross section is too large to exclude the possibility that DM has significant interactions with photons, while for light DM particles ($m_{\mathrm{DM}} \sim \mathrm{MeV}$), the cross section is of the order typically expected for weak interactions. If instead, the cross section is proportional to the temperature squared, we obtain a significantly tighter present-day bound of $\sigma_{\mathrm{DM}-\gamma,0} \leq 2 \times 10^{-39} \, (m_{\mathrm{DM}}/\mathrm{GeV}) \ \mathrm{cm}^2$ (at 95% CL), giving a weaker constraint in the early universe (since $\sigma_{\mathrm{DM}-\gamma} = \sigma_{\mathrm{DM}-\gamma,0} \, a^{-2}$, where a is the cosmological scale factor).

For such a limiting cross section, both the B-modes and the small-scale TT angular power spectrum are suppressed with respect to ΛCDM predictions for $\ell \gtrsim 500$ and $\ell \gtrsim 3000$, respectively. Therefore, stronger results could be achieved with

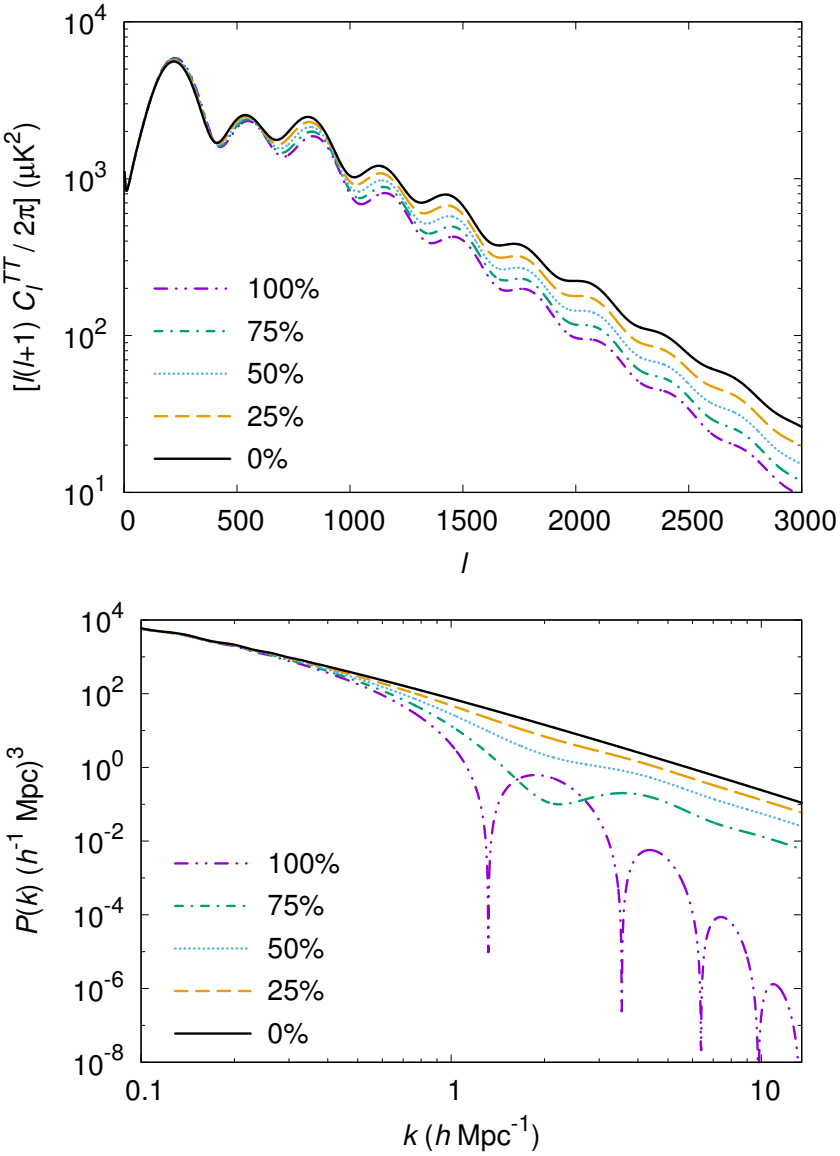

Figure 3.8: Top: the CMB angular power spectrum in the case that only a given fraction of DM interacts with photons, where for the interacting DM component, $u = 10^{-2}$. Bottom: the linear matter power spectrum in the case that only a given fraction of DM interacts with photons, where for the interacting DM component, $u = 10^{-4}$. In each case, we assume $\sigma_{\mathrm{DM}-\gamma}$ is constant and use the '*Planck* + WP' best-fit parameters from Ref. [10].

forthcoming B-mode data and measurements of the temperature spectrum at very high ℓ, provided an excellent knowledge of the foregrounds. However, as we will show in Chapter 5, these limits are weaker than those that one can derive from the matter power spectrum and the results from N-body simulations of such scenarios. Nevertheless, CMB constraints will be important to compare to, since they do not

depend on the non-linear evolution of the matter fluctuations.

Importantly, in this chapter, we have shown that one can effectively use cosmological data to restrict the allowed region of parameter space for DM interactions, independently of any theoretical prejudice. Indeed, any CMB experiment with the ability to measure the C_ℓ spectra at high ℓ could contribute to our fundamental understanding of DM. In Chapter 4, we will provide a comparable analysis for DM–neutrino interactions.

Chapter 4

Constraints on Dark Matter–Neutrino Scattering

I have done something very bad today by proposing a particle that cannot be detected; it is something no theorist should ever do.

— Wolfgang Pauli

4.1 Introduction

It is generally assumed that dark matter (DM) consists of collisionless, cold particles (CDM). However, recent work has shown that small couplings with Standard Model particles (in particular, neutrinos [162, 164, 165, 188, 189], photons [163, 167, 190] and baryons [191–193]) cannot yet be ruled out using cosmological data alone. Additionally, such interactions are expected in the weakly-interacting massive particle (WIMP) paradigm (see Sec. 1.3) and in several extensions of the Standard Model (e.g. Refs. [194–196]). It is also possible that DM interacts with other putative particles in the dark sector [197–200] but we will not consider this case here.

As we have seen in Chapter 3, interactions of DM beyond gravity lead to a suppression of the primordial density fluctuations, erasing structure with a size smaller than the collisional damping scale [162, 165]. This produces noticeable signatures in the cosmic microwave background (CMB) angular power spectrum C_ℓ

and the matter power spectrum $P(k)$, and ultimately impacts on the large-scale structure (LSS) of the universe that we observe today. The effect is enhanced if DM scatters off relativistic particles e.g. neutrinos and photons in the radiation-dominated era, allowing one to set competitive limits on these interactions in the early universe. Unlike direct [104, 105] and indirect [121–131] detection experiments, the results obtained from such analyses are importantly model-independent. Furthermore, any theory that predicts interactions between DM and the visible sector must satisfy these constraints. In this chapter, we focus on DM–neutrino interactions, hereafter νCDM (a similar study for DM–photon interactions can be found in Chapter 3).

While CMB experiments such as *Planck* allow one to constrain the cosmological parameters with unprecedented precision [42], extracting the $P(k)$ from *Planck* or the next-generation of CMB probes (such as COrE+ [201] or PIXIE [202]) will be limited by the large uncertainties involved in foreground modelling, which hinder any analysis of the C_ℓ at large ℓ[1]. Therefore, to unravel the nature of DM, a direct probe of the $P(k)$ is needed. In this chapter, we show that the next generation of LSS surveys could provide us with key information on the particle properties of DM, due to their extremely high precision.

Galaxy clustering surveys [203–209] have already observed the imprint of Baryon Acoustic Oscillations (BAO), a standard ruler to measure the Hubble expansion rate $H(z)$ and the angular diameter distance $D_{\rm A}(z)$. Recently, the *Baryon Oscillation Spectroscopic Survey* (BOSS) collaboration [210] reported a separate extraction of $H(z)$ and $D_{\rm A}(z)$ to a precision of 1% [203]. Here we show that by exploiting all of the information contained in the shape of the full $P(k)$ (rather than solely the BAO geometrical signature [211–213]), one can test the validity of the ΛCDM model at scales below $\sim$ Mpc. We exploit both the current publicly-available galaxy power spectrum data (in particular, from the *WiggleZ* survey [209]) and the expected full-shape power spectrum measurements from the

[1]An additional difficulty is that the C_ℓ are the result of the convolution of the $P(k)$ with a window (Bessel) function that accounts for the angular scale (see Sec. 2.4), thus preventing one from detecting small features in the $P(k)$.

forthcoming *Dark Energy Spectroscopic Instrument* (DESI) [186].

The chapter is organised as follows. In Sec. 4.2, we present the modified perturbation equations that we use to incorporate DM–neutrino interactions and describe their implementation in the Boltzmann code CLASS [48, 146]. In Sec. 4.3, we present bounds on the scattering cross section from the CMB angular power spectrum [Sec. 4.3.1] and the LSS matter power spectrum [Sec. 4.3.2]. The significance of our results for specific DM models is discussed in Sec. 4.4. In Sec. 4.5, we perform a forecast for the sensitivity of planned experiments such as COrE+ and DESI to the νCDM framework. Finally, we provide conclusions in Sec. 4.6.

This chapter is based on the work carried out in Refs. [2, 3].

4.2 Implementation

In analogy to the Thomson scattering terms in the perturbation equations for baryons and photons (see Chapter 2), in the presence of DM–neutrino interactions, the perturbation equations in the conformal Newtonian gauge read[2] [163, 188]

$$\dot{\theta}_{\rm DM} = k^2\psi - \mathcal{H}\theta_{\rm DM} - S^{-1}\dot{\mu}(\theta_{\rm DM} - \theta_\nu) \,, \tag{4.2.1}$$

$$\dot{\theta}_\nu = k^2\psi + k^2\left(\frac{1}{4}\delta_\nu - \sigma_\nu\right) - \dot{\mu}(\theta_\nu - \theta_{\rm DM}) \,, \tag{4.2.2}$$

$$\dot{F}_{\nu 2} = 2\dot{\sigma}_\nu = \frac{8}{15}\theta_\nu - \frac{3}{5}kF_{\nu 3} - \frac{9}{5}\dot{\mu}\sigma_\nu \,, \tag{4.2.3}$$

$$\dot{F}_{\nu\ell} = \frac{k}{2\ell+1}\left[\ell F_{\nu(\ell-1)} - (\ell+1)F_{\nu(\ell+1)}\right] - \dot{\mu}F_{\nu\ell} \,, \quad \ell \geq 3 \tag{4.2.4}$$

where θ_ν and $\theta_{\rm DM}$ are the neutrino and DM velocity divergences, k is the comoving wavenumber, ψ is the gravitational potential, δ_ν and σ_ν are the neutrino density contrast and anisotropic stress potential, $F_{\nu\ell}$ refer to higher ($\ell > 2$) neutrino moments, and $\mathcal{H} \equiv \dot{a}/a$ is the conformal Hubble parameter[3].

[2] All necessary modifications are confined to the thermodynamics and perturbation modules of CLASS (version 1.7).

[3] Note that the modified neutrino Boltzmann hierarchy takes exactly the same form as Eqs. (2.2.67), (2.2.68) and (2.2.69) for the photon hierarchy, without the polarisation components.

The DM–neutrino interaction rate is given by $\dot{\mu} \equiv a\,\sigma_{\mathrm{DM}-\nu}\,c\,n_{\mathrm{DM}}$, where $\sigma_{\mathrm{DM}-\nu}$ is the elastic scattering cross section, $n_{\mathrm{DM}} = \rho_{\mathrm{DM}}/m_{\mathrm{DM}}$ is the DM number density, ρ_{DM} is the DM energy density and m_{DM} is the DM mass. The factor $S \equiv (3/4)(\rho_{\mathrm{DM}}/\rho_{\nu})$ ensures energy conservation and accounts for the momentum transfer in the elastic scattering process [cf. Eq. (2.1.34)].

Note that unlike in the case of DM–photon interactions (see Sec. 3.2.2), we do not need to modify the baryon–photon tight-coupling equations or the line-of-sight integration terms for the photon anisotropies.

To quantify the effect of DM–neutrino interactions on the evolution of primordial density fluctuations, we introduce the dimensionless quantity

$$u \equiv \left[\frac{\sigma_{\mathrm{DM}-\nu}}{\sigma_{\mathrm{Th}}}\right]\left[\frac{m_{\mathrm{DM}}}{100\ \mathrm{GeV}}\right]^{-1}\,, \tag{4.2.5}$$

where σ_{Th} is the Thomson cross section. Since the magnitude of the u parameter determines the collisional damping scale [163], the efficiency of small-scale suppression is essentially governed by the ratio of the interaction cross section to the DM mass.

In the majority of particle physics models, the scattering cross section between DM and neutrinos $\sigma_{\mathrm{DM}-\nu}$ will have one of two distinct behaviours: either constant (i.e. temperature-independent) or proportional to the temperature squared (see Sec. 4.4 for specific examples). For the case in which $\sigma_{\mathrm{DM}-\nu} \propto T^2$, we can write $u(a) = u_0\,a^{-2}$, where u_0 is the present-day value and a is the cosmological scale factor, normalised to unity today.

4.3 Consequences for Cosmological Observables

In this section, we derive constraints on the DM–neutrino elastic scattering cross section from the CMB angular power spectrum [Sec. 4.3.1] and LSS matter power spectrum [Sec. 4.3.2], using the modified version of CLASS described in Sec. 4.2.

4.3.1 Cosmic Microwave Background

In Fig. 4.1, we show the effect of introducing DM–neutrino interactions on the DM density constant $\delta_{\rm DM}$ for a small-scale mode with wavenumber $k = 40$ Mpc^{-1}. Once the DM perturbation has entered the horizon, rather than growing under gravitational collapse as in the case of collisionless CDM ($u = 0$), DM experiences collisional damping. Therefore, at the CMB epoch ($a \sim 10^{-3}$) and today ($a = 1$), $\delta_{\rm DM}$ is suppressed and there is a greater level of isotropy on small scales.

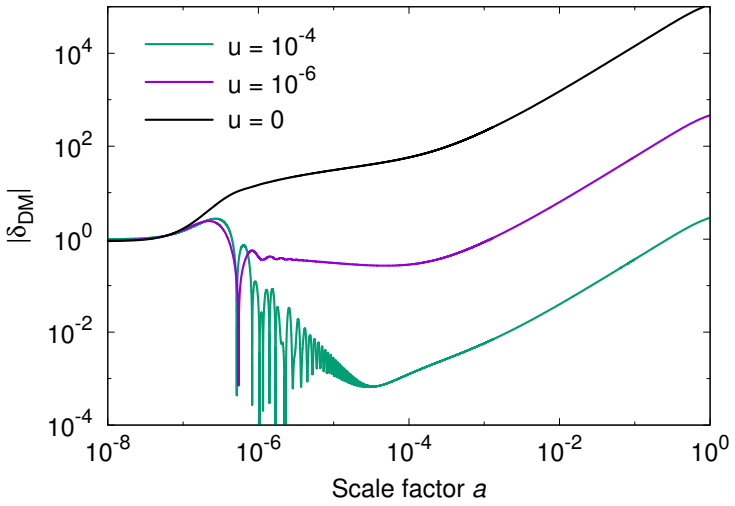

Figure 4.1: The evolution of the normalised DM density contrast $\delta_{\rm DM}$ with and without a coupling to neutrinos, for a small-scale mode with wavenumber $k = 40$ Mpc^{-1}. The curves correspond to DM–neutrino couplings of $u = 0$ (black), $u = 10^{-6}$ (purple), and $u = 10^{-4}$ (green), where u is defined in Eq. (4.2.5) and $\sigma_{{\rm DM}-\nu}$ is constant.

The resulting impact of DM–neutrino interactions on the TT, EE and BB components of the CMB angular power spectrum is illustrated in Fig. 4.2 for specific values of the parameter u. We consider a flat ΛCDM cosmology (with the only addition being the DM–neutrino coupling), where the parameters are taken from the one-year data release of *Planck* [10]. For simplicity, we show the impact of a constant cross section in Fig. 4.2; however, we note that similar effects are obtained for temperature-dependent scenarios.

In the TT (top panel) and EE (middle panel) components of the C_ℓ, we see an increase in the magnitude of the acoustic peaks and a slight shift to larger ℓ with respect to collisionless CDM ($u = 0$). These effects can be understood as follows.

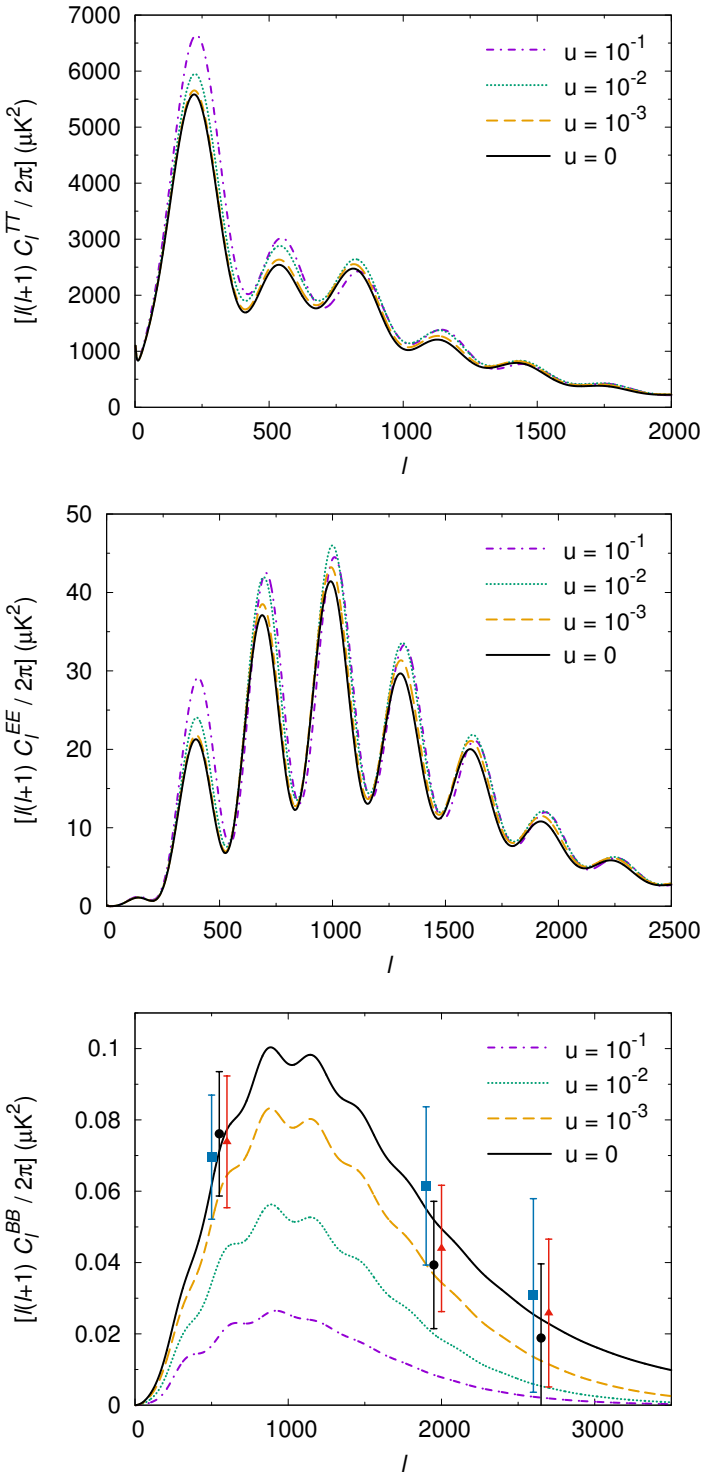

Figure 4.2: The effect of DM–neutrino interactions on the TT (top), EE (middle) and BB (bottom) components of the CMB angular power spectrum, where $u \equiv [\sigma_{\mathrm{DM}-\nu}/\sigma_{\mathrm{Th}}]\,[m_{\mathrm{DM}}/100\ \mathrm{GeV}]^{-1}$. We take $\sigma_{\mathrm{DM}-\nu}$ to be constant and use the '*Planck* + WP' best-fit parameters from Ref. [10]. We have assumed that the tensor-to-scalar ratio $r = 0$. The data points in the BB spectrum are recent measurements from the SPTpol experiment [57].

The shape of the CMB spectrum is affected by the gravitational force that acts on the coupled baryon–photon fluid before recombination. In principle, this force receives contributions from the distribution of free-streaming neutrinos and from that of slowly-clustering DM. In fact, when decomposing the solution to the system of cosmological perturbations into "slow modes" and "fast modes" [214, 215], one sees that the baryon–photon and neutrino perturbations are described by fast modes, while the DM perturbations are described by slow modes. This implies that the baryon–photon fluid only has significant gravitational interactions with the free-streaming neutrinos.

These interactions are especially important during the radiation-dominated era and soon after Hubble crossing, when the baryon–photon perturbation receives a gravitational boost. This boost is attenuated by the fact that neutrinos free-stream, develop anisotropic stress and cluster less efficiently then e.g. a relativistic perfect fluid. Modes crossing the Hubble radius during matter domination do not experience this effect because the gravitational potential is then constant, while DM perturbations grow in proportion to the scale factor.

However, in the presence of an efficient DM–neutrino interaction term, DM experiences damped oscillations like the neutrinos, instead of slow gravitational clustering [188]. Thus, DM perturbations also contribute to the fast modes. At the same time, neutrinos are bound to DM particles and do not free-stream; their anisotropic stress is reduced, making them behave more like a relativistic perfect fluid [189]. Both of these effects contribute to the patterns seen in Fig. 4.2:

1. When perturbations cross the Hubble radius during radiation domination, the baryon–photon fluid feels the gravitational force from neutrinos with reduced anisotropic stress and stronger clustering; this increases the gravitational boost effect. This mechanism can potentially enhance all the peaks but the first one, although the scale at which this effect is important depends on the time at which neutrinos decouple from DM.

2. As long as DM and neutrinos are tightly coupled, the sound speed in this effective fluid is given by $c^2_{\mathrm{DM}-\nu} = [3(1+3\bar{\rho}_{\mathrm{DM}}/4\bar{\rho}_\nu)]^{-1}$, instead of $c^2_{\mathrm{b}-\gamma} = [3(1+3\bar{\rho}_{\mathrm{b}}/4\bar{\rho}_\gamma)]^{-1}$ in the baryon–photon fluid. The ratio $\bar{\rho}_{\mathrm{DM}}/\bar{\rho}_\nu$ is always

larger than the ratio $\bar{\rho}_\mathrm{b}/\bar{\rho}_\gamma$ so the DM–neutrino fluid has a smaller sound speed. Through gravitational interactions and a "DM–neutrino drag" effect, the frequency of the baryon–photon sound waves is then slightly reduced and the acoustic peaks in the temperature and polarisation spectra appear at larger ℓ.

3. When perturbations cross the Hubble radius during matter domination, if DM is still efficiently coupled to neutrinos, it contributes to the fast mode solution. Thus, DM is gravitationally coupled to the baryon–photon fluid, leading to a gravitational boosting effect (unlike in the collisionless CDM model for which metric fluctuations are frozen during matter domination). This effect contributes to the enhancement of the first peak.

4. In the temperature spectrum, there is a well-known asymmetry between the amplitude of the first odd and even peaks, due to the fact that oscillations in the effective temperature $(\delta T/T + \psi)$ are centred around the mean value $\langle \delta T/T + \psi \rangle \sim -(3\bar{\rho}_\mathrm{b}/4\bar{\rho}_\gamma)\psi$. If DM is still efficiently coupled to neutrinos at the time of photon decoupling, the metric fluctuations are strongly suppressed, and the oscillations are centred on zero. This has the opposite effect to increasing the baryon density; it slightly enhances even peaks and suppresses odd peaks.

5. Finally, if DM is still efficiently coupled to neutrinos at the time of photon decoupling, the first peak is further enhanced by a stronger early integrated Sachs-Wolfe effect (see Sec. 1.2.2). This takes place after photon decoupling as a consequence of the fact that metric fluctuations vary with time as long as DM remains efficiently coupled to neutrinos.

Note that among all these effects, the first two can occur even for a small DM–neutrino cross section, since they only assume that neutrinos are coupled to DM until some time near the end of radiation domination. The last three effects are only present for very large cross sections, such that DM is still coupled to neutrinos at the beginning of matter domination. All five effects can be observed in Fig. 4.2 for $u = 10^{-3}$ or larger [corresponding to $\sigma_{\mathrm{DM}-\nu} \gtrsim 10^{-29}\,(m_\mathrm{DM}/\mathrm{GeV})\ \mathrm{cm}^2$]. However, we will see in Sec. 4.3.2 that these values are not compatible with data from the

Lyman-α forest [216, 217]. For realistic cross sections, the only effects on the C_ℓ^{TT} and C_ℓ^{EE} spectra are a small enhancement and shifting of the high-ℓ peaks.

To efficiently sample the parameter space and account for any degeneracies, we run the Markov Chain Monte Carlo (MCMC) code MONTE PYTHON [173] combined with the one-year data release from *Planck*, provided by the *Planck* Legacy Archive [174]. In particular, we use the high-ℓ and low-ℓ temperature data of *Planck* combined with the low-ℓ WMAP polarisation data (corresponding to '*Planck* + WP' in Ref. [10]).

We vary the parameters of the minimal flat ΛCDM cosmology, namely: the baryon density $\Omega_\mathrm{b}h^2$, the DM density $\Omega_\mathrm{DM}h^2$, the reduced Hubble parameter h, the primordial spectrum amplitude A_s, the scalar spectral index n_s, and the redshift of reionisation z_reio, supplemented by the additional parameter u. In a second run, we also allow the effective number of neutrino species N_eff to vary from the standard value of 3.046 [172]. For simplicity, we use the approximation of massless neutrinos[4]. Finally, we marginalise over the nuisance parameters listed in Ref. [10].

The bounds on the various cosmological parameters are given in Table 4.1 and illustrated in Figs. 4.3 and 4.4 for constant and T^2-dependent cross sections, respectively (where we omit the nuisance parameters for clarity).

Fixing $N_\mathrm{eff} = 3.046$, we find that the data prefers a DM–neutrino elastic scattering cross section of

$$\sigma_{\mathrm{DM}-\nu} \leq 3 \times 10^{-28} \, (m_\mathrm{DM}/\mathrm{GeV}) \ \mathrm{cm}^2 \,, \tag{4.3.6}$$

if it is constant, and

$$\sigma_{\mathrm{DM}-\nu,0} \leq 4 \times 10^{-40} \, (m_\mathrm{DM}/\mathrm{GeV}) \ \mathrm{cm}^2 \,, \tag{4.3.7}$$

for the present-day value, if it is proportional to the temperature squared (at 68% CL).

[4] This is in contrast to our MCMC in Chapter 3 and the *Planck* analysis, which assume two massless and one massive neutrino with $m_\nu = 0.06$ eV [10]. Such a small neutrino mass only affects the CMB through a slight shift in the angular diameter distance, which can be exactly compensated by a decrease in $100\,h$ of ~ 0.6 [10].

Parameter	No interaction		$\sigma_{\mathrm{DM}-\nu}$ constant		$\sigma_{\mathrm{DM}-\nu} \propto T^2$	
$100\,\Omega_{\mathrm{b}}h^2$	$2.205^{+0.028}_{-0.028}$	$2.238^{+0.041}_{-0.041}$	$2.225^{+0.029}_{-0.033}$	$2.276^{+0.043}_{-0.048}$	$2.197^{+0.028}_{-0.028}$	$2.262^{+0.042}_{-0.046}$
$100\,\Omega_{\mathrm{DM}}h^2$	$11.99^{+0.27}_{-0.27}$	$12.56^{+0.55}_{-0.55}$	$12.11^{+0.27}_{-0.30}$	$12.99^{+0.59}_{-0.61}$	$11.97^{+0.27}_{-0.27}$	$13.26^{+0.65}_{-0.72}$
$100\,h$	$67.3^{+1.2}_{-1.2}$	$70.7^{+3.2}_{-3.2}$	$69.5^{+1.2}_{-1.2}$	$75.0^{+3.4}_{-3.7}$	$67.8^{+1.2}_{-1.2}$	$75.3^{+3.6}_{-4.0}$
$10^{+9}\,A_s$	$2.196^{+0.051}_{-0.060}$	$2.251^{+0.069}_{-0.085}$	$2.020^{+0.063}_{-0.065}$	$2.086^{+0.068}_{-0.089}$	$2.167^{+0.052}_{-0.059}$	$2.257^{+0.072}_{-0.084}$
n_s	$0.9603^{+0.0073}_{-0.0073}$	$0.977^{+0.016}_{-0.016}$	$0.9330^{+0.0104}_{-0.0095}$	$0.956^{+0.017}_{-0.016}$	$0.9527^{+0.0086}_{-0.0085}$	$0.981^{+0.017}_{-0.017}$
z_{reio}	$11.1^{+1.1}_{-1.1}$	$11.6^{+1.3}_{-1.3}$	$10.8^{+1.1}_{-1.1}$	$11.6^{+1.2}_{-1.3}$	$10.8^{+1.1}_{-1.1}$	$11.9^{+1.3}_{-1.4}$
N_{eff}	(3.046)	$3.51^{+0.39}_{-0.39}$	(3.046)	$3.75^{+0.40}_{-0.43}$	(3.046)	$4.07^{+0.46}_{-0.52}$
$100\,u$	–	–	< 3.99	< 3.27	–	–
$10^{+13}\,u_0$	–	–	–	–	< 0.54	< 2.56

Table 4.1: Mean values and minimum credible intervals at 68% CL of the cosmological parameters set by the '*Planck* + WP' dataset for (i) no DM–neutrino interaction, (ii) a constant cross section, and (iii) a temperature-dependent cross section, where $u \equiv [\sigma_{\mathrm{DM}-\nu}/\sigma_{\mathrm{Th}}]\,[m_{\mathrm{DM}}/100\ \mathrm{GeV}]^{-1}$. In each of these models, we consider either $N_{\mathrm{eff}} = 3.046$ (first column) or N_{eff} free to vary (second column). The collisionless case is shown for comparison, using data from Ref. [10] and the *Planck* Explanatory Supplement (`https://wiki.cosmos.esa.int/planckpla/`). For a fair comparison of h values between the interacting and non-interacting scenarios, one should subtract 0.6 from the mean $100\,h$ values of the last four columns (as we have used the approximation of massless neutrinos, see Footnote 4).

The bound on the constant cross section is rather weak due to significant degeneracies with the other cosmological parameters (in particular: h, A_s and n_s). By performing additional runs, we found that including constraints on σ_8 (the present linear-theory mass dispersion on a scale of $8\,h^{-1}\,\mathrm{Mpc}$ [218]) from e.g. *Planck* SZ clusters [219] and CFHTLens [220] does not help to break the degeneracies. The reason is that for the allowed models, deviations from ΛCDM occur at scales smaller than those probed by these experiments.

For ΛCDM, the *Planck* collaboration found that allowing N_{eff} to vary as a free parameter does not significantly improve the goodness-of-fit for '*Planck* + WP' data. However, it has the remarkable property of enlarging the bounds on h, which relaxes the tension between *Planck* and direct measurements of the local Hubble expansion (without conflicting with BAO data) [10].

This is a result of a well-known parameter degeneracy, involving at least N_{eff}, h and $\Omega_{\mathrm{m}}h^2$. This degeneracy comes from the fact that by simultaneously enhancing

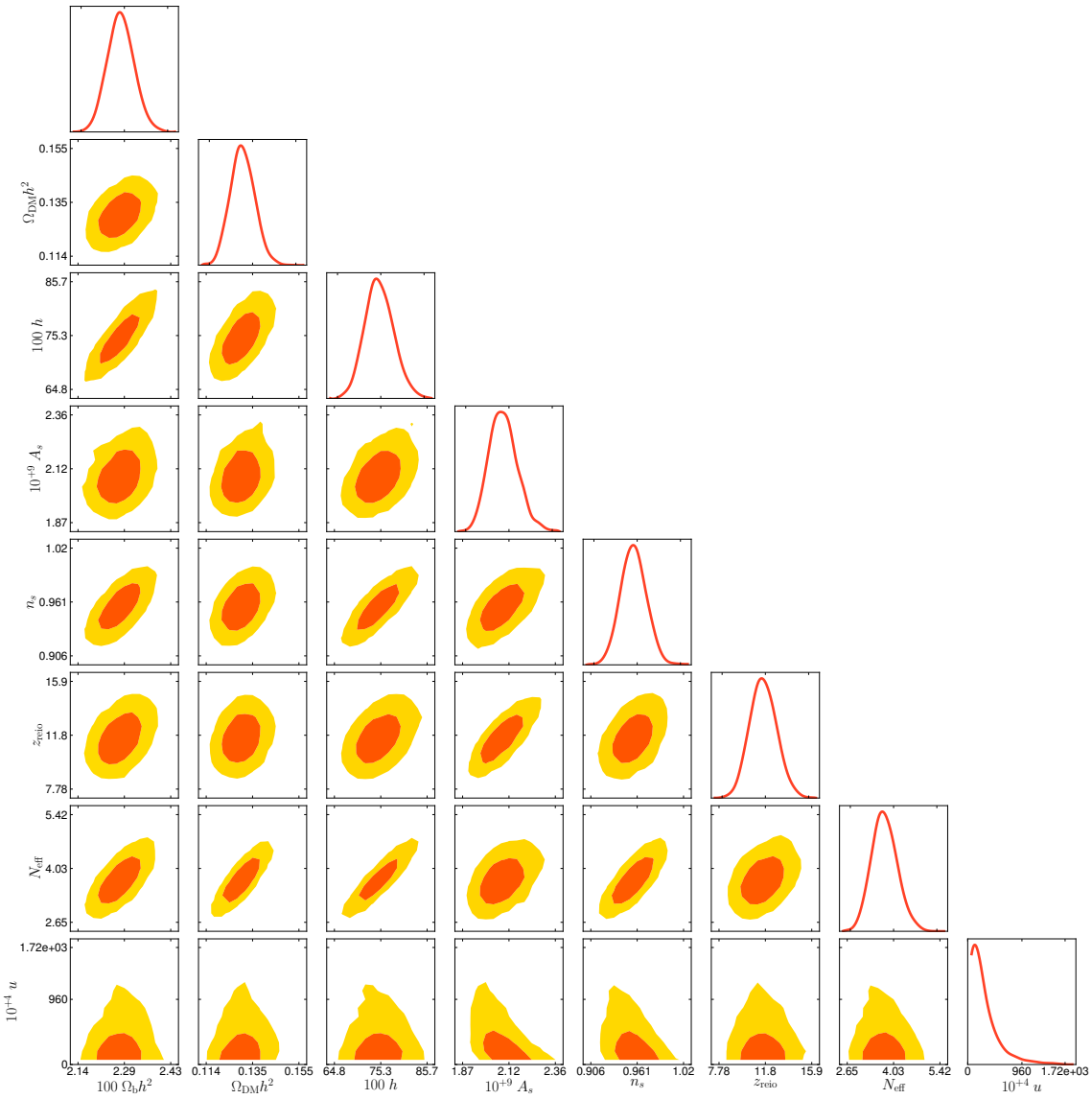

Figure 4.3: Triangle plot showing the one- and two-dimensional posterior distributions of the cosmological parameters set by *Planck* for a constant DM–neutrino cross section, with u and $N_{\rm eff}$ as free parameters. The orange and yellow contours correspond to 68% and 95% CL, respectively.

the radiation, matter and cosmological constant densities in the universe, one does not change the characteristic redshifts and distances affecting the CMB spectrum up to $\ell \sim 800$. Nevertheless, this direction of degeneracy can be constrained because additional degrees of freedom in $N_{\rm eff}$ lead to a stronger Silk damping effect, which is clearly visible for $\ell \gtrsim 800$. Thus, the varying $N_{\rm eff}$ model is not preferred by *Planck* alone, but has the potential to reconcile different cosmological probes that are otherwise in moderate ($\sim 2.5\sigma$) tension.

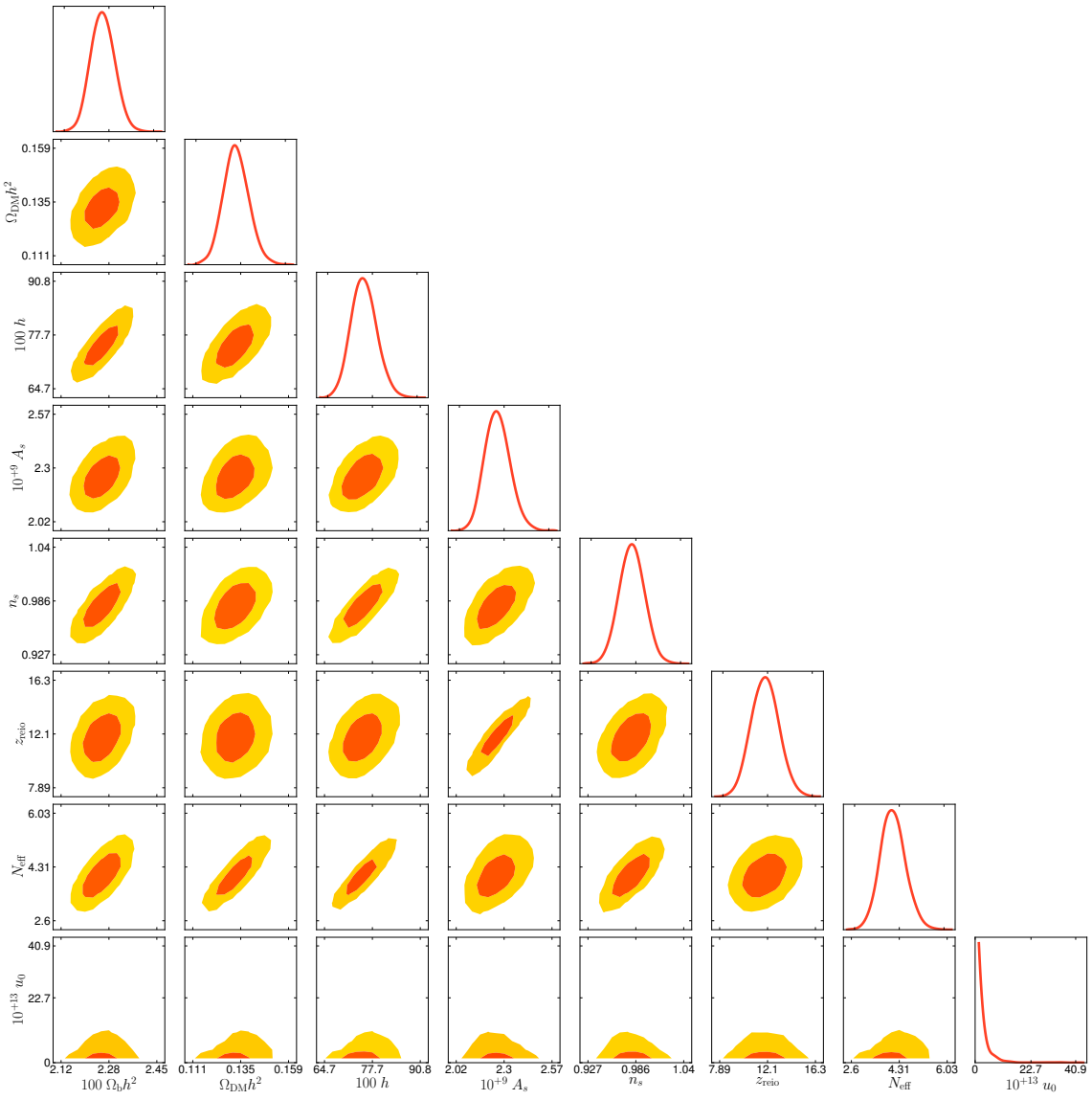

Figure 4.4: Triangle plot showing the one- and two-dimensional posterior distributions of the cosmological parameters set by *Planck* for a temperature-dependent DM–neutrino cross section, with u_0 and $N_{\rm eff}$ as free parameters. The orange and yellow contours correspond to 68% and 95% CL, respectively.

However, in the presence of DM–neutrino interactions, the model with varying $N_{\rm eff}$ turns out to be even more interesting. As in the standard case, it does not significantly improve the goodness-of-fit to '*Planck* + WP' data (the effective χ^2 decreases by $\sim$ two for a constant cross section and ~ 0.5 for a T^2-dependent cross section). However, it opens up an even wider degeneracy in parameter space since the enhancement of the acoustic peaks (shown in Fig. 4.2) can, to some extent, counteract the effect of a larger value of $N_{\rm eff}$ or h.

Therefore, as can be seen in Table 4.1, with the addition of DM–neutrino interactions, the '*Planck* + WP' data can accommodate rather large values of $N_{\rm eff}$ (compatible with one additional thermalised species) and h (in excellent agreement with direct measurements at the 1σ level [221, 222]).

Allowing $N_{\rm eff}$ to vary, we obtain slightly different bounds on the scattering cross section:

$$\sigma_{{\rm DM}-\nu} \leq \ 2 \times 10^{-28} \, (m_{\rm DM}/{\rm GeV}) \ \ {\rm cm}^2 \ , \tag{4.3.8}$$

if it is constant, and

$$\sigma_{{\rm DM}-\nu,0} \leq \ 2 \times 10^{-39} \, (m_{\rm DM}/{\rm GeV}) \ \ {\rm cm}^2 \ , \tag{4.3.9}$$

if it is proportional to the temperature squared (at 68% CL).

Finally, we can also set constraints using the BB spectrum (bottom panel of Fig. 4.2). The B-modes are significantly suppressed due to the effects of collisional damping [162, 165]. Using the first-season data from the SPTpol experiment [57] (shown by the data points), we can already set conservative limits on the cross section of

$$\sigma_{{\rm DM}-\nu} \lesssim \ 10^{-27} \, (m_{\rm DM}/{\rm GeV}) \ \ {\rm cm}^2 \ , \tag{4.3.10}$$

if it is constant, and

$$\sigma_{{\rm DM}-\nu,0} \lesssim \ 10^{-35} \, (m_{\rm DM}/{\rm GeV}) \ \ {\rm cm}^2 \ , \tag{4.3.11}$$

if it is proportional to the temperature squared.

Future polarisation data from e.g. ACTpol [223], POLARBEAR [181] and SPIDER [182] will improve these results and could provide us with a powerful tool to study DM interactions in the future.

4.3.2 Large-Scale Structure

The effects of introducing DM–neutrino interactions on the linear matter power spectrum $P(k)$ are shown in Fig. 4.5 (where for simplicity, we assume that the cross section is constant). As in the case of DM–photon interactions (cf. Fig. 3.7), we obtain a series of damped oscillations, which suppress power on small scales [163].

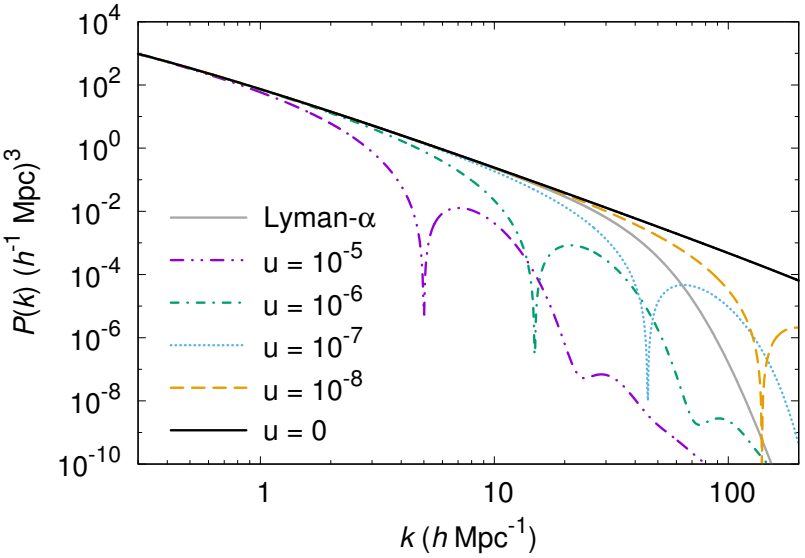

Figure 4.5: The impact of DM–neutrino interactions on the linear matter power spectrum, where $u \equiv [\sigma_{\mathrm{DM}-\nu}/\sigma_{\mathrm{Th}}]\,[m_{\mathrm{DM}}/100\ \mathrm{GeV}]^{-1}$ (such that $u = 0$ corresponds to no coupling). We take $\sigma_{\mathrm{DM}-\nu}$ to be constant and use the '*Planck* + WP' best-fit parameters from Ref. [10]. The grey, solid curve represents the most recent constraint on warm DM from the Lyman-α forest [184]. The new coupling produces (power-law) damped oscillations, reducing the number of small-scale structures with respect to ΛCDM [163].

For the cross sections of interest, significant damping effects are restricted to the non-linear regime (for which $k \gtrsim 0.2\ h\ \mathrm{Mpc}^{-1}$; see Sec. 1.2.3).

The oscillations arise because the DM fluid acquires a non-zero pressure from its interactions with the thermal bath, in a similar manner to the baryon–photon fluid before recombination. Although these oscillations cannot be observed using current data, they provide a characteristic signature for future experiments and high-resolution N-body simulations (see Chapter 5).

However, damped oscillations in the $P(k)$ are also expected for certain types of self-interacting DM [224], late-forming DM [225], atomic DM [226], and DM with a coupling to dark radiation [227, 228]. Taking all of these possibilities into account, it would be difficult to determine the specific nature of the DM coupling from this feature alone. Furthermore, since the oscillations are not as prominent as in the case of DM–photon interactions (cf. Fig. 3.7) or atomic DM in the sDAO (strong dark acoustic oscillation) scenario [229], they may not be resolved. In this case, there could be a degeneracy with both warm DM (WDM) [84] and some axion DM [230]

models, which predict a sharp cut-off in the $P(k)$ at small scales.

In general, the reduction of small-scale power for a DM candidate is described by the transfer function $T(k)$, defined by

$$P(k) = T^2(k)\ P_{\rm CDM}(k)\ , \tag{4.3.12}$$

where $P_{\rm CDM}(k)$ is the equivalent matter power spectrum for collisionless CDM.

For a non-interacting WDM particle, the transfer function can be approximated by the fitting formula [231]

$$T(k) = [1 + (\alpha k)^{2\nu}]^{-5/\nu}\ , \tag{4.3.13}$$

where

$$\alpha = \frac{0.049}{h\ {\rm Mpc}^{-1}} \left(\frac{m_{\rm WDM}}{\rm keV}\right)^{-1.11} \left(\frac{\Omega_{\rm DM}}{0.25}\right)^{0.11} \left(\frac{h}{0.7}\right)^{1.22}\ , \tag{4.3.14}$$

$\nu \simeq 1.12$, and $m_{\rm WDM}$ is the mass of the warm thermal relic [84].

From Fig. 4.5, one can see that cosmological models including DM–neutrino interactions provide an initial reduction of small-scale power in a similar manner to the exponential cut-off of WDM. The presence of damped oscillations is unimportant for setting limits since we are only interested in the cut-off of the spectrum and the power is already significantly reduced by the first oscillation.

Using an analysis of the Lyman-α flux from the HIRES [216] and MIKE spectrographs [217], Ref. [184] obtained a bound on the free-streaming scale of a warm thermal relic, corresponding to a particle mass of $m_{\rm WDM} \simeq 3.3$ keV (or equivalently, $\alpha \simeq 0.012$). This constraint is represented by the solid grey curve in Fig. 4.5.

By comparing νCDM and WDM models, we can effectively rule out cross sections in which the collisional damping scale is larger than the maximally-allowed WDM free-streaming scale. Taking into account the freedom from the other cosmological parameters, we obtain the conservative upper bounds:

$$\sigma_{{\rm DM}-\nu} \lesssim 10^{-33}\,(m_{\rm DM}/{\rm GeV})\ \ {\rm cm}^2\ , \tag{4.3.15}$$

if the cross section is constant, and

$$\sigma_{{\rm DM}-\nu,0} \lesssim 10^{-45}\,(m_{\rm DM}/{\rm GeV})\ \ {\rm cm}^2\ , \tag{4.3.16}$$

Parameter	Lyman-α limit
$100\ \Omega_{\rm b}h^2$	$2.246^{+0.039}_{-0.042}$
$\Omega_{\rm DM}h^2$	$0.1253^{+0.0053}_{-0.0056}$
$100\ h$	$71.5^{+3.0}_{-3.3}$
$10^{+9}\ A_s$	$2.254^{+0.069}_{-0.082}$
n_s	$0.979^{+0.016}_{-0.016}$
$z_{\rm reio}$	$11.7^{+1.2}_{-1.3}$
$N_{\rm eff}$	$3.52^{+0.36}_{-0.40}$

Table 4.2: Best-fit values and minimum credible intervals at 68% CL of the cosmological parameters set by the '*Planck* + WP' dataset for a constant DM–neutrino elastic scattering cross section, where we impose the maximum allowed value obtained in Sec. 4.3.2, i.e. $\sigma_{{\rm DM}-\nu} \simeq 10^{-33}\,(m_{\rm DM}/{\rm GeV})\ {\rm cm}^2$.

if it scales as the temperature squared.

These limits are significantly stronger than those obtained from the CMB analysis in Sec. 4.3.1 and will improve further with forthcoming data from LSS surveys such as DESI [186] (see Sec. 4.5.2). However, CMB constraints are useful as they do not depend on the non-linear evolution of the matter fluctuations.

We now fix the cross section to be the maximum value allowed by these LSS constraints and redo our CMB analysis. Setting $\sigma_{{\rm DM}-\nu} \simeq 10^{-33}\,(m_{\rm DM}/{\rm GeV})\ {\rm cm}^2$ for a constant cross section, we obtain the bounds on the cosmological parameters shown in Table 4.2 and illustrated in Fig. 4.6. These results are similar to the case of collisionless CDM with $N_{\rm eff}$ free to vary (see Table 4.1), especially after correcting the central value of $100\ h$ by 0.6 (as explained in Footnote 4). The reason is that the cross section imposed by the Lyman-α data is small enough to not significantly modify the CMB spectrum.

4.4 Application to Specific Models

The results from Section 4.3 enable us to constrain DM interactions that cannot be directly probed at the LHC and provide us with direct access to physics beyond the Standard Model in the early universe. They are particularly useful for the models proposed in Refs. [94, 160, 164] where the DM particle is light ($\sim$ MeV) and

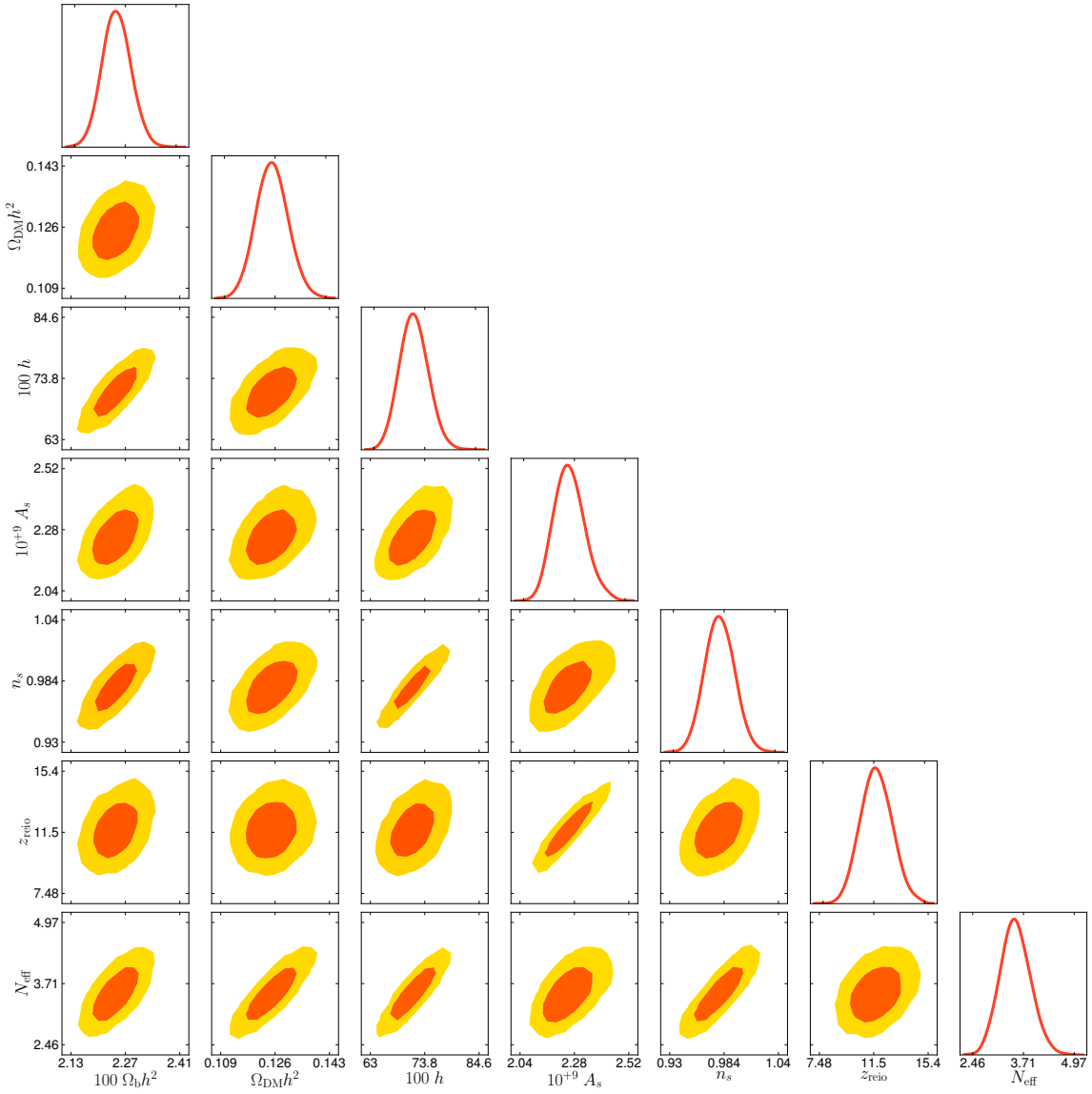

Figure 4.6: Triangle plot showing the one- and two-dimensional posterior distributions of the cosmological parameters set by *Planck* for a constant DM–neutrino cross section, where we impose the maximum allowed value obtained in Sec. 4.3.2, i.e. $\sigma_{\rm DM-\nu} \simeq 10^{-33}\,(m_{\rm DM}/{\rm GeV})\ {\rm cm}^2$. The orange and yellow contours correspond to 68% and 95% CL, respectively.

interactions with neutrinos can occur through the exchange of a scalar mediator if DM is fermionic, or a Dirac/Majorana mediator if DM is a scalar. Our limits could also be applied to the case of fermionic/scalar DM coupled to a light $U(1)$ gauge boson mediator [94, 160] with the caveat that the coupling of such a mediator to neutrinos is constrained by neutrino elastic scattering experiments [232, 233].

In Secs. 4.4.1 and 4.4.2 we consider models in which the DM–neutrino elastic

scattering cross section is constant and T^2-dependent, respectively.

4.4.1 Constant Cross Section

In general, one expects the DM–neutrino elastic scattering cross section to be temperature-dependent. However, a constant cross section is predicted either when (i) there is a strong mass degeneracy between the DM particle and the mediator, or (ii) the mediator is extremely light (which, in the case considered here, would imply that DM decays into the mediator plus a neutrino, unless the couplings are very suppressed).

To illustrate point (i), we consider the particular case of a real scalar DM particle coupled to a Majorana mediator N (in analogy to the sneutrino–neutralino–neutrino coupling in Supersymmetry) in a low-energy effective theory [94, 160]. We then assume a strong mass degeneracy between the DM particle and N, i.e. $|m_N - m_{\rm DM}| \lesssim \mathcal{O}(\text{eV})$ (see e.g. Ref. [234]). In this toy model, the elastic scattering cross section is simply given by

$$\begin{aligned} \sigma_{\text{DM}-\nu} &\simeq \frac{g^4}{4\pi}\frac{1}{m_{\rm DM}^2} \\ &\simeq 3\times 10^{-33}\ \left(\frac{g}{0.1}\right)^4\ \left(\frac{m_{\rm DM}}{\text{GeV}}\right)^{-2}\ \text{cm}^2\ , \end{aligned} \tag{4.4.17}$$

where g is the DM–N–neutrino coupling. The corresponding Feynman diagrams are given in Fig. 4.7.

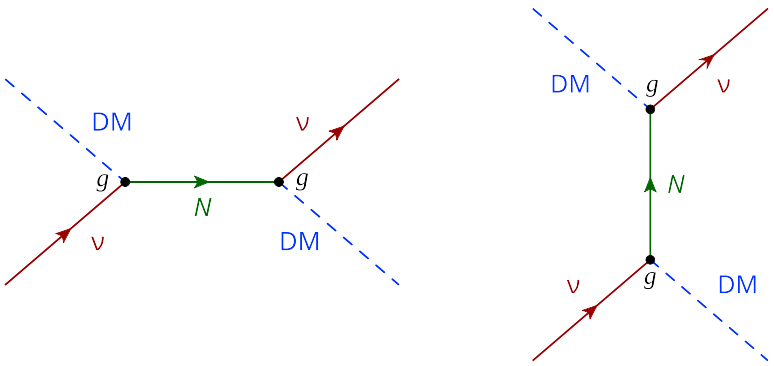

Figure 4.7: The s-channel (left) and u-channel (right) Feynman diagrams contributing to DM–neutrino scattering in the case of a real scalar DM particle and a Majorana mediator N, where g is the DM–N–neutrino coupling.

Our Lyman-α constraint from Sec. 4.3.2 implies the following upper limit on the coupling:

$$g \lesssim 0.1 \left(\frac{m_{\rm DM}}{\rm GeV}\right)^{3/4} . \tag{4.4.18}$$

An additional feature of this model is the self-annihilation of DM into neutrinos, with a thermally-averaged annihilation cross section given by

$$\langle \sigma v \rangle \simeq \frac{g^4}{16\pi} \frac{1}{m_{\rm DM}^2} \times c \ , \tag{4.4.19}$$

in the primordial universe [160]. Thus, the annihilation and elastic scattering cross sections are simply related by

$$\langle \sigma v \rangle \simeq \frac{\sigma_{{\rm DM}-\nu}}{4} \times c \ , \tag{4.4.20}$$

which gives $\langle \sigma v \rangle \simeq 8 \times 10^{-24} \ (m_{\rm DM}/{\rm GeV}) \ {\rm cm}^3 \ {\rm s}^{-1}$ if we apply our Lyman-α bound.

Conversely, if we impose that the DM annihilation cross section into neutrinos is within the range that is needed to explain the observed DM relic abundance[5], we obtain the prediction that

$$\sigma_{{\rm DM}-\nu} \ \simeq \ 4 \times 10^{-36} \left(\frac{\langle \sigma v \rangle}{3 \times 10^{-26} \ {\rm cm}^3 \ {\rm s}^{-1}}\right) \ {\rm cm}^2 \ , \tag{4.4.21}$$

which is comparable to our Lyman-α bound for MeV DM.

Therefore, we deduce that a viable model of MeV DM with a coupling to neutrinos must predict a cut-off in the $P(k)$ at the Lyman-α scale. Note that, in principle, we should also allow for co-annihilations [235, 236] since we assume a strong mass degeneracy between the DM particle and the mediator. A self-annihilation cross section that is ~ 4 times smaller than the value quoted in Eq. (4.4.21) would thus give rise to the observed DM relic abundance.

Interestingly, such a scenario also predicts an increase in $N_{\rm eff}$ with respect to the standard value [237]; typically, one expects $N_{\rm eff} \in [3.1, 3.8]$ by combining the most recent CMB and BBN data [238–241]. This is entirely compatible with the value of

[5]The assumption of dominant annihilations into neutrinos at MeV energies makes sense since significant annihilations into charged particles would require new, relatively light (charged) species. Such particles have not been observed, neither directly at the LHC nor in particle physics experiments (such as the electron/muon $g-2$ [156–159]).

$N_{\rm eff} = 3.5 \pm 0.4$ obtained in Sec. 4.3.2 when we impose our Lyman-α limit. As a result, we predict a rather higher value of $H_0 = 71 \pm 3$ km s^{-1} Mpc^{-1} (see Table 4.2), in good agreement with direct measurements of the local Hubble parameter[6].

Finally, it is worth noting that in this toy model, one expects the (radiative) generation of small neutrino masses. Assuming $\mathcal{O}(1)$ MeV $\lesssim m_N \lesssim 10$ MeV, one obtains neutrino masses in the range 0.01 eV $\lesssim m_\nu \lesssim 1$ eV provided that the coupling g satisfies [160]

$$g \simeq 10^{-3} \sqrt{\frac{m_N}{10 \text{ MeV}}} \left(\frac{\langle \sigma v \rangle}{3 \times 10^{-26} \text{ cm}^3 \text{ s}^{-1}} \right)^{1/4} \sqrt{1 + \left(\frac{m_{\rm DM}}{m_N} \right)^2} \,. \tag{4.4.22}$$

In the case of a strong mass degeneracy between the DM particle and the mediator, Eq. (4.4.22) gives

$$g \simeq 10^{-3} \sqrt{\frac{m_N}{10 \text{ MeV}}} \left(\frac{\langle \sigma v \rangle}{3 \times 10^{-26} \text{ cm}^3 \text{ s}^{-1}} \right)^{1/4} \,, \tag{4.4.23}$$

which is compatible with Eq. (4.4.18) for MeV DM.

In summary, for this specific realisation, we expect a cut-off in the $P(k)$ at the Lyman-α scale, an enhancement in $N_{\rm eff}$ and H_0 with respect to the ΛCDM values, and the possible generation of neutrino masses. Our model assumes a strong mass degeneracy between the DM particle and the mediator, but this could be suggestive of an exact symmetry in the invisible sector (such as unbroken Supersymmetry, without any counterpart in the visible sector). The other requirement is particles in the MeV mass range. Such properties may be challenging to realise in a theoretical framework, yet the model building remains to be done.

Expressions for the DM–neutrino elastic scattering cross section with a Dirac or Majorana DM candidate can be found in Ref. [94]. When there is a strong mass degeneracy, the cross section is expected to be constant and given by

$$\sigma_{\rm DM-\nu} \propto \frac{g^4}{m_{\rm DM}^2} \,, \tag{4.4.24}$$

[6] We emphasise that the values obtained for $N_{\rm eff}$ and H_0 from our MCMC analysis used the *Planck* one-year data release, and would be smaller if we had used the *Planck* 2015 temperature and polarisation data, which points to $N_{\rm eff} \sim 3.0$ and $H_0 \sim 68$ km s^{-1} Mpc^{-1}, assuming ΛCDM [11].

as in the scalar case. The annihilation cross section is also given by a similar expression, so again, for specific values of g [analogous to Eq. (4.4.18)], we expect a cut-off in the $P(k)$ at a relevant cosmological scale and simultaneously, the correct DM relic abundance.

In all the above scenarios, DM could potentially be produced by neutrinos in supernovae. However, here we do not consider a coupling to nucleons and the cross section does not increase with temperature (it remains constant). Therefore, we do not expect a large impact on supernovae cooling, but this would need to be checked in a dedicated study.

4.4.2 Temperature-Dependent Cross Section

If one relaxes the hypothesis of a strong mass degeneracy between the DM particle and the mediator, the DM–neutrino elastic scattering cross section becomes dominated by a term proportional to T^2 (independently of whether we consider a scalar or fermionic DM candidate). If we assume that neutrinos are Majorana particles, we obtain

$$\sigma_{\mathrm{DM}-\nu} \sim \frac{g^4}{\pi} \frac{T^2}{m_N^4} + \mathcal{O}(T^3) \,, \tag{4.4.25}$$

which leads to

$$\sigma_{\mathrm{DM}-\nu,0} \simeq 10^{-46} \, A \, \left(\frac{g}{0.1}\right)^4 \left(\frac{m_N}{\mathrm{MeV}}\right)^{-4} \mathrm{cm}^2 \,, \tag{4.4.26}$$

where $A \sim \mathcal{O}(1)$ is a numerical factor that depends on the exact nature of the DM particle.

Therefore, comparing Eq. (4.4.26) to Eq. (4.3.16), one expects a damping in the $P(k)$ at the Lyman-α scale if the DM mass is in the MeV range and $g \sim 0.1 \times (m_N/\mathrm{MeV})$. For such a configuration, there could be, in addition, a resonance feature in the diffuse supernovae neutrino background [242].

If neutrinos have only right-handed couplings and we do not impose a very strong degeneracy between m_N and m_{DM}, the cross section remains T^2-dependent. Its value would be of the same order as the Lyman-α bound, provided that the DM mass is again in the MeV range and the mass splitting between the mediator and the DM particle is relatively small (about 10%).

A T^2-dependent cross section is easier to achieve than the constant cross section case described in Sec. 4.4.1 since it does not require the mediator and the DM particle to be mass-degenerate. However, the observed DM abundance would be difficult to explain in the thermal case as the annihilation cross section would be too large for $g \gtrsim 0.1$ (although solutions exist e.g. asymmetric DM [243]). One would also lose the relation with the neutrino masses. A similar conclusion is obtained for a DM candidate that is coupled to a new (weakly-coupled) gauge boson (see Ref. [94]).

4.5 Constraints and Forecasts

Finally, in this section, we assess how powerful the constraints from future LSS surveys will be. For comparison, in Sec. 4.5.1, we first derive limits set by current CMB experiments and galaxy clustering surveys. These will serve as a benchmark for our forecasts in Sec. 4.5.2.

4.5.1 Current Constraints

In contrast to the analysis described in Sec. 4.3.1 and Refs. [188, 189], here we select a logarithmic prior distribution for the u parameter, since in principle, it can vary by many orders of magnitude. We also fix the effective number of neutrino species[7] $N_{\rm eff}$ to the standard value of 3.046.

Planck

The current CMB constraints (using *Planck* 2013 + WMAP polarisation data [10]) are shown in Table 4.3. The corresponding upper limits on the DM–neutrino scattering cross section (at 95% CL) are

$$\sigma_{\rm DM-\nu}^{(Planck)} \lesssim 6 \times 10^{-31} \, (m_{\rm DM}/{\rm GeV}) \ \ {\rm cm}^2 \ , \tag{4.5.27}$$

[7] In Sec. 4.3.1, we verified that allowing $N_{\rm eff}$ to vary has an impact on the value of the Hubble parameter H_0 but does not significantly change the sensitivity to the u parameter.

	$\sigma_{\mathrm{DM}-\nu}$ = constant		$\sigma_{\mathrm{DM}-\nu} \propto T^2$	
Parameter	*Planck* 2013	COrE+	*Planck* 2013	COrE+
$\Omega_{\mathrm{b}}h^2$	0.0221 ± 0.0003	0.02223 ± 0.00004	0.0221 ± 0.0003	0.02222 ± 0.00004
$\Omega_{\mathrm{DM}}h^2$	0.120 ± 0.003	0.1199 ± 0.0005	0.119 ± 0.003	0.1197 ± 0.0005
$100\,h$	70.0 ± 1.2	67.3 ± 0.2	68.0 ± 1.2	67.3 ± 0.2
$10^9 A_{\mathrm{s}}$	2.20 ± 0.06	2.207 ± 0.010	2.19 ± 0.06	2.207 ± 0.010
n_{s}	0.961 ± 0.008	0.9656 ± 0.0017	0.961 ± 0.008	0.9639 ± 0.0019
τ_{reio}	0.090 ± 0.015	0.0792 ± 0.0002	0.090 ± 0.013	0.0790 ± 0.0002
$\log_{10}(u_0)$	< -4.04	-4.33	< -13.6	< -14.6

Table 4.3: Marginalised posteriors for constant (left) and T^2-dependent (right) DM–neutrino scattering cross sections, set by the *Planck* 2013 data (+ WMAP polarisation) (see Sec. 4.5.1) and the COrE+ forecast (see Sec. 4.5.2). The errors for the standard ΛCDM parameters represent the 68% CL; the bound on u_0 is at the 95% CL.

if constant, and

$$\sigma_{\mathrm{DM}-\nu,0}^{(Planck)} \lesssim 2 \times 10^{-40}\,(m_{\mathrm{DM}}/\mathrm{GeV})\ \ \mathrm{cm}^2\ , \tag{4.5.28}$$

if T^2-dependent. These results are consistent with those quoted by the authors of Refs. [188, 189], with the caveat that they did not perform a full MCMC analysis.

WiggleZ

We now repeat the previous analysis adding LSS data on the full shape of the matter power spectrum. Concretely, we use the galaxy clustering information from the *WiggleZ* Dark Energy Survey [209]. The *WiggleZ* sample consists of $\sim 238,000$ galaxies and covers a region of 1 Gpc^3 in redshift space. Our calculations have shown that comparable results can be obtained from the BOSS DR11 measurements [203].

Following a similar analysis to Ref. [244], we construct the likelihood function as follows:

$$-2\,\log[L(\vartheta_\alpha)] = \chi^2(\vartheta_\alpha) = \sum_{ij} \Delta_i\, C_{ij}^{-1}\, \Delta_j\ , \tag{4.5.29}$$

where the covariance matrix reads

$$C_{ij} = \langle \hat{P}_{\mathrm{halo}}(k_i)\, \hat{P}_{\mathrm{halo}}(k_j) \rangle - \langle \hat{P}_{\mathrm{halo}}(k_i) \rangle \langle \hat{P}_{\mathrm{halo}}(k_j) \rangle\ , \tag{4.5.30}$$

and

$$\Delta_i \equiv \left[\hat{P}_{\mathrm{halo}}(k_i) - P_{\mathrm{halo},w}(k_i, \vartheta_\alpha) \right]\ . \tag{4.5.31}$$

In Eq. (4.5.31), $\hat{P}_{\rm halo}(k_i)$ is the measured galaxy power spectrum and $P_{{\rm halo},w}(k_i,\vartheta_\alpha)$ is the theoretical expectation for the set of model parameters ϑ_α that are varied in the MCMC. In turn, $P_{{\rm halo},w}(k_i,\vartheta_\alpha)$ is a convolution of the computed galaxy power spectrum with the survey window functions $W(k_i,k_n)$, and is given by

$$P_{{\rm halo},w}(k_i,\vartheta_\alpha) = \sum_n \frac{W(k_i,k_n)\,P_{\rm halo}(k_n/a_{\rm scl},\vartheta_\alpha)}{a_{\rm scl}^3} \ . \tag{4.5.32}$$

In this equation, $a_{\rm scl}$ represents the scaling, which takes into account that the observed galaxy redshift has to be translated into a distance using a fiducial model. In this case, we use the same values as in Ref. [245]: $\Omega_{\rm b} = 0.049$, $\Omega_{\rm m} = 0.297$, $h = 0.7$, $n_{\rm s} = 1$ and $\sigma_8 = 0.8$. The scaling factor is given by Refs. [244, 246]:

$$a_{\rm scl}^3 = \frac{D_A^2(z)\,H(z)}{D_{A,{\rm fid}}^2(z)\,H_{\rm fid}(z)} \ , \tag{4.5.33}$$

where $D_A(z)$ is the angular diameter distance, and the subscript "fid" refers to values in the fiducial model.

The theoretical galaxy power spectrum $P_{\rm halo}(k,\vartheta_\alpha)$ is related to the matter power spectrum $P(k,\vartheta_\alpha)$ through the relation

$$P_{\rm halo}(k,\vartheta_\alpha) = b^2\,P(k,\vartheta_\alpha) \ , \tag{4.5.34}$$

where b is the bias, which is assumed to be constant. We analytically marginalise over b as in Ref. [247]:

$$b^2 = \frac{\sum_{ij} P_{{\rm halo},w}(k_i,\vartheta_\alpha)\,C_{ij}^{-1}\,\hat{P}_{\rm halo}(k_j)}{\sum_{ij} P_{{\rm halo},w}(k_i,\vartheta_\alpha)\,C_{ij}^{-1}\,P_{{\rm halo},w}(k_j,\vartheta_\alpha)} \ . \tag{4.5.35}$$

In Table 4.4, we present the posterior distributions obtained using the combination of *WiggleZ* and CMB data. We perform two separate analyses, including data for which: (i) $k < k_{\rm max} = 0.12\ h\ {\rm Mpc}^{-1}$ (purely linear regime), and (ii) $k < k_{\rm max} = 0.2\ h\ {\rm Mpc}^{-1}$ (weakly non-linear regime).

In terms of the DM–neutrino scattering cross section (at 95% CL) with $k_{\rm max} = 0.12\ h\ {\rm Mpc}^{-1}$ $\{k_{\rm max} = 0.2\ h\ {\rm Mpc}^{-1}\}$, we obtain

$$\begin{aligned} \sigma_{{\rm DM}-\nu}^{(WiggleZ)} &\lesssim 4\times10^{-31}\,(m_{\rm DM}/{\rm GeV})\ \ {\rm cm}^2 \ ; \\ \{ &\lesssim 2\times10^{-31}\,(m_{\rm DM}/{\rm GeV})\ \ {\rm cm}^2 \ \} \ , \end{aligned} \tag{4.5.36}$$

	$\sigma_{\mathrm{DM}-\nu}$ = constant		$\sigma_{\mathrm{DM}-\nu} \propto T^2$	
Parameter	$k_{\mathrm{max}} = 0.12$	$k_{\mathrm{max}} = 0.2$	$k_{\mathrm{max}} = 0.12$	$k_{\mathrm{max}} = 0.2$
$\Omega_{\mathrm{b}}h^2$	0.0220 ± 0.0003	0.0219 ± 0.0003	0.0219 ± 0.0003	0.0218 ± 0.0003
$\Omega_{\mathrm{DM}}h^2$	0.122 ± 0.002	0.123 ± 0.003	0.122 ± 0.002	0.123 ± 0.002
$100\,h$	70.0 ± 1.1	66.6 ± 1.0	66.9 ± 1.1	66.7 ± 1.0
$10^9 A_{\mathrm{s}}$	2.19 ± 0.05	2.19 ± 0.05	2.19 ± 0.05	2.19 ± 0.05
n_{s}	0.956 ± 0.007	0.956 ± 0.006	0.956 ± 0.007	0.955 ± 0.007
τ_{reio}	0.086 ± 0.013	0.086 ± 0.013	0.085 ± 0.013	0.085 ± 0.013
$\log_{10}(u_0)$	< -4.18	-4.57	< -13.7	< -13.9

Table 4.4: Marginalised posteriors for constant (left) and T^2-dependent (right) DM–neutrino scattering cross sections, set by the combination of *WiggleZ* full-shape galaxy power spectrum measurements and *Planck* 2013 (+ WMAP polarisation) data. The errors for the standard ΛCDM parameters represent the 68% CL; the bound on u_0 is at the 95% CL. The values of k_{max} are in units of $[h\ \mathrm{Mpc}^{-1}]$.

for the constant cross section case. As we shall see in the next section, these bounds are competitive with those resulting from our forecasts for the future CMB mission COrE+.

Meanwhile, for $\sigma_{\mathrm{DM}-\nu} \propto T^2$, we obtain

$$\begin{aligned} \sigma^{(WiggleZ)}_{\mathrm{DM}-\nu,0} &\lesssim 1 \times 10^{-40}\,(m_{\mathrm{DM}}/\mathrm{GeV})\ \mathrm{cm}^2\ ; \\ \{ &\lesssim 8 \times 10^{-41}\,(m_{\mathrm{DM}}/\mathrm{GeV})\ \mathrm{cm}^2\ \}\ . \end{aligned} \tag{4.5.37}$$

Therefore, including data in the weakly non-linear regime ($k < 0.2\ h\ \mathrm{Mpc}^{-1}$) only strengthens the constraints by a factor of two (constant) and 1.25 (T^2-dependent) with respect to those in the purely linear regime ($k < 0.12\ h\ \mathrm{Mpc}^{-1}$). We note that, in the constant cross section scenario, the bounds are as much as ~ 3.5 times tighter than those using only CMB measurements, showing the benefits of utilising the full shape of the $P(k)$. The improvement is not as significant for the T^2-dependent case because the suppression appears at larger k (see e.g. Ref. [228]).

4.5.2 Forecasts for Future Experiments

The CMB and LSS analyses in Sec. 4.5.1 allowed us to obtain current constraints on the DM–neutrino elastic scattering cross section. We will now assess the power

of future experiments in (i) *constraining* DM microphysics, and (ii) *detecting* small deviations from ΛCDM in the weakly non-linear regime. These two analyses require slightly different methodologies. In the first case, we construct a mock catalogue based on the ΛCDM cosmology and compute the strongest possible upper limit on the u parameter using the expected sensitivity of future experiments. In the second case, the mock data assumes small but non-negligible DM–neutrino interactions to assess our ability to detect them and more generally, reconstruct potential deviations from ΛCDM. In both cases, we use projected sensitivities.

As in the previous section, we first consider CMB observables only and then include data from LSS surveys. We focus on two planned experiments: (i) COrE+ [201], a CMB space mission currently proposed for the 2015-2025 ESA call, and (ii) DESI [186], a multiplexed fibre-fed spectrograph to detect galaxies and quasars up to redshift $z \sim 2$, which is expected to run in the 2018-2022 time frame.

COrE+

We first produce full mock CMB data sets (temperature and E-mode polarisation, plus lensing). We then compute the fiducial angular power spectra C_ℓ using the best-fit cosmology reported by the *Planck* 2015 final mission, including the TT, TE and EE spectra [42]. To these C_ℓ, we add a noise component N_ℓ consistent with each COrE+ channel specification and given by

$$N_\ell^{IJ} = \delta_{IJ}\,\sigma^I\sigma^J \exp\left[\ell\,(\ell+1)\,\frac{\theta^2}{8\ln 2}\right] \,, \tag{4.5.38}$$

where $\sigma^{I,J}$ correspond to the temperature or polarisation errors (i.e. $I, J \in \{T,E\}$) [201].

Following Ref. [248], the effective χ^2 is given by

$$\chi^2_{\rm eff}(\vartheta_\alpha) = \sum_\ell (2\ell+1) f_{\rm sky}\left(\frac{D}{|\bar{C}|} + \ln\frac{|\bar{C}|}{|\hat{C}|} - 3\right) \,, \tag{4.5.39}$$

where D is a certain function of the noised power spectra (see Eq. (3.4) in Ref. [248]). $|\bar{C}|$ and $|\hat{C}|$ represent the determinants of the theoretical and observed covariance matrices, respectively. Finally, $f_{\rm sky}$ represents the observed fraction of the sky (in practice, it weights the correlations between multipoles when the map does not cover the full sky). For this analysis, we use $f_{\rm sky} = 0.7$ [201].

The third step in our analysis is to compute a Gaussian likelihood around our fiducial spectra, tuned to obtain a 0.01% precision on the C_ℓ [as in Ref. [248], according to Eq. (4.5.39) and with a noise given by Eq. (4.5.38)]. Then, assuming a 4-year sensitivity and using MONTE PYTHON to sample the parameter space, we can predict the sensitivity of COrE+ to the cosmological parameters. Note that, for simplicity, we only consider the *TT*, *TE* and *EE* observables.

The results are presented in Table 4.3. We infer that the future sensitivity of COrE+ to a DM–neutrino coupling would be (at 95% CL)

$$\sigma_{\mathrm{DM}-\nu}^{(\mathrm{COrE+})} \lesssim 3 \times 10^{-31} \, (m_{\mathrm{DM}}/\mathrm{GeV}) \ \mathrm{cm}^2 \ , \tag{4.5.40}$$

if the cross section is constant, and

$$\sigma_{\mathrm{DM}-\nu,0}^{(\mathrm{COrE+})} \lesssim 2 \times 10^{-41} \, (m_{\mathrm{DM}}/\mathrm{GeV}) \ \mathrm{cm}^2 \ , \tag{4.5.41}$$

if $\sigma_{\mathrm{DM}-\nu} \propto T^2$.

While we find that the standard cosmological parameters will be measured to much higher precision than with *Planck*, there is only a modest gain in sensitivity to the DM–neutrino cross section. Furthermore, these limits are slightly weaker than those obtained after combining *Planck* observations with current LSS data in the weakly non-linear regime.

To assess the power of COrE+ to detect and reconstruct the νCDM cosmology or similar deviations to ΛCDM, we also produce mock data sets with $u = 10^{-4}$ and $u = 10^{-5}$ as fiducial models (assuming a constant cross section). We then attempt to reconstruct these models by means of the usual MCMC method.

The $u = 10^{-5}$ case is represented by the magenta contours in Fig. 4.8 (and similarly for $\sigma_{\mathrm{DM}-\nu} \propto T^2$ with $u_0 = 10^{-14}$). With COrE+–like CMB data, one can reconstruct a universe with $u = 10^{-4}$ with a 40% 1σ error. However, the $u = 10^{-5}$ case would provide us with CMB information entirely consistent with $u = 0$, in agreement with Eq. (4.5.40). Therefore, we expect that $u \gtrsim 5 \times 10^{-5}$ is the best sensitivity that one could achieve with CMB experiments in the near future.

DESI

Finally, the DESI survey [186] is expected to provide a wealth of information on the matter distribution in the universe at relatively small scales and up to redshift $z \sim 2$. To forecast the ability of DESI to discover new physics, we first compute the expected errors from the DESI instrument, following a Fisher matrix approach, which is the usual method used to forecast galaxy survey experiments [249].

The Fisher matrix is defined as the expectation value of the second derivative of the likelihood surface around its maximum. As long as the posterior distribution for the parameters is well approximated by a multivariate Gaussian function, its elements are given by [250–252]

$$F_{\alpha\beta} = \frac{1}{2}\,\mathrm{Tr}\left[C^{-1}\,\frac{\partial C}{\partial \vartheta_\alpha}\,C^{-1}\,\frac{\partial C}{\partial \vartheta_\beta}\right] \,, \tag{4.5.42}$$

where $C = S + N$ is the total covariance, which consists of signal S and noise N terms. Once more, we take a fiducial cosmology defined by the parameters that best fit the *Planck* 2015 TT, TE, EE + low$P$ data [11], in the presence of DM–neutrino interactions with $u = 10^{-5}$ in the constant $\sigma_{\mathrm{DM}-\nu}$ scenario and $u_0 = 10^{-14}$ in the $\sigma_{\mathrm{DM}-\nu} \propto T^2$ scenario.

Assuming a Gaussian likelihood for the DESI band powers, the Fisher matrix can be written as:

$$F^{\mathrm{LSS}}_{\alpha\beta} = \int_{\vec{k}_{\mathrm{min}}}^{\vec{k}_{\mathrm{max}}} \frac{\partial \ln P_{\mathrm{gg}}(\vec{k})}{\partial \vartheta_\alpha}\,\frac{\partial \ln P_{\mathrm{gg}}(\vec{k})}{\partial \vartheta_\beta}\,V_{\mathrm{eff}}(\vec{k})\,\frac{d\vec{k}}{2(2\pi)^3} \tag{4.5.43}$$

$$= \int_{-1}^{1}\int_{k_{\mathrm{min}}}^{k_{\mathrm{max}}} \frac{\partial \ln P_{\mathrm{gg}}(k,\mu)}{\partial \vartheta_\alpha}\,\frac{\partial \ln P_{\mathrm{gg}}(k,\mu)}{\partial \vartheta_\beta}\,V_{\mathrm{eff}}(k,\mu)\,\frac{k^2\,\mathrm{d}k\,\mathrm{d}\mu}{2(2\pi)^2} \,, \tag{4.5.44}$$

where V_{eff} is the effective volume of the survey and given by

$$V_{\mathrm{eff}}(k,\mu) = \left[\frac{nP(k,\mu)}{nP(k,\mu)+1}\right]^2 V_{\mathrm{survey}} \,, \tag{4.5.45}$$

where μ is the cosine of the angle between the vector mode $\vec{k}$ and the vector along the line of sight, and n is the galaxy number density (which is assumed to be constant throughout each of the redshift bins).

To perform the analysis, we divide the data in redshift bins of width $\Delta z = 0.1$ and cut the small-scale data at $k = 0.25\ h\ \mathrm{Mpc}^{-1}$ to avoid the highly non-linear

regime. The lowest wavenumber $k_{\rm min}$ (i.e. the largest scale) is chosen to be greater than $2\pi/\Delta V^{1/3}$, where ΔV represents the volume of the redshift shell. We note that using data in the non-linear regime requires numerical simulations of this model (see Chapter 5).

The real-space linear DM power spectrum $P_{\rm DM}$ is related to the linear redshift-space galaxy power spectrum $P_{\rm gg}$ by

$$P_{\rm gg}(k) = P_{\rm DM}(k)\,(b + \beta\,\mu^2)^2 \ , \tag{4.5.46}$$

where b is the bias relating galaxy to DM overdensities in real space [as in Eq. (4.5.34)] and β is the linear growth factor.

DESI is expected to cover 14,000 deg^2 of the sky in the redshift range $0.15 < z < 1.85$. We use the values of the bias given in Ref. [253] for the three types of DESI tracers, namely $b_{\rm ELG}(z)D(z) = 0.84$ for the Emission Line Galaxies (ELGs), $b_{\rm LRG}(z)D(z) = 1.7$ for the Luminous Red Galaxies (LRGs), and $b_{\rm QSO}(z)D(z) = 1.2$ for the high redshift quasars (QSOs). Here, $D(z)$ is the normalised growth factor, and both the bias and the growth factor are assumed to vary in each redshift bin accordingly to these expressions. To combine the Fisher matrices from the three DESI tracers, we use the multi-tracer technique of Ref. [254].

For the constant $\sigma_{{\rm DM}-\nu}$ scenario, we obtain a 1σ error on the u parameter of

$$\delta u^{\rm (DESI)} \simeq 3.7 \times 10^{-6} \ , \tag{4.5.47}$$

for the fiducial value of $u = 10^{-5}$. For $\sigma_{{\rm DM}-\nu} \propto T^2$, we obtain

$$\delta u_0^{\rm (DESI)} \simeq 4.4 \times 10^{-15} \ , \tag{4.5.48}$$

for the fiducial value of $u_0 = 10^{-14}$. Crucially, DESI will ensure a $\sim 2.5\sigma$ detection of DM–neutrino interactions if the strength of such a coupling is $u \simeq 10^{-5}$ (or a $\sim 2\sigma$ detection for $u_0 \simeq 10^{-14}$ if $\sigma_{{\rm DM}-\nu} \propto T^2$).

The main results of this section are summarised in Fig. 4.8. We show the DESI allowed regions in orange (assuming the *Planck* 2015 fiducial cosmology plus an interaction strength of $u = 10^{-5}$ if constant and $u_0 = 10^{-14}$ if T^2-dependent), along with the current constraints in blue, and the COrE+ reconstruction in purple.

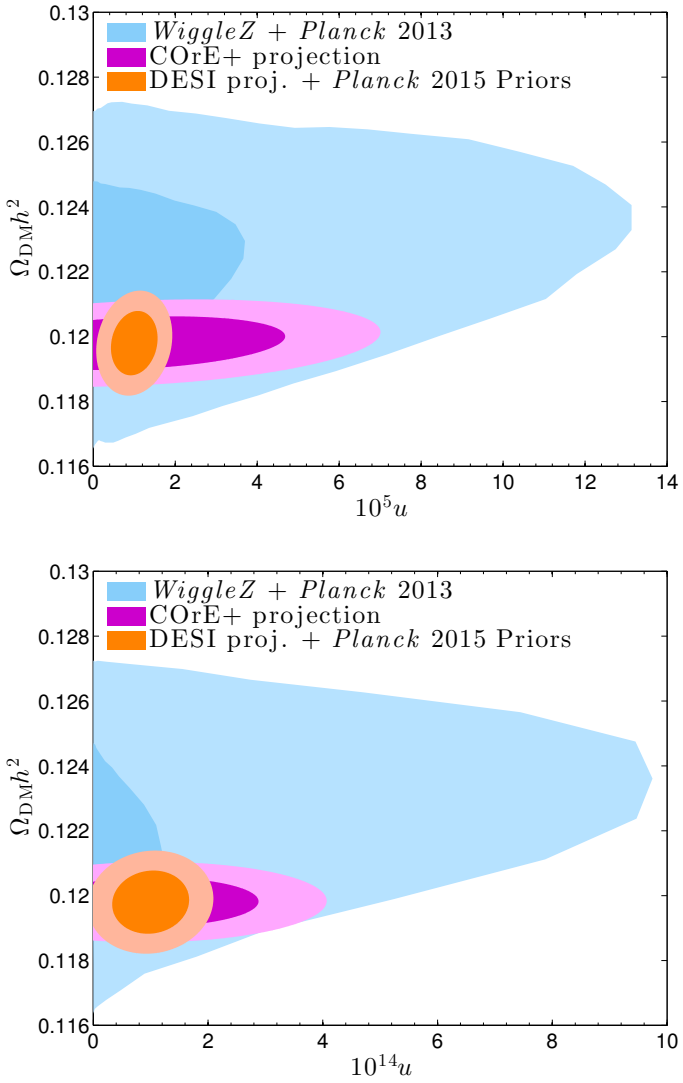

Figure 4.8: The 68% and 95% CL allowed regions in the ($\Omega_{\rm DM}h^2$,u_0) plane for the constant (top) and T^2-dependent (bottom) scenarios. Blue: current constraints from the combination of *WiggleZ* and *Planck* 2013 data, with $k_{\rm max} = 0.12\ h\ {\rm Mpc}^{-1}$. Magenta: projected sensitivity of the upcoming COrE+ CMB experiment, assuming $u = 10^{-5}$ (or $u_0 = 10^{-14}$ if T^2-dependent). Orange: projected sensitivity of the DESI galaxy survey, again assuming $u = 10^{-5}$ (or $u_0 = 10^{-14}$ if T^2-dependent), with $k_{\rm max} = 0.25\ h\ {\rm Mpc}^{-1}$.

One can clearly see the improvement in the extraction of a DM–neutrino coupling that will be provided by the next-generation LSS surveys. Furthermore, our analysis indicates that planned galaxy clustering surveys will provide an extremely powerful tool (competitive or even better than future CMB experiments) to test the fundamental properties of DM.

Since the main impact of νCDM is the damping of structure on small scales,

one of the largest effects will be a reduction in the number of satellites around galaxies such as the Milky Way. Until now, the only way to study interactions at these scales has been via N-body simulations, which show that for DM–radiation couplings greater than $u \simeq 10^{-5}$, the number of satellites in the Milky Way would be much smaller than observed (see Chapter 5). Therefore, with the sensitivity of $u \simeq 3.7 \times 10^{-6}$ expected from DESI, we would have a handle on alternative scenarios to ΛCDM that modify our cosmic neighbourhood, independently of the assumptions that go into N-body simulations.

One potential caveat is that we have assumed the interacting DM species accounts for the entire DM component of the universe; if more than one species were responsible for the observed relic density (see e.g. Ref. [187]), larger DM–neutrino scattering cross sections would be allowed by both CMB and LSS data (see for example, Fig. 4.9).

Aside: Mixed Damping

For DM–neutrino scattering, there is a further potential source of small-scale suppression from "mixed damping", in which DM is coupled to free-streaming neutrinos [162]. The corresponding mixed damping length is given by

$$l_{\rm md}^2 \propto \int_{t_{\rm dec}(\nu)}^{t_{\rm dec(DM-\nu)}} \frac{\rho_\nu\, c^2}{\rho\, H\, a^2}\, {\rm d}t \sim \left(\frac{c\,t}{a}\right)^2 |_{t_{\rm dec(DM-\nu)}} \,, \tag{4.5.49}$$

which requires that $t_{\rm dec(DM-\nu)} > t_{\rm dec(\nu)}$, or equivalently, $T_{\rm dec(\nu)} > T_{\rm dec(DM-\nu)}$ (see Ref. [162] for the derivation). If one also imposes that neutrinos decouple at $\mathcal{O}(1)$ MeV, as in the standard scenario, the condition for mixed damping becomes: $T_{\rm dec(\nu-DM)} > \mathcal{O}(1)$ MeV $> T_{\rm dec(DM-\nu)}$.

Noting that $\Gamma_{\nu-{\rm DM}} \simeq \sigma_{\nu-{\rm DM}}\, c\, n_{\rm DM}$ and $\Gamma_{{\rm DM}-\nu} \simeq \sigma_{\nu-{\rm DM}}\, c\, (T/m_{\rm DM})\, n_\nu$ [163–165], one obtains

$$T_{\rm dec(\nu-DM)} \simeq \frac{0.02}{u}\ {\rm eV}\ , \qquad T_{\rm dec(DM-\nu)} \simeq \frac{0.3}{\sqrt{u}}\ {\rm eV}\ , \tag{4.5.50}$$

assuming a constant DM–neutrino scattering cross section.

Since mixed damping can only take place after the neutrinos have fully decoupled, the relevant temperature range is

$$\mathcal{O}(1)\ {\rm MeV} \gtrsim T \gtrsim \frac{0.3}{\sqrt{u}}\ {\rm eV}\ , \tag{4.5.51}$$

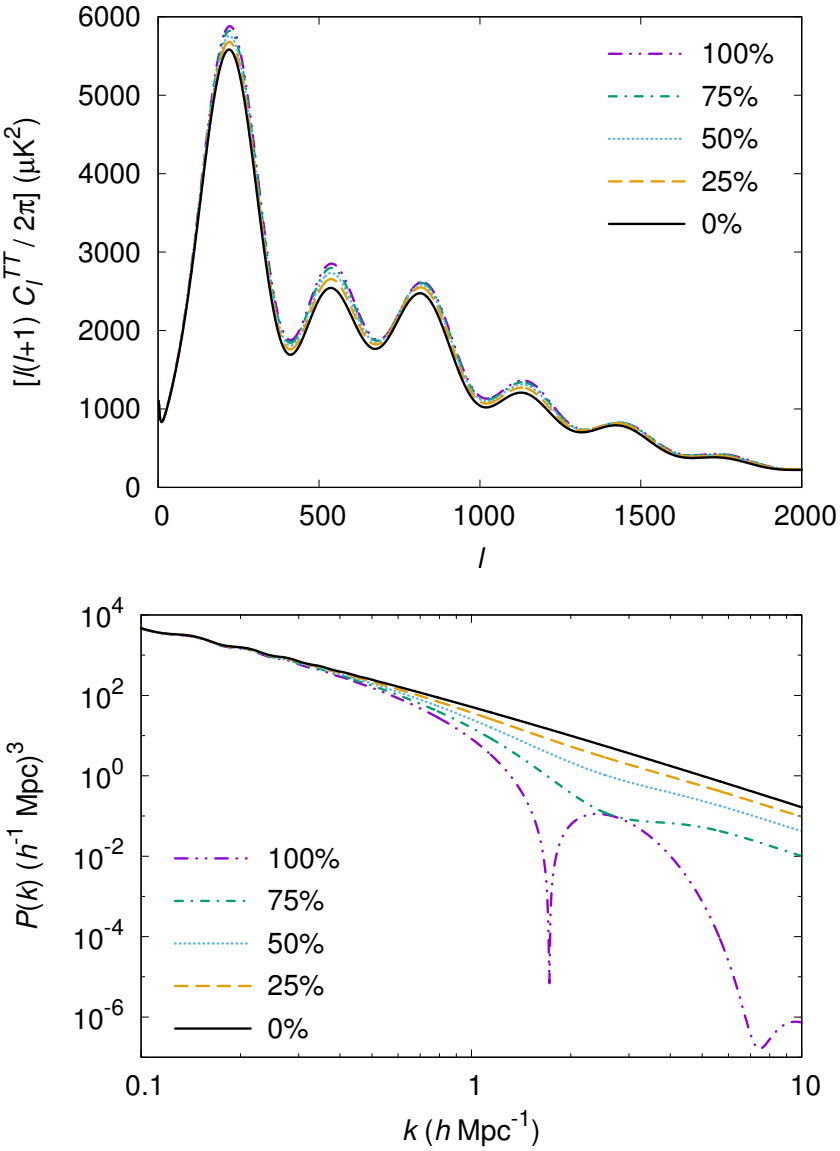

Figure 4.9: Top: the CMB angular power spectrum in the case that only a given fraction of DM interacts with neutrinos, where for the interacting DM component, $u = 10^{-2}$. Bottom: the linear matter power spectrum in the case that only a given fraction of DM interacts with neutrinos, where for the interacting DM component, $u = 10^{-4}$. In each case, we assume $\sigma_{\mathrm{DM}-\nu}$ is constant and use the '*Planck* + WP' best-fit parameters from Ref. [10].

and the requirement for mixed damping is

$$9 \times 10^{-14} \lesssim u \lesssim 2 \times 10^{-8} \ , \tag{4.5.52}$$

as summarised in Fig. 4.10. Work is ongoing to determine the importance of mixed damping when one introduces a DM–neutrino coupling. However, a comprehensive Boltzmann code implementation will be required (see e.g. Ref. [255]).

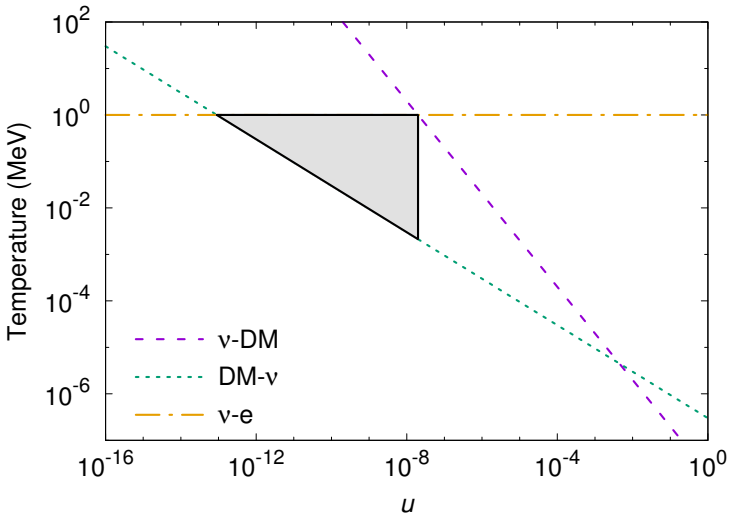

Figure 4.10: The temperature range corresponding to mixed damping as a function of the DM–neutrino scattering parameter u (grey shaded region), assuming $\sigma_{\mathrm{DM}-\nu}$ is constant. The three lines correspond to the neutrino–DM (purple, dashed), DM–neutrino (green, dotted), and neutrino–electron (orange, dashed-dotted) decoupling temperatures. Mixed damping is only possible if $9 \times 10^{-14} \lesssim u \lesssim 2 \times 10^{-8}$. The upper limit arises from the requirement that neutrinos fully decouple at $\mathcal{O}(1)$ MeV, while for small values of u, DM decouples from neutrinos before the latter are free-streaming.

4.6 Conclusion

Cosmology provides a promising tool to measure the particle properties of dark matter (DM). A DM coupling to visible or dark radiation (including neutrinos, axions, dark photons or any other light uncharged particle) can lead to strong departures from ΛCDM, and produce visible signatures for cosmic microwave background (CMB) experiments and large-scale structure (LSS) surveys.

In the specific case of DM–neutrino scattering, one obtains an enhancement of the CMB acoustic peaks due to the fact that DM is strongly coupled to neutrinos and vice versa, which delays the neutrino free-streaming epoch and alters DM clustering with respect to ΛCDM. However, the largest impact is imprinted as a damping in the matter power spectrum, which is surveyed by LSS galaxy surveys.

In this chapter, we have looked for the optimal method to measure such small departures from ΛCDM. As cosmological data may constitute the only tool available to detect such effects, it is crucial to study the potential sensitivity of

future experiments. We have shown that with current CMB measurements from *Planck*, one can probe constant and T^2-dependent DM–neutrino cross sections of $\sigma_{\mathrm{DM}-\nu} \lesssim 6 \times 10^{-31}\,(m_{\mathrm{DM}}/\mathrm{GeV})\ \mathrm{cm}^2$ and $\sigma_{\mathrm{DM}-\nu,0} \lesssim 2 \times 10^{-40}\,(m_{\mathrm{DM}}/\mathrm{GeV})\ \mathrm{cm}^2$, respectively[8] (at 95% CL). By simulating a next-generation CMB experiment (i.e. a COrE+-like mission) by means of a Markov Chain Monte Carlo (MCMC) analysis, we found that one could only weakly improve on the current sensitivity.

Such constraints are importantly model-independent and can be applied to any theory beyond the Standard Model that predicts a coupling between DM and neutrinos. In particular, we found that models involving thermal MeV DM and a constant scattering cross section can accommodate larger values of N_{eff} and H_0 with respect to ΛCDM, produce a cut-off in the matter power spectrum at the Lyman-α scale, and at the same time, generate small neutrino masses.

The prospects for both constraints and detection are far better for future galaxy surveys, such as the DESI or Euclid experiments. Already, current LSS data, combined with *Planck* CMB measurements, provide competitive constraints to those forecast for a future CMB experiment such as COrE+. Future data from the DESI experiment alone could improve the current sensitivity limit by an order of magnitude, and provide an accurate (percent-level) measurement of the scattering cross section for values above that limit.

An interesting question is whether future LSS data would be able to distinguish the $P(k)$ for DM–neutrino scattering (Fig. 4.5) and DM–photon scattering (Fig. 3.7). In particular, the greater number of oscillations for DM–photon scattering could be used to discriminate between the two types of interaction. However, because the power is already significantly reduced with respect to ΛCDM by the second oscillation (by at least two orders of magnitude), the difference in LSS data would be marginal.

In this chapter, we have shown that galaxy clustering surveys are an excellent probe to detect physics beyond ΛCDM. Remarkably, future LSS experiments will be sensitive to effects that until now have only been accessible via N-body simulations.

[8]Note that these *Planck* CMB constraints are about 3 and 10 times stronger than those obtained in Chapter 3 for DM–photon scattering, for constant and T^2-dependent cross sections, respectively.

Chapter 5

Interacting Dark Matter and Structure Formation

There are only two problems with ΛCDM: Λ and CDM.

— Tom Shanks

5.1 Introduction

As we saw in Chapter 1, the cold dark matter (CDM) model has been remarkably successful at explaining a wide range of observations, from the cosmic microwave background (CMB) radiation to the large-scale structure (LSS) of the universe [256]. However, in its simplest form, the model faces persistent challenges on small scales; the most pressing of which are the "missing satellite" [79, 80] and "too big to fail" [81] problems[1]. These discrepancies may indicate the need to consider a richer physics phenomenology in the dark sector (although they were first stated without the inclusion of baryonic physics).

In the standard cosmological picture, galaxies such as the Milky Way (MW) and Andromeda (M31) are embedded in DM haloes that extend far beyond the extent of their visible matter. Such galaxies are typically orbited by smaller "satellite"

[1]DM halo profiles for dwarf galaxies are also less cuspy than predicted by the standard CDM model (the so-called "cusp vs. core" problem [257]), although this is still under debate [78].

galaxies, each residing in their own DM subhaloes. This comparison between theory and observation requires a connection to be made between subhaloes and galaxies; in the absence of a good model for galaxy formation, this is most readily done using the halo orbital or "circular" velocity.

The "missing satellite" problem refers to the overabundance of DM subhaloes in numerical simulations of MW-like haloes, compared to the observed number of MW satellite galaxies (see Fig. 5.1). The problem persists even with the recent discoveries of additional fainter satellite galaxies within the MW halo (see e.g. Refs. [258, 259]). However, subsequent simulations that have taken into account baryonic physics suggest that a reduction in the efficiency of galaxy formation in low-mass DM haloes results in many of the excess subhaloes containing either no galaxy at all or a galaxy that is too faint to be observed [260–263].

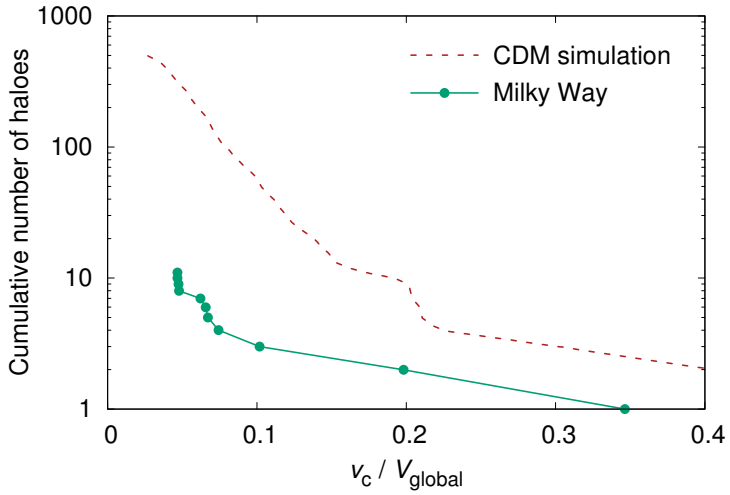

Figure 5.1: The observed abundance of MW satellite galaxies (green, solid curve with data points), compared to the number of subhaloes in numerical simulations of collisionless CDM (red, dashed curve) [79]. The abundance is plotted as a function of the circular velocity v_c, divided by the circular velocity of the parent halo $V_{\rm global}$. Taken at face value, CDM simulations predict a significant overabundance of subhaloes, with respect to the observed number of MW satellites.

As the resolution of numerical simulations continued to improve, the "too big to fail" problem emerged [81] (see Fig. 5.2). This concerns the largest subhaloes, which should be sufficiently massive that their ability to form a galaxy is not hampered by heating of the intergalactic medium via photoionisation, or heating of the interstellar

medium via supernovae. However, in simulations of collisionless CDM, the largest subhaloes are denser and more massive than is inferred from measurements of the MW satellite rotation curves.

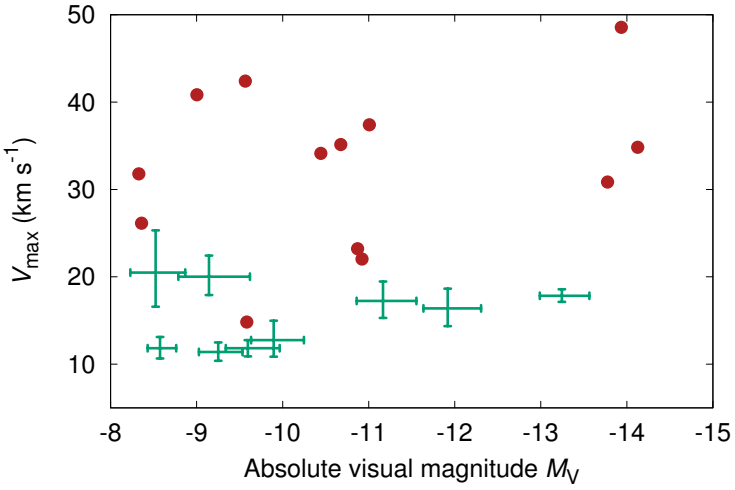

Figure 5.2: The maximum circular velocity $V_{\rm max} \equiv \max[(GM/R)^{1/2}]$ for the nine luminous MW dwarf spheroidal galaxies (green error bars), compared to the most massive subhaloes from numerical simulations of collisionless CDM (red circles), as a function of the absolute visual magnitude $M_{\rm V}$ [264]. Neglecting the impact of baryonic physics, the simulated subhaloes are generally more massive (i.e. have larger values of $V_{\rm max}$) than the observed dwarf spheroidal galaxies.

It is important to note that the severity of the small-scale problems can be reduced if one considers the mass of the MW, which impacts the selection of MW-like haloes in the simulations but remains difficult to determine [265–268].

A range of alternatives to collisionless CDM have also been proposed e.g. warm DM (WDM) [269], interacting DM [162–165, 226, 270], self-interacting DM [229, 271–273], decaying DM [274], and late-forming DM [275]. These "beyond CDM" models generally exhibit a cut-off in the linear matter power spectrum $P(k)$ at small scales (high wavenumbers) that translates into a reduced number of low-mass DM haloes, with respect to collisionless CDM, at late times.

In the WDM scenario, one allows a small (but non-negligible) amount of free-streaming, which can greatly reduce the expected number of small-scale structures with respect to CDM [276]. Given that the free-streaming scale for a DM particle is typically governed by its mass and velocity distribution [see Eq. (1.2.20)], the proposed WDM models require very light ($\sim$ keV) particles.

However, recent work suggests that such light particles cannot simultaneously solve the small-scale problems of CDM and satisfy the mass constraints from the Lyman-α forest and other observations [184, 277].

Most numerical efforts so far to check whether such beyond CDM models can solve the small-scale problems have focussed on either WDM or self-interacting DM. However, it is also possible that DM scattered elastically with Standard Model (SM) particles in the early universe; for example, with photons (γCDM) (see Chapter 3), neutrinos (νCDM) (see Chapter 4), and baryons [191–193].

Such elastic scattering processes are intimately related to the DM annihilation mechanism in the early universe and are thus directly connected to the DM relic abundance in scenarios where DM is a thermal weakly-interacting massive particle (WIMP; see Sec. 1.3). Therefore, rather than being viewed as exotica, interactions between DM and SM particles should be considered as a more realistic realisation of the CDM model. Indeed, instead of assuming that CDM has no interactions beyond gravity, one can actually test this assumption by determining their impact on the $P(k)$ and ruling out values of the cross section that are in contradiction with observations. However, it should be noted that the strength of the scattering and annihilation cross sections can differ by several orders of magnitude, depending on the particle physics model.

While the CDM matter power spectrum predicts the existence of structures at all scales (down to earth mass haloes [278, 279]), the γCDM and νCDM scenarios are characterised by the collisional damping of primordial fluctuations, which can lead to a suppression of small-scale power at late times. The collisional damping scale is determined by a single model-independent parameter: the ratio of the scattering cross section to the DM mass. The larger the ratio, the larger the suppression of the $P(k)$. For allowed models, the suppression occurs for haloes with masses below $10^8 - 10^9\ M_\odot$ (see Chapters 3 and 4).

For simplicity, we focus here on the γCDM model with a constant (temperature-independent) elastic scattering cross section, bearing in mind that similar results are expected for νCDM and temperature-dependent scenarios. We also assume that the interacting DM species accounts for the entire observed relic abundance.

The formalism discussed in Chapter 3 provides an accurate estimate of the collisional damping scale for DM–photon interactions [162, 165]:

$$l_{\mathrm{cd},\gamma}^2 \sim \int_0^{t_{\mathrm{dec}(\mathrm{DM}-\gamma)}} \frac{\rho_\gamma\, v_\gamma^2}{\rho\, \Gamma_\gamma\, a^2}\, \mathrm{d}t \ , \tag{5.1.1}$$

where ρ_γ and v_γ are the photon energy density and velocity, respectively, ρ is the total energy density, Γ_γ is the total photon interaction rate (including all species in thermal equilibrium with photons) and a is the cosmological scale factor.

Eq. (5.1.1) illustrates why interactions with photons can lead to the suppression of power that is needed to tackle the small-scale problems of CDM. In the early universe, photons constituted a large fraction of the energy density, and one can set $v_\gamma = c$. Hence, the numerator in Eq. (5.1.1) is large and fluctuations can be erased on the scale of small galaxies.

In Chapter 3, we computed the consequences of DM interactions with photons in the linear regime. The $P(k)$ for γCDM is damped relative to that of collisionless CDM beyond a scale that depends on the interaction cross section (see Fig. 5.3). This is similar to the damping seen in WDM, except that in this case, instead of an exponential suppression, one obtains a series of oscillations with a power law modulation in their amplitude [163]. We can directly compare the predictions of WDM and γCDM by selecting particle masses m_{WDM} and interaction cross sections $\sigma_{\mathrm{DM}-\gamma}$ that produce damping at a similar wavenumber, relative to collisionless CDM (see the green, dotted curve and the orange, dashed curve in Fig. 5.3).

For γCDM, the comparison with CMB data from *Planck* [10] gave a constraint on the elastic scattering cross section of $\sigma_{\mathrm{DM}-\gamma} \lesssim 10^{-6}\ \sigma_{\mathrm{Th}}\,(m_{\mathrm{DM}}/\mathrm{GeV})$ at 95% CL, where σ_{Th} is the Thomson cross section and m_{DM} is the DM mass. However, this linear approach breaks down once the fluctuations become large, preventing one from studying the effects of weak-strength interactions on DM haloes and in particular, on small-scale objects. We therefore turn to N-body simulations to examine the impact of γCDM in the non-linear regime. We will show that interacting DM can alleviate both the missing satellite and too big to fail problems[2].

[2]Recently, it was also demonstrated that one can simultaneously alleviate the small-scale problems of CDM by including interactions between DM and dark radiation in the linear $P(k)$

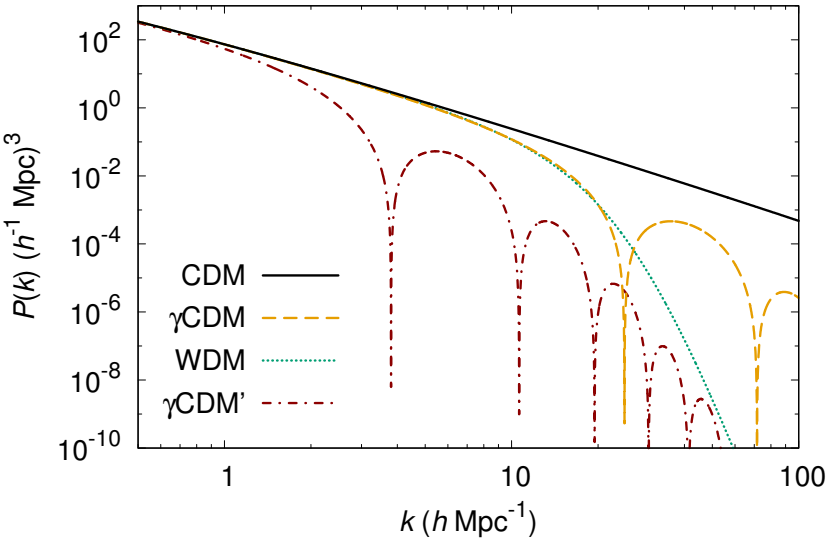

Figure 5.3: The linear matter power spectra for collisionless CDM (black, solid), γCDM with $\sigma_{\mathrm{DM}-\gamma} = 2 \times 10^{-9}\ \sigma_{\mathrm{Th}}\,(m_{\mathrm{DM}}/\mathrm{GeV})$ (orange, dashed), WDM with $m_{\mathrm{WDM}} = 1.24$ keV (green, dotted) and γCDM' with $\sigma_{\mathrm{DM}-\gamma} = 10^{-7}\ \sigma_{\mathrm{Th}}\,(m_{\mathrm{DM}}/\mathrm{GeV})$ (red, dashed-dotted). The γCDM and WDM models have been selected to have the same initial cut-off in the $P(k)$ with respect to CDM. We take $\sigma_{\mathrm{DM}-\gamma}$ to be constant and use the best-fitting cosmological parameters from *Planck* [10].

The chapter is organised as follows. In Sec. 5.2, we describe the simulations that we use to study the missing satellite problem, and derive constraints from the observed abundance of MW satellite galaxies. In Sec. 5.3, we investigate whether interacting DM can alleviate the too big to fail problem by considering the largest subhaloes. Finally, we provide conclusions in Sec. 5.4.

This chapter is based on the work carried out in Refs. [4–6].

5.2 Missing Satellite Problem and Constraints

5.2.1 Simulation Details

To study the impact of DM–photon interactions on the abundance of small structures, we begin our N-body calculations at a sufficiently early epoch (redshift $z = 49$), where the effect of γCDM is fully described by linear perturbation theory (LPT). We note that the DM–photon interaction rate is negligible for $z < 49$. The

and DM self-interactions during non-linear structure formation [280, 281].

initial matter power spectra for CDM, γCDM, WDM and γCDM' (shown in Fig. 5.3) are obtained from the modified version of the Boltzmann code CLASS [48], as described in Sec. 3.2.2, using the best-fitting cosmological parameters from *Planck*[3] [10]. Initial conditions are created using an adapted version of a second-order LPT code.

To make predictions in the non-linear regime, we run a suite of high-resolution N-body simulations using the code GADGET-3 [282]. To provide a suitable dynamical range, we perform simulations in both a large box (100 h^{-1} Mpc, 512^3 particles) and a high-resolution small box (30 h^{-1} Mpc, 1024^3 particles). A subset of simulations is re-run in a high-resolution large box (100 h^{-1} Mpc, 1024^3 particles) to confirm the convergence scale. By comparing the results from different runs, we find that our calculations are reliable for subhaloes with $V_{\rm max} \equiv \max[(GM/R)^{1/2}] \gtrsim 8$ km s^{-1}. Gravitational softening is set to 5% of the mean particle separation. For WDM particles with masses larger than $\sim$ keV, the thermal velocities are sufficiently small that one can safely neglect free-streaming in the non-linear regime without introducing a significant error on the scales of interest [283].

To quantify the impact of γCDM on the satellite abundance of a MW-like galaxy, one needs to define criteria to select haloes that could host the MW. The most crucial condition is the DM halo mass. Motivated by calculations that attempt to reconstruct the MW mass distribution based on the measured kinematics of the observed satellites and stars [267, 284, 285], we consider DM haloes to be MW-like if their mass is in the range $(0.8 - 2.7) \times 10^{12}\, M_\odot$.

The second criterion we apply is based on the environment. The MW appears to be located in an unremarkable region away from larger structures such as the Virgo Cluster and the major filaments feeding the Centaurus Cluster [286]. We therefore reject candidates with similar-sized haloes[4] within a distance of 2 Mpc. The resulting

[3] In principle, one would require each value of the cross section to be studied within its own best-fitting cosmology; however, we find that the ΛCDM parameters lie within 1σ of such best fits. For simplicity, we therefore keep the cosmological parameters fixed for all the models studied here.

[4] This criterion prevents us from obtaining a MW-like candidate that is itself a satellite of a

sample of MW-like haloes is then divided into several subsets based on their virial halo mass. Haloes are identified using a friends-of-friends group finder [256] with a linking length of 20% of the mean particle separation. Finally, subhaloes are identified using SUBFIND [287].

5.2.2 Results

Fig. 5.4 shows the simulated distribution of DM in a MW-sized DM halo. For collisionless CDM (top-left panel), there is an overabundance of subhaloes within the DM halo, which illustrates the MW satellite problem (if one associates each of the subhaloes with a satellite galaxy). The bottom-left panel shows the same halo in a simulation of γCDM, in which the interaction cross section is $\sigma_{\mathrm{DM}-\gamma} = 2 \times 10^{-9}\ \sigma_{\mathrm{Th}}\,(m_{\mathrm{DM}}/\mathrm{GeV})$. Such a cross section should satisfy the constraints from the Lyman-α forest [184]. One can see that the subhalo population is significantly smaller for this model compared to CDM.

However, the suppression of subhaloes is too strong if we consider γCDM' with $\sigma_{\mathrm{DM}-\gamma} = 10^{-7}\ \sigma_{\mathrm{Th}}\,(m_{\mathrm{DM}}/\mathrm{GeV})$ (bottom-right panel), which satisfies the CMB limits from Chapter 3. Therefore, by adjusting the magnitude of the scattering cross section, not only is there scope to address the MW satellite problem, but we can also place a more stringent constraint on the γCDM interaction strength.

For the model of γCDM with $\sigma_{\mathrm{DM}-\gamma} = 2\times10^{-9}\ \sigma_{\mathrm{Th}}\,(m_{\mathrm{DM}}/\mathrm{GeV})$, the distribution of density fluctuations in the linear regime is comparable to that of a WDM particle with a mass of 1.24 keV (top-right panel). However, the suppression of small-scale power in γCDM is less extreme than in generic WDM models due to the presence of oscillations in the linear $P(k)$ (see Fig. 5.3), which may offer a way to distinguish these two scenarios.

For more quantitative estimates, the cumulative number of MW satellite galaxies $N_{>V_{\mathrm{max,sat}}}$ is plotted in Fig. 5.5 as a function of the maximal circular velocity $V_{\mathrm{max,sat}} \equiv \max[(GM/R)^{1/2}]$, which is selected as a measure for the mass

larger cluster, which is not the case for the MW. At the same time, it does not rule out slightly smaller galaxies in the vicinity of the candidate, such as an Andromeda-like companion.

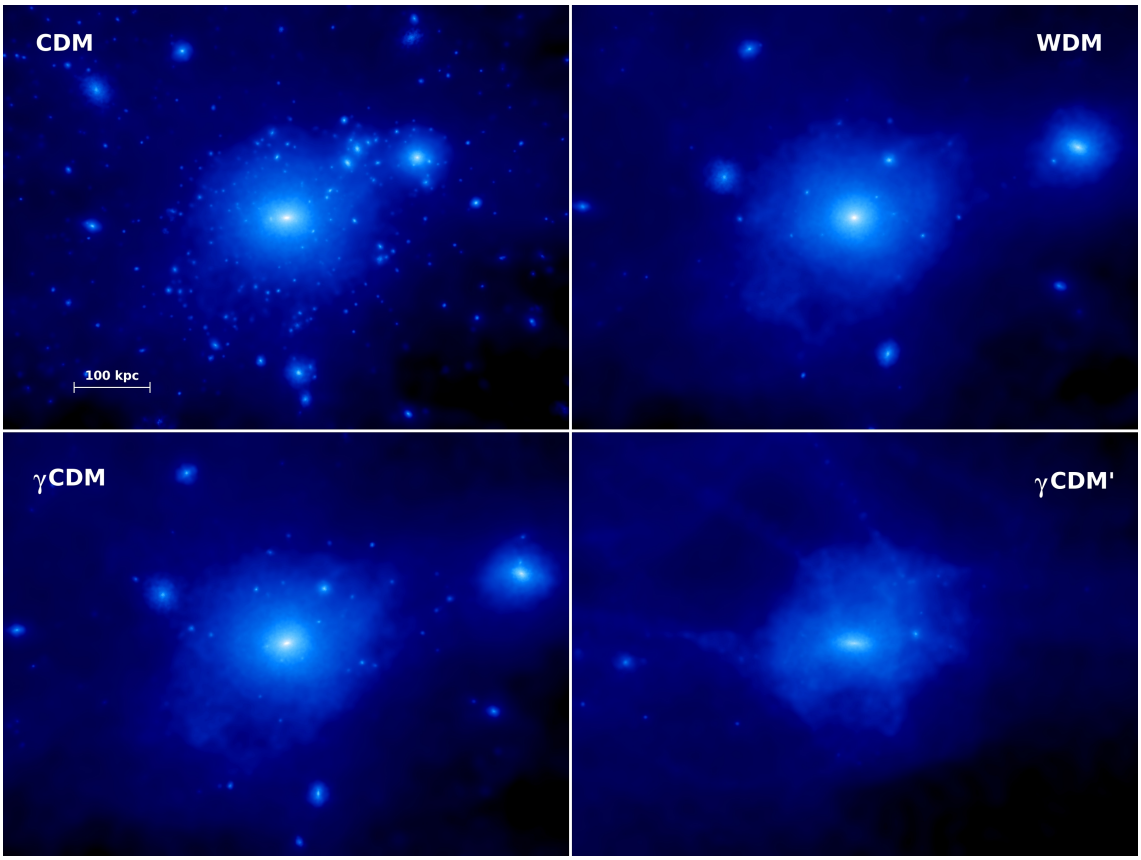

Figure 5.4: The simulated distribution of DM in a MW-like halo. The shading represents the DM density, with brighter colours indicating higher densities. The panels show the halo in simulations of different cosmological models: collisionless CDM (top left), γCDM (CDM plus DM–photon scattering) with $\sigma_{\mathrm{DM}-\gamma} = 2 \times 10^{-9}\ \sigma_{\mathrm{Th}}\,(m_{\mathrm{DM}}/\mathrm{GeV})$ (bottom left), the equivalent model of WDM with $m_{\mathrm{WDM}} = 1.24$ keV (top right), and γCDM' with $\sigma_{\mathrm{DM}-\gamma} = 10^{-7}\ \sigma_{\mathrm{Th}}\,(m_{\mathrm{DM}}/\mathrm{GeV})$ (bottom right).

and is determined directly from the simulations[5]. The simulation results are obtained by averaging over the haloes that satisfy the selection criteria outlined in Sec. 5.2.1. The number of selected MW-like haloes are 11, 13 and 3 for CDM, γCDM and γCDM', respectively.

The left-hand panel shows predictions for the collisionless CDM model, in which the number of subhaloes of a given maximum circular velocity greatly exceeds the observed number of MW satellites. The centre panel shows the results for γCDM

[5] $V_{\mathrm{max,sat}}$ is derived from the observed stellar line-of-sight velocity dispersion $\sigma_\star$ using the assumption that $V_{\mathrm{max}} = \sqrt{3}\,\sigma_\star$ [80].

with $\sigma_{\mathrm{DM}-\gamma} = 2\times10^{-9}\ \sigma_{\mathrm{Th}}\,(m_{\mathrm{DM}}/\mathrm{GeV})$, where there is a good match to the observed number of satellites. Thus, we see that γCDM with a relatively small cross section can alleviate the MW satellite problem. Finally, the right-hand panel of Fig. 5.5 shows the γCDM' model with $\sigma_{\mathrm{DM}-\gamma} = 10^{-7}\ \sigma_{\mathrm{Th}}\,(m_{\mathrm{DM}}/\mathrm{GeV})$. In this case, too many of the small structures have been erased. Note that the reduced scatter for γCDM' is simply a result of the limited statistics in this extreme model.

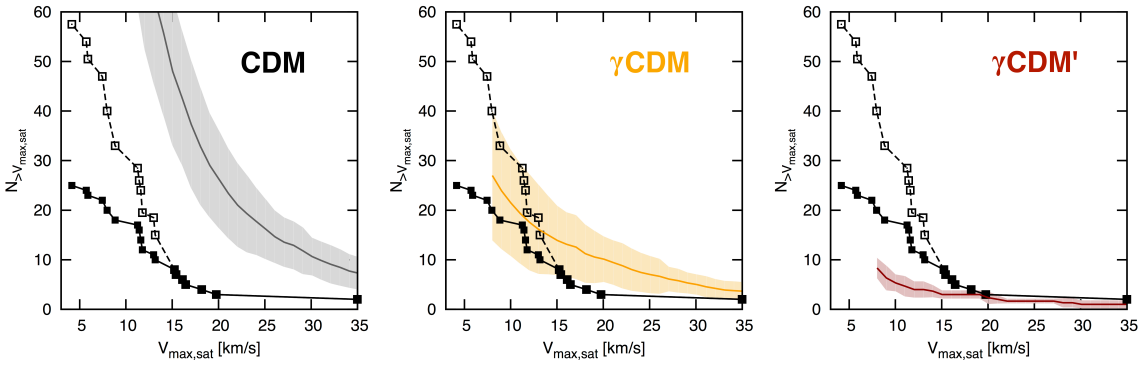

Figure 5.5: The cumulative number of satellite galaxies in a MW-like DM halo as a function of the maximal circular velocity for collisionless CDM (left), γCDM with $\sigma_{\mathrm{DM}-\gamma} = 2\times10^{-9}\ \sigma_{\mathrm{Th}}\,(m_{\mathrm{DM}}/\mathrm{GeV})$ (centre) and γCDM' with $\sigma_{\mathrm{DM}-\gamma} = 10^{-7}\ \sigma_{\mathrm{Th}}\,(m_{\mathrm{DM}}/\mathrm{GeV})$ (right). The lines and shading show the mean cumulative number counts of MW satellites for a simulated DM halo in the mass bin $(2.3-2.7)\times10^{12}\,M_{\odot}$ and the 1σ uncertainty, respectively. Also plotted are the observational results [288] (black, solid lines with data points), which are then corrected for the completeness of the Sloan Digital Sky Survey (SDSS) coverage (dashed lines).

We can also set constraints on the interaction cross section by comparing the observed and predicted numbers of substructures as follows. The uncertainties in the simulation results are derived from the spread in the sample set (for each host halo mass bin). A given model is ruled out if the number of predicted subhaloes is smaller than the observed number, within the combined uncertainties of these observables (see Fig. 5.6, left-hand panel). From this, we conclude that the DM–photon elastic scattering cross section cannot exceed

$$\begin{aligned}\sigma_{\mathrm{DM}-\gamma} &\simeq 5.5\times10^{-9}\ \sigma_{\mathrm{Th}}\ (m_{\mathrm{DM}}/\mathrm{GeV})\\ &\simeq 4\times10^{-33}\ (m_{\mathrm{DM}}/\mathrm{GeV})\ \mathrm{cm}^2\ ,\end{aligned}\tag{5.2.2}$$

at 95% CL. Here we have used the highest mass bin $(2.3-2.7)\times10^{12}\,M_{\odot}$, which provides us with the most conservative limit. Lower MW-like halo masses (see

Fig. 5.6, right-hand panel) result in stronger upper bounds on the cross section as these haloes host fewer satellites.

It should be noted that the observed value of $V_{\max}$ may be underestimated by our approach of directly calculating it from the stellar velocity dispersion [289]. Combined with an expected increase in the number of satellites from additional completeness corrections, this would lead to even stricter constraints on the interaction cross section.

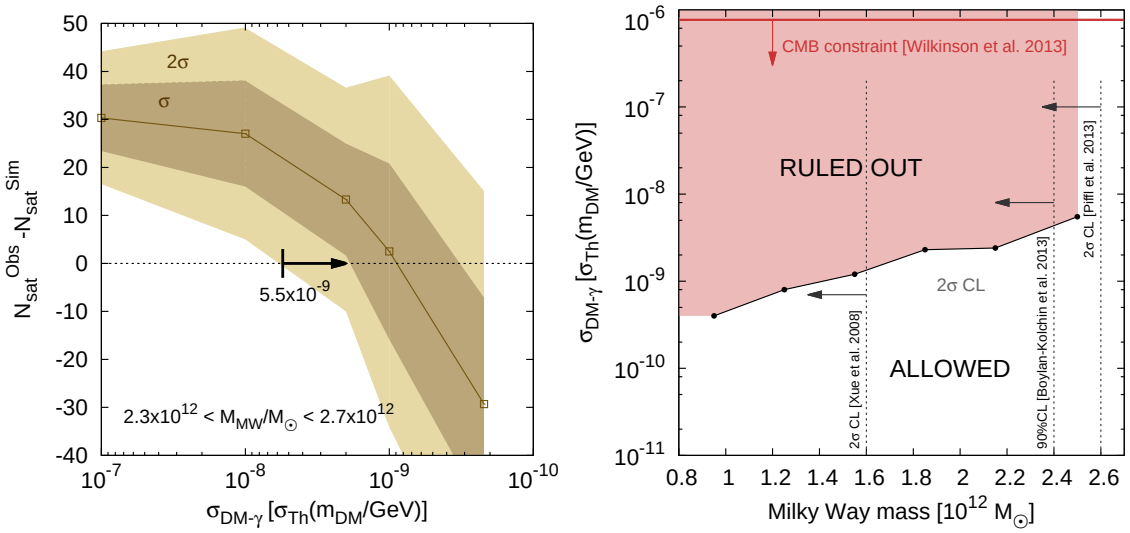

Figure 5.6: Constraints on the DM–photon elastic scattering cross section $\sigma_{\mathrm{DM}-\gamma}$. Left-hand panel: the over/underabundance of satellites versus the scattering cross section for the MW halo mass bin $(2.3 - 2.7) \times 10^{12}\, M_{\odot}$, where the coloured bands represent the 1σ and 2σ uncertainties. Right-hand panel: constraints on the cross section are plotted with respect to the MW halo mass. The most recent CMB constraint from *Planck* (see Chapter 3) and selected upper mass bounds for the MW DM halo [267, 284, 285] are shown for comparison.

5.3 Too Big To Fail Problem

5.3.1 Simulation Details

To reach the resolution required to model the dynamics of DM subhaloes within MW-like DM haloes, we first identify Local Group (LG) candidates[6] in an N-body simulation of a large cosmological volume. We then resimulate the region containing these haloes at much higher mass resolution in a "zoom" resimulation. We use the `DOVE` cosmological simulation to identify haloes for resimulation (the criteria used to select the haloes are listed below) [262]. The `DOVE` simulation follows the hierarchical clustering of the mass within a periodic cube of side length 100 Mpc, using particles of mass $8.8 \times 10^6\ M_\odot$ and assuming a WMAP7 cosmology[7].

Following the `APOSTLE` project [290], which also uses the `DOVE` CDM simulation to identify LG candidates for study at higher resolution, we impose the following three criteria to select candidates for resimulation:

1. **Mass:** there should be a pair of host haloes with masses comparable to the MW and M31, i.e. within the range $(0.5 - 2.5) \times 10^{12}\ M_\odot$.

2. **Environment:** there should be no other large structures nearby, i.e. an environment with an unperturbed Hubble flow out to 4 Mpc.

3. **Dynamics:** the separation between the two haloes should be 800 ± 200 kpc, with relative radial and tangential velocities below 250 km s^{-1} and 100 km s^{-1}, respectively.

These criteria are more restrictive than those employed in Sec. 5.2 as they also take into account the internal kinematics of the LG. After applying the above criteria, we obtain four LG candidates and therefore, eight MW-like haloes (see Table 5.1). If we assume that the gravitational interaction between the LG haloes is limited, the

[6]Here, the Local Group refers to the collection of galaxies that includes the MW, Andromeda (M31) and a large number of smaller dwarf galaxies.

[7]Using an older dataset here is not a concern since we are only interested in the impact of DM–photon interactions on a selected local environment.

ID	$M_{\rm vir}$ $[10^{12}\ M_\odot]$	$V_{\rm max}$ [km s^{-1}]	$\sigma_{\rm DM-\gamma}$ $[\sigma_{\rm Th}\ (m_{\rm DM}/{\rm GeV})]$
AP-1	1.916	200.3	$0,\ 2\times10^{-9}$
AP-2	1.273	151.5	
AP-3	0.987	157.9	$0,\ 2\times10^{-9}$
AP-4	0.991	163.0	
AP-5	2.010	167.5	$0,\ 2\times10^{-9}$
AP-6	1.934	165.1	
AP-7	1.716	163.7	$0,\ 10^{-10},\ 10^{-9},$
AP-8	1.558	193.3	$2\times10^{-9},\ 10^{-8}$

Table 5.1: Key properties of the MW-like haloes in the zoom resimulations (see Section 5.3.1). The first column specifies the `APOSTLE` identifier (ID) for each MW-like halo, while the second and third columns list the virial mass $M_{\rm vir}$ and maximum circular velocity $V_{\rm max}$, respectively (for the CDM model, although halo properties for γCDM only vary by a few percent with respect to CDM). The fourth column lists the various DM–photon interaction cross sections $\sigma_{\rm DM-\gamma}$ used in the zoom resimulations for each LG candidate, where $\sigma_{\rm Th}$ is the Thomson cross section and $\sigma_{\rm DM-\gamma}=0$ corresponds to collisionless CDM.

mass, environment and dynamics of the haloes would not be significantly different if we had run a separate γCDM version of the `DOVE` simulation.

We run resimulations for collisionless CDM (with zero interaction cross section) and for a selection of DM–photon interaction cross sections, as listed in Table 5.1. We note that the γCDM model with $\sigma_{\rm DM-\gamma}=2\times10^{-9}\ \sigma_{\rm Th}\ (m_{\rm DM}/{\rm GeV})$ was shown to solve the missing satellite problem in Sec. 5.2, in the absence of baryonic physics effects. For the γCDM model, we perform resimulations using the N-body code `P-Gadget3` [282], using the same cosmology (WMAP7), random phases and second-order LPT method [291] as Ref. [262]. We resimulate the four LG candidates with a particle mass $m_{\rm part}=7.2\times10^5\ M_\odot$ and a comoving softening length $l_{\rm soft}=216$ pc.

In addition, we resimulate the two host haloes for one of our LG candidates (AP-7/AP-8) at an even higher resolution ($m_{\rm part}=6\times10^4\ M_\odot$, $l_{\rm soft}=94$ pc). These simulations (denoted with the suffix `-HR`) are used to confirm that our results have converged and allow us to obtain more reliable predictions for the innermost region of the haloes. Finally, substructures within the host haloes are identified using the

AMIGA halo finder [292].

5.3.2 Results

The too big to fail problem is illustrated in the top panel of Fig. 5.7. Here the rotation curves of the 11 most massive subhaloes[8] in the CDM resimulation of the halo AP-7-HR (grey curves) clearly lie above the measurements of the MW dwarf spheroidal satellites [293] (black data points). In general, one can see that the largest subhaloes in CDM simulations have a higher circular velocity $V_{\rm circ}$, and therefore more enclosed DM, than is observed at a given radius. Meanwhile, for γCDM with $\sigma_{\rm DM-\gamma} = 2 \times 10^{-9}\ \sigma_{\rm Th}\ (m_{\rm DM}/{\rm GeV})$ (red curves), the rotation curves of the most massive satellites are shifted to lower circular velocities with respect to CDM, indicating that there is less DM enclosed within a given radius. One can interpret this as a lower central density of DM for γCDM haloes (as observed in Ref. [5]).

Note that the circular velocity profiles displayed in the top panel of Fig. 5.7 are plotted using different line styles. The transition occurs at the scale determined by the convergence criteria devised in Ref. [294]. At smaller radii (dashed lines), the velocity profiles are not guaranteed to have converged. However, the key point here is that the CDM and γCDM resimulations have the same resolution and yet show a clear difference at all radii plotted, with a shift to lower circular velocities for γCDM haloes.

The bottom panel of Fig. 5.7 presents a related view of the too big to fail problem; this time showing the peak velocity in the rotation curve $V_{\rm max} \equiv \max[(GM/R)^{1/2}]$ as a function of the radius at which this occurs $R_{\rm max}$. The hatched region indicates the 2σ uncertainty for the observed MW satellites, assuming that the haloes are DM-dominated and have NFW density profiles [295]. We allow the halo concentration parameter to vary, following the same technique and assumptions as described in Ref. [80].

[8] We have included three more simulated subhaloes than the observed number of dwarf satellites since the most massive subhaloes are considered statistical outliers like the Magellanic clouds, which have been omitted in this study.

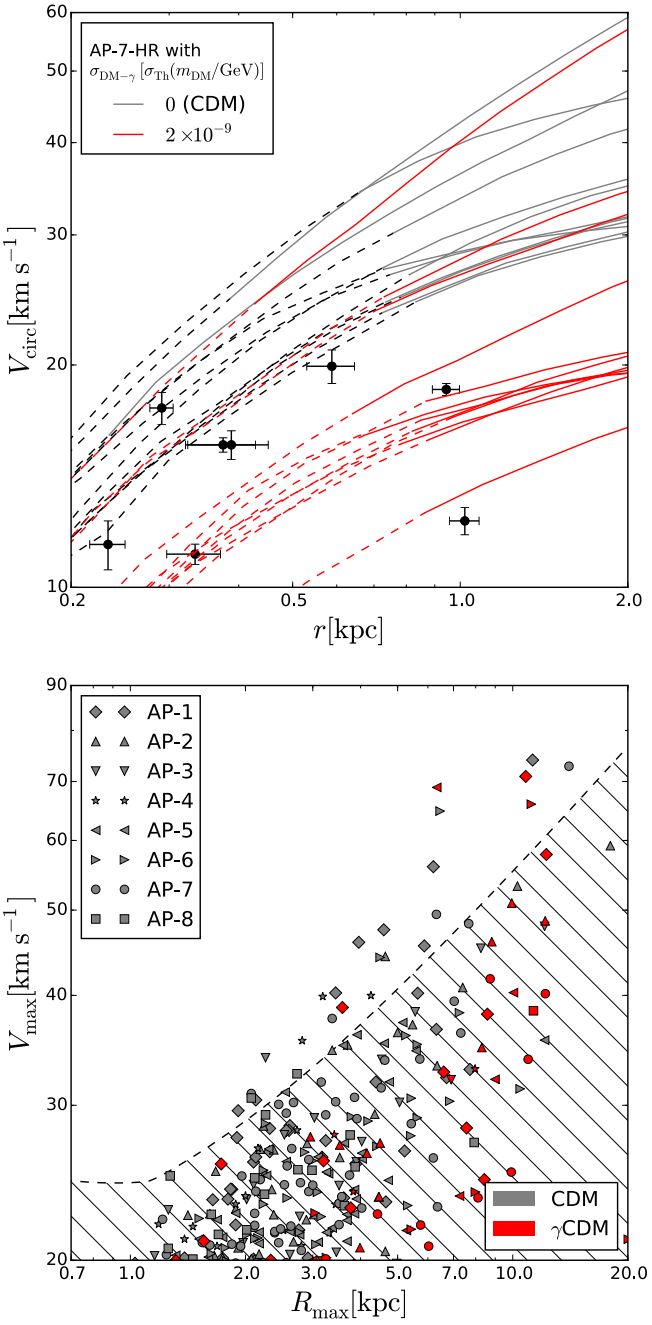

Figure 5.7: Top panel: the circular velocity $V_{\rm circ}$ versus radius r for the eleven most massive subhaloes in AP-7-HR, for collisionless CDM (grey curves) and γCDM with $\sigma_{\rm DM-\gamma} = 2 \times 10^{-9}\ \sigma_{\rm Th}\ (m_{\rm DM}/{\rm GeV})$ (red curves). The dashed lines indicate where $V_{\rm circ}$ can still be extracted from the simulations but convergence cannot be guaranteed, according to the criteria suggested in Ref. [294]. The black data points correspond to the observed MW satellites with 1σ error bars [293]. Bottom panel: the $V_{\rm max}$ versus $R_{\rm max}$ results for all eight MW-like haloes, with the same scattering cross sections as in the top panel. The hatched region marks the 2σ confidence interval for the observed MW satellites. Here, $V_{\rm max}$ is derived from the observed stellar line-of-sight velocity dispersion $\sigma_\star$ using the assumption that $V_{\rm max} = \sqrt{3}\,\sigma_\star$ [80].

In general, the collisionless CDM model predicts satellites that lie outside the 2σ range compatible with observations. Additionally, for CDM, there are many more subhaloes within the range of $V_{\rm max}$–$R_{\rm max}$ plotted than there are observed satellites. The abundance of massive, concentrated subhaloes varies depending on the mass and formation history of the host halo; however, for all of the MW-like candidates, CDM exhibits a too big to fail problem, which is reduced if one includes DM–photon interactions.

In Fig. 5.8, we present the results for AP-7 and AP-8 for a range of DM–photon scattering cross sections. As the cross section is increased, the predicted $V_{\rm max}$ values decrease and shift to larger $R_{\rm max}$. This brings the model predictions well within the region compatible with the observational results and also reduces the number of satellites with such rotation curves. Therefore, one can clearly see that interacting DM can alleviate the too big to fail problem with a cross section $\sigma_{\rm DM-\gamma} \simeq 10^{-9}\ \sigma_{\rm Th}\ (m_{\rm DM}/{\rm GeV})$ that we showed in Sec. 5.2 can also solve the missing satellite problem.

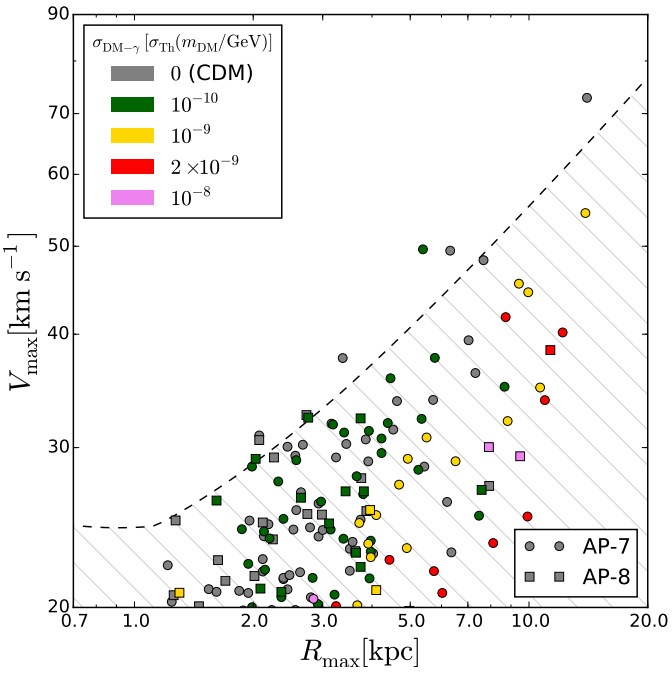

Figure 5.8: The $V_{\rm max}$ versus $R_{\rm max}$ results for the AP-7 (circles) and AP-8 (squares) haloes for a range of DM–photon interaction cross sections. As in Fig. 5.7, the hatched region marks the 2σ confidence interval for the observed MW satellites, following the methodology of Ref. [80].

5.4 Conclusion

There are a multitude of solutions that have been proposed to overcome the small-scale "failures" of cold dark matter (CDM); namely, the "missing satellite" and "too big to fail" problems. Within the collisionless CDM model, these explanations generally either: i) invoke baryonic physics to reduce the efficiency of galaxy formation in low-mass DM haloes [262, 296], or ii) exploit the uncertainty in the mass of the Milky Way (MW) DM halo [265]. Both problems can be diminished if one accounts for one or both of these possibilities.

However, solutions in which the DM properties are varied have also been explored. Ref. [276] showed that replacing CDM by a warm DM (WDM) particle of mass ~ 1.5 keV leads to a reduction in the abundance of subhaloes in MW-like haloes. In addition, massive subhaloes are less concentrated than their CDM counterparts, matching observations of the internal dynamics of the MW satellites. Ref. [273] investigated the impact of self-interacting DM on the properties of satellite galaxies, finding little change in the global properties of the galaxies but variation in their structure.

In this chapter, we have investigated the impact of interactions between DM and radiation on the abundance and structure of the MW satellite galaxies. Such interactions are well-motivated and may have helped to set the abundance of DM inferred in the universe today [94, 297]. As well as its physical basis, this model has the attraction that it is as simple to simulate as CDM. The interactions took place in the early universe when the densities of DM and radiation were much higher, and are negligible over the time period covered by the simulation. The DM particles are still cold, so there are no issues relating to particle velocity distributions, as would arise in high-resolution simulations of WDM, particularly for lighter candidates. The only change compared to a CDM simulation is the modification to the matter power spectrum in linear perturbation theory, i.e. DM–radiation interactions give rise to a series of damped oscillations on small scales.

By performing the first accurate cosmological simulations of DM interactions with radiation (in this case, photons), we find a new means to reduce the population of MW subhaloes, without the need to abandon CDM. The resulting constraints on

the interaction strength between DM and photons are orders of magnitude stronger than is possible from linear perturbation theory considerations.

We have also shown the impact of DM–radiation interactions on the structure of massive subhaloes. Increasing the interaction cross section reduces the mass enclosed within a given radius in the subhaloes, which alleviates the too big to fail problem. When combined with the reduction in the number of MW subhaloes, we find that a model with an elastic scattering cross section of $\sigma_{\mathrm{DM}-\gamma} \simeq 1 \times 10^{-33} \, (m_{\mathrm{DM}}/\mathrm{GeV}) \ \mathrm{cm}^2$ can solve both of the small-scale problems of CDM. We also note that similar results are expected in the case of DM–neutrino interactions.

The next step will be to include baryonic physics. Indeed, recent simulations with both DM and baryons have shown that such processes can alter the appearance of the subhalo mass function [263]. A definitive calculation would include the full impact of these effects; in particular, supernovae feedback and photoionisation heating of the interstellar medium. This would not alter the qualitative conclusions of this chapter, but would further tighten the constraints on the DM–radiation scattering cross section.

Chapter 6

Light WIMPs and the Galactic 511 keV Line

It doesn't matter how beautiful your theory is, it doesn't matter how smart you are. If it doesn't agree with experiment, it's wrong.

— Richard Feynman

6.1 Introduction

The emission of a 511 keV gamma-ray line from a spherically symmetric region around the Galactic centre has been observed by many experiments over more than four decades [115–120] (see Fig. 6.1). By 2003, INTEGRAL/SPI observations had demonstrated that this line originates from the decay of positronium atoms into two photons [298–301]. While this is indicative of an injection of low-energy positrons in the inner kiloparsec of the Milky Way, the signal is uncorrelated with known astrophysical sources. In addition to the "bulge", an extended disk-like structure is also seen. However, it is likely associated with radioactive β-decay of heavy elements produced in stars of the Milky Way disk.

Recently, an analysis of the 11-year data from INTEGRAL/SPI was carried out [302]. After a decade of exposure, the significance of the bulge signal has risen to 56σ, while the disk significance is now 12σ in a maximum likelihood fit. New data allow the collaboration to distinguish a broad bulge (BB) and an off-centre narrow

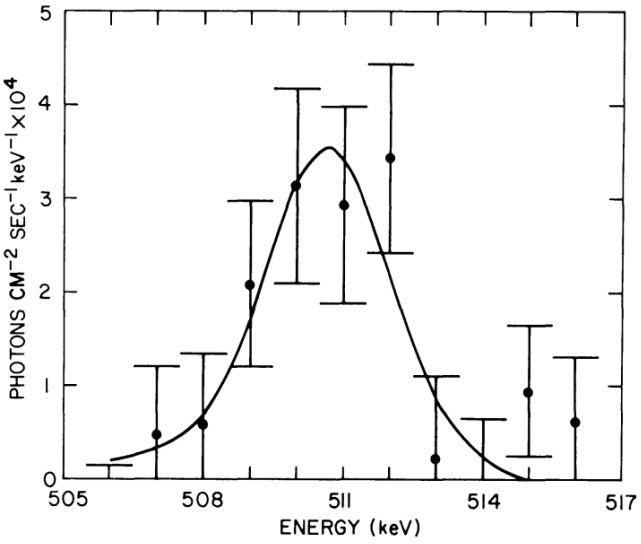

Figure 6.1: Differential photon spectrum measured from the Milky Way Galactic centre in the vicinity of 511 keV by a balloon-borne germanium gamma-ray telescope in 1978 [115]. The solid curve is a least-squares fit to the data (solid points with error bars). In this initial observation, the excess was centred on an energy of 510.7 ± 0.5 keV, with a flux of $(1.22 \pm 0.22) \times 10^{-3}$ photons cm^{-2} s^{-1} at the top of the atmosphere.

bulge (NB). There is also significant evidence (5σ) of a point source at the location of the Sgr A* black hole near the Galactic centre, with a line intensity that is about 10% of the total bulge (BB + NB) flux. Interestingly, greater exposure of the disk has revealed lower surface-brightness regions, leading to a more modest bulge-to-disk ratio of B/D $\sim$ 0.59, compared with previous results that indicated B/D $\sim$ 1–3.

Low mass X-ray binaries [303], pulsars and radioactive isotopes produced from stars, novae and supernovae [304] can yield positrons in the correct energy range for the bulge signal. However, these processes should yield a 511 keV morphology that is correlated with their progenitors' location. For instance, the β^+ decay of ^{26}Al produced in massive stars also yields a line at 1809 keV, which has been measured by INTEGRAL/SPI [305]. As expected, this line is not at all correlated with the Galactic centre 511 keV emission, although it allows up to 70% of the positronium formation in the Galactic disk to be explained [306]. Additionally, estimates of production and escape rates in stars and supernovae suggest that ^{44}Ti and ^{56}Ni β-decay can account for most of the remaining emissivity in the disk [299, 304]. Finally,

higher energy sources such as pulsars, magnetars and cosmic ray processes produce electron–positron ($e^{\pm}$) pairs in the bulge at relativistic energies. However, this would leave a distinct spectral shape above 511 keV, in conflict with the observed spectrum [304]. The fact therefore remains that the high luminosity of the total bulge emission is not explained by known mechanisms.

The similarity between the spherically symmetric, cuspy shape of the central bulge emission and the expected Galactic DM distribution is highly suggestive of a DM origin. Consequently, an interpretation in terms of self-annihilation of DM has been favoured for some time[1] [154, 155, 306–309]. The thermal production of DM through annihilation (as in the WIMP paradigm; see Sec. 1.3) implies ongoing self-annihilation today.

Light DM particles (with a mass $m_{\rm DM} \lesssim 7$ MeV) can produce electron-positron pairs at low enough energies to explain the positronium annihilation signal, while avoiding the overproduction of gamma-rays [307, 310, 311]. Initial studies could also reproduce the spatial shape of the excess with the standard NFW profile [Eq. (1.4.47)]. Later, it was shown that the less cuspy Einasto DM profile [Eq. (1.4.48)] yields a significantly better fit to the 511 keV line morphology. In fact, the Einasto shape gives a better fit to the 8-year data than the NB+BB model, with fewer free parameters [306].

The velocity-averaged annihilation cross section into $e^{\pm}$ pairs required to explain the observed 511 keV flux is $\langle \sigma v \rangle_{e^+e^-} \sim 10^{-30}$ cm^3 s^{-1}. However, a thermally-produced DM particle requires a cross section at freeze-out $\langle \sigma v \rangle \simeq 3 \times 10^{-26}$ cm^3 s^{-1}. The two scenarios that satisfy both requirements are:

1. **Neutrino (ν) sector**: a dominant annihilation cross section into neutrinos $\langle \sigma v \rangle_{\nu\nu} \simeq 3 \times 10^{-26}$ cm^3 s^{-1} at freeze-out.

2. **Electron ($e^{\pm}$) sector**: a velocity-dependent (p-wave) annihilation cross section into electrons $\langle \sigma v \rangle_{e^+e^-} = a + bv^2$, where the term $bv^2 \simeq 3 \times 10^{-26}$ cm^3 s^{-1} dominates at freeze-out.

[1] The spatial morphology disfavours a decaying DM origin [306, 307].

In this chapter, we show that these scenarios are strongly disfavoured by available cosmological data. We begin by presenting their respective impacts on cosmological observables in Secs. 6.2 and 6.3, from the epochs of BBN, recombination and the dark ages. In Sec. 6.4, we show that the latest CMB data and determinations of the primordial abundances rule out the light WIMP explanation of the 511 keV line for both NFW and Einasto DM density profiles. Finally, we provide conclusions in Sec. 6.5.

This chapter is based on the work carried out in Ref. [7].

6.2 Neutrino Sector Thermal Production

Thermal freeze-out requires annihilation into species with smaller masses than the DM particles. In the case of light DM (below the muon mass), this leaves three channels: electrons, photons or neutrinos. Annihilations into electrons and photons are highly constrained by gamma-ray [154] and CMB [312–326] observations. We therefore first consider the scenario in which the relic density originates via the neutrino channel and the subdominant annihilation rate into $e^{\pm}$ explains the 511 keV line.

6.2.1 BBN and Recombination

DM annihilations into neutrinos can increase the entropy in the neutrino sector if the DM particles are lighter than ~ 15 MeV and annihilate after the standard neutrino decoupling at $T_{\mathrm{dec},\nu} \simeq 2.3$ MeV [237–239, 327–329]. This increased energy density is parameterised in terms of the effective number of neutrino species N_{eff}. A larger neutrino energy density increases the expansion rate of the universe. If this occurs during BBN, the neutron-to-proton ratio freezes out earlier, leading to an increase in the primordial helium abundance Y_{P} and deuterium-to-hydrogen ratio D/H (see Sec. 1.2.1).

The same mechanism also results in additional energy in the radiation sector during recombination, again parameterised via N_{eff}. At such low temperatures ($T \ll$

$m_{\rm DM}$), one can write

$$N_{\rm eff}^{{\rm Equil},\nu} \simeq 3.046\left[1+\frac{g_{\rm DM}}{2}\frac{F(y_\nu|_{T_{{\rm dec},\nu}})}{3.046}\right]^{4/3}, \tag{6.2.1}$$

where

$$F(y) = \frac{30}{7\pi^4}\int_y^\infty d\xi\,\frac{(4\xi^2-y^2)\sqrt{\xi^2-y^2}}{e^\xi \pm 1}, \tag{6.2.2}$$

$g_{\rm DM}$ is the number of internal degrees of freedom for DM and $y_\nu|_{T_{{\rm dec},\nu}} \equiv m_{\rm DM}/T_{{\rm dec},\nu}$ [239]. The $+,-$ sign in Eq. (6.2.2) pertains to fermions and bosons, respectively.

The dependence of $N_{\rm eff}$ on the DM mass for two specific types of DM particle [real scalar ($g_{\rm DM}=1$) and Dirac fermion ($g_{\rm DM}=4$)] is illustrated in Fig. 6.2. The increase in $N_{\rm eff}$ enhances the effect of Silk damping and compounds the impact of a higher $Y_{\rm P}$ in reducing power in the tail of the CMB angular power spectrum.

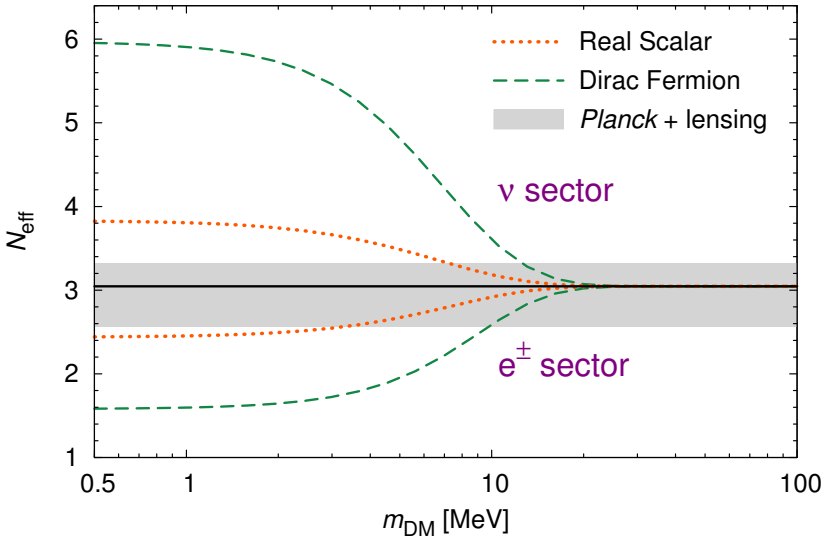

Figure 6.2: The number of relativistic degrees of freedom $N_{\rm eff}$ at the CMB epoch as a function of the DM mass $m_{\rm DM}$ for a real scalar (orange, dotted) and a Dirac fermion (green, dashed). For neutrino sector thermal production, the enhancement of $N_{\rm eff}$ is a result of DM annihilations reheating the neutrino sector, as described by Eq. (6.2.1). For electron sector production, the suppression of $N_{\rm eff}$ is due to DM annihilations into e^+e^- reheating the photon sector, as described by Eq. (6.3.5). The solid black line corresponds to the standard value of 3.046. Also shown is the 95% CL favoured region of $N_{\rm eff}$ from the '*Planck* + lensing' dataset (grey band) assuming ΛCDM, i.e. $N_{\rm eff} = 2.94 \pm 0.38$ [11]. Note that a complete MCMC analysis is required to derive constraints from such modifications to $N_{\rm eff}$ as there are well-known degeneracies with the other cosmological parameters.

Furthermore, DM–neutrino scattering during recombination can erase perturbations on small scales due to collisional damping [162–165]. It also prevents the neutrinos from free-streaming as efficiently, thus enhancing the CMB acoustic peaks (see Chapter 4). To account for DM–neutrino scattering, the coupled Euler equations that govern the evolution of the DM and neutrino fluid perturbations $\delta_{\mathrm{DM}/\nu}$ and their gradients $\theta_{\mathrm{DM}/\nu}$ must be modified to include interaction terms $\propto \sigma_{\mathrm{DM}-\nu}\,(\theta_{\mathrm{DM}} - \theta_\nu)$, where $\sigma_{\mathrm{DM}-\nu}$ is the elastic scattering cross section. The shear σ_ν and higher multipole perturbations $F_{\nu,\ell}$ of the neutrino fluid also acquire terms proportional to $\sigma_{\mathrm{DM}-\nu}$. The corresponding equations and the formalism to modify the Boltzmann code CLASS [48] are described in Chapter 4.

6.2.2 The Dark Ages

Independently of the neutrino sector, the subdominant s-wave annihilations into e^+e^- that are required to produce the Galactic 511 keV signal also have strong, observable consequences during the dark ages between the epochs of recombination and reionisation. These effects are measurable in the CMB angular power spectrum.

At a given redshift z, electromagnetic energy E is injected into the intergalactic medium (IGM) at a rate per unit volume V:

$$\frac{\mathrm{d}E}{\mathrm{d}t\,\mathrm{d}V} = f_{\mathrm{eff}}(m_{\mathrm{DM}})\;\rho_{\mathrm{crit}}^2\;(1+z)^6\;\Omega_{\mathrm{DM}}^2\;\zeta\;\frac{\langle\sigma v\rangle_{e^+e^-}}{m_{\mathrm{DM}}}\;, \tag{6.2.3}$$

where ρ_{crit} is the critical density, $\zeta = 1$ when the DM and its antiparticle are identical, and $1/2$ otherwise, and $f_{\mathrm{eff}}(m_{\mathrm{DM}})$ is the effective efficiency of energy deposition into heating and ionisation, weighted over redshift.

Fig. 6.3 shows the energy deposition efficiency $f_{\mathrm{eff}}(m_{\mathrm{DM}})$ as a function of m_{DM}. At the low masses relevant to the 511 keV signal, energy absorption in the IGM actually becomes quite inefficient, leading to weaker constraints than for heavier WIMPs. This is because much of the energy lost by electrons to inverse Compton scattering in this energy range ends up in photons that are below the 10.2 eV threshold to excite neutral hydrogen. These photons thus stream freely, leading to distortions of the CMB blackbody spectrum but no measurable effect on the ionisation of the IGM [330].

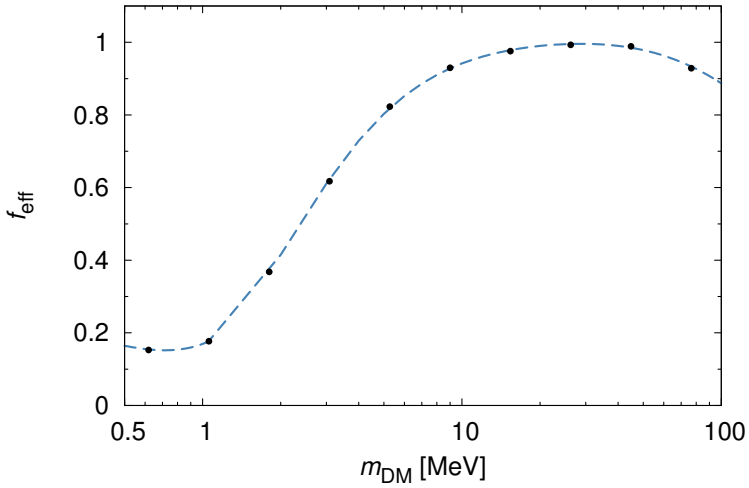

Figure 6.3: The effective energy deposition fraction for the smooth DM background component $f_{\rm eff}$ versus the DM mass $m_{\rm DM}$ for the e^+e^- annihilation channel. The points are taken from `nebel.rc.fas.harvard.edu/epsilon` [325].

Constraints on Eq. (6.2.3) are usually quoted in terms of the redshift-independent quantity

$$p_{\rm ann} \equiv f_{\rm eff}(m_{\rm DM}) \, \frac{\langle \sigma v \rangle_{e^+e^-}}{m_{\rm DM}} \, . \tag{6.2.4}$$

The effect of DM annihilations on the TT, EE and BB components of the CMB angular power spectrum is shown in Fig. 6.4 for large values of $p_{\rm ann}$. Such features can be explained if one considers the impact of DM annihilations on the evolution of the free electron fraction $x_{\rm e}$ from the early recombination era ($z \sim 1100$) to the reionisation epoch at late times ($z \lesssim 10$), see Fig. 6.5.

Firstly, extra electromagnetic energy from DM annihilations ionises the IGM. This ionisation rescatters CMB photons, leading to a broader last-scattering surface and a delay in recombination at $z \sim 1100$. In turn, this enhances $x_{\rm e}$ during the dark ages, with respect to the non-annihilating scenario (see Fig. 6.5). This increases the optical depth $\tau_{\rm reio}$ of the CMB photons as they travel from the last-scattering surface to us so that the visibility function $g(z) = \dot{\kappa}\, {\rm e}^{-\kappa}$, which describes the probability that a scattering process occurs, extends to smaller redshifts. As one can see from Fig. 6.4, there are two main effects on the CMB spectra: (i) a shift in the position of the acoustic peaks to lower ℓ, and (ii) an overall suppression of the spectra due to the broadening of the last-scattering surface [322].

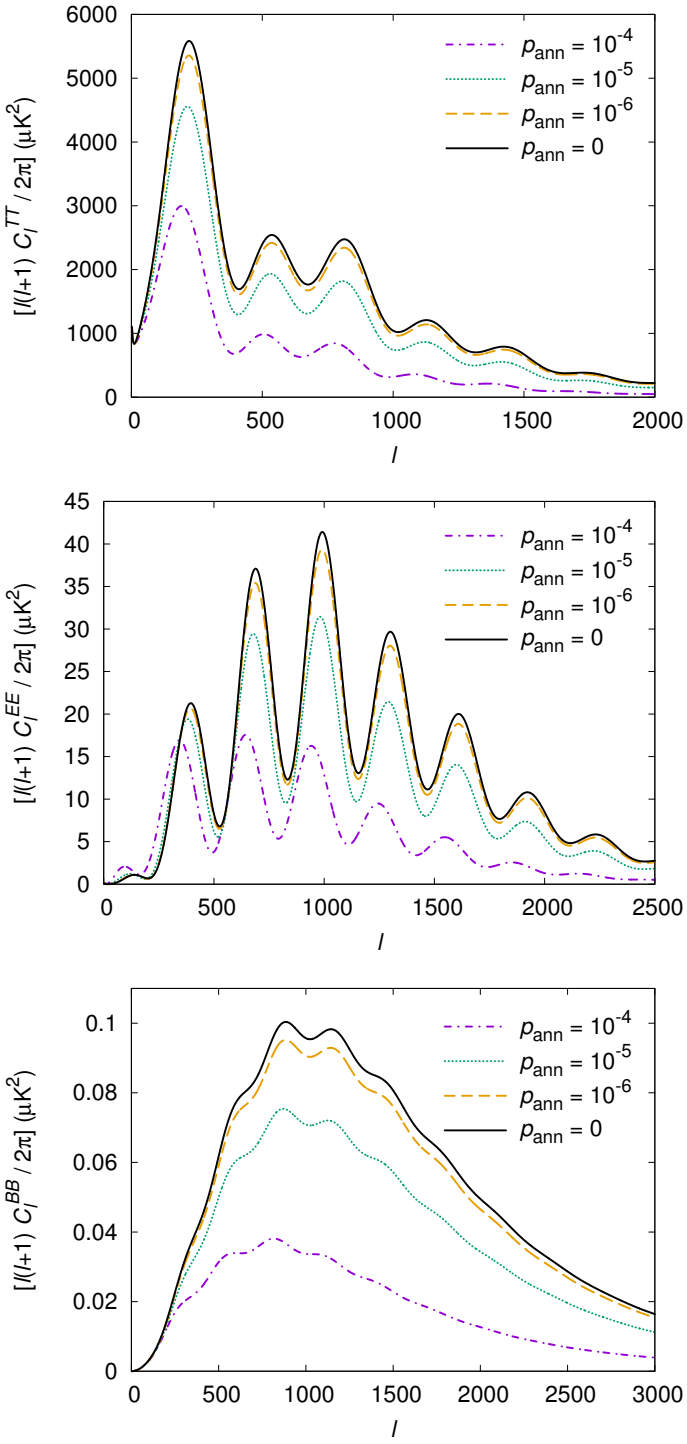

Figure 6.4: The effect of DM annihilations on the TT (top), EE (centre) and BB (bottom) components of the CMB angular power spectrum, where the annihilations are characterised by the parameter $p_{\rm ann} \equiv f_{\rm eff} \langle \sigma v \rangle / m_{\rm DM}$ in units of [m^3 s^{-1} kg^{-1}] ($p_{\rm ann} = 0$ corresponds to no DM annihilations). For the standard cosmological parameters, we use the '*Planck* + lensing' best-fit values from Ref. [11].

The latest CMB measurements from the *Planck* satellite set the strongest constraints on energy-injection from DM to date: $p_{\rm ann} \leq 1.9 \times 10^{-7}$ m^3 s^{-1} kg^{-1} at 95% CL ('*Planck* + lensing') [11].

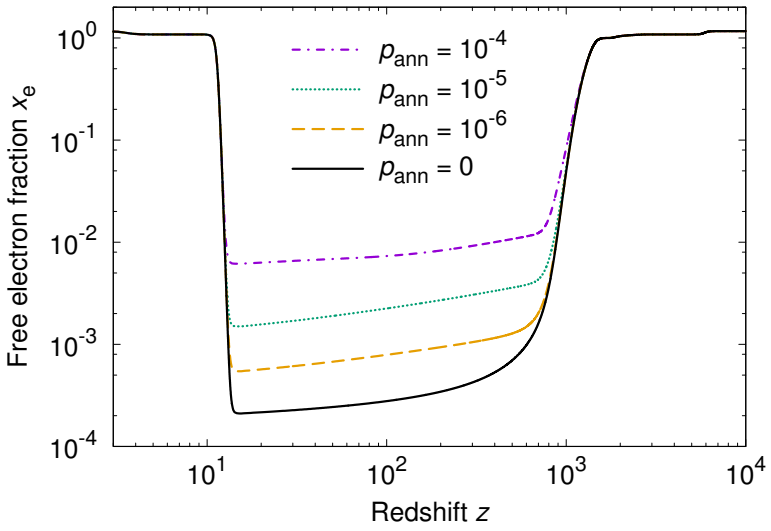

Figure 6.5: The effect of DM annihilations on the free electron fraction $x_{\rm e}$, where the annihilations are characterised by the $p_{\rm ann} \equiv f_{\rm eff} \langle \sigma v \rangle / m_{\rm DM}$ in units of [m^3 s^{-1} kg^{-1}] ($p_{\rm ann} = 0$ corresponds to no DM annihilations). For the standard cosmological parameters, we use the '*Planck* + lensing' best-fit values from Ref. [11].

6.3 Electron Sector Thermal Production

Given the strong constraints in the neutrino sector, it makes sense to examine the alternative scenario of thermal production entirely through e^+e^- annihilation. To accomplish this, the annihilation cross section must be suppressed at late times. A p-wave term, which can be obtained by e.g. the exchange of a Z' mediator [154], can lead to such a suppression, proportional to the velocity squared: $\langle \sigma v \rangle_{e^+e^-} = a + bv^2$.

Assuming $bv^2 \simeq 3 \times 10^{-26}$ cm^3 s^{-1} at freeze-out, the velocity-suppressed p-wave term is too low by over an order of magnitude to reproduce the 511 keV signal. This means that the constant $a \sim 10^{-30}$ cm^3 s^{-1} term is still required. The dark age constraints on the neutrino sector scenario therefore also apply directly to a. However, at present, CMB limits cannot say anything about b due to the low thermal velocities after recombination [324].

Rather than increasing the energy density in the neutrino sector as it becomes non-relativistic, a coupling to electrons leads light DM to transfer entropy into the visible sector [331]. Fixing ρ_γ to the observed value, this translates to an effective decrease of entropy in the neutrino sector and thus a lower $N_{\rm eff}$. In contrast with the previous case, this gives rise to an increase in $Y_{\rm P}$ but to a lower D/H, owing to the different evolution of the baryon-to-photon ratio η [240]. Analogously to Eq. (6.2.1), the value of $N_{\rm eff}$ at recombination ($T \ll m_{\rm DM}$) becomes:

$$N_{\rm eff}^{{\rm Equil},e} \simeq 3.046 \left[1 + \frac{g_{\rm DM}}{2}\frac{7}{22} F(y_\nu|_{T_{{\rm dec},\nu}})\right]^{-4/3} , \tag{6.3.5}$$

where $F(y)$ is given in Eq. (6.2.2). Thus, one obtains a reduction in the relative energy density of the neutrino sector, leaving an overall lower radiation component of the universe. Once again, this is illustrated in Fig. 6.2.

We neglect DM–electron scattering during recombination as the scattering cross section would need to be significantly larger than the annihilation cross section to have a noticeable effect on the CMB acoustic peaks [191, 192].

6.4 New Constraints on Light WIMPs

In order to self-consistently evaluate the effects of each of these scenarios and predict the resulting CMB angular power spectra, the physics described in Secs. 6.2 and 6.3 must be embedded into a CMB code that also accounts for a full recombination calculation. Measurements of the temperature and polarisation angular power spectra from *Planck* already constrain extra ionisation, damping, and modifications of the universe's radiation content to unprecedented accuracy in the ΛCDM model. We thus confront the results of the Boltzmann code CLASS with the data from *Planck*, where we include DM–neutrino scattering (where applicable), in addition to the changes in $N_{\rm eff}$ as a function of the DM mass, and the effect of energy injection in the dark ages due to ongoing DM self-annihilation.

To account for changes in the BBN era, we include in CLASS the modified $Y_{\rm P}$ due to light DM. To this end, we modify the PARTHENOPE [332] code to compute $Y_{\rm P}$ and D/H for arbitrary $\{m_{\rm DM}, \Omega_{\rm b}h^2\}$ pairs. We also update the $d(p,\gamma)^3{\rm He}$, $d(d,n)^3{\rm He}$

and $d(d,p)^3$H reaction rates in PArthENoPE with more precise determinations [333], and take a fixed neutron lifetime $\tau_{\rm n} = 880.3$ s [334]. The effects of hydrogen ionisation and photoionisation are included in the code but we disregard the impact of helium ionisation since it has a negligible impact on the CMB anisotropies [318].

For each scenario, we perform a Markov Chain Monte Carlo (MCMC) search using the Monte Python [173] code. This is in contrast with Refs. [240, 328, 329], who compared predicted changes in $N_{\rm eff}$ directly with derived ΛCDM parameters from *Planck*. By recomputing the full recombination history and comparing directly with the measured angular power spectra, we are able to fully account for the effect of degeneracies between cosmological parameters.

The MCMC searches include the six base ΛCDM parameters (H_0, $\Omega_{\rm DM}h^2$, $\Omega_{\rm b}h^2$, $A_{\rm s}$, $n_{\rm s}$, $\tau_{\rm reio}$). In the neutrino sector scenario, we add the DM mass $m_{\rm DM}$, the energy injection rate $p_{\rm ann}$ [see Eq. (6.2.4)] and a parameterisation of the DM–neutrino scattering cross section

$$u \equiv \left[\frac{\sigma_{\rm DM-\nu}}{\sigma_{\rm Th}}\right]\left[\frac{m_{\rm DM}}{100\ {\rm GeV}}\right]^{-1} , \tag{6.4.6}$$

where $\sigma_{\rm Th}$ is the Thomson cross section. The scattering term u must be marginalised (integrated) over, along with the ΛCDM parameters. In the electron sector case, the additional parameters are simply $m_{\rm DM}$ and $p_{\rm ann}$. Since both u and $p_{\rm ann}$ can vary by many orders of magnitude, we adopt logarithmic prior distributions: $\log(u) \in \{-6, 0\}$ and $\log(p_{\rm ann}) \in \{-8, -2\}$. For simplicity, we use the approximation of massless neutrinos.

For our CMB analysis, we use the "*Planck* + lensing" 2015 dataset, which includes the latest TT, TE, EE and low-ℓ polarisation data [42]. The addition of BAO, supernovae data and an H_0 HST prior do not significantly change our posterior distributions. As explained in Ref. [11], this is due to degeneracies with the other cosmological parameters such as $A_{\rm s}$ and $n_{\rm s}$ at high multipoles.

Before turning to our main results, we first follow the approach of Refs. [238–240, 328, 329] and show constraints from direct measurements of $Y_{\rm P}$ and D/H based on changes during BBN. To this end, we employ the recommended

PDG determinations [334]:

$$\mathrm{D/H} = (2.53 \pm 0.04) \times 10^{-5} \; ; \tag{6.4.7}$$

$$Y_{\mathrm{P}} = 0.2465 \pm 0.0097 \; . \tag{6.4.8}$$

We include a 2% theory error on our D/H calculation, while the experimental error on Y_{P} is dominant [333]. We note that previous studies have used a higher determination of $Y_{\mathrm{P}} = 0.254 \pm 0.003$ [335]. This value is incompatible with the best-fit ΛCDM parameters obtained by the *Planck* experiment at more than 3σ. However, when it is combined with our CMB analysis, it has very little effect on our mass bounds. We thus use the recommended PDG value given above.

The 68% and 95% CL allowed regions are shown as blue bands in Fig. 6.6. Horizontal bands show the allowed 68% and 95% CL posterior regions for $\Omega_{\mathrm{b}}h^2$ from *Planck* data for a real scalar WIMP (orange) and a Dirac fermion WIMP (green). The other possibilities (complex scalar, Majorana fermion or vector) would be more constrained than the real scalar case. For clarity, we do not show them.

In each case, only the overlapping regions shown in grey are allowed. Therefore, $m_{\mathrm{DM}} \gtrsim 8$ MeV is required for Dirac DM, in conflict with the spectral constraints ($m_{\mathrm{DM}} \lesssim 7$ MeV) from INTEGRAL/SPI observations [307, 310, 311]. In the real scalar case, this restriction is relaxed to $m_{\mathrm{DM}} \gtrsim 4$ MeV (electron sector) and $m_{\mathrm{DM}} \gtrsim$ 0.8 MeV (neutrino sector).

The contours in Fig. 6.6 are in general agreement with those presented in Refs. [240, 328, 329] for a Majorana fermion DM particle, bearing in mind the updated BBN and CMB data used in our analysis. While Fig. 6.6 gives an indication of the combined power of CMB and BBN constraints, our MCMC scan using CMB observables alone provides the most robust exclusions, especially given the significant differences between primordial abundance measurements. We therefore turn to these results.

Fig. 6.7 shows the marginalised posterior limits from our MCMC for each scenario, compared with the cross section required to explain the 511 keV line with an annihilating WIMP. The hatched bands show the values of $\langle \sigma v \rangle_{e^+e^-}$ ($= a$ in the electron sector case) that fit the 511 keV intensity and morphology, including the

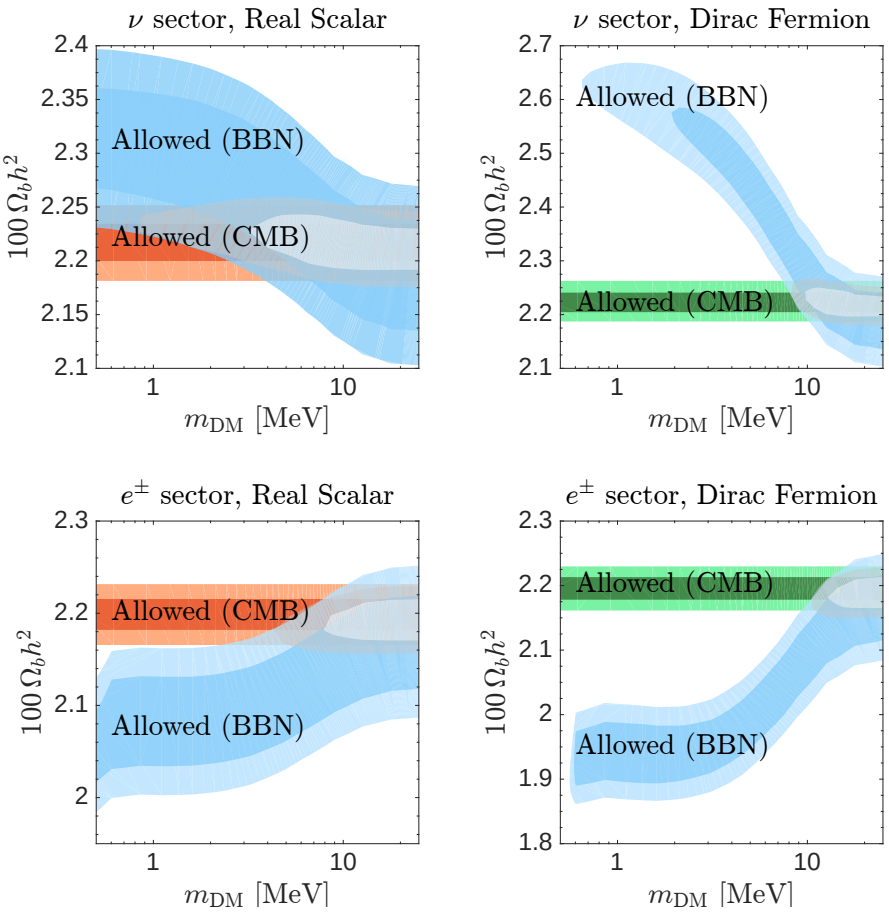

Figure 6.6: Constraints on the baryon content $\Omega_b h^2$ versus the light DM mass $m_{\rm DM}$ for the four considered scenarios. In orange/green, 68% and 95% CL regions allowed by *Planck*; in blue, 68% and 95% CL allowed regions from direct measurements of $Y_{\rm P}$ and D/H. Only overlapping regions shown in grey are compatible with both datasets. BBN requirements on a Dirac fermion are in tension with the restriction that $m_{\rm DM} \lesssim 7$ MeV to avoid overproduction of bremsstrahlung gamma-rays [307, 310, 311]. An extensive MCMC analysis of CMB data is necessary to firmly rule out all possibilities (see Fig. 6.7).

$\pm 2\sigma$ uncertainty from the DM flux, halo shape and stellar disk component [306]. The upper black band shows the best-fit region for an Einasto DM profile; the corresponding band for an NFW profile, which gives a significantly worse fit to the signal's morphology, is shown below it, in blue.

The grey contours show the 68% and 95% CL constraints on $\langle \sigma v \rangle_{e^+e^-}$ alone, due to ionisation of the IGM as described in Eq. (6.2.3). Their shape is due to the mass-dependence of $f_{\rm eff}$ (see Fig. 6.3), leading to the requirement that $m_{\rm DM} \lesssim 1.5$ MeV (Einasto) and $m_{\rm DM} \lesssim 5$ MeV (NFW) at 95% CL to explain the signal.

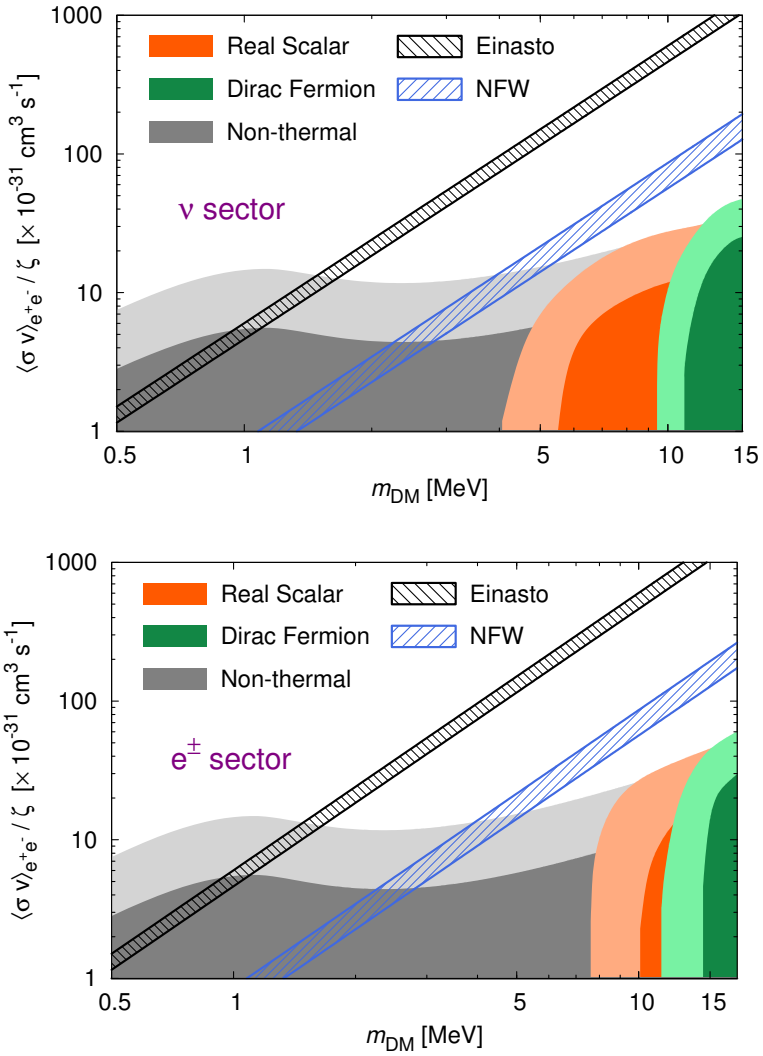

Figure 6.7: The DM annihilation cross section into e^+e^- as a function of the mass of a DM particle that was thermally produced via the neutrino sector (top) and the electron sector (bottom). Hatched bands show the values of $\langle\sigma v\rangle_{e^+e^-}$ vs. $m_{\rm DM}$ that are necessary to explain the 511 keV line for Einasto (black, upper) and NFW (blue, lower) DM density profiles, including the $\pm 2\sigma$ uncertainty from the DM flux, halo shape and stellar disk component [306]. In both panels, values of $\langle\sigma v\rangle_{e^+e^-}$ above the grey regions are excluded by *Planck* CMB limits on energy injection in the dark ages [42]. The coloured contours correspond to the 68% and 95% CL regions that are allowed by *Planck* CMB data for a real scalar WIMP (orange) and a Dirac fermion WIMP (green). Bounds on the DM mass from the entropy transfer [Eqs. (6.2.1) and (6.3.5)] constrain the coloured regions from the left, while bounds from late-time energy injection on $\langle\sigma v\rangle_{e^+e^-}$ constrain them from above. The combination of these effects allows us to rule out the DM mass range that is required to explain the 511 keV line.

This constraint is compatible with the most recent limit on $p_{\rm ann}$ given by the *Planck* collaboration [11]. These bounds are independent of the relic density requirement, which we apply next, and therefore, directly constrain both thermal and non-thermal DM.

In both the neutrino and electron scenarios, the regions allowed by *Planck* CMB observations (shown in orange and green) lie at DM masses and cross sections into $e^{\pm}$ that are respectively too heavy and too weak to reproduce the INTEGRAL/SPI signal. In all cases, the required annihilation rate to produce the positronium signal is outside the 99% CL (3σ) containment region.

In the neutrino sector case, the lower bound[2] at 95% CL on the WIMP mass between 4 and 10 MeV (for $g_{\rm DM} \in \{1, 4\}$) is mainly due to the high sensitivity of *Planck* at larger multipoles to changes in $N_{\rm eff}$ and $Y_{\rm P}$. In the electron sector, these effects yield an even stronger bound, between 7 and 11 MeV at 95% CL. Combined with the constraints on $p_{\rm ann}$ which limit the allowed regions from above, our results show that a light self-annihilating WIMP cannot be responsible for the 511 keV Galactic line without severe disagreement with CMB data.

6.5 Conclusion

The WIMP hypothesis requires an origin of the relic density of DM via thermal freeze-out in the early universe. To simultaneously reproduce the Galactic 511 keV line from positronium annihilation, the remaining branching fraction must be "hidden" from Galactic and cosmological constraints. We have shown that the two methods of accomplishing this are insufficient: i) thermal production via the neutrino sector which, although invisible today, leads to a radiation component that is too large for early universe observables; or ii) p-wave (velocity-suppressed) production via the electromagnetic sector, giving too large of a reduction in the universe's radiation content.

[2]Note that these constraints would be slightly stronger if we had not marginalised over the DM–neutrino scattering parameter u.

More exotic scenarios exist; for example, eXciting dark matter (XDM) has been explored in depth (see e.g. Refs. [336, 337]) as an alternative mechanism to evade the suppressed self-annihilation cross sections. As pointed out by Ref. [338], our dark ages constraints can also be applied to XDM; indeed, their forecasts show that *Planck* should rule out XDM models with a mass splitting larger than ~ 1.5 MeV. Smaller splittings are possible but require tuning of the DM model.

We also note that one can mitigate the effects of entropy transfer and late-time energy injection by adding an extra component of dark radiation, or an extra source of photons or neutrinos between the epochs of neutrino decoupling and recombination. Such a coincidence would weaken our constraints; however, this type of model-building goes beyond the scope of our analysis.

In summary, the favoured DM explanation of the Galactic 511 keV line – an anomaly that has endured for over four decades – is thus in fundamental disagreement with the latest cosmological data. As the origin of the positrons in the Galactic bulge remains unknown, an alternative DM model may yet be responsible; however, the light WIMP hypothesis is no longer viable.

Chapter 7

Conclusion

The most incomprehensible thing about the world is that it is comprehensible.

— Albert Einstein

The aim of this thesis was to study the potential interactions of dark matter (DM) beyond gravity, to hopefully provide a step towards understanding its fundamental properties. In particular, we have focussed on the scattering of DM with radiation, i.e. photons (γCDM) and neutrinos (νCDM), and annihilations of DM in the weakly-interacting massive particle (WIMP) paradigm. In Table 7.1, we summarise the main constraints obtained in this thesis for the γCDM and νCDM scenarios using observations of the cosmic microwave background (CMB) and large-scale structure (LSS) of the universe.

Cosmological Observation	γCDM $[(m_{\rm DM}/{\rm GeV})\ {\rm cm}^2]$	νCDM $[(m_{\rm DM}/{\rm GeV})\ {\rm cm}^2]$
CMB	$\lesssim 2 \times 10^{-30}$ [Eq. (3.3.25)]	$\lesssim 6 \times 10^{-31}$ [Eq. (4.5.27)]
Large-Scale Structure	$\lesssim 4 \times 10^{-33}$ [Eq. (5.2.2)]	$\lesssim \mathcal{O}(10^{-33})$ [Eq. (4.3.15)]

Table 7.1: A summary of the constraints derived in this thesis on the DM–photon (γCDM) and DM–neutrino (νCDM) elastic scattering cross sections, in the case that they are constant (temperature-independent), at 95% CL. The top row corresponds to the constraints set by *Planck* CMB data [10]. The second row corresponds to constraints from LSS observations (the Milky Way satellite abundance [288] in the case of γCDM and the Lyman-α forest [184] in the case of νCDM).

In Chapter 3, we explored the impact of primordial DM–photon interactions on the evolution of density perturbations and in particular, the CMB angular power spectrum C_ℓ. Using the latest data from *Planck*, in combination with a modified version of the Boltzmann code CLASS, we derived upper limits on the elastic scattering cross section for both constant and T^2-dependent scenarios: $\sigma_{\rm DM-\gamma} \lesssim 2 \times 10^{-30}\,(m_{\rm DM}/{\rm GeV})$ cm^2 and $\sigma_{\rm DM-\gamma,0} \lesssim 2 \times 10^{-39}\,(m_{\rm DM}/{\rm GeV})$ cm^2, respectively (at 95% CL). These constraints are importantly model-independent as one does not need to specify whether DM is annihilating, decaying or asymmetric. We also highlighted the effect on the polarisation spectra and matter power spectrum $P(k)$, showing that forthcoming data from CMB polarisation experiments (provided an excellent knowledge of the foregrounds) and LSS surveys will help to both constrain and characterise the dark sector.

In Chapter 4, we presented analogous constraints for DM–neutrino interactions. We showed that *Planck* data limits the DM–neutrino scattering cross section to be: $\sigma_{\rm DM-\nu} \lesssim 6 \times 10^{-31}\,(m_{\rm DM}/{\rm GeV})$ cm^2 and $\sigma_{\rm DM-\nu,0} \lesssim 2 \times 10^{-40}\,(m_{\rm DM}/{\rm GeV})$ cm^2, for the constant and T^2-dependent cases, respectively (at 95% CL). By simulating a next-generation CMB experiment, we found that one could only weakly improve on the current sensitivity. The strongest limits are currently set by observations of the Lyman-α forest, demonstrating the power of LSS surveys in probing such "invisible" interactions. Restricting ourselves to the mildly non-linear regime, future data from the DESI experiment alone could improve the current *Planck* limits by an order of magnitude and provide a percent-level measurement of the cross section for values above that limit. Finally, we showed that thermal MeV DM with a constant scattering cross section naturally predicts (i) a cut-off in the $P(k)$ at the Lyman-α scale, (ii) an enhancement of the Hubble rate H_0 and the effective number of neutrino species $N_{\rm eff}$, and (iii) the possible generation of neutrino masses.

In Chapter 5, we investigated the impact of DM–radiation interactions on the abundance and structure of the Milky Way (MW) satellite galaxies. By performing the first accurate cosmological simulations of such scenarios, we found a new means to reduce the population of MW subhaloes and thus solve the "missing satellite" problem, without the need to abandon CDM. Furthermore, the resulting constraints

on the DM–photon scattering cross section are orders of magnitude stronger than is possible from linear perturbation theory considerations. We also showed the impact of DM–radiation interactions on the structure of massive subhaloes. Increasing the interaction cross section reduces the mass enclosed within a given radius in the subhaloes, which alleviates the "too big to fail" problem. When combined with the reduction in the number of MW subhaloes, we found that a model of γCDM with a (constant) elastic scattering cross section of $\sigma_{\mathrm{DM}-\gamma} \simeq 1 \times 10^{-33}\,(m_{\mathrm{DM}}/\mathrm{GeV})\ \mathrm{cm}^2$ can simultaneously solve both of these small-scale problems.

Finally, in Chapter 6, we addressed an excess of 511 keV gamma-rays that has been observed from the Galactic centre of the MW for four decades and is uncorrelated with known astrophysical sources. DM in the form of light ($\lesssim$ 10 MeV) WIMPs annihilating into electron–positron pairs has been one of the leading hypotheses of the observed emission. However, given the small required cross section, $\sim 10^{-30}\ \mathrm{cm}^3\ \mathrm{s}^{-1}$, a further coupling to lighter particles is required to produce the correct relic density. We showed that the two methods of accomplishing this are insufficient: i) thermal production via the neutrino sector which, although invisible today, leads to a radiation component that is too large for early universe observables; ii) p-wave (velocity-suppressed) production via the electromagnetic sector gives too large of a reduction in the universe's radiation content. Using these results, we showed that the light WIMP explanation of the 511 keV excess is ruled out by the latest cosmological data for both Navarro–Frenk–White (NFW) and Einasto DM density profiles, suggesting an astrophysical or more exotic DM source of the signal.

Our results have shown that one can effectively use cosmological observations to probe the intrinsic properties of DM. Furthermore, interactions beyond gravity may be essential to make predictions of DM in simulations of structure formation. The DM puzzle remains one of the key challenges faced by both the particle physics and cosmology communities; however, knowledge of its nature will undoubtedly provide us with new and exciting realms of physics in the future.

Bibliography

[1] R. J. Wilkinson, J. Lesgourgues, and C. Boehm, "Using the CMB angular power spectrum to study Dark Matter-photon interactions," JCAP **1404**, 026 (2014), arXiv:1309.7588.

[2] R. J. Wilkinson, C. Boehm, and J. Lesgourgues, "Constraining Dark Matter-Neutrino Interactions using the CMB and Large-Scale Structure," JCAP **1405**, 011 (2014), arXiv:1401.7597.

[3] M. Escudero, O. Mena, A. C. Vincent, R. J. Wilkinson, and C. Boehm, "Exploring dark matter microphysics with galaxy surveys," JCAP **1509**, 034 (2015), arXiv:1505.06735.

[4] C. Boehm, J. Schewtschenko, R. Wilkinson, C. Baugh, and S. Pascoli, "Using the Milky Way satellites to study interactions between cold dark matter and radiation," MNRAS **445**, L31–L35 (2014), arXiv:1404.7012.

[5] J. A. Schewtschenko, R. J. Wilkinson, C. M. Baugh, C. Boehm, and S. Pascoli, "Dark matter-radiation interactions: the impact on dark matter haloes," MNRAS **449**, 3587–3596 (2015), arXiv:1412.4905.

[6] J. A. Schewtschenko, C. M. Baugh, R. J. Wilkinson, C. Boehm, S. Pascoli, and T. Sawala, "Dark matter-radiation interactions: the structure of Milky Way satellite galaxies," (2015), 10.1093/mnras/stw1078, arXiv:1512.06774.

[7] R. J. Wilkinson, A. C. Vincent, C. Boehm, and C. McCabe, "Ruling out the light WIMP explanation of the galactic 511 keV line," (2016), arXiv:1602.01114.

[8] C. Bennett et al. (WMAP), "Nine-Year Wilkinson Microwave Anisotropy Probe (WMAP) Observations: Final Maps and Results," Astrophys.J.Suppl. **208**, 20 (2013), arXiv:1212.5225.

[9] G. Hinshaw et al. (WMAP), "Nine-Year Wilkinson Microwave Anisotropy Probe (WMAP) Observations: Cosmological Parameter Results," Astrophys. J. Suppl. **208**, 19 (2013), arXiv:1212.5226.

[10] P. Ade et al. (Planck Collaboration), "Planck 2013 results. XVI. Cosmological parameters," Astron.Astrophys. **571**, A16 (2014), arXiv:1303.5076.

[11] P. Ade et al. (Planck Collaboration), "Planck 2015 results. XIII. Cosmological parameters," (2015), arXiv:1502.01589.

[12] F. Zwicky, "Die Rotverschiebung von extragalaktischen Nebeln," Helv. Phys. Acta **6**, 110–127 (1933).

[13] A. Vikhlinin, A. Kravtsov, W. Forman, C. Jones, M. Markevitch, S. S. Murray, and L. Van Speybroeck, "Chandra sample of nearby relaxed galaxy clusters: Mass, gas fraction, and mass-temperature relation," Astrophys. J. **640**, 691–709 (2006), arXiv:astro-ph/0507092.

[14] K. Freese, "Review of Observational Evidence for Dark Matter in the Universe and in upcoming searches for Dark Stars," EAS Publ. Ser. **36**, 113–126 (2009), arXiv:0812.4005.

[15] R. B. Metcalf and P. Madau, "Compound gravitational lensing as a probe of dark matter substructure within galaxy halos," Astrophys. J. **563**, 9 (2001), arXiv:astro-ph/0108224.

[16] R. B. Metcalf and H. Zhao, "Flux ratios as a probe of dark substructures in quadruple-image gravitational lenses," Astrophys. J. **567**, L5 (2002), arXiv:astro-ph/0111427.

[17] A. Einstein, "The Foundation of the General Theory of Relativity," Annalen Phys. **49**, 769–822 (1916), [Annalen Phys.14,517(2005)].

[18] D. Clowe, A. Gonzalez, and M. Markevitch, "Weak lensing mass reconstruction of the interacting cluster 1E0657-558: Direct evidence for the existence of dark matter," Astrophys. J. **604**, 596–603 (2004), arXiv:astro-ph/0312273.

[19] M. Bradac, S. W. Allen, T. Treu, H. Ebeling, R. Massey, R. G. Morris, A. von der Linden, and D. Applegate, "Revealing the properties of dark matter in the merging cluster MACSJ0025.4-1222," Astrophys. J. **687**, 959 (2008), arXiv:0806.2320.

[20] A. Mahdavi, H. y. Hoekstra, A. y. Babul, D. y. Balam, and P. Capak, "A Dark Core in Abell 520," Astrophys. J. **668**, 806–814 (2007), arXiv:0706.3048.

[21] M. J. Jee, H. Hoekstra, A. Mahdavi, and A. Babul, "Hubble Space Telescope/Advanced Camera for Surveys Confirmation of the Dark Substructure in A520," Astrophys. J. **783**, 78 (2014), arXiv:1401.3356.

[22] D. Clowe, M. Bradac, A. H. Gonzalez, M. Markevitch, S. W. Randall, C. Jones, and D. Zaritsky, "A direct empirical proof of the existence of dark matter," Astrophys. J. **648**, L109–L113 (2006), arXiv:astro-ph/0608407.

[23] M. Milgrom, "A modification of the Newtonian dynamics as a possible alternative to the hidden mass hypothesis," ApJ **270**, 365–370 (1983).

[24] M. Milgrom, "A modification of the Newtonian dynamics - Implications for galaxies," ApJ **270**, 371–389 (1983).

[25] M. Milgrom, "A Modification of the Newtonian Dynamics - Implications for Galaxy Systems," ApJ **270**, 384 (1983).

[26] S. Dodelson, "The Real Problem with MOND," Int. J. Mod. Phys. **D20**, 2749–2753 (2011), arXiv:1112.1320.

[27] E. Hubble, "A relation between distance and radial velocity among extra-galactic nebulae," Proc. Nat. Acad. Sci. **15**, 168–173 (1929).

[28] S. Jha, Exploding stars, near and far, Ph.D. thesis, Harvard U. (2002).

[29] D. J. Fixsen, "The Temperature of the Cosmic Microwave Background," Astrophys. J. **707**, 916–920 (2009), arXiv:0911.1955.

[30] A. Friedman, "On the Curvature of space," Z. Phys. **10**, 377–386 (1922), [Gen. Rel. Grav.31,1991(1999)].

[31] A. G. Riess et al. (Supernova Search Team), "Observational evidence from supernovae for an accelerating universe and a cosmological constant," Astron. J. **116**, 1009–1038 (1998), arXiv:astro-ph/9805201.

[32] S. Perlmutter et al. (Supernova Cosmology Project), "Measurements of Omega and Lambda from 42 high redshift supernovae," Astrophys. J. **517**, 565–586 (1999), arXiv:astro-ph/9812133.

[33] A. D. Dolgov, "Big bang nucleosynthesis," Nucl. Phys. Proc. Suppl. **110**, 137–143 (2002), arXiv:hep-ph/0201107.

[34] R. A. Alpher, H. Bethe, and G. Gamow, "The origin of chemical elements," Phys. Rev. **73**, 803–804 (1948).

[35] J. Beringer et al. (Particle Data Group), "Review of Particle Physics (RPP)," Phys. Rev. **D86**, 010001 (2012).

[36] R. Ichimasa, R. Nakamura, M. Hashimoto, and K. Arai, "Big-Bang Nucleosynthesis in comparison with observed helium and deuterium abundances: possibility of a nonstandard model," Phys. Rev. **D90**, 023527 (2014), arXiv:1404.4831.

[37] B. D. Fields, "The primordial lithium problem," Ann. Rev. Nucl. Part. Sci. **61**, 47–68 (2011), arXiv:1203.3551.

[38] P. Peebles, "Recombination of the Primeval Plasma," Astrophys.J. **153**, 1 (1968).

[39] A. A. Penzias and R. W. Wilson, "A Measurement of excess antenna temperature at 4080-Mc/s," Astrophys. J. **142**, 419–421 (1965).

[40] J. C. Mather et al., "Measurement of the Cosmic Microwave Background spectrum by the COBE FIRAS instrument," Astrophys. J. **420**, 439–444 (1994).

[41] N. Straumann, "From primordial quantum fluctuations to the anisotropies of the cosmic microwave background radiation," Annalen Phys. **15**, 701–847 (2006), arXiv:hep-ph/0505249.

[42] R. Adam et al. (Planck Collaboration), "Planck 2015 results. I. Overview of products and scientific results," (2015), arXiv:1502.01582.

[43] G. F. Smoot et al., "Structure in the COBE differential microwave radiometer first year maps," Astrophys. J. **396**, L1–L5 (1992).

[44] J. L. Sievers et al. (Atacama Cosmology Telescope), "The Atacama Cosmology Telescope: Cosmological parameters from three seasons of data," JCAP **1310**, 060 (2013), arXiv:1301.0824.

[45] R. Keisler, C. Reichardt, K. Aird, B. Benson, L. Bleem, et al., "A Measurement of the Damping Tail of the Cosmic Microwave Background Power Spectrum with the South Pole Telescope," Astrophys.J. **743**, 28 (2011), arXiv:1105.3182.

[46] U. Seljak and M. Zaldarriaga, "A Line of sight integration approach to cosmic microwave background anisotropies," Astrophys.J. **469**, 437–444 (1996), arXiv:astro-ph/9603033.

[47] A. Lewis, A. Challinor, and A. Lasenby, "Efficient computation of CMB anisotropies in closed FRW models," Astrophys.J. **538**, 473–476 (2000), arXiv:astro-ph/9911177.

[48] J. Lesgourgues, "The Cosmic Linear Anisotropy Solving System (CLASS) I: Overview," (2011), arXiv:1104.2932.

[49] R. K. Sachs and A. M. Wolfe, "Perturbations of a cosmological model and angular variations of the microwave background," Astrophys. J. **147**, 73–90 (1967), [Gen. Rel. Grav.39,1929(2007)].

[50] J. Silk, "Cosmic black body radiation and galaxy formation," Astrophys. J. **151**, 459–471 (1968).

[51] W. H. McMaster, "Polarization and the Stokes Parameters," American Journal of Physics **22**, 351–362 (1954).

[52] M. Zaldarriaga, "CMB polarization experiments," Astrophys. J. **503**, 1 (1998), arXiv:astro-ph/9709271.

[53] M. Kamionkowski and E. D. Kovetz, "The Quest for B Modes from Inflationary Gravitational Waves," (2015), arXiv:1510.06042.

[54] P. Ade et al. (Planck), "Planck 2015 results. XX. Constraints on inflation," (2015), arXiv:1502.02114.

[55] M. Zaldarriaga and U. Seljak, "Gravitational lensing effect on cosmic microwave background polarization," Phys. Rev. **D58**, 023003 (1998), arXiv:astro-ph/9803150.

[56] J. Kovac, E. M. Leitch, C. Pryke, J. E. Carlstrom, N. W. Halverson, and W. L. Holzapfel, "Detection of polarization in the cosmic microwave background using DASI," Nature **420**, 772–787 (2002), arXiv:astro-ph/0209478.

[57] D. Hanson et al. (SPTpol), "Detection of B-mode Polarization in the Cosmic Microwave Background with Data from the South Pole Telescope," Phys. Rev. Lett. **111**, 141301 (2013), arXiv:1307.5830.

[58] P. Ade et al. (BICEP2, Planck), "Joint Analysis of BICEP2/Keck Array and Planck Data," Phys. Rev. Lett. **114**, 101301 (2015), arXiv:1502.00612.

[59] J. F. Navarro, C. S. Frenk, and S. D. M. White, "The Structure of cold dark matter halos," Astrophys. J. **462**, 563–575 (1996), arXiv:astro-ph/9508025.

[60] V. Springel et al., "Simulating the joint evolution of quasars, galaxies and their large-scale distribution," Nature **435**, 629–636 (2005), arXiv:astro-ph/0504097.

[61] V. Springel, J. Wang, M. Vogelsberger, A. Ludlow, A. Jenkins, A. Helmi, J. F. Navarro, C. S. Frenk, and S. D. M. White, "The Aquarius Project: the subhalos of galactic halos," MNRAS **391**, 1685–1711 (2008), arXiv:0809.0898.

[62] J. Diemand, M. Kuhlen, and P. Madau, "Dark matter substructure and gamma-ray annihilation in the Milky Way halo," Astrophys. J. **657**, 262–270 (2007), arXiv:astro-ph/0611370.

[63] J. Diemand, M. Kuhlen, P. Madau, M. Zemp, B. Moore, et al., "Clumps and streams in the local dark matter distribution," Nature **454**, 735–738 (2008), arXiv:0805.1244.

[64] E. R. Harrison, "Fluctuations at the threshold of classical cosmology," Phys. Rev. **D1**, 2726–2730 (1970).

[65] Ya. B. Zeldovich, "A Hypothesis, unifying the structure and the entropy of the universe," Mon. Not. Roy. Astron. Soc. **160**, 1P–3P (1972).

[66] S. Tsujikawa, "Introductory review of cosmic inflation," (2003) arXiv:hep-ph/0304257.

[67] P. Meszaros, "The behaviour of point masses in an expanding cosmological substratum," Astron. Astrophys. **37**, 225–228 (1974).

[68] M. Tegmark et al. (SDSS), "The 3-D power spectrum of galaxies from the SDSS," Astrophys. J. **606**, 702–740 (2004), arXiv:astro-ph/0310725.

[69] J. R. Bond and A. S. Szalay, "The Collisionless Damping of Density Fluctuations in an Expanding Universe," Astrophys. J. **274**, 443–468 (1983).

[70] J. Lesgourgues and S. Pastor, "Massive neutrinos and cosmology," Phys.Rept. **429**, 307–379 (2006), arXiv:astro-ph/0603494.

[71] P. Fayet and S. Ferrara, "Supersymmetry," Phys. Rept. **32**, 249–334 (1977).

[72] G. Jungman, M. Kamionkowski, and K. Griest, "Supersymmetric dark matter," Phys. Rept. **267**, 195–373 (1996), arXiv:hep-ph/9506380.

[73] S. P. Martin, "A Supersymmetry primer," (1997), arXiv:hep-ph/9709356.

[74] K. Griest and M. Kamionkowski, "Supersymmetric dark matter," Phys. Rept. **333**, 167–182 (2000).

[75] R. Peccei and H. R. Quinn, "CP Conservation in the Presence of Instantons," Phys.Rev.Lett. **38**, 1440–1443 (1977).

[76] R. D. Peccei and H. R. Quinn, "Constraints Imposed by CP Conservation in the Presence of Instantons," Phys. Rev. **D16**, 1791–1797 (1977).

[77] J. Preskill, M. B. Wise, and F. Wilczek, "Cosmology of the Invisible Axion," Phys.Lett. **B120**, 127–132 (1983).

[78] C. Frenk and S. D. White, "Dark matter and cosmic structure," Annalen Phys. **524**, 507–534 (2012), arXiv:1210.0544.

[79] B. Moore, S. Ghigna, F. Governato, G. Lake, T. R. Quinn, et al., "Dark matter substructure within galactic halos," Astrophys.J. **524**, L19–L22 (1999), arXiv:astro-ph/9907411.

[80] A. A. Klypin, A. V. Kravtsov, O. Valenzuela, and F. Prada, "Where are the missing Galactic satellites?" Astrophys.J. **522**, 82–92 (1999), arXiv:astro-ph/9901240.

[81] M. Boylan-Kolchin, J. S. Bullock, and M. Kaplinghat, "Too big to fail? The puzzling darkness of massive Milky Way subhaloes," MNRAS **415**, L40 (2011), arXiv:1103.0007.

[82] S. Dodelson and L. M. Widrow, "Sterile-neutrinos as dark matter," Phys.Rev.Lett. **72**, 17–20 (1994), arXiv:hep-ph/9303287.

[83] A. Boyarsky, O. Ruchayskiy, and M. Shaposhnikov, "The Role of sterile neutrinos in cosmology and astrophysics," Ann.Rev.Nucl.Part.Sci. **59**, 191–214 (2009), arXiv:0901.0011.

[84] M. Viel, J. Lesgourgues, M. G. Haehnelt, S. Matarrese, and A. Riotto, "Constraining warm dark matter candidates including sterile neutrinos and

light gravitinos with WMAP and the Lyman-alpha forest," Phys.Rev. **D71**, 063534 (2005), arXiv:astro-ph/0501562.

[85] A. Dolgov and S. Hansen, "Massive sterile neutrinos as warm dark matter," Astropart.Phys. **16**, 339–344 (2002), arXiv:hep-ph/0009083.

[86] R. N. Mohapatra et al., "Theory of neutrinos: A White paper," Rept. Prog. Phys. **70**, 1757–1867 (2007), arXiv:hep-ph/0510213.

[87] M. Drewes, "The Phenomenology of Right Handed Neutrinos," Int. J. Mod. Phys. **E22**, 1330019 (2013), arXiv:1303.6912.

[88] E. W. Kolb and M. S. Turner, "The Early Universe," Front. Phys. **69**, 1–547 (1990).

[89] B. Audren, J. Lesgourgues, G. Mangano, P. D. Serpico, and T. Tram, "Strongest model-independent bound on the lifetime of Dark Matter," JCAP **1412**, 028 (2014), arXiv:1407.2418.

[90] G. Steigman, B. Dasgupta, and J. F. Beacom, "Precise Relic WIMP Abundance and its Impact on Searches for Dark Matter Annihilation," Phys. Rev. **D86**, 023506 (2012), arXiv:1204.3622.

[91] D. Hooper, "Particle Dark Matter," (2010) pp. 709–764, arXiv:0901.4090.

[92] B. W. Lee and S. Weinberg, "Cosmological Lower Bound on Heavy Neutrino Masses," Phys. Rev. Lett. **39**, 165–168 (1977).

[93] P. Hut, "Limits on Masses and Number of Neutral Weakly Interacting Particles," Phys. Lett. **B69**, 85 (1977).

[94] C. Boehm and P. Fayet, "Scalar dark matter candidates," Nucl.Phys. **B683**, 219–263 (2004), arXiv:hep-ph/0305261.

[95] L. J. Hall, K. Jedamzik, J. March-Russell, and S. M. West, "Freeze-In Production of FIMP Dark Matter," JHEP **03**, 080 (2010), arXiv:0911.1120.

[96] M. W. Goodman and E. Witten, "Detectability of Certain Dark Matter Candidates," Phys. Rev. **D31**, 3059 (1985).

[97] T. Marrodán Undagoitia and L. Rauch, "Dark matter direct-detection experiments," J. Phys. **G43**, 013001 (2016), arXiv:1509.08767.

[98] R. J. Gaitskell, "Direct detection of dark matter," Ann. Rev. Nucl. Part. Sci. **54**, 315–359 (2004).

[99] A. K. Drukier, K. Freese, and D. N. Spergel, "Detecting Cold Dark Matter Candidates," Phys. Rev. **D33**, 3495–3508 (1986).

[100] P. Belli, R. Cerulli, N. Fornengo, and S. Scopel, "Effect of the galactic halo modeling on the DAMA / NaI annual modulation result: an Extended analysis of the data for WIMPs with a purely spin independent coupling," Phys. Rev. **D66**, 043503 (2002), arXiv:hep-ph/0203242.

[101] A. M. Green, "Effect of halo modeling on WIMP exclusion limits," Phys. Rev. **D66**, 083003 (2002), arXiv:astro-ph/0207366.

[102] D. Stiff and L. M. Widrow, "Fine structure of dark matter halos and its effect on terrestrial detection experiments," Phys. Rev. Lett. **90**, 211301 (2003), arXiv:astro-ph/0301301.

[103] A. L. Fitzpatrick, W. Haxton, E. Katz, N. Lubbers, and Y. Xu, "The Effective Field Theory of Dark Matter Direct Detection," JCAP **1302**, 004 (2013), arXiv:1203.3542.

[104] D. Akerib et al. (LUX Collaboration), "First results from the LUX dark matter experiment at the Sanford Underground Research Facility," Phys.Rev.Lett. **112**, 091303 (2014), arXiv:1310.8214.

[105] R. Agnese et al. (SuperCDMS), "Search for Low-Mass Weakly Interacting Massive Particles with SuperCDMS," Phys. Rev. Lett. **112**, 241302 (2014), arXiv:1402.7137.

[106] D. S. Akerib et al. (LUX), "Improved WIMP scattering limits from the LUX experiment," Phys. Rev. Lett. **116**, 161301 (2016), arXiv:1512.03506.

[107] W. B. Atwood et al. (Fermi-LAT), "The Large Area Telescope on the Fermi Gamma-ray Space Telescope Mission," Astrophys. J. **697**, 1071–1102 (2009), arXiv:0902.1089.

[108] F. Stoehr, S. D. M. White, V. Springel, G. Tormen, and N. Yoshida, "Dark matter annihilation in the halo of the Milky Way," Mon. Not. Roy. Astron. Soc. **345**, 1313 (2003), arXiv:astro-ph/0307026.

[109] A. A. Abdo et al. (Fermi-LAT), "Observations of Milky Way Dwarf Spheroidal galaxies with the Fermi-LAT detector and constraints on Dark Matter models," Astrophys. J. **712**, 147–158 (2010), arXiv:1001.4531.

[110] A. W. Graham, D. Merritt, B. Moore, J. Diemand, and B. Terzic, "Empirical models for Dark Matter Halos. I. Nonparametric Construction of Density Profiles and Comparison with Parametric Models," Astron. J. **132**, 2685–2700 (2006), arXiv:astro-ph/0509417.

[111] A. A. Dutton and A. V. Macciò, "Cold dark matter haloes in the Planck era: evolution of structural parameters for Einasto and NFW profiles," Mon. Not. Roy. Astron. Soc. **441**, 3359–3374 (2014), arXiv:1402.7073.

[112] L. Pieri, J. Lavalle, G. Bertone, and E. Branchini, "Implications of High-Resolution Simulations on Indirect Dark Matter Searches," Phys. Rev. **D83**, 023518 (2011), arXiv:0908.0195.

[113] J. I. Read, "The Local Dark Matter Density," J. Phys. **G41**, 063101 (2014), arXiv:1404.1938.

[114] A. Birkedal, K. T. Matchev, M. Perelstein, and A. Spray, "Robust gamma ray signature of WIMP dark matter," (2005), arXiv:hep-ph/0507194.

[115] M. Leventhal, C. J. MacCallum, and P. D. Stang, "Detection of 511 keV positron annihilation radiation from the galactic center direction," ApJ **225**, L11–L14 (1978).

[116] F. Albernhe, J. F. Le Borgne, G. Vedrenne, D. Boclet, P. Durouchoux, and J. M. da Costa, "Detection of the positron annihilation gamma ray line from the Galactic Center region," Astron.Astrophys. **94**, 214–218 (1981).

[117] M. Leventhal, C. J. MacCallum, A. F. Huters, and P. D. Stang, "Current status of the galactic center positron-annihilation source," ApJ **302**, 459–461 (1986).

[118] G. H. Share, R. L. Kinzer, J. D. Kurfess, D. C. Messina, W. R. Purcell, E. L. Chupp, D. J. Forrest, and C. Reppin, "SMM detection of diffuse Galactic 511 keV annihilation radiation," ApJ **326**, 717–732 (1988).

[119] W. R. Purcell, D. A. Grabelsky, M. P. Ulmer, W. N. Johnson, R. L. Kinzer, J. D. Kurfess, M. S. Strickman, and G. V. Jung, "OSSE observations of Galactic 511 keV positron annihilation radiation - Initial phase 1 results," ApJ **413**, L85–L88 (1993).

[120] W. R. Purcell, L.-X. Cheng, D. D. Dixon, R. L. Kinzer, J. D. Kurfess, M. Leventhal, M. A. Saunders, J. G. Skibo, D. M. Smith, and J. Tueller, "OSSE Mapping of Galactic 511 keV Positron Annihilation Line Emission," ApJ **491**, 725–748 (1997).

[121] M. Ackermann et al. (LAT Collaboration), "Fermi LAT Search for Dark Matter in Gamma-ray Lines and the Inclusive Photon Spectrum," Phys.Rev. **D86**, 022002 (2012), arXiv:1205.2739.

[122] F. Aharonian et al. (HESS), "Observations of the Crab Nebula with H.E.S.S," Astron. Astrophys. **457**, 899–915 (2006), arXiv:astro-ph/0607333.

[123] J. Aleksic et al. (MAGIC), "Performance of the MAGIC stereo system obtained with Crab Nebula data," Astropart. Phys. **35**, 435–448 (2012), arXiv:1108.1477.

[124] J. Holder et al., "Status of the VERITAS Observatory," AIP Conf. Proc. **1085**, 657–660 (2009), arXiv:0810.0474.

[125] M. L. Proper, J. P. Harding, and B. Dingus (HAWC), "First Limits on the Dark Matter Cross Section with the HAWC Observatory," (2015) arXiv:1508.04470.

[126] J. Ahrens et al. (IceCube), "Sensitivity of the IceCube detector to astrophysical sources of high energy muon neutrinos," Astropart. Phys. **20**, 507–532 (2004), arXiv:astro-ph/0305196.

[127] M. Ageron et al. (ANTARES), "ANTARES: the first undersea neutrino telescope," Nucl. Instrum. Meth. **A656**, 11–38 (2011), arXiv:1104.1607.

[128] Y. Fukuda et al. (Super-Kamiokande), "The Super-Kamiokande detector," Nucl. Instrum. Meth. **A501**, 418–462 (2003).

[129] P. Blasi, "The Origin of Galactic Cosmic Rays," Astron. Astrophys. Rev. **21**, 70 (2013), arXiv:1311.7346.

[130] O. Adriani et al. (PAMELA Collaboration), "An anomalous positron abundance in cosmic rays with energies 1.5-100 GeV," Nature **458**, 607–609 (2009), arXiv:0810.4995.

[131] A. Kounine, "The Alpha Magnetic Spectrometer on the International Space Station," Int. J. Mod. Phys. **E21**, 1230005 (2012).

[132] H. Fuke et al., "Current status and future plans for the general antiparticle spectrometer (GAPS)," Adv. Space Res. **41**, 2056–2060 (2008).

[133] V. Khachatryan et al. (CMS), "Search for dark matter particles in proton-proton collisions at sqrt(s) = 8 TeV using the razor variables," (2016), arXiv:1603.08914.

[134] I. M. Shoemaker and L. Vecchi, "Unitarity and Monojet Bounds on Models for DAMA, CoGeNT, and CRESST-II," Phys. Rev. **D86**, 015023 (2012), arXiv:1112.5457.

[135] O. Buchmueller, M. J. Dolan, and C. McCabe, "Beyond Effective Field Theory for Dark Matter Searches at the LHC," JHEP **01**, 025 (2014), arXiv:1308.6799.

[136] S. Chatrchyan et al. (CMS), "Search for dark matter and large extra dimensions in monojet events in pp collisions at $\sqrt{s} = 7$ TeV," JHEP **09**, 094 (2012), arXiv:1206.5663.

[137] G. Aad et al. (ATLAS), "Search for dark matter candidates and large extra dimensions in events with a jet and missing transverse momentum with the ATLAS detector," JHEP **04**, 075 (2013), arXiv:1210.4491.

[138] V. F. Mukhanov, H. A. Feldman, and R. H. Brandenberger, "Theory of cosmological perturbations. Part 1. Classical perturbations. Part 2. Quantum theory of perturbations. Part 3. Extensions," Phys. Rept. **215**, 203–333 (1992).

[139] C.-P. Ma and E. Bertschinger, "Cosmological perturbation theory in the synchronous and conformal Newtonian gauges," Astrophys.J. **455**, 7–25 (1995), arXiv:astro-ph/9506072.

[140] E. Lifshitz, "On the Gravitational stability of the expanding universe," J. Phys.(USSR) **10**, 116 (1946).

[141] T. H.-C. Lu, K. Ananda, C. Clarkson, and R. Maartens, "The cosmological background of vector modes," JCAP **0902**, 023 (2009), arXiv:0812.1349.

[142] L. Pogosian, I. Wasserman, and M. Wyman, "On vector mode contribution to CMB temperature and polarization from local strings," (2006), arXiv:astro-ph/0604141.

[143] L. Husdal, "Viscosity in a Lepton-Photon Universe," (2016), arXiv:1606.02481.

[144] J. R. Bond and G. Efstathiou, "Cosmic background radiation anisotropies in universes dominated by nonbaryonic dark matter," Astrophys. J. **285**, L45–L48 (1984).

[145] P. J. E. Peebles and J. T. Yu, "Primeval adiabatic perturbation in an expanding universe," Astrophys. J. **162**, 815–836 (1970).

[146] D. Blas, J. Lesgourgues, and T. Tram, "The Cosmic Linear Anisotropy Solving System (CLASS) II: Approximation schemes," JCAP **1107**, 034 (2011), arXiv:1104.2933.

[147] U. Seljak, "A Two fluid approximation for calculating the cosmic microwave background anisotropies," Astrophys. J. **435**, L87–L90 (1994), arXiv:astro-ph/9406050.

[148] K. Petraki and R. R. Volkas, "Review of asymmetric dark matter," Int. J. Mod. Phys. **A28**, 1330028 (2013), arXiv:1305.4939.

[149] J. Barreto et al. (DAMIC Collaboration), "Direct Search for Low Mass Dark Matter Particles with CCDs," Phys.Lett. **B711**, 264–269 (2012), arXiv:1105.5191.

[150] G. M. Fuller, A. Kusenko, I. Mocioiu, and S. Pascoli, "Pulsar kicks from a dark-matter sterile neutrino," Phys.Rev. **D68**, 103002 (2003), arXiv:astro-ph/0307267.

[151] A. Boyarsky, A. Neronov, O. Ruchayskiy, and M. Shaposhnikov, "Constraints on sterile neutrino as a dark matter candidate from the diffuse x-ray background," MNRAS **370**, 213–218 (2006), arXiv:astro-ph/0512509.

[152] C. R. Watson, J. F. Beacom, H. Yuksel, and T. P. Walker, "Direct X-ray Constraints on Sterile Neutrino Warm Dark Matter," Phys.Rev. **D74**, 033009 (2006), arXiv:astro-ph/0605424.

[153] K. N. Abazajian, M. Markevitch, S. M. Koushiappas, and R. C. Hickox, "Limits on the Radiative Decay of Sterile Neutrino Dark Matter from the Unresolved Cosmic and Soft X-ray Backgrounds," Phys.Rev. **D75**, 063511 (2007), arXiv:astro-ph/0611144.

[154] C. Boehm, T. Ensslin, and J. Silk, "Can Annihilating dark matter be lighter than a few GeVs?" J.Phys. **G30**, 279–286 (2004), arXiv:astro-ph/0208458.

[155] C. Boehm, D. Hooper, J. Silk, M. Casse, and J. Paul, "MeV dark matter: Has it been detected?" Phys.Rev.Lett. **92**, 101301 (2004), arXiv:astro-ph/0309686.

[156] C. Boehm and Y. Ascasibar, "More evidence in favour of light dark matter particles?" Phys.Rev. **D70**, 115013 (2004), arXiv:hep-ph/0408213.

[157] C. Boehm and J. Silk, "A New test of the light dark matter hypothesis," Phys.Lett. **B661**, 287–289 (2008), arXiv:0708.2768.

[158] D. Hanneke, S. F. Hoogerheide, and G. Gabrielse, "Cavity Control of a Single-Electron Quantum Cyclotron: Measuring the Electron Magnetic Moment," Phys. Rev. **A83**, 052122 (2011), arXiv:1009.4831.

[159] R. Bouchendira, P. Clade, S. Guellati-Khelifa, F. Nez, and F. Biraben, "New determination of the fine structure constant and test of the quantum electrodynamics," Phys.Rev.Lett. **106**, 080801 (2011), arXiv:1012.3627.

[160] C. Boehm, Y. Farzan, T. Hambye, S. Palomares-Ruiz, and S. Pascoli, "Is it possible to explain neutrino masses with scalar dark matter?" Phys.Rev. **D77**, 043516 (2008), arXiv:hep-ph/0612228.

[161] L. Bergstrom and J. Kaplan, "Gamma-ray lines from TeV dark matter," Astropart.Phys. **2**, 261–268 (1994), arXiv:hep-ph/9403239.

[162] C. Boehm, P. Fayet, and R. Schaeffer, "Constraining dark matter candidates from structure formation," Phys.Lett. **B518**, 8–14 (2001), arXiv:astro-ph/0012504.

[163] C. Boehm, A. Riazuelo, S. H. Hansen, and R. Schaeffer, "Interacting dark matter disguised as warm dark matter," Phys.Rev. **D66**, 083505 (2002), arXiv:astro-ph/0112522.

[164] C. Boehm, H. Mathis, J. Devriendt, and J. Silk, "Non-linear evolution of suppressed dark matter primordial power spectra," MNRAS **360**, 282–287 (2005), arXiv:astro-ph/0309652.

[165] C. Boehm and R. Schaeffer, "Constraints on dark matter interactions from structure formation: Damping lengths," Astron.Astrophys. **438**, 419–442 (2005), arXiv:astro-ph/0410591.

[166] S. D. McDermott, H.-B. Yu, and K. M. Zurek, "Turning off the Lights: How Dark is Dark Matter?" Phys.Rev. **D83**, 063509 (2011), arXiv:1011.2907.

[167] K. Sigurdson, M. Doran, A. Kurylov, R. R. Caldwell, and M. Kamionkowski, "Dark-matter electric and magnetic dipole moments," Phys.Rev. **D70**, 083501 (2004), arXiv:astro-ph/0406355.

[168] S. Gardner, "Shedding Light on Dark Matter: A Faraday Rotation Experiment to Limit a Dark Magnetic Moment," Phys.Rev. **D79**, 055007 (2009), arXiv:0811.0967.

[169] S. Chang, N. Weiner, and I. Yavin, "Magnetic Inelastic Dark Matter," Phys.Rev. **D82**, 125011 (2010), arXiv:1007.4200.

[170] L. Bergstrom and P. Ullio, "Full one loop calculation of neutralino annihilation into two photons," Nucl.Phys. **B504**, 27–44 (1997), arXiv:hep-ph/9706232.

[171] J. Hisano, S. Matsumoto, and M. M. Nojiri, "Unitarity and higher order corrections in neutralino dark matter annihilation into two photons," Phys.Rev. **D67**, 075014 (2003), arXiv:hep-ph/0212022.

[172] G. Mangano, G. Miele, S. Pastor, T. Pinto, O. Pisanti, et al., "Relic neutrino decoupling including flavor oscillations," Nucl.Phys. **B729**, 221–234 (2005), arXiv:hep-ph/0506164.

[173] B. Audren, J. Lesgourgues, K. Benabed, and S. Prunet, "Conservative Constraints on Early Cosmology: an illustration of the Monte Python cosmological parameter inference code," JCAP **1302**, 001 (2013), arXiv:1210.7183.

[174] P. A. R. Ade et al. (Planck Collaboration), "Planck 2013 results. I. Overview of products and scientific results," (2013), arXiv:1303.5062.

[175] Z. Hou et al., "Constraints on Cosmology from the Cosmic Microwave Background Power Spectrum of the 2500 deg^2 SPT-SZ Survey," Astrophys. J. **782**, 74 (2014), arXiv:1212.6267.

[176] A. Arbey, M. Battaglia, and F. Mahmoudi, "Supersymmetry with Light Dark Matter confronting the recent CDMS and LHC Results," Phys. Rev. **D88**, 095001 (2013), arXiv:1308.2153.

[177] J. Jaeckel and A. Ringwald, "The Low-Energy Frontier of Particle Physics," Ann.Rev.Nucl.Part.Sci. **60**, 405–437 (2010), arXiv:1002.0329.

[178] A. Prinz, R. Baggs, J. Ballam, S. Ecklund, C. Fertig, et al., "Search for millicharged particles at SLAC," Phys.Rev.Lett. **81**, 1175–1178 (1998), arXiv:hep-ex/9804008.

[179] T. M. Crawford et al., "A Measurement of the Secondary-CMB and Millimeter-wave-foreground Bispectrum using 800 deg^2 of South Pole Telescope Data," Astrophys. J. **784**, 143 (2014), arXiv:1303.3535.

[180] E. Calabrese et al., "Cosmological parameters from pre-planck cosmic microwave background measurements," Phys. Rev. **D87**, 103012 (2013), arXiv:1302.1841.

[181] Z. Kermish et al., "The POLARBEAR Experiment," Proc. SPIE Int. Soc. Opt. Eng. **8452**, 1C (2012), arXiv:1210.7768.

[182] B. P. Crill et al., "SPIDER: A Balloon-borne Large-scale CMB Polarimeter," Proc. SPIE Int. Soc. Opt. Eng. **7010**, 2P (2008), arXiv:0807.1548.

[183] D. Boyanovsky and J. Wu, "Small scale aspects of warm dark matter : power spectra and acoustic oscillations," Phys.Rev. **D83**, 043524 (2011), arXiv:1008.0992.

[184] M. Viel, G. D. Becker, J. S. Bolton, and M. G. Haehnelt, "Warm dark matter as a solution to the small scale crisis: New constraints from high redshift Lyman-α forest data," Phys.Rev. **D88**, 043502 (2013), arXiv:1306.2314.

[185] R. Laureijs et al. (EUCLID Collaboration), "Euclid Definition Study Report," (2011), arXiv:1110.3193.

[186] M. Levi et al. (DESI), "The DESI Experiment, a whitepaper for Snowmass 2013," (2013), arXiv:1308.0847.

[187] C. Boehm, P. Fayet, and J. Silk, "Light and heavy dark matter particles," Phys.Rev. **D69**, 101302 (2004), arXiv:hep-ph/0311143.

[188] G. Mangano, A. Melchiorri, P. Serra, A. Cooray, and M. Kamionkowski, "Cosmological bounds on dark matter-neutrino interactions," Phys.Rev. **D74**, 043517 (2006), arXiv:astro-ph/0606190.

[189] P. Serra, F. Zalamea, A. Cooray, G. Mangano, and A. Melchiorri, "Constraints on neutrino – dark matter interactions from cosmic microwave background and large scale structure data," Phys.Rev. **D81**, 043507 (2010), arXiv:0911.4411.

[190] A. Dolgov, S. Dubovsky, G. Rubtsov, and I. Tkachev, "Constraints on millicharged particles from Planck data," Phys.Rev. **D88**, 117701 (2013), arXiv:1310.2376.

[191] X.-l. Chen, S. Hannestad, and R. J. Scherrer, "Cosmic microwave background and large scale structure limits on the interaction between dark matter and baryons," Phys.Rev. **D65**, 123515 (2002), arXiv:astro-ph/0202496.

[192] C. Dvorkin, K. Blum, and M. Kamionkowski, "Constraining Dark Matter-Baryon Scattering with Linear Cosmology," Phys.Rev. **D89**, 023519 (2014), arXiv:1311.2937.

[193] A. Aviles and J. L. Cervantes-Cota, "Dark degeneracy and interacting cosmic components," Phys. Rev. **D84**, 083515 (2011), [Erratum: Phys. Rev.D84,089905(2011)], arXiv:1108.2457.

[194] Y. Farzan, S. Pascoli, and M. A. Schmidt, "AMEND: A model explaining neutrino masses and dark matter testable at the LHC and MEG," JHEP **1010**, 111 (2010), arXiv:1005.5323.

[195] M. Lindner, D. Schmidt, and T. Schwetz, "Dark Matter and Neutrino Masses from Global $U(1)_{B-L}$ Symmetry Breaking," Phys.Lett. **B705**, 324–330 (2011), arXiv:1105.4626.

[196] S. S. Law and K. L. McDonald, "A Class of Inert N-tuplet Models with Radiative Neutrino Mass and Dark Matter," JHEP **1309**, 092 (2013), arXiv:1305.6467.

[197] L. Ackerman, M. R. Buckley, S. M. Carroll, and M. Kamionkowski, "Dark Matter and Dark Radiation," Phys.Rev. **D79**, 023519 (2009), arXiv:0810.5126.

[198] F.-Y. Cyr-Racine, R. de Putter, A. Raccanelli, and K. Sigurdson, "Constraints on Large-Scale Dark Acoustic Oscillations from Cosmology," Phys. Rev. **D89**, 063517 (2014), arXiv:1310.3278.

[199] S. Andreas, M. D. Goodsell, and A. Ringwald, "Hidden Photons in connection to Dark Matter," AIP Conf. Proc. **1563**, 114–117 (2013), arXiv:1306.1168.

[200] U. Franca, R. A. Lineros, J. Palacio, and S. Pastor, "Probing interactions within the dark matter sector via extra radiation contributions," Phys.Rev. **D87**, 123521 (2013), arXiv:1303.1776.

[201] F. Bouchet et al. (COrE Collaboration), "COrE (Cosmic Origins Explorer) A White Paper," (2011), arXiv:1102.2181.

[202] A. Kogut, D. Fixsen, D. Chuss, J. Dotson, E. Dwek, et al., "The Primordial Inflation Explorer (PIXIE): A Nulling Polarimeter for Cosmic Microwave Background Observations," JCAP **1107**, 025 (2011), arXiv:1105.2044.

[203] L. Anderson et al. (BOSS), "The clustering of galaxies in the SDSS-III Baryon Oscillation Spectroscopic Survey: Baryon Acoustic Oscillations in the Data Release 10 and 11 galaxy samples," MNRAS **441**, 24–62 (2014), arXiv:1312.4877.

[204] L. Anderson et al., "The clustering of galaxies in the SDSS-III Baryon Oscillation Spectroscopic Survey: measuring D_A and H at z = 0.57 from the baryon acoustic peak in the Data Release 9 spectroscopic Galaxy sample," MNRAS **439**, 83–101 (2014), arXiv:1303.4666.

[205] F. Beutler, C. Blake, M. Colless, D. H. Jones, L. Staveley-Smith, et al., "The 6dF Galaxy Survey: Baryon Acoustic Oscillations and the Local Hubble Constant," MNRAS **416**, 3017–3032 (2011), arXiv:1106.3366.

[206] C. Blake et al., "The WiggleZ Dark Energy Survey: mapping the distance-redshift relation with baryon acoustic oscillations," MNRAS **418**, 1707–1724 (2011), arXiv:1108.2635.

[207] N. Padmanabhan, X. Xu, D. J. Eisenstein, R. Scalzo, A. J. Cuesta, et al., "A 2 per cent distance to z=0.35 by reconstructing baryon acoustic oscillations - I. Methods and application to the Sloan Digital Sky Survey," MNRAS **427**, 2132–2145 (2012), arXiv:1202.0090.

[208] W. J. Percival et al. (SDSS), "Baryon Acoustic Oscillations in the Sloan Digital Sky Survey Data Release 7 Galaxy Sample," MNRAS **401**, 2148–2168 (2010), arXiv:0907.1660.

[209] D. Parkinson, S. Riemer-Sorensen, C. Blake, G. B. Poole, T. M. Davis, et al., "The WiggleZ Dark Energy Survey: Final data release and cosmological results," Phys.Rev. **D86**, 103518 (2012), arXiv:1210.2130.

[210] K. S. Dawson et al. (BOSS), "The Baryon Oscillation Spectroscopic Survey of SDSS-III," Astron.J. **145**, 10 (2013), arXiv:1208.0022.

[211] J. Hamann, S. Hannestad, J. Lesgourgues, C. Rampf, and Y. Y. Wong, "Cosmological parameters from large scale structure - geometric versus shape information," JCAP **1007**, 022 (2010), arXiv:1003.3999.

[212] E. Giusarma, R. De Putter, and O. Mena, "Testing standard and nonstandard neutrino physics with cosmological data," Phys.Rev. **D87**, 043515 (2013), arXiv:1211.2154.

[213] E. Giusarma, R. de Putter, S. Ho, and O. Mena, "Constraints on neutrino masses from Planck and Galaxy Clustering data," Phys.Rev. **D88**, 063515 (2013), arXiv:1306.5544.

[214] S. Weinberg, Cosmology, Cosmology (OUP Oxford, 2008).

[215] L. Voruz, J. Lesgourgues, and T. Tram, "The effective gravitational decoupling between dark matter and the CMB," JCAP **1403**, 004 (2014), arXiv:1312.5301.

[216] S. Vogt, S. Allen, B. Bigelow, L. Bresee, B. Brown, et al., "HIRES: the high-resolution echelle spectrometer on the Keck 10-m Telescope," Proc.SPIE Int.Soc.Opt.Eng. **2198**, 362 (1994).

[217] G. M. Bernstein, A. E. Athey, R. Bernstein, S. M. Gunnels, D. O. Richstone, and S. A. Shectman, "Volume-phase holographic spectrograph for the Magellan telescopes," Proc. SPIE Society of Photo-Optical Instrumentation Engineers (SPIE) Conference Series, **4485**, 453–459 (2002).

[218] O. Lahav and A. R. Liddle, "The Cosmological Parameters 2014," (2014), arXiv:1401.1389.

[219] P. A. R. Ade et al. (Planck), "Planck 2013 results. XX. Cosmology from Sunyaev–Zeldovich cluster counts," Astron. Astrophys. **571**, A20 (2014), arXiv:1303.5080.

[220] C. Heymans et al., "CFHTLenS tomographic weak lensing cosmological parameter constraints: Mitigating the impact of intrinsic galaxy alignments," Mon. Not. Roy. Astron. Soc. **432**, 2433 (2013), arXiv:1303.1808.

[221] A. G. Riess, L. Macri, S. Casertano, H. Lampeitl, H. C. Ferguson, et al., "A 3% Solution: Determination of the Hubble Constant with the Hubble Space Telescope and Wide Field Camera 3," Astrophys.J. **730**, 119 (2011), arXiv:1103.2976.

[222] W. L. Freedman, B. F. Madore, V. Scowcroft, C. Burns, A. Monson, et al., "Carnegie Hubble Program: A Mid-Infrared Calibration of the Hubble Constant," Astrophys.J. **758**, 24 (2012), arXiv:1208.3281.

[223] M. Niemack, P. Ade, J. Aguirre, F. Barrientos, J. Beall, et al., "ACTPol: A polarization-sensitive receiver for the Atacama Cosmology Telescope," Proc.SPIE Int.Soc.Opt.Eng. **7741**, 77411S (2010), arXiv:1006.5049.

[224] F. Atrio-Barandela and S. Davidson, "Interacting hot dark matter," Phys. Rev. **D55**, 5886–5894 (1997), arXiv:astro-ph/9702236.

[225] S. Das and N. Weiner, "Late Forming Dark Matter in Theories of Neutrino Dark Energy," Phys. Rev. **D84**, 123511 (2011), arXiv:astro-ph/0611353.

[226] F.-Y. Cyr-Racine and K. Sigurdson, "Cosmology of atomic dark matter," Phys.Rev. **D87**, 103515 (2013), arXiv:1209.5752.

[227] R. Diamanti, E. Giusarma, O. Mena, M. Archidiacono, and A. Melchiorri, "Dark Radiation and interacting scenarios," Phys.Rev. **D87**, 063509 (2013), arXiv:1212.6007.

[228] M. Blennow, E. Fernandez-Martinez, O. Mena, J. Redondo, and P. Serra, "Asymmetric Dark Matter and Dark Radiation," JCAP **1207**, 022 (2012), arXiv:1203.5803.

[229] M. R. Buckley, J. Zavala, F.-Y. Cyr-Racine, K. Sigurdson, and M. Vogelsberger, "Scattering, Damping, and Acoustic Oscillations: Simulating the Structure of Dark Matter Halos with Relativistic Force Carriers," Phys. Rev. **D90**, 043524 (2014), arXiv:1405.2075.

[230] R. Hlozek, D. Grin, D. J. Marsh, and P. G. Ferreira, "A search for ultralight axions using precision cosmological data," Phys. Rev. **D91**, 103512 (2015), arXiv:1410.2896.

[231] P. Bode, J. P. Ostriker, and N. Turok, "Halo formation in warm dark matter models," Astrophys.J. **556**, 93–107 (2001), arXiv:astro-ph/0010389.

[232] C. Boehm, "Implications of a new light gauge boson for neutrino physics," Phys.Rev. **D70**, 055007 (2004), arXiv:hep-ph/0405240.

[233] C.-W. Chiang, G. Faisel, Y.-F. Lin, and J. Tandean, "Constraining Nonstandard Neutrino-Electron Interactions due to a New Light Spin-1 Boson," JHEP **1310**, 150 (2013), arXiv:1204.6296.

[234] A. Arhrib, C. Bœhm, E. Ma, and T.-C. Yuan, "Radiative Model of Neutrino Mass with Neutrino Interacting MeV Dark Matter," JCAP **1604**, 049 (2016), arXiv:1512.08796 [hep-ph].

[235] P. Binetruy, G. Girardi, and P. Salati, "Constraints on a System of Two Neutral Fermions From Cosmology," Nucl.Phys. **B237**, 285 (1984).

[236] K. Griest and D. Seckel, "Three exceptions in the calculation of relic abundances," Phys.Rev. **D43**, 3191–3203 (1991).

[237] P. D. Serpico and G. G. Raffelt, "MeV-mass dark matter and primordial nucleosynthesis," Phys. Rev. **D70**, 043526 (2004), arXiv:astro-ph/0403417.

[238] C. Boehm, M. J. Dolan, and C. McCabe, "A Lower Bound on the Mass of Cold Thermal Dark Matter from Planck," JCAP **1308**, 041 (2013), arXiv:1303.6270.

[239] C. Boehm, M. J. Dolan, and C. McCabe, "Increasing Neff with particles in thermal equilibrium with neutrinos," JCAP **1212**, 027 (2012), arXiv:1207.0497.

[240] K. M. Nollett and G. Steigman, "BBN And The CMB Constrain Light, Electromagnetically Coupled WIMPs," Phys.Rev. **D89**, 083508 (2014), arXiv:1312.5725.

[241] G. Steigman, "Equivalent Neutrinos, Light WIMPs, and the Chimera of Dark Radiation," Phys.Rev. **D87**, 103517 (2013), arXiv:1303.0049.

[242] Y. Farzan and S. Palomares-Ruiz, "Dips in the Diffuse Supernova Neutrino Background," JCAP **1406**, 014 (2014), arXiv:1401.7019.

[243] D. E. Kaplan, M. A. Luty, and K. M. Zurek, "Asymmetric Dark Matter," Phys.Rev. **D79**, 115016 (2009), arXiv:0901.4117.

[244] B. A. Reid, W. J. Percival, D. J. Eisenstein, L. Verde, D. N. Spergel, et al., "Cosmological Constraints from the Clustering of the Sloan Digital Sky Survey DR7 Luminous Red Galaxies," MNRAS **404**, 60–85 (2010), arXiv:0907.1659.

[245] S. Riemer-Sorensen, C. Blake, D. Parkinson, T. M. Davis, S. Brough, et al., "The WiggleZ Dark Energy Survey: Cosmological neutrino mass constraint from blue high-redshift galaxies," Phys.Rev. **D85**, 081101 (2012), arXiv:1112.4940.

[246] M. Tegmark et al. (SDSS), "Cosmological Constraints from the SDSS Luminous Red Galaxies," Phys.Rev. **D74**, 123507 (2006), arXiv:astro-ph/0608632.

[247] A. Lewis and S. Bridle, "Cosmological parameters from CMB and other data: A Monte Carlo approach," Phys.Rev. **D66**, 103511 (2002), arXiv:astro-ph/0205436.

[248] L. Perotto, J. Lesgourgues, S. Hannestad, H. Tu, and Y. Y. Wong, "Probing cosmological parameters with the CMB: Forecasts from full Monte Carlo simulations," JCAP **0610**, 013 (2006), arXiv:astro-ph/0606227.

[249] H.-J. Seo and D. J. Eisenstein, "Probing dark energy with baryonic acoustic oscillations from future large galaxy redshift surveys," Astrophys.J. **598**, 720–740 (2003), arXiv:astro-ph/0307460.

[250] M. Tegmark, A. Taylor, and A. Heavens, "Karhunen-Loeve eigenvalue problems in cosmology: How should we tackle large data sets?" Astrophys.J. **480**, 22 (1997), arXiv:astro-ph/9603021.

[251] G. Jungman, M. Kamionkowski, A. Kosowsky, and D. N. Spergel, "Cosmological parameter determination with microwave background maps," Phys.Rev. **D54**, 1332–1344 (1996), arXiv:astro-ph/9512139.

[252] R. A. Fisher, "The logic of inductive inference," Journal of the Royal Statistical Society **98**, pp. 39–82 (1935).

[253] A. Font-Ribera, P. McDonald, N. Mostek, B. A. Reid, H.-J. Seo, et al., "DESI and other dark energy experiments in the era of neutrino mass measurements," JCAP **1405**, 023 (2014), arXiv:1308.4164.

[254] L. R. Abramo and K. E. Leonard, "Why multi-tracer surveys beat cosmic variance," MNRAS **432**, 318 (2013), arXiv:1302.5444.

[255] E. Bertschinger, "The Effects of Cold Dark Matter Decoupling and Pair Annihilation on Cosmological Perturbations," Phys.Rev. **D74**, 063509 (2006), arXiv:astro-ph/0607319.

[256] M. Davis, G. Efstathiou, C. S. Frenk, and S. D. White, "The Evolution of Large Scale Structure in a Universe Dominated by Cold Dark Matter," Astrophys.J. **292**, 371–394 (1985).

[257] J. Dubinski and R. Carlberg, "The Structure of cold dark matter halos," Astrophys.J. **378**, 496 (1991).

[258] S. E. Koposov, V. Belokurov, G. Torrealba, and N. W. Evans, "Beasts of the Southern Wild: Discovery of nine Ultra Faint satellites in the vicinity of the Magellanic Clouds," Astrophys. J. **805**, 130 (2015), arXiv:1503.02079.

[259] K. Bechtol et al. (DES), "Eight New Milky Way Companions Discovered in First-Year Dark Energy Survey Data," Astrophys. J. **807**, 50 (2015), arXiv:1503.02584.

[260] A. J. Benson, C. Lacey, C. Baugh, S. Cole, and C. Frenk, "The Effects of photoionization on galaxy formation. 1. Model and results at z = 0," MNRAS **333**, 156 (2002), arXiv:astro-ph/0108217.

[261] R. S. Somerville, "Can Photoionization Squelching Resolve the Substructure Crisis?" ApJ **572**, L23–L26 (2002), astro-ph/0107507.

[262] T. Sawala et al., "Local Group galaxies emerge from the dark," (2014), arXiv:1412.2748.

[263] T. Sawala et al., "Bent by baryons: the low mass galaxy-halo relation," Mon. Not. Roy. Astron. Soc. **448**, 2941–2947 (2015), arXiv:1404.3724.

[264] M. Boylan-Kolchin, J. S. Bullock, and M. Kaplinghat, "The Milky Way's bright satellites as an apparent failure of ΛCDM," MNRAS **422**, 1203–1218 (2012), arXiv:1111.2048.

[265] J. Wang, C. S. Frenk, J. F. Navarro, L. Gao, and T. Sawala, "The missing massive satellites of the Milky Way," MNRAS **424**, 2715–2721 (2012), arXiv:1203.4097.

[266] M. Cautun, C. S. Frenk, R. van de Weygaert, W. A. Hellwing, and B. J. T. Jones, "Milky Way mass constraints from the Galactic satellite gap," MNRAS **445**, 2049 (2014), arXiv:1405.7697.

[267] T. Piffl and et al., "The RAVE survey: the Galactic escape speed and the mass of the Milky Way," Astron. & Astrop. **562**, A91 (2014), arXiv:1309.4293.

[268] W. Wang, J. Han, A. P. Cooper, S. Cole, C. Frenk, and B. Lowing, "Estimating the dark matter halo mass of our Milky Way using dynamical tracers," MNRAS **453**, 377–400 (2015), arXiv:1502.03477.

[269] R. Schaeffer and J. Silk, "Cold, warm, or hot dark matter - Biased galaxy formation and pancakes," Astrophys.J. **332**, 1–16 (1988).

[270] X. Chu and B. Dasgupta, "Dark Radiation Alleviates Problems with Dark Matter Halos," Phys.Rev.Lett. **113**, 161301 (2014), arXiv:1404.6127.

[271] D. N. Spergel and P. J. Steinhardt, "Observational evidence for selfinteracting cold dark matter," Phys. Rev. Lett. **84**, 3760–3763 (2000), arXiv:astro-ph/9909386.

[272] M. Rocha, A. H. Peter, J. S. Bullock, M. Kaplinghat, S. Garrison-Kimmel, et al., "Cosmological Simulations with Self-Interacting Dark Matter I: Constant Density Cores and Substructure," MNRAS **430**, 81–104 (2013), arXiv:1208.3025.

[273] M. Vogelsberger, J. Zavala, C. Simpson, and A. Jenkins, "Dwarf galaxies in CDM and SIDM with baryons: observational probes of the nature of dark matter," MNRAS **444**, 3684 (2014), arXiv:1405.5216.

[274] M.-Y. Wang, A. H. G. Peter, L. E. Strigari, A. R. Zentner, B. Arant, et al., "Cosmological Simulations of Decaying Dark Matter: Implications for Small-scale Structure of Dark Matter Halos," MNRAS **445**, 614 (2014), arXiv:1406.0527.

[275] S. Agarwal, P.-S. Corasaniti, S. Das, and Y. Rasera, "Small scale clustering of late forming dark matter," Phys. Rev. D. **92**, 063502 (2015), arXiv:1412.1103.

[276] M. R. Lovell, C. S. Frenk, V. R. Eke, A. Jenkins, L. Gao, et al., "The properties of warm dark matter haloes," MNRAS **439**, 300–317 (2014), arXiv:1308.1399.

[277] A. Schneider, D. Anderhalden, A. Maccio, and J. Diemand, "Warm dark matter does not do better than cold dark matter in solving small-scale inconsistencies," Mon. Not. Roy. Astron. Soc. **441**, 6 (2014), arXiv:1309.5960.

[278] J. Diemand, B. Moore, and J. Stadel, "Earth-mass dark-matter haloes as the first structures in the early Universe," Nature **433**, 389–391 (2005), astro-ph/0501589.

[279] R. E. Angulo and S. D. M. White, "The Birth and Growth of Neutralino Haloes," MNRAS **401**, 1796 (2010), arXiv:0906.1730.

[280] F.-Y. Cyr-Racine, K. Sigurdson, J. Zavala, T. Bringmann, M. Vogelsberger, and C. Pfrommer, "ETHOS - An Effective Theory of Structure Formation: From dark particle physics to the matter distribution of the Universe," (2015), arXiv:1512.05344.

[281] M. Vogelsberger, J. Zavala, F.-Y. Cyr-Racine, C. Pfrommer, T. Bringmann, and K. Sigurdson, "ETHOS - An Effective Theory of Structure Formation: Dark matter physics as a possible explanation of the small-scale CDM problems," (2015), arXiv:1512.05349.

[282] V. Springel, "The Cosmological simulation code GADGET-2," MNRAS **364**, 1105–1134 (2005), arXiv:astro-ph/0505010.

[283] P. Colin, O. Valenzuela, and V. Avila-Reese, "On the Structure of Dark Matter Halos at the Damping Scale of the Power Spectrum with and without Relict Velocities," Astrophys.J. **673**, 203–214 (2008), arXiv:0709.4027.

[284] X. Xue et al. (SDSS Collaboration), "The Milky Way's Circular Velocity Curve to 60 kpc and an Estimate of the Dark Matter Halo Mass from Kinematics of 2400 SDSS Blue Horizontal Branch Stars," Astrophys.J. **684**, 1143–1158 (2008), arXiv:0801.1232.

[285] M. Boylan-Kolchin, J. S. Bullock, S. T. Sohn, G. Besla, and R. P. van der Marel, "The Space Motion of Leo I: The Mass of the Milky Way's Dark Matter Halo," Astrophys.J. **768**, 140 (2013), arXiv:1210.6046.

[286] H. M. Courtois, D. Pomarede, R. B. Tully, and D. Courtois, "Cosmography of the Local Universe," Astron.J. **146**, 69 (2013), arXiv:1306.0091.

[287] V. Springel, N. Yoshida, and S. D. White, "GADGET: A Code for collisionless and gasdynamical cosmological simulations," New Astron. **6**, 79 (2001), arXiv:astro-ph/0003162.

[288] B. Willman, "In Pursuit of the Least Luminous Galaxies," Adv.Astron. **2010**, 285454 (2010), arXiv:0907.4758.

[289] J. S. Bullock, "Notes on the Missing Satellites Problem," (2010), arXiv:1009.4505.

[290] A. Fattahi, J. F. Navarro, T. Sawala, C. S. Frenk, K. A. Oman, R. A. Crain, M. Furlong, M. Schaller, J. Schaye, T. Theuns, and A. Jenkins, "The APOSTLE project: Local Group kinematic mass constraints and simulation candidate selection," ArXiv e-prints (2015), arXiv:1507.03643.

[291] A. Jenkins, "Second-order Lagrangian perturbation theory initial conditions for resimulations," MNRAS **403**, 1859–1872 (2010), arXiv:0910.0258.

[292] S. R. Knollmann and A. Knebe, "Ahf: Amiga's Halo Finder," Astrophys.J.Suppl. **182**, 608–624 (2009), arXiv:0904.3662.

[293] J. Wolf, G. D. Martinez, J. S. Bullock, M. Kaplinghat, M. Geha, R. R. Muñoz, J. D. Simon, and F. F. Avedo, "Accurate masses for dispersion-supported galaxies," MNRAS **406**, 1220–1237 (2010), arXiv:0908.2995.

[294] C. Power, J. Navarro, A. Jenkins, C. Frenk, S. D. White, et al., "The Inner structure of Lambda CDM halos. 1. A Numerical convergence study," MNRAS **338**, 14–34 (2003), arXiv:astro-ph/0201544.

[295] J. F. Navarro, C. S. Frenk, and S. D. White, "A Universal density profile from hierarchical clustering," Astrophys.J. **490**, 493–508 (1997), arXiv:astro-ph/9611107.

[296] T. Sawala et al., "The APOSTLE simulations: solutions to the Local Group's cosmic puzzles," Mon. Not. Roy. Astron. Soc. **457**, 1931 (2016), arXiv:1511.01098.

[297] A. H. G. Peter, "Dark Matter: A Brief Review," ArXiv e-prints (2012), arXiv:1201.3942.

[298] E. Churazov, R. Sunyaev, S. Sazonov, M. Revnivtsev, and D. Varshalovich, "Positron annihilation spectrum from the Galactic Center region observed by SPI/INTEGRAL," MNRAS **357**, 1377–1386 (2005), arXiv:astro-ph/0411351.

[299] J. Knodlseder et al., "The all-sky distribution of 511-keV electron positron annihilation emission," Astron. Astrophys. **441**, 513–532 (2005), arXiv:astro-ph/0506026.

[300] P. Jean, J. Knodlseder, W. Gillard, N. Guessoum, K. Ferriere, et al., "Spectral analysis of the galactic e+ e- annihilation emission," Astron.Astrophys. **445**, 579–589 (2006), arXiv:astro-ph/0509298.

[301] G. Weidenspointner, C. Shrader, J. Knoedlseder, P. Jean, V. Lonjou, et al., "The sky distribution of positronium annihilation continuum emission

measured with spi/integral," Astron.Astrophys. **450**, 1012 (2006), arXiv:astro-ph/0601673.

[302] T. Siegert, R. Diehl, G. Khachatryan, M. G. H. Krause, F. Guglielmetti, J. Greiner, A. W. Strong, and X. Zhang, "Gamma-ray spectroscopy of Positron Annihilation in the Milky Way," Astron. Astrophys. **586**, A84 (2016), arXiv:1512.00325.

[303] G. Weidenspointner, G. Skinner, P. Jean, J. Knodlseder, P. von Ballmoos, et al., "An asymmetric distribution of positrons in the Galactic disk revealed by gamma-rays," Nature **451**, 159–162 (2008).

[304] N. Prantzos et al., "The 511 keV emission from positron annihilation in the Galaxy," Rev. Mod. Phys. **83**, 1001–1056 (2011), arXiv:1009.4620.

[305] R. Diehl, H. Halloin, K. Kretschmer, A. Strong, W. Wang, et al., "26al in the inner galaxy," Astron.Astrophys. **449**, 1025–1031 (2006), arXiv:astro-ph/0512334.

[306] A. C. Vincent, P. Martin, and J. M. Cline, "Interacting dark matter contribution to the Galactic 511 keV gamma ray emission: constraining the morphology with INTEGRAL/SPI observations," JCAP **1204**, 022 (2012), arXiv:1201.0997.

[307] Y. Ascasibar, P. Jean, C. Boehm, and J. Knoedlseder, "Constraints on dark matter and the shape of the Milky Way dark halo from the 511-keV line," MNRAS **368**, 1695–1705 (2006), arXiv:astro-ph/0507142.

[308] J. M. Cline and A. R. Frey, "Abelian dark matter models for 511 keV gamma rays and direct detection," Annalen Phys. **524**, 579–590 (2012), arXiv:1204.1965.

[309] M. H. Chan, "Electron–positron pair production near the Galactic Centre and the 511 keV emission line," Mon. Not. Roy. Astron. Soc. **456**, L113–L116 (2016), arXiv:1511.07933.

[310] J. F. Beacom and H. Yuksel, "Stringent constraint on galactic positron production," Phys.Rev.Lett. **97**, 071102 (2006), arXiv:astro-ph/0512411.

[311] P. Sizun, M. Casse, S. Schanne, and B. Cordier, "Constraints on the injection energy of positrons in the Galactic centre region," (2007), [ESA Spec. Publ.622,61(2007)], arXiv:astro-ph/0702061.

[312] L. Zhang, X. Chen, M. Kamionkowski, Z.-g. Si, and Z. Zheng, "Constraints on radiative dark-matter decay from the cosmic microwave background," Phys. Rev. **D76**, 061301 (2007), arXiv:0704.2444.

[313] S. Galli, F. Iocco, G. Bertone, and A. Melchiorri, "CMB constraints on Dark Matter models with large annihilation cross-section," Phys. Rev. **D80**, 023505 (2009), arXiv:0905.0003.

[314] T. R. Slatyer, N. Padmanabhan, and D. P. Finkbeiner, "CMB Constraints on WIMP Annihilation: Energy Absorption During the Recombination Epoch," Phys. Rev. **D80**, 043526 (2009), arXiv:0906.1197.

[315] T. Kanzaki, M. Kawasaki, and K. Nakayama, "Effects of Dark Matter Annihilation on the Cosmic Microwave Background," Prog. Theor. Phys. **123**, 853–865 (2010), arXiv:0907.3985.

[316] J. Hisano, M. Kawasaki, K. Kohri, T. Moroi, K. Nakayama, and T. Sekiguchi, "Cosmological constraints on dark matter models with velocity-dependent annihilation cross section," Phys. Rev. **D83**, 123511 (2011), arXiv:1102.4658.

[317] G. Hutsi, J. Chluba, A. Hektor, and M. Raidal, "WMAP7 and future CMB constraints on annihilating dark matter: implications on GeV-scale WIMPs," Astron. Astrophys. **535**, A26 (2011), arXiv:1103.2766.

[318] S. Galli, F. Iocco, G. Bertone, and A. Melchiorri, "Updated CMB constraints on Dark Matter annihilation cross-sections," Phys. Rev. **D84**, 027302 (2011), arXiv:1106.1528.

[319] D. P. Finkbeiner, S. Galli, T. Lin, and T. R. Slatyer, "Searching for Dark Matter in the CMB: A Compact Parameterization of Energy Injection from New Physics," Phys. Rev. **D85**, 043522 (2012), arXiv:1109.6322.

[320] T. R. Slatyer, "Energy injection and absorption in the cosmic dark ages," Phys. Rev. D **87**, 123513 (2013), arXiv:1211.0283.

[321] S. Galli, T. R. Slatyer, M. Valdes, and F. Iocco, "Systematic Uncertainties In Constraining Dark Matter Annihilation From The Cosmic Microwave Background," Phys. Rev. **D88**, 063502 (2013), arXiv:1306.0563.

[322] L. Lopez-Honorez, O. Mena, S. Palomares-Ruiz, and A. C. Vincent, "Constraints on dark matter annihilation from CMB observations before Planck," JCAP **1307**, 046 (2013), arXiv:1303.5094.

[323] M. S. Madhavacheril, N. Sehgal, and T. R. Slatyer, "Current Dark Matter Annihilation Constraints from CMB and Low-Redshift Data," Phys. Rev. **D89**, 103508 (2014), arXiv:1310.3815.

[324] R. Diamanti, L. Lopez-Honorez, O. Mena, S. Palomares-Ruiz, and A. C. Vincent, "Constraining Dark Matter Late-Time Energy Injection: Decays and P-Wave Annihilations," JCAP **1402**, 017 (2014), arXiv:1308.2578.

[325] T. R. Slatyer, "Indirect dark matter signatures in the cosmic dark ages. I. Generalizing the bound on s-wave dark matter annihilation from Planck results," Phys. Rev. **D93**, 023527 (2016), arXiv:1506.03811.

[326] M. Kawasaki, K. Nakayama, and T. Sekiguchi, "CMB Constraint on Dark Matter Annihilation after Planck 2015," Phys. Lett. **B756**, 212–215 (2016), arXiv:1512.08015.

[327] E. W. Kolb, M. S. Turner, and T. P. Walker, "The Effect of Interacting Particles on Primordial Nucleosynthesis," Phys. Rev. **D34**, 2197 (1986).

[328] K. M. Nollett and G. Steigman, "BBN And The CMB Constrain Neutrino Coupled Light WIMPs," Phys. Rev. **D91**, 083505 (2015), arXiv:1411.6005.

[329] G. Steigman and K. M. Nollett, "Light WIMPs, Equivalent Neutrinos, BBN, and the CMB," Mem. Soc. Ast. It. **85**, 175 (2014), arXiv:1401.5488.

[330] T. R. Slatyer, "Indirect Dark Matter Signatures in the Cosmic Dark Ages II. Ionization, Heating and Photon Production from Arbitrary Energy Injections," Phys. Rev. **D93**, 023521 (2016), arXiv:1506.03812.

[331] C. M. Ho and R. J. Scherrer, "Limits on MeV Dark Matter from the Effective Number of Neutrinos," Phys. Rev. **D87**, 023505 (2013), arXiv:1208.4347.

[332] O. Pisanti, A. Cirillo, S. Esposito, F. Iocco, G. Mangano, et al., "PArthENoPE: Public Algorithm Evaluating the Nucleosynthesis of Primordial Elements," Comput.Phys.Commun. **178**, 956–971 (2008), arXiv:0705.0290.

[333] A. Coc, P. Petitjean, J.-P. Uzan, E. Vangioni, P. Descouvemont, C. Iliadis, and R. Longland, "New reaction rates for improved primordial D/H calculation and the cosmic evolution of deuterium," Phys. Rev. **D92**, 123526 (2015), arXiv:1511.03843.

[334] K. A. Olive et al. (Particle Data Group), "Review of Particle Physics," Chin. Phys. **C38**, 090001 (2014).

[335] Y. I. Izotov, G. Stasinska, and N. G. Guseva, "Primordial 4He abundance," Astron. Astrophys. **558**, A57 (2013), arXiv:1308.2100.

[336] D. P. Finkbeiner and N. Weiner, "Exciting Dark Matter and the INTEGRAL/SPI 511 keV signal," Phys.Rev. **D76**, 083519 (2007), arXiv:astro-ph/0702587.

[337] M. Pospelov and A. Ritz, "The galactic 511 keV line from electroweak scale WIMPs," Phys.Lett. **B651**, 208–215 (2007), arXiv:hep-ph/0703128.

[338] A. R. Frey and N. B. Reid, "Cosmic microwave background constraints on dark matter models of the Galactic center 511 keV signal," Phys. Rev. **D87**, 103508 (2013), arXiv:1301.0819.